UNIVERSITY OF SOUTHAMPTON

Active structural acoustic control of sound transmission through a plate

by Thomas Christopher Sors

A thesis submitted for the degree of
Doctor of Philosophy

Signal Processing and Control Group
Institute of Sound and Vibration Research
Faculty of Engineering and Applied Science

November 2000

UNIVERSITY OF SOUTHAMPTON

ABSTRACT

FACULTY OF ENGINEERING AND APPLIED SCIENCE
INSTITUTE OF SOUND AND VIBRATION RESEARCH

Doctor of Philosophy

ACTIVE STRUCTURAL ACOUSTIC CONTROL OF SOUND TRANSMISSION THROUGH A PLATE

by Thomas Christopher Sors

This thesis is concerned with the development of systems for active structural acoustic control (ASAC) of sound transmission through a plate.

The theory of plate vibrations and the subsequent sound radiation are described. Plate vibrations are analysed in terms of the conventional structural mode approach, and in terms of radiation modes, which are a set of independently radiating velocity distributions. The first radiation mode is much more efficient than the others at low frequencies and has a shape approximately corresponding to the volume velocity of the plate. This is thus chosen as the variable to be controlled in later parts of the thesis.

A comparison of different actuators and sensors follows. Ideally, a uniform force actuator would be used with a volume velocity sensor. There are inherent problems with using a distributed uniform force actuator with a distributed volume velocity sensor, so in this work piezoceramic actuators are used instead. The placing of the actuators and sensors should be such that the frequency response function between them has as little phase loss as possible for the purposes of feedback control.

Feedback control and a number of related issues are discussed. One control architecture called Internal Model Control (IMC) is analysed in more detail and is then used in a real-time experiment to cancel the output of a volume velocity sensor using piezoceramic actuators.

The distributed volume velocity sensor is then replaced by a number of accelerometers on the plate and several different cost functions are investigated, including summing their integrated outputs to estimate volume velocity, multi-channel cost functions, such as the control of higher order radiation modes and control of the frequency dependent shape of the first radiation mode, and a configuration using multiple local control systems on a structure. A control architecture is also outlined which uses structural reference sensors and acoustic error sensors. This method is then tested in real-time experiments.

Contents

Acknowledgements

First, I would like to express my thanks to Professor S. J. Elliott. He has been an excellent supervisor and I am deeply grateful to him.

Thank you also to all the SPCG and especially those who shared an office with me during the last four years. Special thanks also to Marty Johnson and Boaz Rafaely who have helped me a great deal, especially in the early stages of the project.

My parents and family have been the ones to love and support me throughout my time here and I would like to thank them for this.

This work has been sponsored by the TNO Institute of Applied Physics, Delft, The Netherlands. Many thanks to Niek Doelman, Ed Doppenberg, and Arthur Berkhoff from the TPD as well as all others who I called upon during my visits there.

Chapter 1

Introduction

1.1 Objectives and contribution of thesis

This thesis describes the development of several active structural acoustic control (ASAC) systems for reducing the transmission of sound through a plate. This development has two major stages; in the first stage, the structure to be controlled is modelled and an understanding of the physical processes which give rise to the sound radiation is used to provide insight into which control strategies might work best for the purposes of controlling sound transmission. The second stage is to implement the chosen control system, and in order to do this successfully a number of practical issues need to be considered.

ASAC is a subject which has developed largely within the last ten to fifteen years. It combines the fields of active sound control and active vibration control to create a more subtle control system which reduces sound transmission through, or equivalently the radiation from, structures by altering their vibrations in such a way that the overall radiation efficiency of the structure is reduced.

ASAC brings together a number of engineering disciplines. In the first place, an understanding of the physical processes which give rise to sound radiation or transmission through a plate is needed, involving the fields of acoustics and of structural vibrations. Once these physical processes are well understood, the development of an appropriate controller involves signal processing, control systems design, and in a more practical sense, a knowledge of transducers

and of Digital Signal Processing (DSP) chip programming.

The four main objectives of the thesis are

1. To compare the physical limitations of different actuators and sensors and their placement for active structural acoustic control purposes.

2. To investigate the use of Internal Model Control (IMC) and its implementation for active structural acoustic control purposes.

3. To compare the physical limitations of different cost functions for active structural acoustic control.

4. To investigate the interaction between the physical limitations and control limitations of active structural acoustic control.

In relation to these, the main contributions to research in the field of ASAC from this thesis are

1. In the comparison of transducers for ASAC; particular attention is brought to the use of multiple accelerometers as structural sensors compared to the distributed volume velocity sensor.

2. An extension to the IMC algorithm is also developed which includes separate structural reference sensors and acoustic error sensors, as opposed to normal IMC systems which only use one set of sensors.

3. A discussion of important implementation issues, especially robustness and controller delay.

4. A discussion of the interaction between physical limitations and control limitations of ASAC.

1.2 Structure of thesis

In this thesis a plate is chosen to be the structure on which active structural acoustic control is demonstrated, as this gives a clear physical understanding of the concepts but avoids the details of larger, more complicated structures which are ultimately the ones which need to be controlled if the technique is to have any practical use. The broad steps in the thesis are firstly to understand and model the physical system and the processes giving rise to sound radiation. This gives some insight into which cost or error functions might work best to reduce sound power radiation through physical reasoning. These cost functions are first of all tested using feedforward control simulations as these give an indication of the best possible attenuation that could be achieved for a given physical system. Feedforward control is fairly well understood and works for tonal or predictable disturbances where an external reference signal can be measured easily. This thesis however, focuses on the control of more random or broadband disturbances and hence feedback control is used. The lack of a time-advanced reference signal and the need for robust stability inevitably lead to a decrease in performance with respect to feedforward control. The aim, however, is to get as close as possible to the attenuations obtained through feedforward control by using feedback control with appropriate actuators and sensors. After these control simulations, the final stage is implementation and again, there are inevitable losses in performance at this stage but the aim is to achieve attenuations as close to those predicted through simulations as possible. Some of this work has been reported at conferences [1, 2] and in a journal paper [3].

Going through these stages of development, the thesis is divided into nine chapters.

Chapter 2 gives the background and context to the thesis and a short history of active control and ASAC. The literature relevant to the thesis is reviewed and the current state of research in ASAC is described.

Chapter 3 is concerned with modelling the sound radiation from plates. Plate vibrations and sound radiation are described in terms of the standard method of structural modes and the Rayleigh integral respectively and then, in terms of a set of independently radiating velocity distributions, called radiation modes. It is shown that, at low frequencies, the shape of the first radiation mode is proportional to the volume velocity of the plate. As the first radiation mode accounts for most sound radiation at low frequencies, it follows that if it can be controlled, then

the overall sound radiation is reduced and this provides the motivation for much of the rest of the thesis. The relationships between the two approaches of structural and radiation modes are then discussed.

Chapter 4 describes the different actuators and sensors which can be used for ASAC. Three different types of structural actuator are considered; the point force actuator, the piezoceramic actuator, and a uniform force actuator. In direct analogy, three corresponding structural sensors are modelled; the accelerometer, the piezoceramic patch sensor, and the distributed volume velocity sensor. Plate excitation by an acoustic plane wave, an enclosed source, and the use of microphones, to measure the far field radiated sound power are also covered in this chapter. The placement of transducers on a structure for ASAC is also an important consideration and this is also discussed. Feedforward simulations are used to demonstrate the effectiveness of the different transducers and various transducer locations for ASAC purposes. The best combination of transducers is found to be a uniform force actuator used with a distributed volume velocity sensor but, as a practical uniform force actuator has not yet been developed, a design using piezoceramic actuators and a distributed volume velocity sensor is used in the following chapters of the thesis.

In chapter 5 feedback control is used in an application where no suitable reference signal is easily measurable. A number of issues which arise when using feedback controllers are introduced. One particular method of designing feedback controllers is called Internal Model Control (IMC) and this is reviewed in more detail. Using the transducer configuration developed above, an experimental rig is designed with a distributed volume velocity sensor and piezoceramic actuators. Measured frequency response functions between the actuators and sensors are then used to conduct simulations of IMC. After these simulations, the implementation of a real-time IMC controller and the resulting implementation issues are described.

Chapter 6 then considers a number of different cost functions for ASAC purposes, all using accelerometers. Active structural acoustic control aims to reduce sound transmission or radiation from a structure by altering the structural vibrations. The goal is then to design a structural sensor whose output is strongly related to radiated sound pressure so that minimizing the magnitude of the sensor output signal will also minimize the total radiated sound power [4]. Summing the output of an increasing number of accelerometers is compared with measuring the true volume velocity and, as the number of accelerometers is increased, their output

approximates the true volume velocity more and more closely. Other cost functions using accelerometers considered are multi-channel feedforward control, control of higher order radiation modes, which does not give significant improvements over controlling the volume velocity, and controlling the changing shape of the first radiation mode, which does give a slight increase in performance. Another configuration which uses a large number of local control systems on the structure, each with its own actuator, sensor, and controller is also considered and may hold some promise for future applications. In this chapter, feedforward simulations are again used to compare the best possible performance which can be obtained with each different cost function.

In chapter 7, an extension to the normal IMC algorithm is also developed which uses separate reference sensors and error sensors. This has particular relevance to ASAC as it enables reference sensors to be placed on the structure and error sensors to be placed in the far-field. Again, simulations using modelled frequency response functions are performed.

Chapter 8 then considers the implementation of a real-time ASAC system using a modified experimental rig and the new cost function with structural reference sensors and acoustic error sensors. A new experimental arrangement, using multiple accelerometers in place of the distributed volume velocity sensor, is described and, using measured responses, the performance of a real-time control system is predicted. This real-time IMC system is then implemented and the results are presented. During the implementation new issues arise and these are discussed.

Finally, chapter 9 presents the conclusions and a number of possible directions for future work.

Two appendices are included the first of which compares the different plate boundary conditions which are used in this thesis and the second of which describes a common mathematical formulation for analysing two of the different cost functions which are used in the thesis.

Chapter 2

Background and historical perspective

2.1 An introduction to active control

2.1.1 Why active control?

Reducing noise, or noise control, has always been one of the main reasons for developing an understanding in acoustics. Conventional noise control techniques typically require the addition of mass or damping to the system to be controlled or system modification through re-design. These techniques usually imply a significant mass increase and it can be difficult to predict their precise effect. They also tend to be ineffective at low frequencies. For example, consider an anechoic room which is required to stop reflections down to a frequency of around $100Hz$. At these frequencies, the wavelength of sound in air is around $3.43m$ and, in order for porous materials to be effective they need to be of a thickness around a quarter of the wavelength of the incident sound [5]. Foam wedges of approximately $0.85m$ length are then required on the walls, floors and ceilings of the room. Obviously, these passive techniques are impractical in many circumstances and an alternative technology which is becoming popular is the use of active noise control techniques. An excellent review of passive control techniques is given by Bies and Hansen [6].

By definition, active control can be said to be a method of altering the behaviour of a system by the introduction of an energy source whose output is dependent on the response of the system. Conversely then, passive control is when no energy is introduced to the system to alter its behaviour [7]. Active control processes can range from the small scale, for example control of chemical reactions, to the large scale where active methods are used to control the vibrations of buildings subject to seismic vibrations for example. There are also examples of active control seen in natural biological systems such as in the human ear or in the central nervous system.

This thesis is however concerned specifically with controlling sound radiation using active methods. Active control of sound thus refers to the reduction of noise using some type of sound-generating actuator and some type of sensor which can measure the sound field or sound-related variables. Normally, this refers to the use of loudspeakers as actuators, and microphones as sensors which measure the response of the system.

A number of applications in which active noise control is used are outlined in the next section. These tend to be in situations where space and weight are important considerations such as in aircraft or other forms of transportation. The cost of active control is often large compared to passive control but, as the price of fast DSP chips and transducers fall, active control should become an increasingly attractive solution to noise control problems in the future. A brief comparison of active control and passive control is given in table 2.1.

Passive control	Active control
Most effective at high frequency	Most effective at low frequency
Adds extra mass and damping	Uses compact and lightweight transducers
May involve large-scale changes to system	Only minor changes to system may be needed
Low-cost to implement	Relatively expensive to implement

Table 2.1: Comparison of passive control and active control

Figure 2.1 shows a feedback control system but has the essential components of any active control system. The disturbance is the response of the physical system under control, to the original, or primary, excitation. The three blocks which make up the control system can take many different forms, the most important of which for active control of sound (ACS) and ASAC will be covered in the following sections, but the structure essentially remains the same for any active control system. The first element, the sensors, measure the response of the system in some way. The measured signal is then fed to a controller which processes the information in some

way to produce a control signal. There are various ways of processing the measured signals dealt with in control systems theory. This thesis will deal mainly with one possible method called internal model control. The control signals are then fed to the secondary actuators which affect the total response of the system. The final, altered, response of the system is a superposition of the effects from the primary disturbance and the effects of the secondary actuators. An additional definition used in describing active control systems is the plant. This is defined as the complete system between the electrical input to the control actuators and the electrical ouputs from the sensors. This includes the response of the transducers and that of the physical system under control.

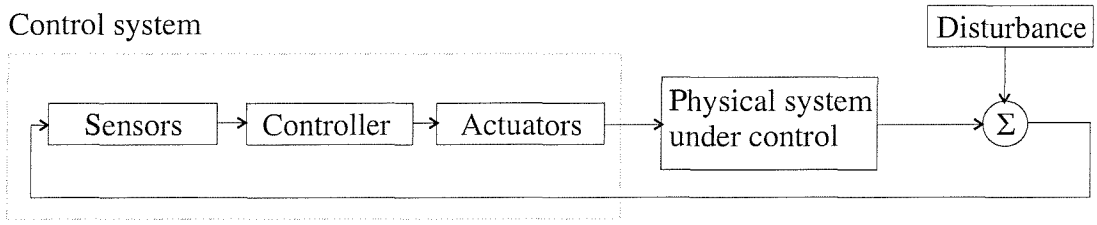

Figure 2.1: Block diagram of an active control system

Although this thesis deals with a specific type of active control, namely ASAC feedback control, some of the latest research in active control technology is into hybrid active-passive methods which take the advantages of both active and passive control which are combined to give materials with good noise control performance over a large frequency range [5, 8].

2.1.2 A brief history of active control of sound

The concept of active control applied to noise control problems is not a new one and as early as 1934, Paul Lueg had filed a patent which described a technique for controlling sound using the introduction of additional sound [9]. He suggested using out-of-phase sound radiation from a secondary source to cancel a one-dimensional wave in a duct using the principle of superposition. His method used a microphone to measure a plane wave travelling along the duct. This microphone signal was fed through an electronic controller to a loudspeaker. The task of the electronic controller was to send the correct signal to the loudpseaker so that it produced a sound wave in anti-phase to the original primary wave and cancellation would then take place due to the principle of superposition. It is interesting to note that, although the technology to implement this system was not available at the time, mainly in terms of producing

an electronic controller which could change the amplitude and phase of the measured signal by the appropriate amounts, almost all the components which are now viewed as being essential in modern control systems were present. These are the primary source or disturbance (plane wave in duct), the reference sensor (microphone), the secondary actuator (loudspeaker), and the controller (see figure 2.1). These components are arranged for feedforward control, which can be used when an external reference signal or the excitation is easily measured before the point of control. However Lueg included neither an error sensor nor adaptation in his method. The error sensors in this case could be a second microphone downstream of the secondary actuator to check that the primary wave had indeed been cancelled or to adapt the controller to track changes in the system.

Another classic paper which was published well before the current digital technologies were available, was written in 1953 by Olson and May [10]. Using analogue equipment available at the time, they described an 'electronic sound absorber' and some possible applications for it. The sound absorber works by measuring the sound with a microphone and feeding it back through an electronic controller to a loudspeaker to produce sound in anti-phase with the disturbance. By making sure the phase shift between the input to the microphone and the output from the loudpseaker is minimised and by using negative feedback, a simple 180^o phase shift between the loudspeaker output and the microphone input is achieved and perfect cancellation takes place. A major difference between this formulation and that of Lueg is that in this case, there is no reference sensor and so the control is termed feedback control. However, Olson and May again foresaw the essential parts of a feedback control system and also predicted many of the applications which feedback control is currently being used in, such as to produce zones of quiet in headrests of chairs or in ear defenders where active components are mixed with passive hearing protection to provide an increased frequency range of attenuation.

However, it is only due to the recent advance in a number of technologies that active control has become a viable technique for controlling noise in real applications.

The first technology which has developed over recent years is the production of cheaper, more reliable and faster DSP chips, which allow rapid processing of the reference or error signals to calculate the necessary control signals. Coupled with this has been progress in the mathematics of control engineering. New and efficient techniques for calculation of the control signals have been developed. The final technology, which has been an area of increased research more

recently is transducer technology which has led to the development of new actuators and sensors that allow control systems to be used in increasing numbers of applications with increasing effectiveness. This is especially important for active structural acoustic control (section 2.2).

Active control thus brings together a number of disciplines: control theory, acoustics, structural vibrations, and knowledge of which transducers would be the most suitable for different applications. Even though the principles of active control are not new and may be well understood, technological feasibility can rely on novel methods which have only recently become available.

Since the middle of the 1980's applications of active noise control have started to appear in commercial products and, corresponding to the increasing number of applications, greater insight into its possibilities has developed. The next few paragraphs describe the general trends of active control research. An excellent overview of active control of sound is given by Nelson and Elliott [11].

Following Lueg's first suggestion of controlling a plane wave travelling along a duct, the first applications of active noise control were the feedforward control of sound in an air-duct. The main reason for this is the simplicity of the problem both in terms of its physical modelling and in terms of the control techniques which are required for single frequency plane waves. This particular application of active control had the additional advantage of achieving large reductions for tonal disturbances at low frequencies in an important problem where passive techniques had proved to be difficult and did not achieve very large reductions. Although some systems which worked under very specific conditions had been developed around 1970 (see [12] for example), the first system which could be applied to reduce sound over a wider frequency range and which was useful in many real situations, as well as being self-adaptive and robust, was developed by Roure [13].

The next steps were to develop sytems which had more than one input and output i.e. a move from Single-Input Single-Output (SISO) to Multi-Input Multi-Output (MIMO) and a corresponding move to control in two and three dimensional spaces. These spaces could either refer to small areas of the free-field or enclosed spaces. The analogue systems suggested by Olson and May [10] are also generally converted to digital systems which requires the use of anti-aliasing and reconstruction filters, DSP programming, and Analogue to Digital and Digital to Analogue convertors (ADC/DAC). Moving to three-dimensional enclosures allowed more

applications such as controlling the sound in aircraft cabins and inside cars. As the transport industries give rise to applications where space and weight are at a premimum, active control has been largely funded by aerospace, automotive, and nautical industries but other uses have followed. For example, an increasing problem is due to noise carried between neighbouring houses and active control offers a possible solution in this area [14].

Another general trend in active control research has been from the control of tonal or predictable disturbances to more random and broadband ones. There has been a corresponding move from feedforward control to feedback control. Feedforward control requires a reference signal and relies heavily on Wiener filtering and Least Mean Square (LMS) methods. Applications which use feedback control include hearing protectors or active headphones which reduce unwanted signals but leave important signals (these are especially important to prevent fatigue for pilots for example), and headrests with zones of quiet. A final area of development has been in transducer technology. This has been of use mainly in active vibration control (ACV) and in ASAC which are dealt with in section 2.2. In active noise control, the loudspeakers and microphones which are conventionally used have changed little over the last fifteen years apart from a fall in their prices.

An overview of the development of active control application developments shows five main trends for research:

1. From control at a single spatial point to control at a number of points or over a region of space (Curtis [15] shows that complete global control could be achieved in theory if an infinite number of control sources were available).

2. An increase in the number of control channels from SISO (one actuator and one sensor) to MIMO control (control with a number of actuators for a number of measurement points)

3. From feedforward to feedback control. Feedback control, which can be used in a broader range of applications, is generally more difficult to implement in distributed-parameter systems such as those which support acoustic disturbances.

4. Corresponding to the move from feedforward control to feedback control is a move from the control of tonal or predictable sound to the control of more random and broadband sounds.

5. The degree of integration of the control system components with the system to be controlled. Initially far-field acoustic actuators and sensors have been used. There has been a movement to more integrated systems where actuators and sensors are integrated with the vibrating structure generating the noise and thereby tackling the source of the noise instead of the radiated noise itself.

Figure 2.2, taken from Fuller and von Flotow [16], summarises these trends in active sound control research and the increasing complexity of control. The three variables shown are spatial extent, corresponding to the first development listed above, spectral extent, corresponding to the fourth development listed above, and the level of passive damping in the system to be controlled. The amount of damping has two effects which are important for active control purposes. On the one hand, a lightly-damped structure may allow larger attenuations than a similar heavily-damped one. The same light damping however, also results in more uncertainty in the true position of resonant frequencies and so more care must be taken to ensure stability of feedback systems. An increase in the number of channels or a move from feedforward to feedback control generally increases the amount of computer processing required to perform the control. The simplest control of SISO feedforward control of single-point, narrowband disturbances is, by now, fairly straightforward and well-understood and can be implemented with some success. The movement is more and more into the most complex corner of the figure which encompasses MIMO feedback control of broadband, spatially-distributed disturbances. This is the area of the graph which also imposes the greatest physical limitations on the maximum attenuation possible. The search is thus getting harder and harder to achieve smaller and smaller attenuations.

References which provide a good overview of active control including its history and the major developments outlined above include [11, 16–18]. Berkman and Bender [18] in particular draw attention to the major achievements in the implementation of active control technologies.

2.2 Active structural acoustic control (ASAC)

Section 2.1.2 gave an overview of the history of active control of sound and the aim of this thesis is to describe one method of achieving such active sound control. However, instead of

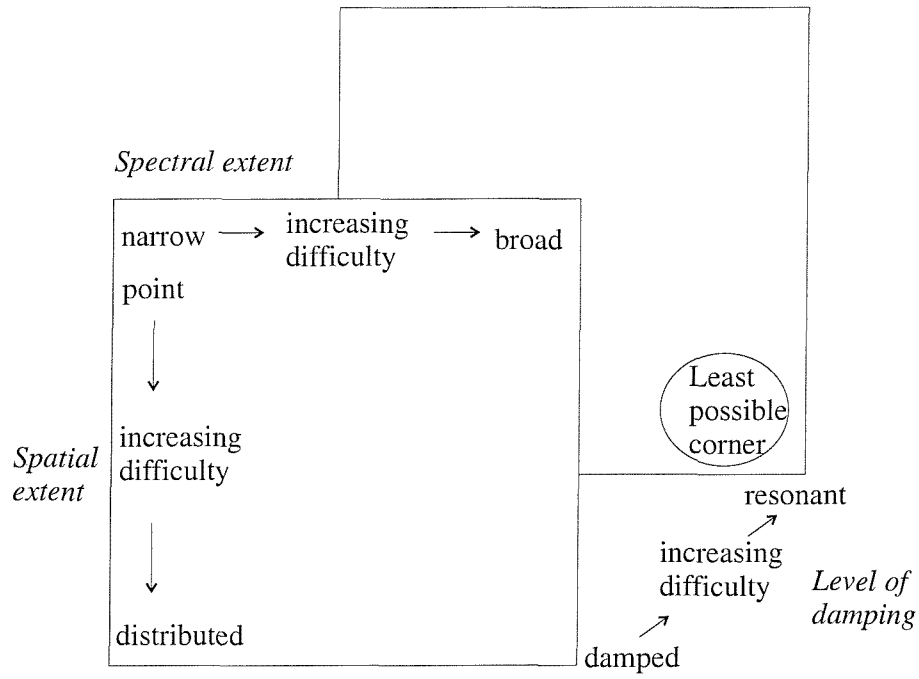

Figure 2.2: General trends in progression of active control research (from [16])

using the loudspeakers and microphones which would be used in conventional ACS, a subset of active sound control called Active Structural Acoustic Control will be used. This is a mixture between ACS and Active Vibration Control (ACV) in which the vibrations of a structure are altered in such a way that its overall sound radiation is reduced.

Applications where controlling sound transmission would be desirable include the control of boundary layer noise through an aircraft fuselage, reducing road and tyre noise inside a car, and even reducing noise transmitted through walls from neighbours.

2.2.1 What is active structural acoustic control?

Active structural acoustic control (ASAC) refers to the process of reducing sound power transmission or radiation from a structure using actuators integrated with the structure itself.

In reducing the sound radiation from structures, there are generally two types of control sources or actuators which can be used. The first of these is the use of acoustic control sources within the region where control is required. Control of sound using these control sources, loudspeakers for instance, is termed as Active Control of Sound (ACS) [11]. However, it is found that when

the primary sound source is complex or distributed over multiple surfaces, many acoustic control sources are required in order to provide global control [19]. ASAC then takes advantage of the nature of the structural-acoustic coupling and allows a reduction in the dimensionality of the controller and this will be seen to be important both in terms of the performance of a control system and in terms of the overall cost of the control system. Furthermore, it is often impractical to have secondary acoustic sources located away from the radiating structure. Using acoustic transducers can also lead to unwanted noise in positions between the sensors [20]. This is one example of spillover, a process which results in unwanted increases in some variable as a result of some control process.

The second type of control source is integrated with the struture itself and in this case, the aim is to change the vibration distribution of the structure such that the overall sound radiation is reduced. This method was first introduced by Fuller and his co-workers . It differs slightly from conventional active vibration control (ACV, reviewed by Fuller *et al.* in [19]) in that it attempts to control only the vibrations which are important to sound radiation or which radiate sound efficiently. Pure vibration control on the other hand, attempts to reduce the vibrations of a structure as much as possible with no concern for the result on the sound radiated by the structure. Obviously, if the vibrations of a structure are completely eliminated, then the structure will cease to radiate sound. It will be shown later, in section 4.5 however, that there is a subtle difference between these two techniques and this type of control has been called active structural acoustic control (ASAC). ASAC takes into account the fact that different modes of vibration contribute by different amounts to the noise radiation and the object of ASAC is to create a reduced order controller which only focuses on these important sound radiating modes. The effect is thus to reduce the radiation efficiency of the structure rather than the actual vibrations. A side effect of this is that AVC can actually lead to increases in radiated sound levels and conversely, a reduction in radiated sound power can lead to an increase in structural vibration levels. The effects of spillover in the radiated acoustic field are generally reduced when using structural actuators.

A block diagram of an ASAC system is shown in figure 2.3 and falls within the framework of active control systems in general (c.f. figure 2.1). The three essential components are the structure to be controlled, the transducers (actuators and sensors), and the controller, which commonly includes the digital-to-analogue convertor (DAC) and analogue-to-digital convertor (ADC). These will all be dealt with separately in the thesis, the structure being dealt with in

chapter 3, the transducers in chapter 4, and the controller in chapters 5 to 7.

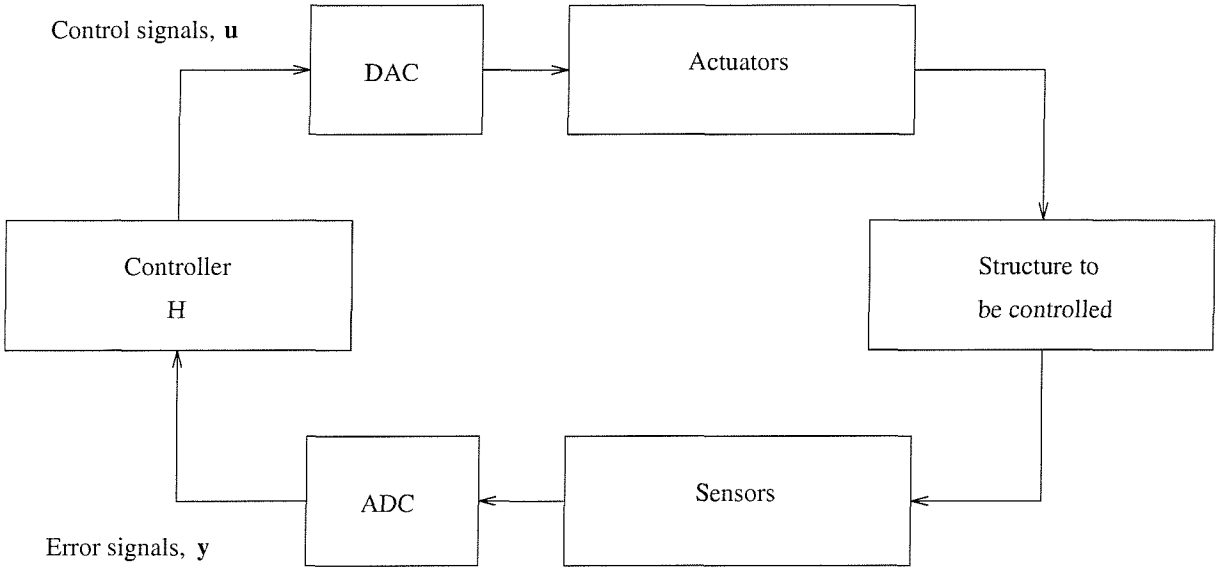

Figure 2.3: Block diagram of an active structural acoustic control system

Although ASAC normally refers to applications in which control inputs are applied directly to the structure rather than ANC where control inputs would be in the acoustic field, the error information is conventionally also measured in the radiated acoustic field, with microphones for instance. Evidently, after changing from acoustic actuators to integrated actuators, a further step can be taken by integrating the sensors with the structure itself rather than using far-field sensors. In this case, it is important to measure a variable which is strongly related to the radiated acoustic power.

2.2.2 A brief history of active structural acoustic control

The first references to ASAC were by Fuller and his co-workers in around 1985 [21] and at the same time by Vyalyshev *et al.* [22]. They first suggested using structural actuators instead of acoustic actuators in order to reduce spillover which arises with the latter and the possibility of a reduced order controller when using structural actuators. Initially, point force actuators were used and the radiated sound power was measured using microphones. Initial experiments comparing the use of vibration inputs and sound sources were also conducted by Fuller [23]. These also concluded that in general, the control by structural inputs was more effective than control using far-field acoustic sources.

The main developments which have allowed more successful implementations of ASAC systems have been in new transducers. Piezoelectric materials which are lightweight, are cheap to manufacture, and can be integrated into the structure, were found to be more practical than the point sources used in the intial simulations and experiments, which would require cumbersome reaction mounts [24].

Rather than using microphones in the far field to measure the radiated sound, a natural progression was then made to integrate sensors with the structure to be controlled as well as the actuators. A major advantage when both actuators and sensors are integrated is that the system can be used when it would be impractical to have transducers placed in the far field. Again, the development of piezoelectric materials enabled new sensors to be designed. Many of these focused on the use of PVDF film which could be shaped easily to target the control of individual modes although there are significant practical problems with their implementation [25, 26].

The developments in transducers have been coupled with more research into the most efficient way of controlling structural vibrations such that the radiated sound power is reduced. These control strategies have included controlling single structural modes, the development of the radiation mode approach, and more elaborate methods of trying to predict the radiated sound power using structurally-measured variables measured at a number of points [27].

A number of other materials which have useful transducer properties have also been developed recently. These include magnetostrictive materials [28] and Shape Memory Alloys (SMA's) [29] for example and a good overview of these materials is given in [19]. Electrorheological fluids and magnetorheological fluids can be used in semi-active systems. A semi-active actuator is a passive element which can store or dissipate energy but whose mechanical properties can be changed by the application of a control signal.

2.3 Feedback control

One of the essential blocks of an ASAC system is the controller itself as shown in figure 2.3. The controller receives information from the various sensors available and processes this information to calculate control signals which are fed to the actuators, which then alter the state of the system. Controllers are generally considered to be either feedforward or feedback. The choice of

controller type depends mainly on whether a suitable external reference signal can be measured close to the disturbance source or sufficiently downstream of the secondary source to allow the controller time to make the necessary calculations. Feedforward control can also be used for tonal or predictable disturbances, due to engine noise or rotational machinery noise for example, where a tachometer can be used to generate a reference signal, whereas feedback control must be used when no external reference is available. This thesis concentrates on feedback control used for ASAC applications, which is still a relatively new area of research.

A further comparison of feedforward and feedback control is outlined below and diagrams of both methods are shown in figure 2.4.

Feedforward control in which the controller has two types of inputs. Reference sensors measure the disturbance downstream of the controller and are fed-forward to cancel the signal at error sensors which measure the overall performance of the controller. The reference signals are commonly measured close to the source of the disturbance and are mostly unaffected by the action of the controller and actuators. The error signals adapt the way in which the controller works. Wiener techniques or Least Mean Square techniques are commonly used. An example would be to use a tachometer on an engine to measure the RPM which could be used as a reference signal.

Feedback control is used where obtaining a reference signal is unsuitable. This is normally when the disturbance is more broadband or there are multiple disturbance sources or, if the disturbance is not sufficiently upstream of controller. The signals from the error sensors are used directly in the controller and this can give rise to the phenomenon of instability.

This thesis works mainly with a particular type of feedback control called Internal Model Control (IMC). IMC is one of several possible feedback control methods and the reasons for focusing on this technique are outlined in chapter 5.

Feedforward control, by calculating the control at individual frequencies, gives the best possible control that can be achieved from a given physical system and for this reason, it is used as a reference control case in this thesis. Feedback control introduces new control issues such as stability and robustness which make it more complex than feedforward control. These issues

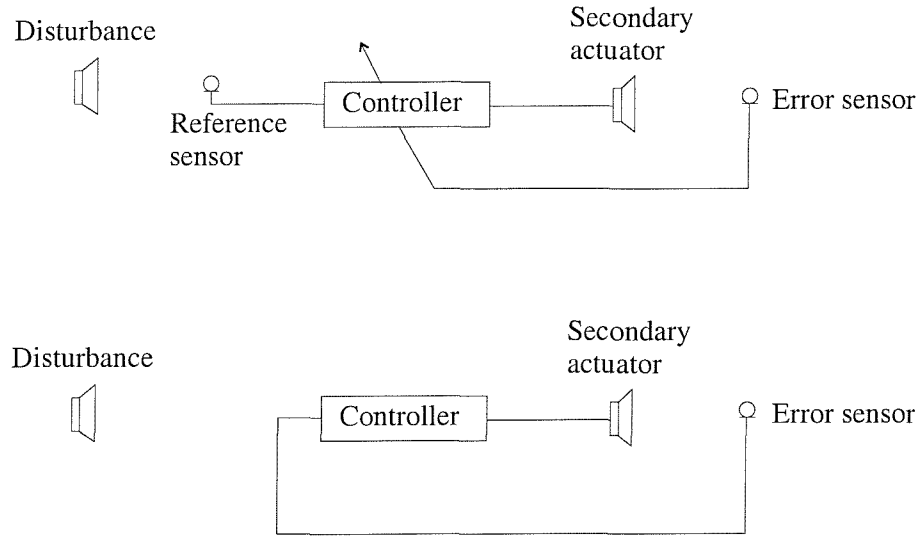

Figure 2.4: Diagrams of feedforward and feedback control systems

will be dealt with in section 5.1. Examples of feedback control go back many centuries and the history of feedback is described by [17, 30].

Although feedforward and feedback control have been dealt with as two distinct cases, the only difference between the two is the location of sensors. More recent control systems include both feedforward and feedback paths ([31, 32]) and the IMC feedback control used in this report reformulates the feedback problem as a feedforward one. There is thus a range of configurations in between these two extremes. This will become clearer as the use of different sensors are discussed.

Chapter 3

Modelling sound radiation from plates

3.1 Introduction to plate vibrations

The first step in designing any type of control system is to understand the physical processes which need to be controlled. In active structural acoustic control, this corresponds to the structure to be controlled and its resulting sound radiation. In this thesis, the structure considered is a thin rectangular plate. One of the most common problems in ASAC research is reducing the radiated or transmitted sound from such a vibrating panel as this represents the simplest idealisation of a whole class of problems of practical interest involving the radiation from some form of structure. Some examples are sound radiation from the hull of a submarine, the transmission of sound through the fuselage of an aircraft, through the shell of a car, or even through walls between neighbouring houses. There are good reasons for analysing a simple system like this, including the fact that plates are fairly easy to model and the theory of their vibrations is well understood. Furthermore, larger structures can often be considered as being made up of a number of small plates.

The vibrations and sound radiation from such a rectangular plate are considered in this chapter and most of this is established theory.

In the first place, the plate vibrations are analysed in terms of structural modes. This approach to analysing structural vibrations is the conventional approach and the basis of most structural vibration analysis. After considering the form of the vibrations themselves, the sound radiation due to these structural modes is considered by using the Rayleigh integral and it is shown that there is a complex interaction between the structural modes as a result of which they do not radiate sound independently of each other. There are many books which deal with this sound radiation from structures and amongst the best of these are by Cremer *et al.* [33] and by Fahy [34].

Radiation modes are another, fairly recent, way of analysing plate vibrations and the subsequent sound radiation and these are then described. Unlike the structural modes, these radiate sound independently of each other and this proves to be an important concept used during the rest of the thesis. Both formulations use different ways of describing the vibrations in terms of orthogonal eigenvectors. There are a number of other ways in which the vibrations could be expressed, but these two methods provide good physical insight to the vibrational patterns and the subsequent sound radiation. The mathematical relationship between the two approaches is also described.

3.2 Theory of plate vibrations

3.2.1 Structural modes

When a plate is subjected to a mechanical excitation it begins to vibrate. The resulting vibrations can be mathematically modelled in a number of different ways. The most common of these methods, using structural modes, is described in this section.

Consider a plate whose co-ordinate system is shown in figure 3.1. The lengths of the sides in the x and y directions are given by l_x and l_y respectively. Movement in the direction of the z axis is denoted by w and only this form of vibration will be considered here since it is the out of plane vibration which gives rise to sound radiation.

Free vibrations of the plate can be derived by first considering the equation of motion for the transverse displacement of a thin plate [19, 33, 35]. The equation of motion is an extension of

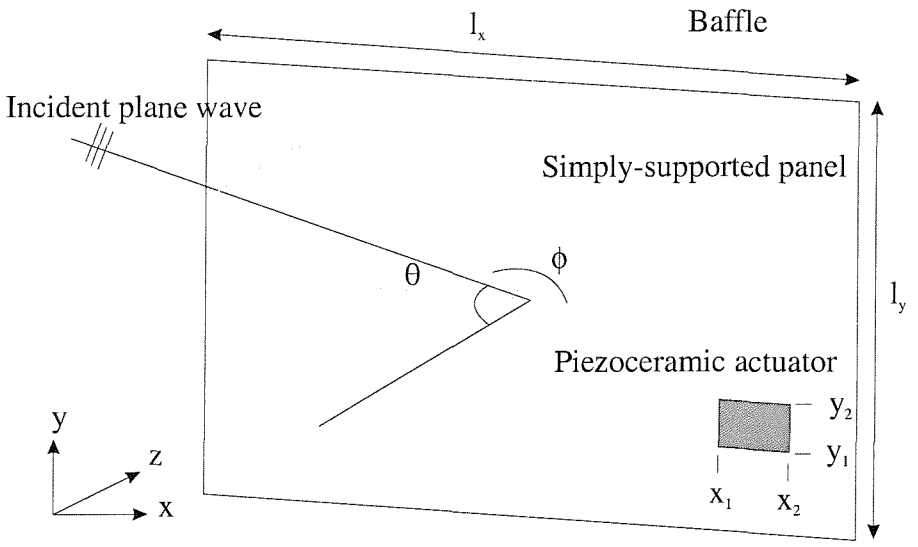

Figure 3.1: Coordinate system of a thin rectangular plate

the equation of motion of a beam and is given by Leissa [35] as the function of $w(x, y, t)$ and time t as

$$D\nabla^4 w(x, y, t) + \rho h \frac{\partial^2 w(x, y, t)}{\partial t^2} = 0 \tag{3.1}$$

where ρ is the density of the plate material, h is the plate thickness, $\nabla^4 = \nabla^2\nabla^2$ is the Laplacian operator, and D is the bending stiffness given by

$$D = \frac{h^3 E}{12(1 - \nu^2)} \tag{3.2}$$

where E is the Young's modulus, and ν is Poisson's ratio.

In this model, fluid loading, which takes into account the effect of the fluid, or acoustic medium, on the vibrations of the structure are neglected. For a discussion of fluid loading effects, the reader is referred to Fahy [34] for instance. The equation of motion (3.1) is derived under the assumptions that the plate is homogeneous through its thickness, isotropic, and that there are no in-plane forces. It is furthermore assumed that the plate is thin with respect to the wavelength and transverse shear and rotary inertia of the plate motion are also ignored. These assumptions are only valid at low frequencies, which is however, the frequency range of interest

for ASAC applications. The derivation of the equation of motion itself arises from a combination of equilibrium equations for small deflections in the plate, stress-strain relationships between principal axes of the plate and, force and moment integrals. The derivation is discussed by Leissa [35] and by Cremer *et al.* [33].

The Laplacian operator ∇^2 allows the waves on the plate to be mathematically described in a number of different coordinate systems but, when using the cartesian, or rectangular, coordinate system which is used above in figure 3.1, it becomes

$$\nabla^2 = \frac{\partial^2}{\partial x^2} + \frac{\partial^2}{\partial y^2} \tag{3.3}$$

and the equation of free motion (3.1) becomes

$$D\left(\frac{\partial^4 w}{\partial x^4} + 2\frac{\partial^4 w}{\partial x^2 \partial y^2} + \frac{\partial^4 w}{\partial y^4}\right) + \rho h \frac{\partial^2 w}{\partial t^2} = 0 \tag{3.4}$$

the implicit dependence of w on x, y and t has been suppressed here and, as the motion with no applied pressure is being considered, this is termed as free motion.

It should be noted that all real systems possess mechansims by which energy is dissipated i.e. damping, although these are not taken into account in the differential equation of motion above (3.4). The free waves considered here, without damping, are able to travel continuously whereas, if damping were present, this would not be the case and the waves would attenuate with distance from the point of excitation.

Although different types of wave motion can take place in a solid structure, for example longitudinal, quasi-longitudinal, shear waves, all of which are discussed by Fahy [34], it is flexural, or transverse waves which are of greatest significance when structure-fluid interaction is considered at audio frequencies because they involve substantial displacements in directions transverse to the direction of propagation, i.e. in the direction of the z-axis, which can effectively disturb the adjacent fluid. The other types of wave motion do not give rise to significant displacements in the direction of the z-axis. Additionally, the transverse impedance of structures carrying

bending waves can be of a similar magnitude to sound waves in the adjacent fluid facilitating energy exchange between the two media.

A flexural structural wave of amplitude A and frequency ω can be described by the equation

$$w(x, y, t) = Ae^{j\omega t - jk_x x - jk_y y} \tag{3.5}$$

k_x, k_y are the component wavenumbers in the directions of the two axes and can also be combined to give a single free wavenumber k_f such that

$$k_f^2 = k_x^2 + k_y^2 \tag{3.6}$$

The component wavenumbers are then given by

$$\begin{aligned} k_x &= k_f \cos\alpha \\ k_y &= k_f \sin\alpha \end{aligned} \tag{3.7}$$

where α is the angle which the waves makes with the x axis as shown in figure 3.2.

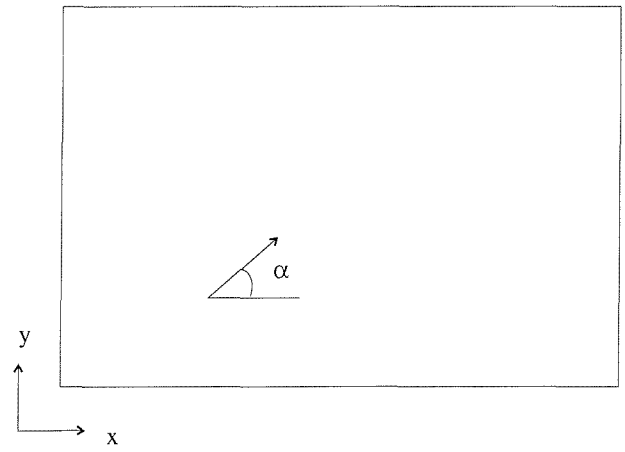

Figure 3.2: Direction of travel of a flexural wave on a plate

As the plate considered so far is unbounded, and no damping has been considered, the wave described by equation (3.5) can propogate freely and endlessly away from the point of excitation.

However, all real physical systems are spatially bounded and, when these boundaries are taken into consideration, the plate flexural waves become subject to the effects of refraction, diffraction and reflection. Reflection is the most important of these as it gives rise to a set of frequencies and corresponding spatial patterns of vibration which are the eigenfunctions and eigenfrequencies of the plate, more commonly known as the mode shapes and natural frequencies respectively [34]. These take place due to the superposition of reflected waves on incident waves setting up pure standing waves. An infinitely large plate can thus vibrate freely at any frequency however, a bounded plate can only vibrate freely at its natural frequencies and with the vibrational patterns given by the eigenfunctions.

Boundary conditions thus impose a constraint on the equation of motion whose solutions then give the eigenfrequencies and eigenfunctions of the plate which can be used to describe the vibrational patterns. In general though, a solution to the equation of motion (3.4) with the appropriate boundary conditions cannot be found analytically. A number of approximation methods exist for solving these equations with arbitrary boundary conditions and these are reviewed by Leissa [35] and Meirovitch [36]. However, one set of boundary conditions does give rise to analytical solutions and these are for the simply-supported plate. Further discussion of different plate boundary conditions is given in appendix A, but the simply-supported boundary gives rise to very simple mode shapes and will be used as an example to demonstrate vibrational patterns.

Simply-supported boundary conditions allow rotation of the plate at the edges but no displacement or moment. The transverse modal displacement for a simply-supported plate is given by the solution to equation (3.1) with the suitable boundary conditions and is given by

$$w_{mn}(x,y,t) = W_{mn}\sin(k_m x)\sin(k_n y)e^{j\omega t} \tag{3.8}$$

where W_{mn} is the modal amplitude and m and n give the mode number and are called modal indices. The values of k_m and k_n depend on the modal indices and are given by

$$k_m = \frac{\pi x}{l_x}$$
$$k_n = \frac{\pi y}{l_y} \tag{3.9}$$

So far, only free vibrations have been considered. No input forces to the plate have been present. Now consider the response of a structure to a disturbance by including a forcing term in the equation of motion (3.4). Equation (3.4) can be altered slightly to give the response of a plate to a two dimensional distributed forcing function such that

$$D\left(\frac{\partial^4 w}{\partial x^4} + 2\frac{\partial^4 w}{\partial x^2 \partial y^2} + \frac{\partial^4 w}{\partial y^4}\right) + \rho h \frac{\partial^2 w}{\partial t^2} = -F(x,y)e^{j\omega t} \tag{3.10}$$

where $F(x,y)e^{j\omega t}$ is the two-dimensional forcing function.

The total response of the plate to such a force is given by the superposition of the individual eigensolutions or modes i.e.

$$w(x,y,t) = \sum_{m=1}^{\infty}\sum_{n=1}^{\infty} W_{mn}\Psi_{mn}(x,y)e^{j\omega t} \tag{3.11}$$

where $\Psi_{mn}(x,y)$ represents the two-dimensional mn'th mode shape. This is normally truncated to a finite number of modes so that

$$w(x,y,t) \approx \sum_{m=1}^{M}\sum_{n=1}^{N} W_{mn}\Psi_{mn}(x,y)e^{j\omega t} \tag{3.12}$$

where M and N are the number of modes used in the plate model.

Returning to the example of the plate with simply-supported modes, the response of the plate can then be written in terms of a sum of modes of the free response of the plate vibrating at the forcing frequency

$$w(x,y,t) = \sum_{m=1}^{\infty}\sum_{n=1}^{\infty} W_{mn}\sin(k_m x)\sin(k_n y)e^{j\omega t} \tag{3.13}$$

The amplitude of each mode, in turn, can be described by the equation

$$W_{mn} = A_{mn}F_{mn} \tag{3.14}$$

where the two terms are

i) The forcing of the mode F_{mn} due to the coupling between the acoustic or structural excitation and the structural waves.

$$F_{mn} = \int_S \Psi_{mn}(x,y)F(x,y)dxdy \tag{3.15}$$

where S is the surface of the plate.

ii) A complex resonance term $A_{mn}(\omega)$ which takes into account the dynamics of the plate and the frequency of excitation,

$$A_{mn}(\omega) = \frac{1}{\rho h S((\omega_{mn}^2 - \omega^2) + j\omega D_{mn})} \tag{3.16}$$

where S is the area of the plate, ω_{mn} is the natural frequency of the mn'th mode, which can be calculated using standard plate theory [35, 37], and D_{mn} is the damping of the mn'th mode given by $D_{mn} = 2\zeta\omega_{mn}$ where ζ is the viscous damping ratio, which is assumed here to be the same for each mode. There are a number of different models of damping outlined by Cremer *et al.* [33] for example. This particular model, using viscous damping, is the most commonly used and the simplest. The effects of damping are to dissipate energy from the vibrating structure and the effects on the frequency response function are to broaden the sharp resonance peaks and to reduce their amplitude.

3.2.2 Sound radiation from structural modes

The final aim of an ASAC system is to control the sound radiated from a structure rather than the vibrations of the structure themselves and so, an understanding of the sound radiation due to a given vibration distribution is required.

In this section, the sound radiation from a plate will be considered. The simply-supported plate analysed above will again be used as an example due to its simple solutions to the equation of motion and because it provides a physical interpretation which is easy to understand but the approach is entirely analogous for other sets of boundary conditions. The sound radiation can be analysed by considering the interaction between the vibrating structure and the acoustic field or adjoining fluid. Some books which give a good overview of the sound field radiated by structures include Fahy [34], Cremer *et al.* [33], and Junger and Feit [38].

The Rayleigh integral ([19, 34, 38, 39]) can be used to calulate the radiation from a baffled planar surface with an arbitrary velocity distribution $w(x, y)$ under anechoic conditions i.e. where no reflections are present in the sound field. The pressure at a given field point in spherical coordinates $p(\boldsymbol{r}) = p(r, \theta, \phi)$ can be calculated by integrating the velocity distribution over the surface S of the plate and by considering the source strength at the position $w(\boldsymbol{r}_s)$ on the plate to be proportional to the amplitude of vibration at that point. If the time dependence $e^{j\omega t}$ is suppressed for notational simplicity,

$$p(\boldsymbol{r}) = \int_S \frac{j\omega\rho_0 w(\boldsymbol{r}_s)e^{-jkR}}{2\pi R} dS \tag{3.17}$$

where $R = |\boldsymbol{r} - \boldsymbol{r}_s|$ and ρ_0 is the density of the acoustic medium. Provided $R \gg l_x, l_y$ approximations to R are usually made [19] such that $R \approx r - x\sin\theta\cos\phi - y\sin\theta\sin\phi$ in the exponential term, and $R \approx r$ in the denominator. The first approximation is always justified if the smallest distance between the sound source and the observation point is much larger than the dimension of the source. The second approximation is less stringent than this. The geometry for the Rayleigh integral is shown graphically in figure 3.3.

The total radiation consists of a superposition of radiation from structural modes and their interference in this radiated field is discussed below. First though, consider an individual

simply-supported mode. The velocity distribution $w(\boldsymbol{r}_s)$ due to the mn'th mode of the simply-supported plate is given

$$w(\boldsymbol{r}_s) = W_{mn} \sin(k_m x) \sin(k_n y) \tag{3.18}$$

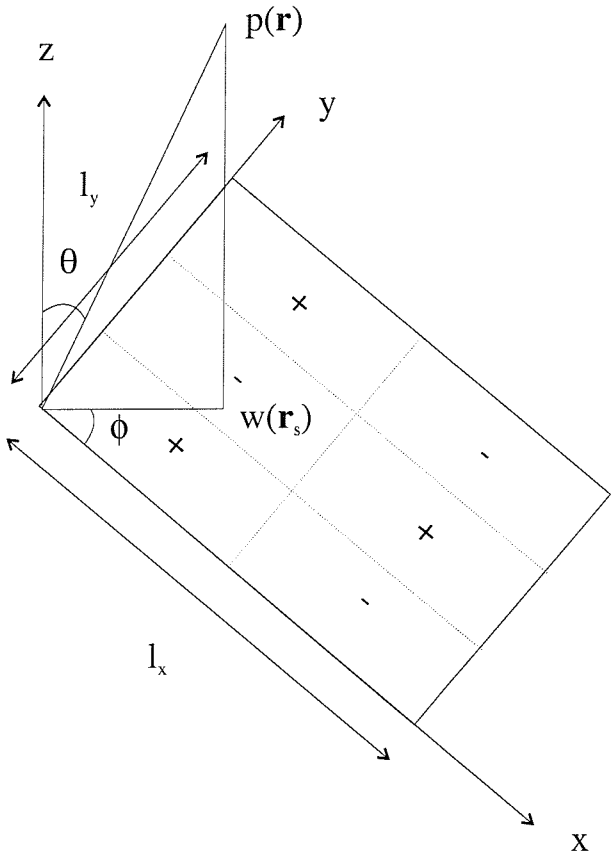

Figure 3.3: Geometry for computing the Rayleigh integral (vibrations of (2,3) mode shown)

and, after substituing this into (3.17), the far-field pressure from the mn'th mode is found to be

$$p(\boldsymbol{r}) = \frac{j\omega\rho_0 W_{mn} e^{-jkr}}{2\pi r} \int_0^{l_y} \int_0^{l_x} \sin(k_m x) \sin(k_n y)\, e^{j(\alpha x/l_x + \beta y/l_y)} dx dy \tag{3.19}$$

where

$$\begin{aligned} \alpha &= kl_x \sin\theta \cos\phi \\ \beta &= kl_y \sin\theta \sin\phi \end{aligned} \tag{3.20}$$

Wallace [39] has evaluated this integral analytically and found that the pressure at the far-field point $\boldsymbol{r}$ due to a single mode of a simply-supported plate is given by

$$p(\boldsymbol{r}) = \frac{j\omega\rho_0 W_{mn} e^{-jkr}}{2\pi r} \frac{l_x l_y}{mn\pi^2} \left[\frac{(-1)^m e^{-j\alpha} - 1}{(\alpha/m\pi)^2 - 1}\right] \left[\frac{(-1)^n e^{-j\beta} - 1}{(\beta/n\pi)^2 - 1}\right] \tag{3.21}$$

The sound intensity, which gives a measure of the radiated sound power per unit area, is then given by

$$\frac{|p(\boldsymbol{r})^2|}{2\rho_0 c_0} = 2\rho_0 c_0 |W_{mn}|^2 \left(\frac{kl_x l_y}{\pi^3 rmn}\right)^2 \left\{\frac{fn(\frac{\alpha}{2}) fn(\frac{\beta}{2})}{[(\alpha/m\pi)^2 - 1][(\beta/n\pi)^2 - 1]}\right\}^2 \tag{3.22}$$

where c_0 is the speed of sound in air, $fn(\frac{\alpha}{2})$ is replaced by $\cos(\frac{\alpha}{2})$ when m is an odd integer and by $\sin(\frac{\alpha}{2})$ when m is an even integer and $fn(\frac{\beta}{2})$ is replaced by $\cos(\frac{\beta}{2})$ when n is an odd integer and by $\sin(\frac{\beta}{2})$ when n is even.

Once the pressure field radiated by the plate is known, a single global measure of the radiated sound is given by the total radiated acoustic power. This value will later be used as the one which must be minimised through the use of ASAC. The acoustic power is defined as the integral of the acoustic intensity over a surface surrounding the source [6]. For a baffled planar surface, this surface could be a hemisphere surrounding the plate for example.

The total radiated power from the mn'th mode is given by

$$W = \int_0^{\pi/2} \int_0^{2\pi} \frac{|p(r,\theta,\phi)|^2 r^2 \sin\theta}{2\rho_0 c_0} d\theta d\phi \tag{3.23}$$

To allow the radiation from different mode orders to be compared more directly, Wallace [39] has defined the modal radiation efficiency to be

$$\sigma_{mn} = \frac{W}{\langle |w_{mn}|^2 \rangle \rho_0 c_0 l_x l_y} \tag{3.24}$$

where $\langle |w_{mn}|^2 \rangle$ is the spatial and temporal average modal velocity of the plate and for the velocity distribution given by equation (3.8) is $\frac{|W_{mn}|^2}{8}$. These modal efficiencies can only be used in isolation when the structure is driven at frequencies which are close to the relevant resonance so that only one mode is dominant.

In general, however, to describe the sound radiation from a structure, the multimodal response must be taken into account as the sound power radiated by any one structural mode is dependent on the amplitude and phase of every other structural mode. Hence for multimode excitation, the total radiated power is given by

$$W = \frac{\rho_0 c_0 l_x l_y}{2} \sum_{k=1}^{\infty} \sum_{l=1}^{\infty} \sum_{m=1}^{\infty} \sum_{n=1}^{\infty} W_{kl}^* \sigma_{kl,mn} W_{mn} \tag{3.25}$$

where $\sigma_{kl,mn}$ are the self-radiation (when $kl = mn$) or cross-radiation (when $kl \neq mn$) efficiencies [19]. These structural mode efficiencies are shown in figure 3.4 as functions of non-dimensional frequency Ω which is defined by

$$\Omega = k l_x \tag{3.26}$$

and are calculated using an elemental approach which is described below. For the plate used throughout the thesis, $kl_x = 1$ corresponds to a frequency of approximately $200Hz$.

For the purposes of control, it is the cross-radiation efficiencies which cause difficulties as reducing the amplitude of one structural mode does not necessarily give rise to a decrease in the total radiated power. This effect is called spillover and is discussed in chapter 4.

A second way of examining the sound power which is radiated from the plate in terms of structural modes is by using the near-field or elemental radiator approach [7, 40, 41].

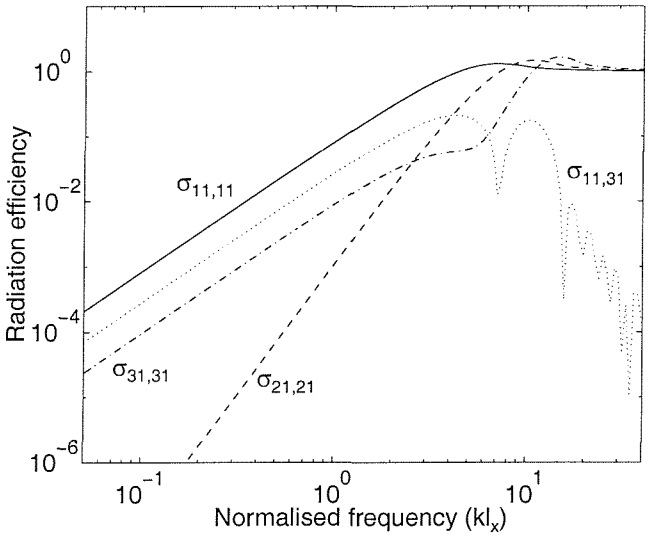

Figure 3.4: Radiation efficiencies of low order structural modes of a simply-supported plate

In this approach, the vibration of the plate is approximated by dividing the surface into a large number, I, of elemental sources which are small compared with the acoustic wavelength and which oscillate harmonically. The power radiated, W_{el}, by a single element el is given by the element's complex velocity, v_{el}, and the complex pressure, p_{el}, at the elemental position

$$W_{el} = \left(\frac{S_{el}}{2}\right) \Re(v_{el}^{*} p_{el}) \tag{3.27}$$

where S_{el} is the elemental area, $\Re$ denotes the real part, and $*$ denotes conjugation.

The total power, W, radiated by the panel can then be calculated by defining vectors $\boldsymbol{v}$ and $\boldsymbol{p}$ whose elements are the velocities and pressures of each element and the total power output can be written

$$W = \left(\frac{S_{el}}{2}\right) \Re(\boldsymbol{v}^{H} \boldsymbol{p}) \tag{3.28}$$

The pressure at each elemental position can also be expressed as a function of the velocity of each of the elemental sources

$$\boldsymbol{p} = \boldsymbol{Z}\boldsymbol{v} \tag{3.29}$$

where $\boldsymbol{Z}$ is a matrix of acoustic transfer impedances which relates the pressure at each element to the velocity at each element and, the total acoustic power radiated is thus

$$W = \left(\frac{S_{el}}{2}\right) \Re(\boldsymbol{v}^H \boldsymbol{Z}\boldsymbol{v}) = \boldsymbol{v}^H \boldsymbol{R}\boldsymbol{v} \tag{3.30}$$

where

$$\boldsymbol{R} = \left(\frac{S_{el}}{2}\right) \Re(\boldsymbol{Z}) \tag{3.31}$$

and the symmetry of $\boldsymbol{Z}$ due to reciprocity has been used.

Here, $\boldsymbol{R}$ is a purely real, symmetric and positive definite matrix which has orthogonal real eigenvectors with positive real eigenvalues. The matrix must be positive definite on physical grounds as the power output of the plate must be greater than zero unless the velocity is zero.

The velocity distribution of the plate can be calculated from a summation of the structural modes, and by dividing the plate into a sufficiently large number of elements, the power radiated from the plate can then be calculated using equation (3.30). Only variables local to the surface are used to calculate the net power output, with no need to explicitly calculate the far field pressure [40]. For planar surfaces in an infinite baffle, the radiation resistance matrix $\boldsymbol{R}$ can also be calculated analytically.

The specific acoustic transfer impedance between elements i and j (which is the i,j'th element of $\boldsymbol{Z}$) is given by [7, 42]

$$Z_{ij} = \frac{j\omega\rho_0 S_{el}}{2\pi r_{ij}} e^{-jkr_{ij}} \tag{3.32}$$

r_{ij} is the distance between elements i and j. This equation is derived from the equation for radiation from a baffled, pulsating half sphere [7]. The elements of $\boldsymbol{R}$ are then given by

$$R_{ij} = \frac{\omega^2 \rho_0 S_{el}^2}{4\pi c_0} \left[\frac{\sin(kr_{ij})}{kr_{ij}} \right] \tag{3.33}$$

so that

$$\boldsymbol{R} = \frac{\omega^2 \rho_0 S_{el}^2}{4\pi c_0} \begin{bmatrix} 1 & \frac{\sin kr_{12}}{kr_{12}} & \cdots & \frac{\sin kr_{1I}}{kr_{1I}} \\ \frac{\sin kr_{21}}{kr_{21}} & 1 & \cdots & \cdots \\ \cdots & \cdots & \cdots & \cdots \\ \frac{\sin kr_{I1}}{kr_{I1}} & \cdots & \cdots & 1 \end{bmatrix} \tag{3.34}$$

Two approaches to examining the sound power radiated from plates have been presented above; a far field method, using Rayleigh's integral, and a near field, or elemental, method. These are different mathematical representations of the radiated power and must be equivalent. This can be shown if, in the near-field or elemental approach, the vibrations of the structure are described as a summation of structural modes. An infinite number of modes would need to be considered to model the vibrations of the plate exactly but normally, this inifinite sum is truncated to include a finite number of modes MN (equation 3.12). This approximation works especially well at low frequencies where the modal density is relatively low.

The amplitudes of the MN modes can be represented in a vector $\boldsymbol{a}$ and then, the sound power radiated by the modes can be written in terms of a matrix $\boldsymbol{M}$ of radiation resistances. In this matrix, the diagonal terms represent self-radiation resistances and the off-diagonal terms represent mutual-radiation resistances which take into account the cross coupling between structural modes.

$$W = \boldsymbol{a}^H \boldsymbol{M} \boldsymbol{a} \tag{3.35}$$

Now, the near field and far field approaches described above can be unified as the elements of

$\boldsymbol{M}$ can be calculated using the near field method and compared to the radiation efficiencies used in the far field or Rayleigh method, $\sigma_{kl,mn}$.

First of all consider the self-radiation resistances which describe the sound radiation due to a single mode. In the far field method these can be derived from equation (3.23) [7, 39] and

$$W_{mn,mn} = \int_0^{2\pi} \int_0^{\pi/2} \frac{|p_{mn,mn}|^2 r^2 \sin\theta}{2\rho_0 c_0} d\theta d\phi \tag{3.36}$$

$p_{mn,mn}$ is the far-field pressure due to the mn'th structural mode excited with unit amplitude and can be calculated using equation (3.19) with $\Psi_{mn}(x, y)$, the relevant mode shapes, substituted for the sinusoidal terms.

In the near field method, the diagonal terms of $\boldsymbol{M}$ can be calculated using the velocities of each element due to each mode

$$(v_{mn})_i = \Psi_{mn}(x_i, y_i) \tag{3.37}$$

where (x_i, y_i) is the coordinates of the centre of element i. The diagonal terms of $\boldsymbol{M}$, which give the self-radiation efficiencies, are then given by equation 3.30 as

$$M_{mn,mn} = \boldsymbol{v}_{mn}^H \boldsymbol{R} \boldsymbol{v}_{mn} \tag{3.38}$$

$\boldsymbol{v}_{mn}$ is the I length vector of elemental velocities (where I is the total number of elements) due to the mn'th structural mode. The radiated power from this mode alone is then given by equation (3.35).

For the off-diagonal terms or cross-radiation efficiencies, in the far field method, equation (3.23) can again be used

$$W_{mn,lk} = \int_0^{2\pi} \int_0^{\pi/2} \frac{p_{mn}^* p_{lk} r^2 \sin\theta}{2\rho_0 c_0} d\theta d\phi \tag{3.39}$$

p_{mn} and p_{lk} are the pressures due to the modes mn and lk respectively where $mn \neq lk$.

The near field approach, in an analogous way to above, gives

$$M_{mn,lk} = \boldsymbol{v}_{mn}^H \boldsymbol{R} \boldsymbol{v}_{lk} \tag{3.40}$$

As all the elements of $\boldsymbol{M}$ can be calculated as illustrated above and, if the modal amplitudes are known, equation (3.35) can be used to calculate the total radiated power. This should evidently give a value which is the same as that obtained when calculating the radiated power by equation (3.23) or (3.25).

The off-diagonal, or cross-radiation efficiency, terms in $\boldsymbol{M}$ mean that the radiated power due to any one structural mode is influenced by other structural modes [40]. It will be shown later that in terms of both analysing and controlling sound radiation, it would be useful to have a set of velocity distributions which radiate sound power independently of each other. These are termed radiation modes and are dealt with in the next section.

An I by NM matrix $\boldsymbol{\Phi}$ can also be defined whose rows are equal to the elemental velocities due to each mode such that

$$\boldsymbol{\Phi} = [\boldsymbol{v}_1^T \boldsymbol{v}_2^T \ldots \boldsymbol{v}_{NM}^T] \tag{3.41}$$

The vector of velocities at each of the elements can then be written

$$\boldsymbol{v} = \boldsymbol{\Phi} \boldsymbol{a} \tag{3.42}$$

and so, using equation (3.30)

$$W = \boldsymbol{v}^H \boldsymbol{R} \boldsymbol{v} = \boldsymbol{a}^H \boldsymbol{\Phi}^H \boldsymbol{R} \boldsymbol{\Phi} \boldsymbol{a} \tag{3.43}$$

When this is compared to equation (3.35) it is evident that the matrix of modal radiation resistances is

$$\boldsymbol{M} = \boldsymbol{\Phi}^H \boldsymbol{R} \boldsymbol{\Phi} \tag{3.44}$$

As an example of the power of this elemental technique, self and mutual radiation efficiencies of the modes of a clamped panel have been calculated, which would be very difficult to do analytically. These are shown in figure 3.5 and seen to be very similar to the radiation efficiencies of the simply-supported structural modes shown in figure 3.4. In this thesis, most of the simulations assume simply-supported boundary conditions whereas the experimental rigs have clamped boundary conditions, but due to the similarity between the modal radiation efficiencies, this should not cause a significant difference in the radiated sound power.

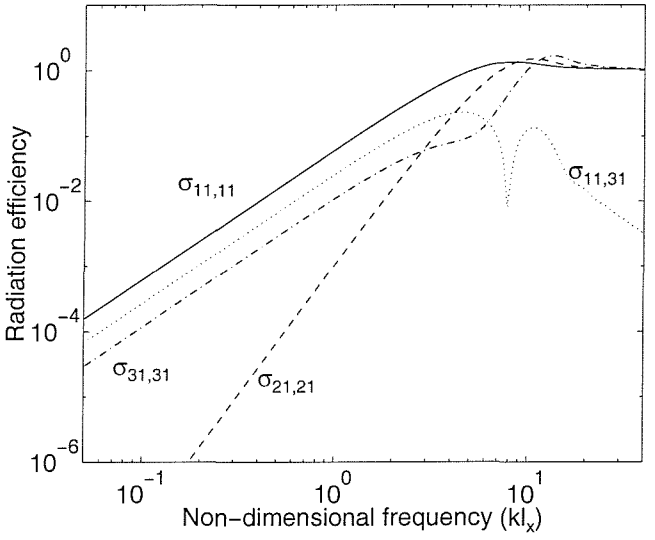

Figure 3.5: Radiation efficiencies of low order structural modes of a clamped plate

A few further points about the elemental method and modelling accuracy are worth pointing out. The method assumes that the elements are each oscillating harmonically and that they are small compared to the acoustic wavelength. Evidently then, the higher the frequency range required for accurate modelling, the greater number of elements required. As an example, the plate considered in this thesis has dimensions $0.278m$ by $0.247m$. If this is split into 20 elements along each side, then the smallest element has dimensions of approximately $0.013m$. At frequencies of $1kHz$ which corresponds to the highest frequency of interest for control during

this thesis, the wavelength of sound in air is $0.343m$. It is evident that even at the highest frequency of interest, the elemental dimensions are an order of magnitude less than the acoustic wavelength. The second consideration in using the elemental approach is that, in order to prevent spatial aliasing, the number of elements used in the model should be greater than the number of modes to be modelled and, preferably more than twice this value. This is analogous to the normal aliasing which occurs when a signal is not sampled at a sufficiently high rate. With 20 by 20 elements, most simulations in this report generally use $M = N = 7$ i.e. a maximum of 49 modes and any spatial aliasing is clearly avoided. Increasing the frequency range of interest would also require a larger number of modes in the model.

3.2.3 Radiation modes

A technique for analysing sound radiation due to plate vibrations which has been developed more recently is to use a summation of radiation modes instead of the structural modes described above.

There are a number of ways of considering radiation modes but in this section the near field or elemental approach which has been used in the previous section will be used. Other approaches are outlined in references [7, 19, 40, 41]. The link between structural and radiation modes is discussed in section 3.2.4 below.

Looking back at equation (3.30), the matrix $\boldsymbol{R}$ is found to be symmetric (due to reciprocity), real (proportional to $\Re(\boldsymbol{Z})$), and positive definite (as the power output of the plate must be greater than zero unless velocity is zero). This means that it can be decomposed into a set of orthogonal real eigenvectors with positive real eigenvalues.

$$\boldsymbol{R} = \boldsymbol{Q}^T \boldsymbol{\Lambda} \boldsymbol{Q} \tag{3.45}$$

where $\boldsymbol{Q}^T$ is a real and unitary matrix of orthogonal eigenvectors, and $\boldsymbol{\Lambda}$ is a diagonal matrix whose elements λ_i are the eigenvalues and are positive real numbers.

If this eigenvector/eigenvalue decomposition (equation 3.45) is substituted into the equation representing radiated power for the elemental radiator approach, equation (3.30)

$$W = \boldsymbol{v}^H \boldsymbol{R} \boldsymbol{v} = \boldsymbol{v}^H \boldsymbol{Q}^T \boldsymbol{\Lambda} \boldsymbol{Q} \boldsymbol{v} \tag{3.46}$$

Now define $\boldsymbol{y} = \boldsymbol{Q}\boldsymbol{v}$, as the vector of radiation mode amplitudes, in terms of the velocities of individual elements so that

$$W = \boldsymbol{y}^H \boldsymbol{\Lambda} \boldsymbol{y} = \sum_{i=1}^{I} \lambda_i |y_i|^2 \tag{3.47}$$

where the final form follows from the fact that $\boldsymbol{\Lambda}$ is diagonal.

The power output due to any one of these eigenvectors is then equal to its amplitude squared multiplied by its corresponding eigenvalue. This equation also shows that the modes are radiating independently (due to the diagonal nature of matrix $\boldsymbol{\Lambda}$, i.e. no cross terms), in contrast to the structural modes described above, hence the term radiation modes. The total radiated sound power can be calculated as a sum of individual mode amplitudes squared multiplied by their corresponding eigenvalues.

It has already been shown in equation (3.34) above that for sources mounted in an infinite baffle the matrix $\boldsymbol{R}$ takes the form

$$\boldsymbol{R} = \frac{\omega^2 \rho S^2}{4\pi c_0} \begin{bmatrix} 1 & \frac{\sin kr_{12}}{kr_{12}} & \dots & \frac{\sin kr_{1I}}{kr_{1I}} \\ \frac{\sin kr_{21}}{kr_{21}} & 1 & \dots & \dots \\ \dots & \dots & \dots & \dots \\ \frac{\sin kr_{I1}}{kr_{I1}} & \dots & \dots & 1 \end{bmatrix}$$

The eigenvalue/eigenvector decomposition of this matrix thus gives the radiation mode shapes and radiation efficiencies.

Figure 3.6 shows the radiation efficiencies of the first few radiation modes as a function of non-dimensional frequency obtained by the eigenvalue/eigenvector decomposition. It is clear that, at low frequencies, the radiation efficiency of the first radiation mode is very large in

comparison with the efficiencies of the other modes which would suggest that controlling this radiation mode would be a good strategy and this is much of what the remainder of this thesis focuses on. Figure 3.7 shows the shapes of the first six radiation modes at a low frequency of $100Hz$. The first radiation mode shows each element of the plate vibrating with almost the same phase and amplitude, and this is the volume velocity of the plate. The changing shape of the first radiation mode with frequency will also be considered for control purposes in later chapters. The shape of the first radiation mode, obtained from the eiegenvectors of $\boldsymbol{R}$, at $100Hz$ and $1kHz$ are shown in figure 3.8. There is clearly a significant difference in this shape over this frequency range.

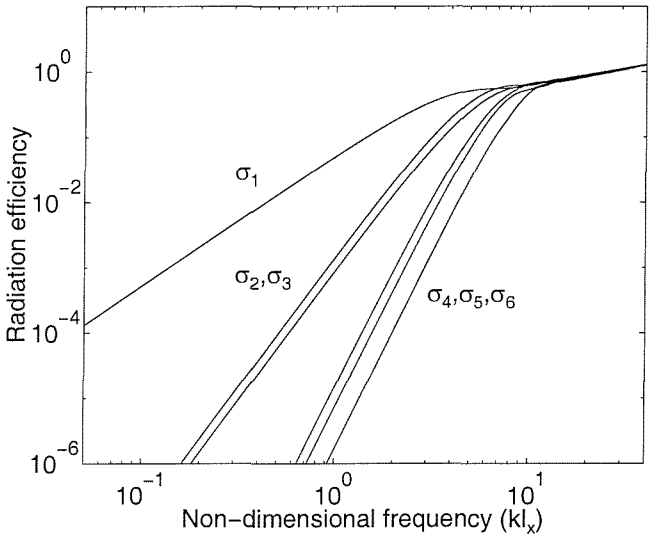

Figure 3.6: Radiation efficiencies of low order radiation modes

Although the matrix $\boldsymbol{R}$ is a function of geometry of the surface, it is independent of the dynamic properties of the surface. The structural mode content of a vibrating structure will therefore affect the amplitudes of the radiation modes but will not affect their shapes or radiation efficiencies.

These radiation modes are found to have a number of advantages when it comes to active structural acoustic control. First of all, the fact that they radiate sound independently means that reducing the amplitude of any one radiation mode without affecting the others is sure to cause a reduction in the total radiated sound power. This is in contrast to the control of a single structural mode outlined above. Furthermore, the first radiation mode is seen to have a much larger radiation efficiency than the other radiation modes at low frequencies. The shape of this first radiation mode is found to have a very simple form. At very low frequencies, it corresponds

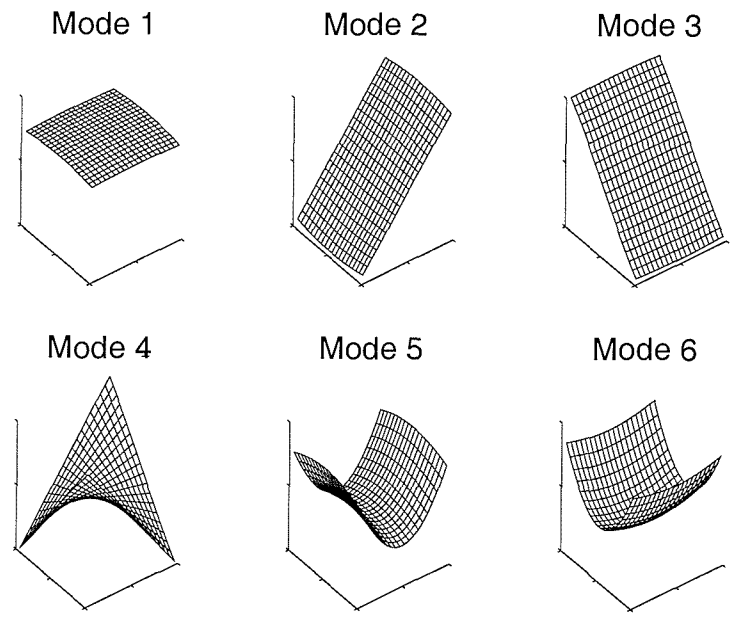

Figure 3.7: Shapes of first six radiation modes at 100Hz

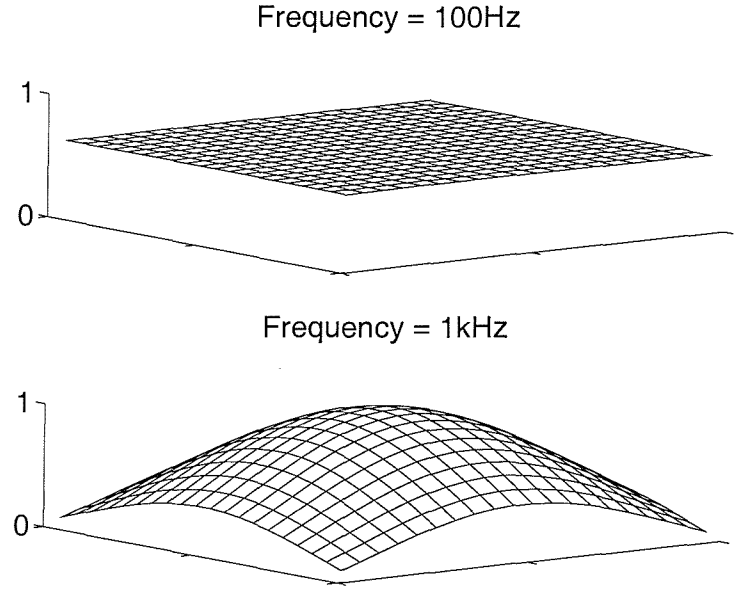

Figure 3.8: Shape of first radiation mode at $100Hz$ and $1kHz$ (normalised amplitudes)

to the volume velocity of the plate. This is the motivation for looking at the control of volume velocity during the rest of the thesis; by reducing the volume velocity, the total radiated power should also be reduced.

3.2.4 Relationship between radiation modes and structural modes

The two methods of describing plate vibrations outlined above, using either structural or radiation modes, are only two of the many different ways of describing the same plate vibrations. Although the two approaches have already been dealt with under the same framework of the near field approach above, this section is intended to show further how the two types of modes can be dealt with in a unified approach. Although this is mostly taken from [7] and [40], there are many other references, [43, 44] for example, which have dealt with this topic in some detail and using slightly different mathematical representations and interpretations.

In section 3.2.2 the radiation resitance matrix $\boldsymbol{M}$ was introduced and two methods of how the individual elements of this matrix could be calculated were shown. The matrix is real, symmetric and positive definite and, as with the matrix $\boldsymbol{R}$ above, it has an eigenvalue/eigenvector decomposition

$$\boldsymbol{M} = \boldsymbol{P}^T \boldsymbol{\Omega} \boldsymbol{P} \tag{3.48}$$

where $\boldsymbol{P}^T$ is an orthogonal matrix of eigenvectors (c.f. $\boldsymbol{Q}$) and $\boldsymbol{\Omega}$ is a diagonal matrix whose elements Ω_i are the real, positive eigenvalues (c.f. $\boldsymbol{\Lambda}$).

Using equation (3.35) the power output can then be written

$$W = \boldsymbol{a}^H \boldsymbol{M} \boldsymbol{a} = \boldsymbol{a}^H \boldsymbol{P}^T \boldsymbol{\Omega} \boldsymbol{P} \boldsymbol{a} \tag{3.49}$$

and, if a vector of transformed radiation mode amplitudes is now defined $\boldsymbol{b} = \boldsymbol{P}\boldsymbol{a}$, then the expression for the radiated power can be written

$$W = \boldsymbol{b}^H \boldsymbol{\Omega} \boldsymbol{b} = \sum_{n=1}^{NM} \Omega_n |b_n|^2 \tag{3.50}$$

The diagonal nature of the matrix $\boldsymbol{\Omega}$ allows the radiation to be expressed as a sum of modulus squared amplitudes of the elements of the vector $\boldsymbol{b}$ times their corresponding eigenvalues. The structural mode amplitudes given in $\boldsymbol{a}$ are combined with the eigenvectors of $\boldsymbol{P}$ to give velocity distributions which radiate sound independently and these are again termed radiation modes. The off-diagonal terms in $\boldsymbol{M}$ which give rise to the interdependence between structural modes are not present in the matrix $\boldsymbol{\Omega}$ which means that the new velocity distributions are orthogonal and the radiation of each one is unaffected by the amplitudes of the other radiation modes. This formulation is seen to be very similar to the previous radiation mode formulation given in equation (3.47). Both methods result in eigenfunctions which radiate independently. When the radiation modes are determined from the structural mode amplitudes, then NM modes are required to describe the sound radiation fully and when the radiation modes are determined from the decomposition of $\boldsymbol{R}$ then I modes are needed to describe the sound radiation.

This formulation was also used by Cunefare [43] and is similar to the analysis of Baumann *et al.* [45]. Other variations on the radiation mode approach include designing a set of frequency-independent basis functions which are recombined with frequency-dependent weighting matrices to give the radiated power as described by Borgiotti and Jones [46] for example or dividing a structure into sections and controlling local volume velocity instead of global volume velocity [47–49].

3.3 Conclusions

This chapter has covered the modelling of plate vibrations and the subsequent sound radiation from the vibrating plates. Structural modes were described which is the common method of describing plate vibrations. The sound radiation was then calculated using both the Rayleigh integral and with a near-field or elemental approach. The advantage of the elemental approach is that only variables local to the plate need to be measured to calculate the radiated power.

Radiation modes were then used to describe the plate vibrations and the sound power radiated.

The advantage of the radiation modes is that they radiate sound independently of each other and so, by reducing the amplitude of one radiation mode, the total radiated power is sure to be decreased. This is not the case with structural modes which have a complex interaction with each other. The first radiation modes also turns out to radiate sound far more efficiently than the other modes at low frequencies and is found to have a shape similar to the volume velocity of the plate. This provides the basis for the rest of the thesis; that by reducing the volume velocity of the plate, the sound radiation should also be reduced.

Although this chapter has mostly covered established theory it is important to the rest of the thesis as controlling the radiation modes, and especially the volume velocity, is one of the major aims of the thesis.

Chapter 4

Transducers for active structural acoustic control

4.1 Introduction to transducers

There are several areas of research, outlined in the introduction, which are brought together in studying ASAC. One field which is allowing rapid progress in ASAC is the development of new transducers which allows new and efficient methods of applying control forces to structures and new ways of sensing appropriate structural error signals.

The piezoelectric materials used for ASAC purposes combine good performance as well as relatively low prices and ease of manufacture. They can also be shaped easily during manufacture and this will be shown to be important for the control of selected modes. The shaping can be performed to correspond either to structural or radiation modes.

In this chapter, mathematical models for the various transducers are developed. For more details on how the piezoelectric materials work, the reader is referred to Lee [50].

The first section of this chapter looks at general models of actuators and sensors and how these transducers models can be combined into the models and equations developed in chapter 3 by means of relevant forcing and sensing functions. Three specific types of actuator are then discussed in more detail and then, three sensors, which are seen to have direct analogies with these

actuators, are also described. The transducer models are then used to compare the performance of various transducer arrangements for ASAC applications. Feedforward simulations are used as they provide the best possible control performance which can be obtained from a given set of transducers. Control performance is measured in terms of the amount of attenuation achieved in the power transmission ratio after feedforward control.

Another important consideration which has significant effects on performance is the positioning of the transducers on the structure. Although there are various methods of positioning the transducers in an optimal way, such as numerical optimization methods [51], exhaustive searches, and natural algorithms [52] (all of which are reviewed by [53]), these tend to be highly computationally intensive and in this chapter an approach based more on physical arguments will be used to place them.

4.2 Modelling of transducers

In chapter 3, it was shown that the complex vibrations of a simply-supported plate can be described by the equation

$$w(x,y,t) = \sum_{m=1}^{\infty}\sum_{n=1}^{\infty} W_{mn}(\omega)\sin(k_m x)\sin(k_n y) \tag{4.1}$$

which shows a summation of structural modes, each with a frequency dependent amplitude $W_{mn}(\omega)$ and where a time dependence of the form $e^{j\omega t}$ has been assumed. Where several sources of excitation are present, the overall vibration of the plate can be calculated by superposition of the forcing coefficients. For example, if four sources of excitation are present, say an incident wave and three control actuators

$$W_{mn}(\omega) = A_{mn}(\omega)[F_{mn1} + F_{mn2} + F_{mn3} + F_{mn4}] \tag{4.2}$$

where F_{mni} is the excitation from the i'th source. The plate vibrations are then given by

$$w(x,y,\omega) = \sum_{m=1}^{\infty}\sum_{n=1}^{\infty}\sum_{i=1}^{I} A_{mn}(\omega)F_{mni}\sin(k_m x)\sin(k_n y) \tag{4.3}$$

where I is the total number of sources of excitation.

Equation (4.2) clearly shows the effect of different sources of excitation on the plate vibrations and in section 4.3, the forcing coefficients F_{mni} will be derived for different actuators and sources of excitation.

A similar method can be used to model sensors through the use of a sensitivity coefficient S_{mn} which gives the sensitivity of a sensor to each mode so that the sensor output y is given by

$$y = \sum_{m=1}^{\infty}\sum_{n=1}^{\infty} S_{mn}W_{mn} \tag{4.4}$$

If instead of having a direct measurement of the full velocity distribution of the plate, some type of sensors, which each have their own characteristics or frequency response functions are used, then the whole frequency response function between the input to the actuators and the output from the sensors must be considered. This can be considered to be a combination of three separate frequency response functions; that due to the actuators $G_f(\omega)$, due to the structure itself $G_p(\omega)$, and due to the sensors $G_s(\omega)$. These are combined such that

$$y(\omega) = G_{tot}(\omega)u(\omega) \tag{4.5}$$

where $u(\omega)$ is the input voltage to the actuators and

$$G_{tot}(\omega) = G_f(\omega)G_p(\omega)G_s(\omega) \tag{4.6}$$

When using the modal methods outlined above, this can be written

$$G(\omega) = \sum_{m=1}^{\infty} \sum_{n=1}^{\infty} F_{mn} S_{mn} A_{mn}(\omega) \tag{4.7}$$

These sensitivity coefficients are described, for a variety of sensors, in section 4.4. The combination of actuators and sensors, as shown in equation (4.7), is discussed in section 4.5.

4.3 Actuators

Actuators are used to apply control signals in order to change the system response in the required manner and this section deals with actuators and various sources of excitation. In the first place, a point force is modelled. This is the most simple type of actuator. The second and third actuators use piezoceramic materials whose uses are becoming widespread and allow spatially-distributed excitation which will be seen to be an important property. As incident plane waves are used as a source of primary disturbance in this thesis, the response of the plate to an incoming plane wave is also calculated and finally, the response of the plate to an excitation within an enclosure is derived.

For each different actuator, a short discussion is given outlining the basic mechanisms by which the actuators excite the structure and the relevant forcing coefficient F_{mn} is given.

4.3.1 Point force actuators

Point force actuators are fairly straightforward to model and so they have been used often in active control simulations. In this section, the forcing function F_{mn} of a point force is derived from the equations of motion of the plate. A thin rectangular plate is again considered for simplicity and to continue with previous examples, this is again assumed to be simply-supported. Other boundary conditions would not give rise to the exact solutions which follow but the method of solution is the same.

Referring to the equation of motion due to a force, the excitation due to a point force with coordinates x_p, y_p and amplitude A_p can be expressed

$$F(x,y)e^{j\omega t} = A_p\delta(x-x_p)\delta(y-y_p)e^{j\omega t} \tag{4.8}$$

To demonstrate how this would excite a simply-supported plate for example, this expression is substituted into equation (3.15) and then, using the orthogonality property of the plate structural modes and the sifting property of the dirac delta function,

$$F_{mn}^{p} = 4A_p \sin k_m x_p \sin k_n y_p \tag{4.9}$$

Fuller was one of the first to consider using these structural point forces for controlling sound radiation [54, 55]. He found this to be quite a successful strategy requiring only a small number of control channels. Using point forces resulted in higher order mode vibration distributions with lower radiation efficiencies and the overall sound radiation from the plate was reduced.

Although the location of actuators is dealt with in detail below, it is evident that the placement of the point force is critical. A central point force for example, would only be able to excite odd-odd modes as it is located on the nodal line for even modes. Similarly, in the centre it is at a point of maximum amplitude for odd-odd modes and so this would be the best position to excite these modes.

4.3.2 Piezoceramic actuators

The point force actuators described in 4.3.1 were the first actuators used for ASAC but the use of distributed piezoceramic actuators has recently become more common. One disadvantage of the point forces is in their practical implementation. Electromagnetic shakers, for example, are heavy and cumbersome and, most importantly, they require a reaction mount. As ASAC is often intended for lightweight structures, these point forces are normally impractical. In contrast, the piezoelectric transducers available are low cost, lightweight, and are easy to incorporate into the structures to be controlled. Another advantage of these distributed piezoceramic actuators is the fact that they can be easily shaped. Merovitch and Norris [56] first describe a move from using single point force actuators towards using distributed actuators. The most complete comparison of point force actuators and piezoceramic actuators is given by Wang *et al.* [24].

Further discussions of the relative performance of point forces and distributed actuators is left to section 4.5. In this section, a brief introduction to piezoelectric materials is given and then, following an analogous approach to the point force, the forcing function F^c_{mn} due to a piezoceramic patch is derived. Piezoelectric transducers rely on the piezoelectric effect, which was first discovered by Pierre and Jacques Curie in 1880 and causes piezoelectric materials to produce an electric polarization when mechanically stressed and, reciprocally, the same materials produce a mechanical strain when an electrical current is applied.

There are many of these piezoelectric materials, most of them having crystalline structures and, being brittle, are difficult to manufacture and shape. However, some piezoelectric materials in the form of ceramics have also been developed and these have a number of advantages over their crystal counterparts including that they are hard, dense, have high stiffness, and can be manufactured to almost any shape or size. Furthermore, the electrical properties of the ceramic can be controlled during the poling process. An example of these piezoceramic materials which is commonly used for actuators is PZT or Lead Zirconate Titanate [7, 19]. Some typical properties for PZT are shown in table 4.1.

Property	Symbol	Value
Young's modulus	E_{pe}	$6.3\text{x}10^{10} N/m^2$
density	ρ_{pe}	$7650 kg/m^3$
Poisson's ratio	ν_{pe}	0.30
piezoelectric strain constant	d_{31}=d_{32}	$-166\text{x}10^{-12} m/V$
piezoelectric strain constant	d_{36}	0

Table 4.1: Properties of PZT, G1195

For each piezoelectric material, there is a relationship between the electric voltage applied to the material and its subsequent change in shape. This relationship depends on the material of the actuator, its size, shape, and how it is oriented with respect to the structure it is bonded to. The piezoceramic is described in terms of its three axes termed 1, 2 and 3 in the x, y and, z directions respectively (indices 4, 5 and 6 represent negative changes in the directions of these principal axes). These axes are set during the poling process. Piezoelectric coefficients then give the relationships between the electrical properties (voltage applied or charge produced) in one axis direction and the mechanical strain produced or measured in another direction, represented by subscripts in the coefficients. For example, the piezoelectric strain constant d is the ratio of

developed free strain, ε, to the applied electric field V. The coefficient d_{31} then implies that the voltage is applied in the 3 (positive z) direction and the resulting displacement or force is in the 1 (positive x) direction. This is found to be the most important piezoelectric coefficient for the purposes of this project and the relationship between the applied voltage and the resulting strain is given by

$$\varepsilon_{pe} = \frac{d_{31}V}{h_a} \tag{4.10}$$

ε_{pe} is the strain in the x direction, h_a is the piezoceramic thickness, and V is the applied voltage.

When such a voltage is applied, the resulting force on the structure itself is calculated by assuming the piezoceramic behaves linearly and by coupling the piezoceramic strain-voltage equations (equation (4.10) for example) with equation (3.10) governing the deflection of the structure under a given applied force. The equivalent static force or moment due to the actuator is then calculated and used as a frequency-independent amplitude for harmonic input to the system. This model is accurate well below the internal resonant frequency of the piezoceramic, typically $1MHz$, which covers the frequency range of interest for this thesis.

To derive the forcing coefficient, consider a piezoelectric patch with edges defined by x_1, x_2, y_1, y_2, as shown in figure 3.1, which produces a strain over its area. It is assumed that purely bending waves are generated and in-plane forces are ignored. On a thin, flat, isotropic plate, the strain produced by this actuator is proportional to the second derivative of the out of plane displacement with respect to x and y. The forcing of each mode is then obtained by taking the integral, over the area of the piezoelectric, of the second derivative of the displacement due to that mode. The modal forcing coefficient can then be calculated using the same equations as developed above for the point force.

Consider the harmonic excitation of a simply-supported thin plate by a single actuator. The actuator produces line moments along its edges such that

$$F(x,y) = C_0\varepsilon_{pe}[H(x-x_1) - H(x-x_2)][H(y-y_1) - H(y-y_2)] \tag{4.11}$$

$C_0\varepsilon_{pe}$ are constants of the piezoelectric material and $H(x)$ is the Heaviside function.

The actuator is assumed to be driven by a harmonically oscillating voltage and inertial and end effects of the actuator are ignored. This is the static model of piezoceramics as outlined by Crawley and de Luis [57] for example. The actuator is also assumed to be perfectly bonded to the plate but not to change its mode shapes or modal frequencies. Then, by substituting the forces due to the actuator (4.11) into the equation of motion (3.10)

$$\begin{aligned} &D\nabla^4 w + \rho\frac{\partial^2 w}{\partial t^2} = C_0\varepsilon_{pe}[\delta'(x-x_1) - \delta'(x-x_2)] \\ &[H(y-y_1) - H(y-y_2)] + C_0\varepsilon_{pe}^3[H(x-x_1) - H(x-x_2)][\delta'(y-y_1) - \delta'(y-y_2)] \end{aligned} \tag{4.12}$$

Turning again to the example using the simply-supported plate

$$w(x,y,\omega) = \sum_{m=1}^{\infty}\sum_{n=1}^{\infty} W_{mn}(\omega)\sin\left(\frac{m\pi x}{l_x}\right)\sin\left(\frac{n\pi y}{l_y}\right)$$

then, after substituting this form of vibration back into the equation of motion (4.12) and again using the orthogonality property of the structural modes, the modal amplitudes are found to be given by

$$\begin{aligned} W_{mn} =& \frac{2C_0\varepsilon_{pe}}{mn\pi^2\rho h l_x l_y((\omega_{mn}^2 - \omega^2) - j\omega D_{mn})} \\ &\left[\frac{(k_m^2 + k_n^2)}{k_m k_n}(\cos k_m k_1 - \cos k_m x_2)(\cos k_n y_1 - \cos k_n y_2)\right] \end{aligned} \tag{4.13}$$

when this is compared with the equation for the modal coefficients (3.14), the modal forcing function is found to be given by

$$F_{mn}^c = \frac{2C_0\varepsilon_{pe}}{mn\pi^2}\frac{(k_m^2 + k_n^2)}{k_m k_n}(\cos k_m x_1 - \cos k_m x_2)(\cos k_n y_1 - \cos k_n y_2) \tag{4.14}$$

A similar analysis has been performed for circular actuators by Sonti *et al.* [58]. In terms of the way in which a piezoelectric actuator excites a structure there seems to be little difference

between circular and rectangular actuators. However, it has been suggested that circular actuators may be slighty less brittle than rectangular ones, which can produce defects around their edges and corners after long-term usage. For a more complete description of how piezoelectric materials can be used as actuators and sensors see [19, 25, 50, 57, 59].

4.3.3 Uniform force actuators

Section 3.2.3 introduced the concept of radiation modes and went on to show that the first radiation mode, which accounts for most of the sound power radiated by a plate at low frequencies, is the volume velocity of the plate. This corresponds to the piston motion of the plate or, in the elemental approach, to the sum of the elemental velocities. Johnson [7] investigated the control of volume velocity of a structure to reduce sound radiation and showed it to be an effective and simple control strategy. It is also shown below (section 4.6) that collocated and matched transducers have advantages in feedback control systems. By matched, it is meant that the spatial distribution of the forcing function should be the same as the spatial distribution of the sensing function. It would then make sense to develop some kind of actuator which forces the volume velocity or piston motion of the plate. In the elemental approach, this would correspond to forcing each element with the same amplitude.

The modal forcing coefficient for a uniform force actuator with amplitude A_u, and with edges x_1, x_2, y_1, y_2 as shown in figure 3.1 is given by integrating the force due to the actuator over the plate and by equating with the equation of motion of the plate (3.1) as shown by Fuller *et al.* [19] such that

$$F_{mn}^{u} = \frac{A_u}{mn\pi^2}(\cos k_m x_1 - \cos k_m x_2)(\cos k_n y_1 - \cos k_n y_2) \tag{4.15}$$

In principle, since a volume velocity sensor has already been developed and using the reciprocity effects of piezoelectric materials, it should be fairly straightforward to develop a uniform force actuator. However, current efforts to develop a matched actuator/sensor pair have been unsuccessful and, at the time of writing this thesis, a reliable uniform force actuator has not yet been developed. One of the major problems is that the uniform force actuators currently available

produce in-plane as well as bending forces. The design of a uniform force actuator and the problems involved in its implementation are discussed by Gardonio *et al.* [26].

On the subject of shaped actuators, it would in principle be possible to design an actuator which only excites a particular structural mode of a beam or plate. On a simply-supported beam, this would take the form

$$F(x) = F_m \sin k_n x \tag{4.16}$$

The orthogonality of the structural modes means that the response of other modes to this form of excitation would be zero and this would prevent spillover. This type of modal excitation has been investigated by a number of people [19, 25].

4.3.4 Plate excitation by an acoustic plane wave

Excitation of the plate by an acoustic plane wave can be dealt with under the same framework as above i.e. by calculating its contribution to plate vibrations due to a forcing factor F^i_{mn}.

The plane wave is assumed to have angles of incidence θ, ϕ as shown in figure 3.1 and when the plate is simply-supported, and light fluid loading is assumed so that radiation loading effects on plate dynamics can be neglected, the excitation can be calculated analytically. This analysis has been performed by Roussos [60] and is also covered by Wang [61] and by Fuller *et al.* [19]. As above, the mode shapes and forcing function are put into the differential equation of motion of the plate, equation (3.10). When the simply-supported boundary conditions are used, the integration can be carried out in closed form to obtain the generalized forcing pressure for each mode.

A harmonic wave incident on the plate with angles θ, ϕ and amplitude P_i will create a pressure field in the plane of the plate given by

$$p(x, y, t) = P_i e^{j(\omega t - k_x x - k_y y)} \tag{4.17}$$

where the wavenumbers in the x and y directions are given by

$$\begin{aligned} k_x &= k \sin\theta \cos\phi \\ k_y &= k \sin\theta \sin\phi \end{aligned} \tag{4.18}$$

The modal forcing coefficient due to this pressure is calculated by Roussos [60] and is given by

$$F^i_{mn} = 8 P_i I_m I_n \tag{4.19}$$

where I_m and I_n are due to the geometric coupling between the plane wave and the mn'th mode shape and are given by

$$\begin{aligned} I_m &= \frac{m\pi \left[1 - (-1)^m e^{-j \sin\theta \cos\phi (\omega l_x / c)}\right]}{[m\pi]^2 - [\sin\theta \cos\phi (\omega l_x / c_0)]^2} \\ &\text{if} \\ m\pi &\neq \pm \sin\theta \cos\phi \left(\frac{\omega l_x}{c_0}\right) \end{aligned} \tag{4.20}$$

or

$$\begin{aligned} m\pi &= \left(\frac{j}{2}\right) sgn(\sin\theta \cos\phi) \\ &\text{if} \\ m\pi &= \pm \sin\theta \cos\phi \left(\frac{\omega l_x}{c_0}\right) \end{aligned} \tag{4.21}$$

and

$$\begin{aligned} I_n &= \frac{n\pi \left[1 - (-1)^n e^{-j \sin\theta \sin\phi (\omega l_y / c)}\right]}{[n\pi]^2 - [\sin\theta \sin\phi (\omega l_y / c_0)]^2} \\ &\text{if} \\ n\pi &\neq \pm \sin\theta \sin\phi \left(\frac{\omega l_y}{c_0}\right) \end{aligned} \tag{4.22}$$

or

$$n\pi = \left(\frac{j}{2}\right) sgn(\sin\theta \sin\phi)$$

$$\text{if} \tag{4.23}$$

$$n\pi = \pm \sin\theta \sin\phi \left(\frac{\omega l_y}{c_0}\right)$$

where $sgn()$ implies taking the sign of the term in brackets.

4.3.5 Plate excitation by an enclosed source

This section derives the plate vibrations due to a loudspeaker within an enclosure. The plate is assumed to replace one wall of the enclosure, which is otherwise assumed to be rigid-walled. A weakly-coupled model is used which does not take into account the effects of the vibrating plate on the pressure in the enclosure. This model is suitable if the pressure produced by the vibrating plate is neglibile compared to the pressure produced by the primary disturbance. For details of the fully-coupled model, see [62]. The following analysis can be found in [11, 63, 64].

The enclosure, shown in figure 4.1 has dimensions L_x, L_y, L_z in the (x, y, z) directions.

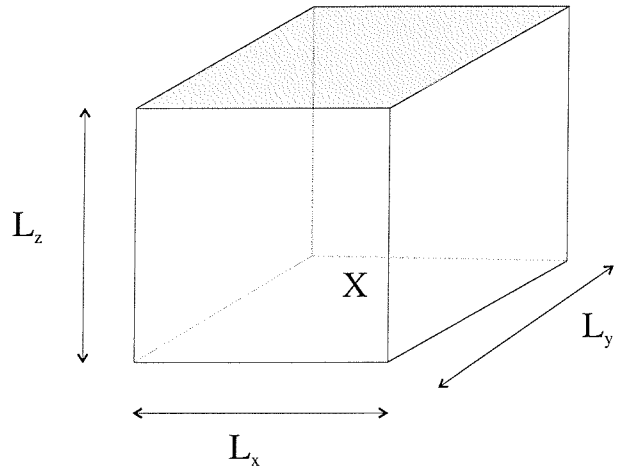

Figure 4.1: Figure of enclosure on which plate (shaded) is mounted. X marks position of disturbance loudspeaker.

The pressure at a point $\boldsymbol{x}$ in a rigid walled enclosure can be written as the sum of a series of

acoustic modes which are given by the eigenfunctions of the Helmholtz equation such that

$$\nabla^2\phi_n(\boldsymbol{x}) + k_n^2\phi_n(\boldsymbol{x}) = 0 \tag{4.24}$$

where $\phi_n(\boldsymbol{x})$ is the eigenfunction or mode shape and k_n^2 is the eigenvalue corresponding to the n'th eigenfunction which can be expressed as

$$k_n^2 = \frac{\omega_n^2}{c_0^2} = \left[\frac{n_1\pi}{L_x}\right]^2 + \left[\frac{n_2\pi}{L_y}\right]^2 + \left[\frac{n_3\pi}{L_z}\right]^2 \tag{4.25}$$

where n_1, n_2, n_3 are modal indices which must be integers.

The eigenfunctions must also satisfy the rigid walled boundary condition

$$\boldsymbol{\nabla}\phi_n(\boldsymbol{x}).\boldsymbol{n} = 0 \tag{4.26}$$

on the surface of the enclosure where $\boldsymbol{n}$ is the unit vector on the surface of the enclosure pointing outwards. The solution to the equations for a rectangular enclosure is given by

$$\phi_n(\boldsymbol{x}) = \sqrt{\epsilon_{n1}\epsilon_{n2}\epsilon_{n3}}\cos\frac{n_1\pi l_x}{L_x}\cos\frac{n_2\pi l_y}{L_y}\cos\frac{n_3\pi l_z}{L_z} \tag{4.27}$$

The ϵ_* are normalisation factors derived below.

As the modes must be orthonormal the product of two modes over the enclosure volume must be zero

$$\int_V \phi_n(\boldsymbol{x})\phi_m(\boldsymbol{x})dV = 0 \qquad n \neq m \tag{4.28}$$

and

$$\int_V \phi_n^2(\boldsymbol{x})dV = V \tag{4.29}$$

which requires $\epsilon_{n*} = 1$ if $n_* = 0$ or $\epsilon_{n*} = 2$ if $n_* > 0$. These orthonormality equations can be summarised with the equation

$$\int_V \phi_n(\boldsymbol{x})\phi_m(\boldsymbol{x})dV = V\delta_{nm} \tag{4.30}$$

where δ_{nm} is the delta function.

Now the mode shapes of the rigid walled enclosure are known, they can be used to calculate the sound pressure field inside a lightly damped enclosure due to a primary disturbance as given in [19] for example. The pressure at a point $\boldsymbol{x} = (x, y, z)$ in the enclosure is given by

$$p(\boldsymbol{x}) = \sum_{n=0}^{\infty} a_n \phi_n(\boldsymbol{x}) \tag{4.31}$$

The enclosure mode shapes are already given above in equation (4.27) and the modal amplitudes a_n can be calculated by

$$a_n = \frac{\omega \rho_0 c_0^2}{V[2\zeta_n \omega_n \omega + j(\omega^2 - \omega_n^2)]} \int_V \phi_n(\boldsymbol{x}_s) q_{vol}(\boldsymbol{x}_s) dV \tag{4.32}$$

for a given source distribution in the enclosure given by $q_{vol}(\boldsymbol{x}_s)$. Here viscous damping has been included in the model by the coefficient ζ_n. This equation is seen to have a very similar form to the complex resonance term A_{mn} in equation (3.16) and so equation (4.32) can be rewritten

$$a_n = A_n^{encl} \int_V \phi_n(\boldsymbol{x}_s) q_{vol}(\boldsymbol{x}_s) dV \tag{4.33}$$

where

$$A_n^{encl} = \frac{\omega \rho_0 c_0^2}{V[2\zeta_n \omega_n \omega + j(\omega^2 - \omega_n^2)]} \tag{4.34}$$

For a monopole source within the enclosure of strength q_p at position $\boldsymbol{x}_s$

$$q_{vol} = q_s \delta(\boldsymbol{x} - \boldsymbol{x}_s) \tag{4.35}$$

and so the modal amplitudes become

$$a_n = A_n q_s \phi_n(\boldsymbol{x}_s) \tag{4.36}$$

The loudspeaker in the enclosure can be modelled as such a monopole source and it is clear that the way in which the primary source excites the modes of the enclosure is very dependent on the position of the source. The plate is assumed to be positioned at a height of L_z (see figure 4.1) and to calculate the vibration distribution of the plate, due to this primary disturbance, the pressure field in the plane of the plate is calculated: $p(x, y, L_z, \omega)$. This is equivalent to the spatial forcing distribution of the plate. The resulting vibration distribution is calculated by integrating this force over the area of the plate to calculate the amplitude of each plate mode by using equation (4.9). The modal forcing coefficient (for a simply-supported plate for example) can then be calculated to be

$$F_{mn}^{encl} = \int_S 4p(x, y, L_z) \sin k_m x \sin k_n y dS \tag{4.37}$$

Further information on excitations within enclosures can be found in [63] or [64]. The fully-coupled (c.f. weakly-coupled used here) case is described by [62] and [65].

Enclosure natural frequencies, based on the physical properties of the enclosure used in experiments later in the thesis, are given in table 4.2 and can be compared with the plate natural

frequencies given in tables A.1 and A.3. Apart from the volumetric $(0,0,0)$ mode of the enclosure, the natural frequencies are relatively high compared to the low-order plate natural frequencies which helps to justify the use of the weakly-coupled model.

x	y	z	frequency (Hz)
0	0	0	0
1	0	0	429
0	1	0	490
0	0	1	572
1	1	0	651
1	0	1	715
0	1	1	753
2	0	0	858
1	1	1	866
2	1	0	988

Table 4.2: Enclosure natural frequencies

4.4 Sensors

Sensors are needed in control systems for measurements which give important disturbance information and system variables [19]. There are two basic types of sensor which will be dealt with in this thesis; acoustic sensors, such as microphones in the far-field, or sensors which are integrated with the structure itself. The aim when using a structural sensor, as opposed to a far-field acoustic sensor, is to measure a variable which gives a good indication of the radiated power which has to be controlled. By only sensing important sound-radiating modes of the structure, it may also be possible to reduce the number of channels relative to the case where acoustic sensors are used. A further advantage in using structural sensors is that for feedback control, it will be shown that the phase in the plant frequency response function (FRF) must be as small as possible and, this is seen to be the case when structural actuators are used with structural sensors.

This section deals with three specific types of structural sensor and the use of microphones. The three structural sensors discussed are accelerometers, piezocelectric sensors, and the distributed

volume velocity sensor. These are reciprocal sensors to the actuators considered in section 4.3 and this spatial matching will be seen to be important (section 4.6).

The sensors will also be modelled by analogy with section 4.3 and by modelling the sensing functions introduced in equation (4.4). This equation shows that, just as each actuator forces a given mode by a certain amount, F_{mn}, so each sensor measures the mode by a certain amount given by its sensing coefficient S_{mn}.

4.4.1 Accelerometers

The accelerometer is the sensor equivalent to the point force, measuring the response (acceleration) of a structure at a single point.

Accelerometers are the most common devices for measuring vibrations and come in a variety of sizes, different specifications, and costs. Various experimental handbooks are available for the correct use of accelerometers in practice [66, 67].

The output of an accelerometer placed at a point (x_a, y_a) is proportional to the acceleration at that point on the plate. In contrast to the point force however, which has limited practical applications due to the requirement of a reaction mount, the accelerometer is one of the most practical and easy methods of measuring structural variables. The modal sensitivity is given by

$$S_{mn} = \Psi(x_a, y_a) \tag{4.38}$$

which, for the case of a simply-supported plate, is

$$S_{mn} = \sin k_m x_a \sin k_n y_a \tag{4.39}$$

If, instead of the acceleration, the velocity of the points on the plate are required, then the relationship between acceleration a, velocity v, and displacement d of a point is given by

$$a = \frac{d(v)}{dt} = \frac{d^2(d)}{dt^2} \tag{4.40}$$

The points on the plate are assumed to vibrate harmonically and hence are proportional to $e^{j\omega t}$ so that

$$a = j\omega v = (j\omega)^2 d = -\omega^2 d \tag{4.41}$$

4.4.2 Piezoelectric sensors

Piezoelectric materials which were introduced in section 4.3.2 can also be used as sensors due to the reciprocity effect described by Lee [25, 50]. However, distributed piezoelectric sensors tend to be made from the more flexible polyvinylidene fluoride (PVDF) film rather than the stiffer and more brittle piezoceramic PZT. Advantages of PVDF include its flexibility, light weight and, its high piezoelectric charge constant resulting in large charge ouputs for small strains.

The equations used to derive the output of a sensor can be derived in analogy with the corresponding actuator equations and by using the properties of the piezoelectric ([19, 25, 50] for further details).

For a deflection of the plate surface, the strain produced in the x direction at the surface of the sensor is

$$\varepsilon(x,t) = \frac{\partial^2 w(x,t)}{\partial x^2}\left(\frac{h}{2} + h_s\right) \tag{4.42}$$

h_s is the thickness of the sensor. This deformation of the sensor produces a charge across its electrodes which is proportional to the second derivative of displacement with respect to x and y. By integrating over the area of the sensor, the charge output of the sensor is given by

$$q_e = \left(h_s + \frac{h}{2}\right) \sum_{m=1}^{M} \sum_{n=1}^{N} W_{mn} \left[e_{31} \frac{ml_x}{nl_y} + e_{32} \frac{nl_x}{ml_y} \right] (\cos k_m x_2 - \cos k_m x_1)(\cos k_n y_2 - \cos k_n y_1) \tag{4.43}$$

where (x_1, y_1) are the coordinates of the lower left hand corner of the piezoceramic element and (x_2, y_2) are the coordinates of the upper right hand corner and e_{31} and e_{32} are piezoelectric stress constants. The sensing coefficient, S_{mn} is then given by

$$S_{mn} = \left(h_s + \frac{h}{2}\right) \left[e_{31} \frac{ml_x}{nl_y} + e_{32} \frac{nl_x}{ml_y} \right] (\cos k_m x_2 - \cos k_m x_1)(\cos k_n y_2 - \cos k_n y_1) \tag{4.44}$$

4.4.3 Distributed volume velocity sensor

Chapter 3 introduced radiation modes and showed that, at low frequencies, the first radiation mode is a much more efficient radiator of sound than higher order radiation modes. Furthermore, at these low frequencies, this radiation mode was found to have a shape corresponding to the volume velocity of the plate. It thus makes sense to try and control the volume velocity of a plate and this section deals with a sensor which can measure the volume velocity of the plate.

In simulations, when using the near-field approach, this is fairly straightforward. The volume velocity, Q, of a structure can be found by taking the sum of complex velocities at each of the elemental positions and so the charge output of a volume velocity sensor is also proportional to this value.

$$Q = \boldsymbol{q}_1^T \boldsymbol{v} \tag{4.45}$$

where $\boldsymbol{q_1}$ is a vector in which every element is equal to the elemental area.

Due to the easy shaping of PVDF film during manufacture, it has also recently become possible to produce a sensor which measures the volume displacement of the plate. The net volume displacement of the plate is given by

$$U = \int_0^{l_y} \int_0^{l_x} w(x,y) dx dy \tag{4.46}$$

The volume velocity of the plate can then be inferred by differentiating the output of the volume displacement sensor.

The PVDF film sensitivity $S(x,y)$ can be controlled by shaping the PVDF film. The shaping required to build a volume velocity sensor is discussed in [7, 68–70]. The total charge output of the film is then [7]

$$\begin{aligned} q = & \int_0^{l_y} \int_0^{l_x} S(x,y) \\ & \left[e_{31} \frac{\partial u}{\partial x} + e_{32} \frac{\partial v}{\partial y} + e_{36} \left(\frac{\partial u}{\partial y} + \frac{\partial v}{\partial x} \right) - h e_{31} \frac{\partial^2 w}{\partial x^2} - h e_{32} \frac{\partial^2 w}{\partial y^2} - 2 h e_{36} \frac{\partial^2 w}{\partial x \partial y} \right] dx dy \end{aligned} \tag{4.47}$$

This equation can be interpreted in two parts. The first part of the equation gives the charge due to the strain caused by the stretching of the midplane of the plate. For a plate fixed at its edges, there may be a contribution due to the elongation of the plate when some modes are excited. This is generally neglected as it is small in comparison to the other terms [50]. The second part of the equation ($\frac{\partial^2 w}{\partial x^2}$, $\frac{\partial^2 w}{\partial y^2}$, and $\frac{\partial^2 w}{\partial x \partial y}$) is caused by the bending of the plate and is dependent on the distance between the film and the neutral axis of the plate. As e_{36} is zero, the equation for the closed circuit charge output can be written

$$q = \int_0^{l_y} \int_0^{l_x} -h S(x,y) \left[e_{31} \frac{\partial^2 w}{\partial x^2} - e_{32} \frac{\partial^2 w}{\partial y^2} \right] dx dy \tag{4.48}$$

A beam with fixed ends is first considered, as these boundary conditions prevent whole body displacements which do not cause surface strain and so could not be measured with strain sensors such as the PVDF film even though they could be considered to be volumetric and would give rise to significant sound radiation.

In a beam, the displacement w is purely a function of x and so, equation (4.48) can be simplified to

$$q = -hl_y e_{31} \int_0^{l_x} S(x) \frac{\partial^2 w}{\partial x^2} dx \tag{4.49}$$

Integrating by parts gives

$$q = hl_y e_{31} \left[- \left[S(x) \frac{\partial w}{\partial x} \right]_0^{l_x} + \left[\frac{\partial S(x)}{\partial x} w \right]_0^{l_x} - \int_0^{l_x} \frac{\partial^2 S(x)}{\partial x^2} w dx \right] \tag{4.50}$$

Now define the sensitivity $S(x)$ to be quadratic in the x-direction so that it equals zero at the two ends of the beam

$$S(x) = \alpha(l_x x - x^2) \tag{4.51}$$

where α is a constant. This quadratic shaping was first suggested by Rex [68]. By substituting this sensitivity into equation (4.50) and taking into account that, as $S(x)$ is defined to be zero at the two ends, so the first term in equation (4.50) must also be zero, also as the ends are fixed, the displacement $w(x) = 0$ at the two ends and so the second term must also be zero. Then

$$q = -hl_y e_{31} \int_0^{l_x} \frac{\partial^2 S(x)}{\partial x^2} w(x) dx = 2hl_y e_{31} \alpha \int_0^{l_x} w(x) dx = 2he_{31} \alpha U \tag{4.52}$$

So it is seen that choosing a quadratic sensitivity gives rise to charge output which is proportional to the volume displacement, U, of the beam.

If a plate is now considered where w varies with both x and y then equation (4.48) can be split into two separate parts in these directions and the total charge output is the sum of the two charge outputs in the two directions

$$\begin{aligned} q_x &= -h \int_0^{l_y} \int_0^{l_x} -hS(x,y) e_{31} \frac{\partial^2 w(x,y)}{\partial x^2} dx dy \\ q_y &= -h \int_0^{l_y} \int_0^{l_x} -hS(x,y) e_{32} \frac{\partial^2 w(x,y)}{\partial y^2} dx dy \end{aligned} \tag{4.53}$$

Again, integrating by parts gives

$$q_x = he_{31} \int_o^{l_x} \left[- \left[S(x,y) \frac{\partial w}{\partial x} \right]_0^{l_x} + \left[\frac{\partial S(x,y)}{\partial x} w \right]_0^{l_x} - \int_0^{l_x} \frac{\partial^2 S(x,y)}{\partial x^2} w dx \right] dy \tag{4.54}$$

and defining the sensitivity $S(x,y)$ to be quadratic in the x-direction and zero at the two ends of the plate and independent of y

$$S(x,y) = \alpha(l_x x - x^2) \tag{4.55}$$

As $S(x,y)$ is zero at $x = 0$ and $x = l_x$ the first component of (4.54) is zero. If the plate is clamped then $w(l_x, y)$ and $w(0,y)$ will also be zero and so the second term of (4.54) will also be zero. Then, after substituing the sensitivity,

$$q_x = 2he_{31}\alpha \int_0^{l_y} \int_0^{l_x} w(x,y) dx dy = 2he_{31}\alpha U \tag{4.56}$$

This is seen to be proportional to the volume displacement of the whole plate. The output due to the bending in the y-direction should thus be zero. This is shown to be the case by Johnson [69].

This shows that, for the clamped plates used in the experiments, the PVDF sensor should be quadratically shaped in one direction. This has been achieved by etching in the PVDF film. This is a fairly simple process and described by Johnson [7] which also includes a discussion of the possible errors in the manufacture of the sensor. The template used for generating the volume velocity sensor is shown in figure 4.2.

For a simply-supported plate, this calculation is slightly more complicated as the gradients of the plate at its edges are not zero and so the q_y component is not zero. It has been suggested that this can be overcome by placing two quadratically shaped PVDF sensors perpendicular to each other as described by Johnson [7].

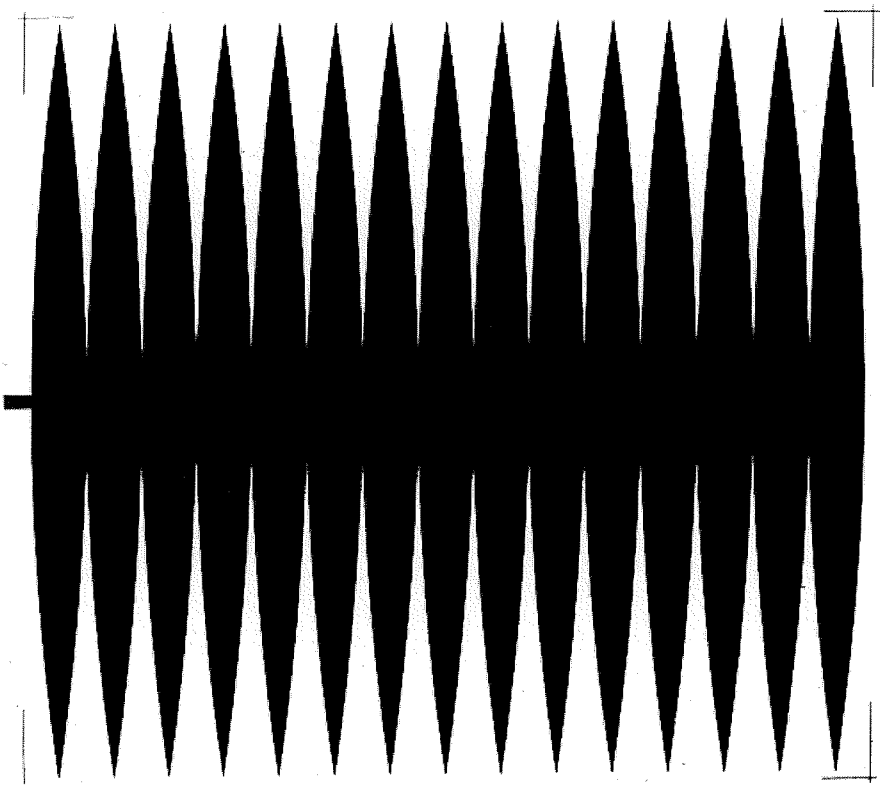

Figure 4.2: Quadratic strip shaping for a volume velocity sensor. Shaded area shows remaining electrode and white area shows where electrode has been stripped away.

4.4.4 Microphones

Conventional ACS and the first ASAC systems used microphones in the far-field to measure the radiated sound field. Although this gives the best measure of radiated power if a sufficient number of microphones are available, there a number of disadvantages:

1. A large number of microphones are needed to give an accurate representation of the radiated sound power. This is in contrast to the measurement of structural variables where it is hoped that as little as one variable, for example volume velocity, needs to be measured to give a good approximation to the radiated sound power. However, it has also been shown that a single microphone located normal to a finite planar structure in the far field will give a signal proportional to the volume velocity of the structure [71].

2. Even with a large number of sensors, spillover can take place at the intermediate positions where the sound pressure can be significantly increased.

3. Microphones in the far-field may be impractical in some applications especially where the space is needed for movement of a head or body for example.

The Rayleigh integral (section 3.2.2) for calculating the radiated pressure from a vibrating structure can be used to predict the signal at the microphone positions.

4.5 Comparison of transducers for ASAC

This section compares different combinations of actuators and sensors and their use in control systems. The performance of each actuator-sensor combination is compared through the use of feedforward simulations, which work at a single frequency and give the maximum attenuation which could be achieved using a given physical system and thus provide a reference set of results.

The block diagram for the feedforward simulations is shown in figure 4.3. In the diagram, G represents the plant and W represents the controller. It is assumed that a reference signal r can be obtained upstream of the controller. For each simulation, only the actuator and sensor is changed, the control algorithm remains the same in each case.

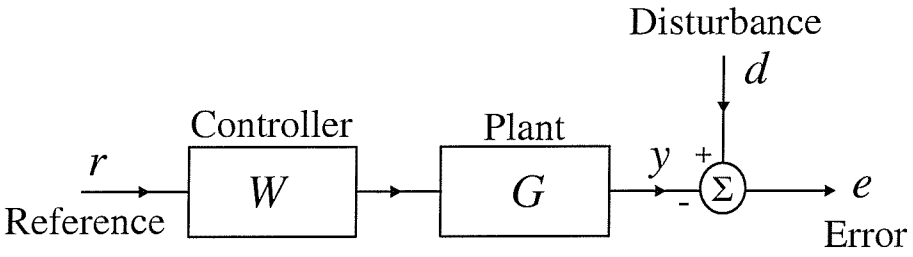

Figure 4.3: Block diagram of feedforward control

The properties of the modelled plate used are shown in table 4.3 and the frequency response function (FRF) is calculated using the modal methods of chapter 3

Property	Value
length (x-direction)	$0.278m$
length (y-direction)	$0.247m$
thickness	$1mm$
Young's modulus	$71\text{x}10^9 N.m^3$
Poisson's ratio	0.33
density	$2720kg.m^{-3}$
damping ratio	0.2%
unity non-dimensional frequency	$195Hz$
(i.e. when kl_x=1)	

Table 4.3: Material properties of plate

In each simulation, the primary excitation was assumed to be a plane wave with angles of incidence $\theta = \phi = 45^0$ which was chosen to excite all structural modes. Some angles of incidence only excite a selection of modes of the plate and so, for the purposes of analysing control methods, are not as good.

Two different feedforward control strategies are examined below. Both strategies involve minimisation at a single known frequency of excitation. In the first strategy, the total radiated power will be minimised. In practice, this method would require the use of a large number of error microphones in the far-field. This is often impractical and so error sensors bonded directly to the structure itself are used in the second control strategy which minimises the output of such an error sensor either in the form of an accelerometer, a piezoceramic patch or, a distributed volume velocity sensor. The aim is to get as close to the ideal control, given by the minimum

radiated power, as possible.

For the first control strategy of controlling radiated sound power, the complex velocity distribution of the plate due to tonal excitation can be expressed as a combination of velocities due to primary (disturbance) and secondary (control) forces. Furthermore, the velocity distribution due to secondary actuators can be expressed as the velocity vector due to a unit input voltage, $\boldsymbol{g}$, multiplied by a complex control signal u, such that

$$\boldsymbol{v} = \boldsymbol{v}_p + \boldsymbol{g}u \tag{4.57}$$

where $\boldsymbol{v}_p$ is the velocity distribution due to the primary incident wave.

By substituting this into the equation for sound radiation, (3.30), it can be rearranged into the well-known Hermitian quadratic form,

$$W = u^* A u + u^* b + b^* u + c \tag{4.58}$$

where

$$\begin{aligned} A &= \boldsymbol{g}^h \boldsymbol{R} \boldsymbol{g} \\ b &= \boldsymbol{g}^H \boldsymbol{R} \boldsymbol{v}_p \\ c &= \boldsymbol{v}_p^T \boldsymbol{R} \boldsymbol{v}_p \end{aligned} \tag{4.59}$$

which is minimised by using the complex control voltage, u_m, given by

$$u_m = -A^{-1} b \tag{4.60}$$

The second control strategy focuses on the cancellation of the error sensor output and can be calculated in a similar way to that above. The aim is to cancel the total charge output of the sensors attached to the panel.

The charge output can be written as a combination of contributions from primary and secondary sources

$$q_{tot} = q_p + q_h u \tag{4.61}$$

where q_h is the charge output due to a unit input voltage to the actuator.

To set q_{tot} to zero, the control voltage is

$$u_e = -\frac{q_p}{q_h} \tag{4.62}$$

Using the different transducers and control strategies described above, simulations were performed to find the combination of actuators and sensors which give the best acoustic performance. As the excitation of the plate is assumed to be tonal, with a known frequency, the control problem reduces to adjustment of the amplitude and phase of the complex control input, u, at that frequency. In each case which follows, corresponding to different combinations of actuators and sensors, the following curves are shown:

1. The power transmission ratio before control is defined to be

$$T = \frac{W_r}{W_i} \tag{4.63}$$

   where W_r is the sound power radiated by the panel and the incident acoustic power is defined by Roussos [60] to be

$$W_i = \frac{|P_i^2| l_x l_y \cos(\theta)}{2\rho_0 c_0} \tag{4.64}$$

2. The power transmission ratio after the input to the actuator has been adjusted at each frequency to minimise the radiated sound power

3. The power transmission ratio after the input to the actuator has been adjusted at each frequency to cancel the sensor output whether that is an accelerometer, piezoceramic sensor or, volume velocity sensor.

For the first simulation, consider a point force actuator positioned at the centre of the plate. Figure 4.4 shows the calculated results when a single centrally-placed point force is used as an actuator and a single, centrally-placed, accelerometer, and a volume velocity sensor are used as error sensors.

The ideal control curve, obtained by minimising sound radiation, is lower than the curve which shows the power transmission ratio before control at all frequencies as would be expected. This is the reference curve which shows the best possible attenuation which can be achieved using the given transducer configuration. The total attenuation over the $1kHz$ frequency range is $7.9dB$ but at any single frequency can be very large. The value for overall attenuation is weighted towards high frequencies where the overall sound power radiation is increased. However, this is the frequency region with the lowest attenuation so the overall attenuation does not give a good indication of the control performance at low frequencies.

The dash-dot curve in figure 4.4, which shows the power transmission ratio after the output of the accelerometer has been cancelled, shows poor control at many low frequencies and the overall level of sound radiation is significantly increased ($5.5dB$). This effect can be understood by considering the change in the dynamics of the plate when using this actuator sensor configuration. As an example, consider the $(1,1)$ mode which is shown after control in figure 4.5. It might be expected that, since the actuator excites the centre of the plate, the accelerometer should also couple into the $(1,1)$ mode and drive the amplitude of the mode to zero. It is evident from the figure however that the displacement or acceleration at the position of the accelerometer is driven to zero, but the general velocity is not being controlled. The effect of the sensor is to pin that part of the plate and the dynamics of the plate are thus changed and the structure displays a new frequency response function with a new set of resonances. The overall effect is similar to imposing an additional boundary condition or constraint on the equation of motion. Controlling the output of a single accelerometer turns out to be closer to AVC than ASAC as shown in chapter 6.

Using the point force actuator in conjunction with a volume velocity sensor also provides good

control up to about $700Hz$. The total attenuation over the $1kHz$ bandwidth however is reduced compared to the ideal control case as there is some loss of attenuation at higher frequencies. As the frequency is increased, the radiation efficiency of the first mode relative to the radiation efficiencies of other radiation modes is decreased and so control of volume velocity only works well at low frequencies. This is another form of spillover which is discussed in chapter 6.

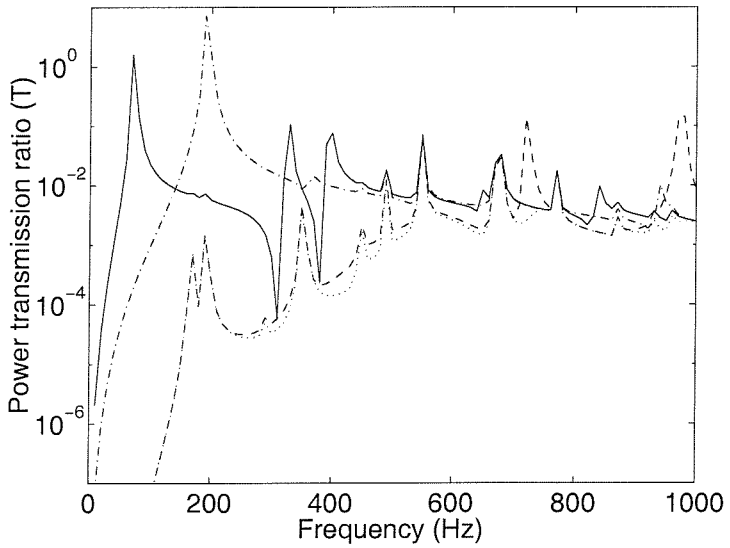

Figure 4.4: Power transmission ratio before and after control using feedforward control with a centrally-placed point force actuator and a variety of sensors. a) Before control (solid line) b) After control of radiated sound power (dotted line) c) After control of volume velocity (dashed line) d) After control of the output of a centrally-placed accelerometer (dash-dot line)

In the second set of simulations, a $25mm$ by $25mm$ piezoceramic patch at the centre of the panel was used with the different types of sensors including a $25mm$ by $25mm$ collocated piezoceramic sensor. The control results are shown in figure 4.6.

It is again evident that the control of sound power and the control of volume velocity are good control strategies. However, control of the collocated piezoelectric sensor does not result in attenuation. As above, this can be explained by examining the vibration distribution of the plate before and after control and by analysing the action of the piezoelectric sensors in more detail. Again, consider control of the $(1,1)$ mode as an example. It might be expected that, since the actuator excites the plate in the centre, so the sensor should perfectly couple into this mode and drive the displacement of the centre of the plate to zero, thus controlling the mode. However, the behaviour of the sensor prevents this from happening. The sensor cannot

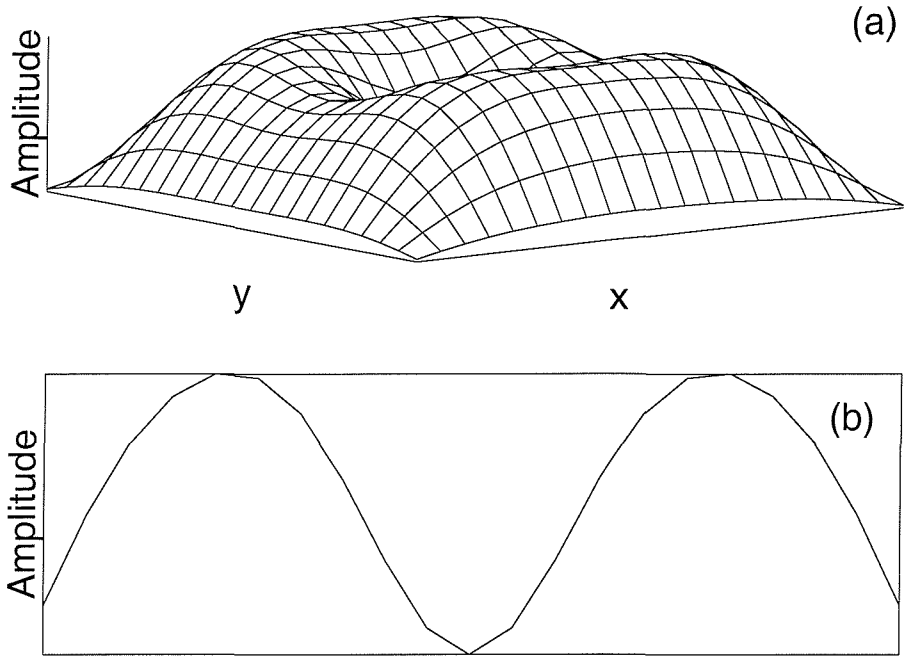

Figure 4.5: Vibration distribution of plate after control of the $(1,1)$ mode using a centrally-placed point force and collocated accelerometer (and a symmetric disturbance) a) Whole plate b) Section through mid-plane of plate

measure the absolute displacement from the equilibrium plane of the plate. Instead, the charge output of the sensor is proportional to the second derivative of the out of plane displacement with respect to x and y i.e. the bending of the plate. If the sensor is assumed to be perfectly bonded to the plate then its charge output will be zero when the integral of the gradient of the plate around the edges of the piezoceramic patch is zero. The vibration distribution of the plate after control of the $(1,1)$ mode is shown in figure 4.7 and it is clear that the effect of cancelling the output of the sensor is to flatten the top of the plate resulting in a vibration distribution in which the gradient at the edges of the piezoelectric patch is zero as required (for this figure, the piezoelectric actuator and sensor were chosen to be 82mm by 82mm to demonstrate this flattening effect more clearly). The amplitude of vibration is also reduced slightly after control. The effect of controlling the collocated sensors is thus again to change the dynamics of the plate and to change the resonant frequencies of the plate. The effect of minimising sound power and volume velocity using the piezoceramic patch actuator are seen to be remarkably similar to that achieved with the point force actuator and this is expected as the piezoceramic patch actuator also acts on only a local part of the plate.

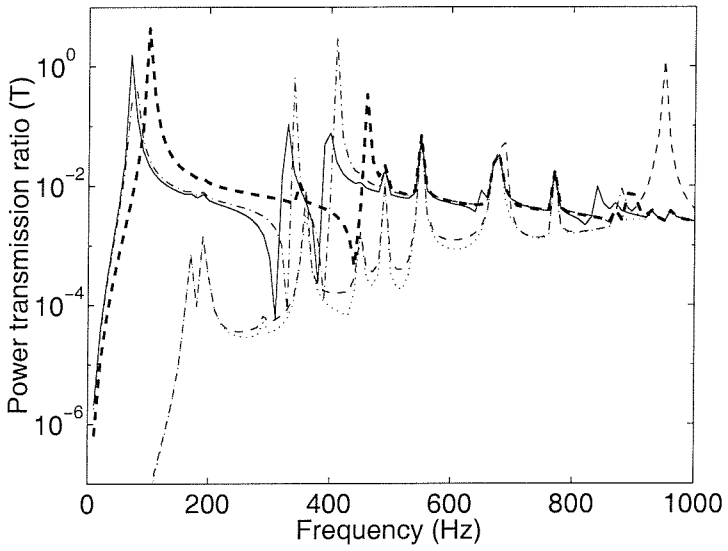

Figure 4.6: Power transmission ratio before and after control using feedforward control with a centrally-placed piezoceramic patch actuator and a variety of sensors. a) Before control (solid line) b) After control of radiated sound power (dotted line) c) After control of volume velocity (thin dashed line) d) After control of the output of a centrally-placed piezoceramic patch sensor (dash-dot line) e) After control of the output of a centrally-placed accelerometer (thick dashed line)

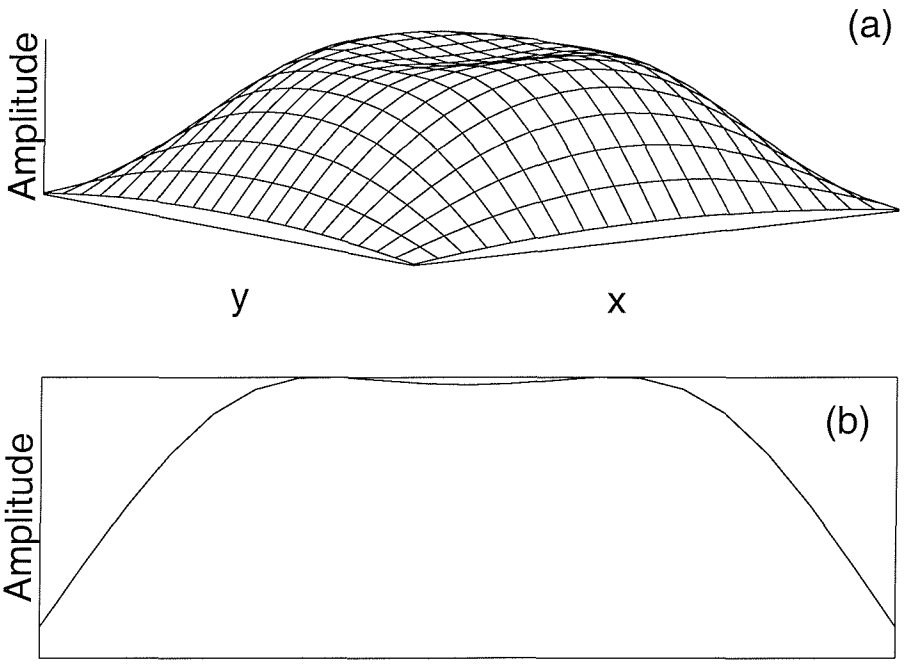

Figure 4.7: Vibration distribution of plate after control of the (1,1) mode using a centrally-placed piezoceramic actuator and collocated sensor. Note that the actuators used here are slightly larger than in previous simulations and the disturbance is symmetric. a) Whole plate b) Section through mid-plane of plate

The final control graph 4.8 shows the results where a uniform force actuator and various sensors are used. The dash-dot line, representing control of a piezoelectric patch sensor using a uniform force actuator, can be thought of as the reciprocal case to the single piezoceramic patch actuator and volume velocity sensor as shown in figure 4.6 and, the results are found to be quite similar.

The combination of uniform force actuator and volume velocity sensor also give rise to control performance which is close to that obtained by minimising radiated sound power. This gives the best performance when constrained to the use of structural sensors.

From the simulations described above, a few general conclusions on the choice of transducers can be drawn

1. Using a uniform force actuator with a volume velocity sensor is almost as good a control strategy as minimising the total radiated power using far-field error sensors for frequencies up to around $800Hz$.

2. Using a uniform force actuator and piezoelectric sensors, or, a volume velocity sensor and piezoceramic actuators provide similar results to each other and which are quite close to (1) above.

3. Using discrete actuators and sensors together does not provide good control of radiated sound power (but may result in good vibration control).

The conclusions above would suggest that the desired configuration of transducers is a uniform force actuator and a volume velocity sensor. At the time of writing, no uniform force actuator was available and so, the second best configuration, using piezoceramic patch actuators and a volume velocity sensor was chosen for a first experimental arrangement.

Although the results of different control simulations have been given here, a more detailed discussion on the actual control mechanisms, spillover, and the effect on plate vibrations is given in chapter 6.

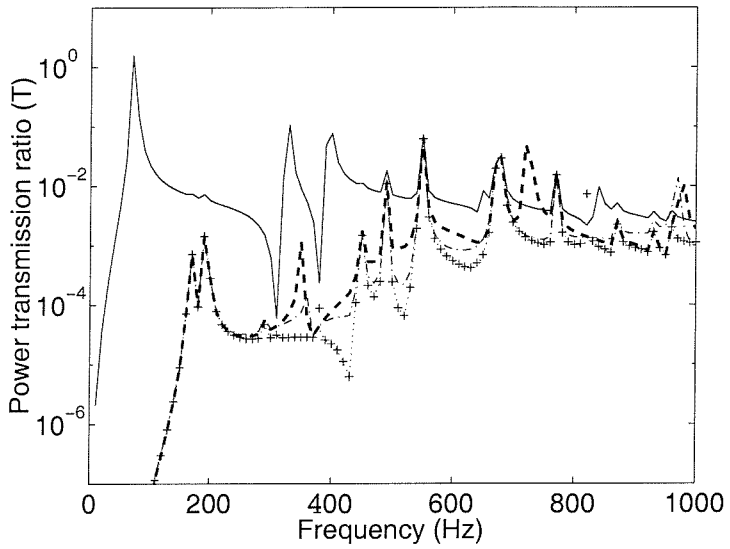

Figure 4.8: Power transmission ratio before and after control using uniform force actuator and a variety of sensors. a) Before control (solid line) b) After control of radiated sound power (dotted line) c) After control of volume velocity (crosses) almost indistinguishable from (b) up to $1kHz$ d) After control of the output of a centrally-placed accelerometer (dash-dot line) e) After control of a centrally-placed piezoceramic patch sensor (thick dashed line)

4.6 Placement of transducers

The previous section compared the performance of different actuator-sensor combinations but, in general, the discrete transducers were all placed in the middle of the plate. The actual position of a given transducer on the plate also has significant effects on the control system and this is discussed in this section.

That the position of the transducers is important can first be explained using an intuitive argument: An actuator placed in the centre of the plate for instance cannot excite any even modes. Similarly, a sensor placed one third of the way along the plate for example, would not be able to measure any $(3, *)$ modes which are important to sound radiation (* refers to any integer).

Although there are many different techniques for calculating the best position of transducers, such as Genetic Algorithms (GA's) or exhaustive searches [51–53], these normally rely on intensive computing techniques and can be time-consuming. In this thesis, more practical arguments

will be used to arrive at transducer positions which may not necessarily be optimal, but will have a good enough performance for the purposes of this thesis. This is offset with the progression from feedforward to feedback control and then to implementation which all result in inevitable performance losses. These performance losses would eventually outweigh the small performance increases which could be obtained by making improvements to the transducer positions.

The argument presented below is based on the fact that the performance of a feedback controller is dependent on the phase of the plant frequency response function. The aim of the controller in feedback control will later be shown to be to come as close as possible to inverting the plant response and this is only successful when no phase accumulation is present in the frequency response function (FRF) of the plant. This section shows how the phase accumulation can be kept to a minimum by repositioning of the transducers on the plate. This follows the analysis given by Johnson *et al.* [1] and Sors and Elliott [3].

The frequency response of the entire plant, including sensors, has been shown to be given by

$$G(\omega) = \sum_{m=1}^{M} \sum_{n=1}^{N} A_{mn}(\omega) F_{mn} S_{mn}$$

Each mode can now be considered to be associated with a pole which acts with a given gain or residue [72]. The residue is defined by

$$R_{mn} = F_{mn} S_{mn} \tag{4.65}$$

and this is determined by the position and type of the actuator and sensor used.

In between the poles, zeros are created and their positions depend on the values of the residues; if two consecutive residues have the same sign, then a zero will be created between them. The phase response of the zero then compensates for the phase response of the poles and no phase accumulation takes place. If there is a change in sign between two consecutive residues, the zero will be created somewhere else in the s-plane and phase accumulation will take place. The aim of changing the configuration of the transducers is thus to position them such that the residues all have the same sign.

A detailed description of the residue technique is described in [1, 27] and in this thesis, it will be demonstrated by means of a simple example: Consider the $(1,1)$ mode and $(3,1)$ modes of a plate and the sensitivity of a volume velocity sensor to each mode. The sensitivity to the mn'th structural mode is

$$S_{mn} = B \int_S \Psi_{mn}(x,y) dS \tag{4.66}$$

where B is a sensitivity constant, S implies integration over the area of the plate, and $\Psi_{mn}(x,y)$ is the velocity profile of the structural mode, which, for a simply-supported plate, is given by

$$\Psi_{mn}(x,y) = W_{mn} \sin(k_m x) \sin(k_n y)$$

It turns out that the volume velocity sensor is only sensitive to odd-odd structural modes and that in these cases $S_{mn} \propto 1/mn$. The table of resulting sensitivity coefficients is shown in table 4.4 and it is clear that all coefficients are either positive or zero. The coefficients are normalised such that the sensitivity to the $(1,1)$ mode is 1.

n/m	1	2	3	4	5
1	1	0	1/3	0	1/5
2	0	0	0	0	0
3	1/3	0	1/9	0	1/15
4	0	0	0	0	0
5	1/5	0	1/15	0	1/25

Table 4.4: Normalised sensitivity coefficients for a volume velocity sensor on a simply-supported plate.

Now, examine the forcing coefficients for two different configuration of piezoceramic actuators, F_{mn} as calculated from equation (4.14). The coefficients for a centrally-placed actuator are shown in table 4.5, normalised such that the forcing coefficient for the first mode is 1.

The residues are obtained by multiplying the forcing and sensitivity coefficients for each mode, as shown by equation (4.65), and the results are also shown in table 4.6. It is clear that the

n/m	1	2	3	4	5
1	1	0	-4.06	0	8.21
2	0	0	0	0	0
3	-4.76	0	7.02	0	-9.89
4	0	0	0	0	0
5	9.22	0	-10.29	0	11.33

Table 4.5: Normalised forcing coefficients for a centrally-placed piezoelectric actuator on a simply-supported plate.

signs of the residues change between consecutive modes and so phase loss will occur. The origin of the signs in table 4.5 can be seen more clearly by examining figure 4.9. For the $(1,1)$ mode, the central actuator is in a positive cell and for the $(3,1)$ mode, the actuator is in a negative cell thus changing the sign of the forcing coefficient in between modes.

n/m	1	2	3	4	5
1	1	0	-1.35	0	1.64
2	0	0	0	0	0
3	-1.59	0	0.78	0	-0.66
4	0	0	0	0	0
5	1.84	0	-0.69	0	0.45

Table 4.6: Normalised residues for a centrally-placed piezoelectric actuator on a simply-supported plate with a volume velocity sensor.

If five actuators, all driven in phase, are now used as shown in figure 4.10(b), then actuators are placed closer to the corners. Figure 4.9 then shows that the corner actuators are in positive cells for both the $(1,1)$ and $(3,1)$ modes and so there is no change of sign between the two modes. The tables of forcing coefficients and resulting residues for this particular actuator configuration are shown in tables 4.7 and 4.8 respectively.

It is evident that the mode at which the first negative sign appears in the forcing coefficients depends on the positions of the actuators relative to nodal lines. The actuators should be placed as close to the corners as possible. There is then a trade-off between the minimum phase properties of the frequency response function and the amount of force which the actuators can provide to the plate, which decreases as the actuators are placed closer to the corners. Bearing

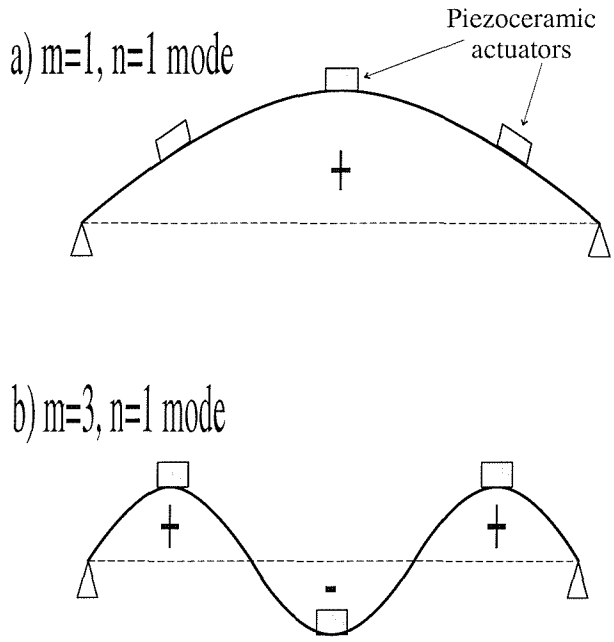

Figure 4.9: Mid-plane view of (1,1) and (3,1) modes of a simply-supported plate

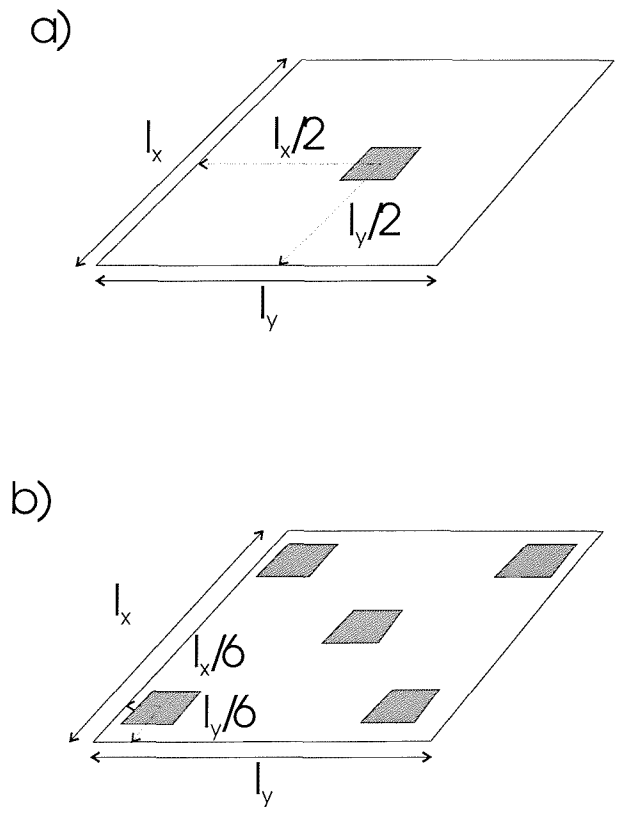

Figure 4.10: Different configurations of transducers on the plate a) Single, centrally-placed, transducer b) Five transducers; one centrally-placed, one placed a sixth of the way into each corner of the plate

n/m	1	2	3	4	5
1	1	0	2.04	0	8.21
2	0	0	0	0	0
3	2.37	0	17.55	0	4.95
4	0	0	0	0	0
5	9.22	0	5.15	0	11.33

Table 4.7: Normalised forcing coefficients for five actuators on a simply-supported plate. (First negative forcing coefficient occurs at $1600Hz$ for $(7,1)$ mode)

n/m	1	2	3	4	5
1	1	0	0.68	0	1.64
2	0	0	0	0	0
3	0.79	0	1.95	0	0.33
4	0	0	0	0	0
5	1.84	0	0.34	0	0.45

Table 4.8: Normalised residues for five actuators on a simply-supported plate with a volume velocity sensor.

in mind the limited frequency range over which control of volume velocity works, placing the actuators one sixth of the way into each corner was chosen as a compromise between these two factors. This led to two experimental configurations shown in figure 4.10 which are examined further in the next chapter. In the configuration using the actuators in the corners, the central actuator is kept to increase the control force, especially on the odd-odd modes which give rise to the volumetric plate vibrations and cause the most sound power radiation.

The simulated frequency response functions of the plant using a distributed volume velocity sensor and the two configurations of piezoceramic actuators (figure 4.10) are shown in figure 4.11. The phase lag for the five actuator configuration is much less than for the single actuator configuration as expected. An increase in amplitude for the five actuator case relative to the single actuator case can also be seen and is due to the fact that the four corner actuators are driven in addition to the central one. Driving the four corner actuators alone would result in a lower amplitude than for the single actuator.

Mathematically, the phase loss due to the signs of the residues can be treated more rigorously as described in [72]. As an example, consider the addition of poles p_1 and p_2

$$G(s) = \frac{R_1}{(p_1 - s)} + \frac{R_2}{(p_2 - s)} = \frac{(R_1 + R_2)\left[\frac{R_1 p_2 + R_2 p_1}{R_1 + R_2} - s\right]}{(p_1 - s)(p_2 - s)} \tag{4.67}$$

This equation shows that although the poles stay in the same place, a zero will be created whose position is dependent on the residues R_1 and R_2 i.e. when

$$s = \frac{R_1 p_2 + R_2 p_1}{R_1 + R_2} \tag{4.68}$$

The zero is created at a point where the contribution from the two adjacent poles cancel each other. When the residues have the same sign, the position of the zero in between the poles compensates for the added phase due to each pole and so the system does not accumulate phase or create non-minimum phase zeros [72].

Taking the concept of reducing the phase in the FRF of the plant a step further results in the use of matched and collocated transducers. These give a minimum phase plant FRF. A

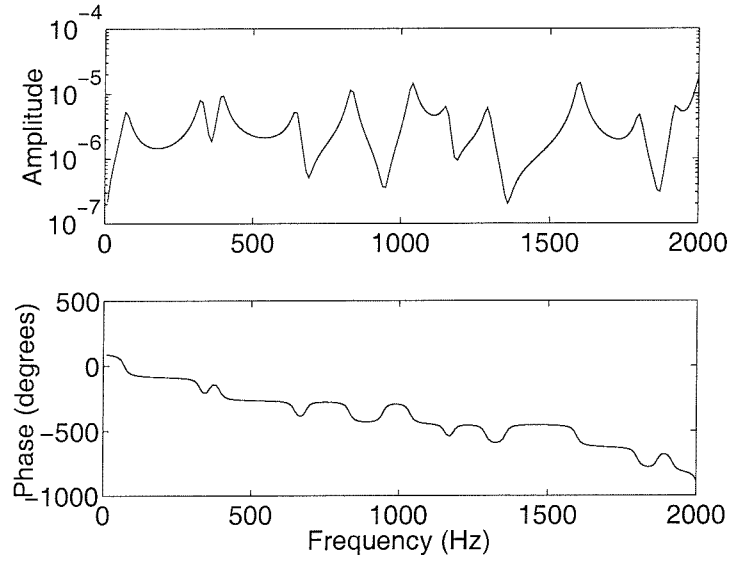

(a)

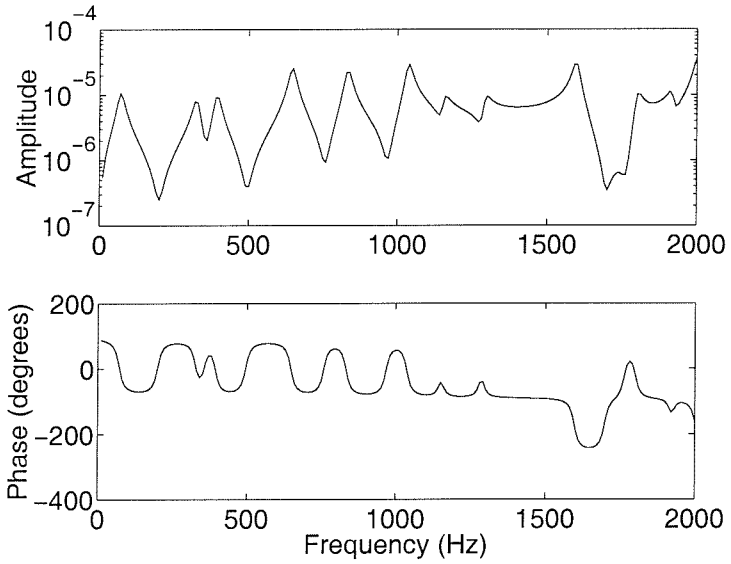

(b)

Figure 4.11: Calculated frequency response functions a) Using a centrally-placed piezoceramic patch actuator and a distributed volume velocity sensor b) Using piezoceramic actuators placed as shown in figure 4.10(b) and a distributed volume velocity sensor

minimum phase FRF is one which has all its zeros on the left hand side of the s-plane. A matched sensor-actuator pair is one in which the spatial distribution of the force input to the structure is the same as that of the spatial sensitivity of the response from the structure at the sensor. In some cases, a transducer can be used as both an actuator and a sensor as described in [73, 74] for example, and these would qualify as a matched pair. A perfect uniform force actuator and volume velocity sensor would also create a matched pair if the problems described in [26] could be avoided.

The following discussion of matched transducers follows Johnson and Elliott [41] and the concept of collocation is described in more detail by [74]. If the actuator is assumed to have force distribution $\eta(x, y)$ with an input voltage $u(\omega)$ then the resulting amplitude of the mn'th mode is

$$W_{mn}(\omega) = u(\omega) A_{mn}(\omega) \int\int \Psi_{mn}(x, y)\eta(x, y)dxdy \tag{4.69}$$

If a sensor is now implemented having exactly the same sensitivity distribution $\eta(x, y)$ then the output of the sensor will be

$$y(\omega) = \int\int w(x, y, \omega)\eta(x, y)dxdy \tag{4.70}$$

and using equations (4.69) this can be written

$$y(\omega) = u(\omega) \sum_{m=1}^{\infty} \sum_{m=1}^{\infty} A_{mn}(\omega) \left[\int\int \Psi_{mn}(x, y)\eta(x, y)dxdy \right]^2 \tag{4.71}$$

The term in square brackets must be positive and real for all structural modes and can be represented by C_{mn} so the FRF of the transducer pair can be written

$$G(\omega) = \frac{y(\omega)}{u(\omega)} = \sum_{m=1}^{\infty} \sum_{n=1}^{\infty} A_{mn}(\omega) C_{mn} \tag{4.72}$$

The phase of each modal contribution to the FRF will thus be equal at their respective natural frequencies. This has been expressed in the Laplace domain by [72] and gives rise to a minimum phase pole-zero structure. As no phase accumulation occurs with frequency, this minimum phase FRF has a stable and causal inverse. In principle it would then be possible to create a feedback system which performs as well as its feedforward counterpart. An example of a minimum phase FRF, modelled between a uniform force actuator and a volume velocity sensor is shown in figure 4.12.

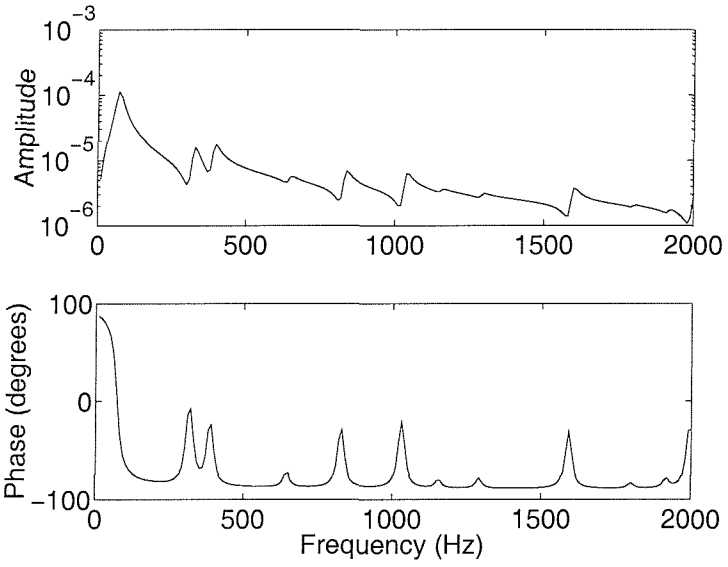

Figure 4.12: Minimum phase FRF modelled between uniform force actuator and a distributed volume velocity sensor

The positioning of actuators and sensors is also linked to the concepts of controllability and observability which are used widely in state-space control. A point force placed in the centre of a simply-supported plate for example, would not be able to control any even modes of the plate. A similar analysis applies to sensors. Controllability and observability are treated more rigorously by Franklin and Powell [75] for example.

These give rise to some conclusions on the choice of transducers further to those listed at the end of section 4.5 above.

1. By changing the position of actuators on the plate, the phase loss in the plant frequency response function can be kept to a minimum and hence increased control performance can be obtained. In particular, the five actuator configuration shown in figure 4.10(b)

performs better than the single actuator configuration, figure 4.10(a).

2. Collocated transducers give rise to a minimum phase plant FRF which is an important consideration for feedback control. Simulations were also made using other positions for actuators and sensors but the results were not found to be significantly better than those presented here.

4.7 Conclusions

The plate models derived previously have been used in this chapter and the various different integrated actuators and sensors which could be used for ASAC have been analysed in terms of their forcing functions and sensing functions. Special focus has been on piezoelectric materials which have advantages for ASAC such as their cost and physical properties.

An analysis of the plant frequency reponse functions shows that, as well as choosing the types of actuators, their positions must be chosen carefully to make the frequency response as minimum phase as possible. This can also be achieved by using matched and collocated transducers.

It is found that the ideal combination for ASAC would be to use a uniform force actuator and a volume velocity sensor. However, the uniform force actuator still has some problems in its development and so instead, five piezoceramic actuators are used in an experimental arrangement which will be tested further in the next chapter.

Chapter 5

Feedback control for active structural acoustic control

5.1 Introduction to feedback control

Chapter 2 included a brief comparison of feedforward and feedback control and their respective advantages and disadvantages. Simulations in the previous chapters used feedforward control, which gives the best performance which can be obtained from a given physical system and thus give a set of benchmark results against which other control strategies can be gauged. This chapter will now deal with feedback control.

The use of feedback control introduces some important issues such as controller stability and robustness. A fundamental requirement from a control system is that it should maintain closed-loop stability during operation i.e. the closed-loop system should remain stable for all perturbed plants around a nominal model. The performance of a feedback control system is always less than its feedforward counterpart, assuming that a suitable time-advanced external reference signal is available, because of these factors. The aim then, is to design a feedback controller which is robustly stable and has a performance which is as close to its feedforward counterpart as possible.

5.1.1 Feedback control issues: Performance, robustness, and stability

There are many references which describe feedback control in detail for example [11, 17, 19, 30]. This section outlines the compromise between performance and stability which arises due to the feedback loop. Stability normally implies that for any Bounded Input to the system there should be a Bounded Output (BIBO stability). This section will consider Single Input-Single Output (SISO) control but the same general rules apply for Multiple Input-Multiple Output (MIMO) control.

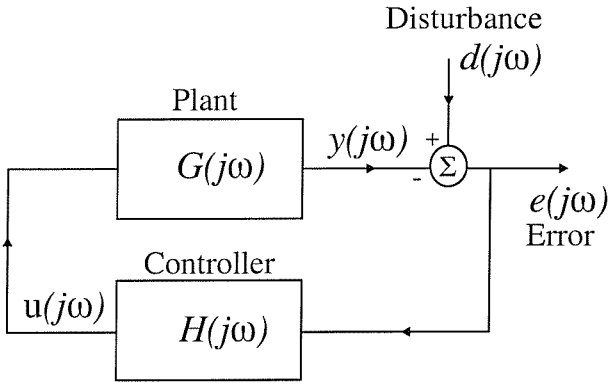

Figure 5.1: Block diagram of a feedback control system

The block diagram of a feedback system is shown in figure 5.1 and control theory provides a variety of methods of designing the controller, $H(j\omega)$, which generates control signals $u(j\omega)$ from the error signals $e(j\omega)$. The error signal $e(j\omega)$ is a combination of contributions due to the primary disturbance $d(j\omega)$ and due to the output of the control system and plant $y(j\omega)$. The feedback is assumed to be negative so that the controller and plant output is subtracted from the primary disturbance. This is consistent with most of the control literature and means that if $y(j\omega)$ is similar to $d(j\omega)$ then the error ouput will be small and large attenuations are achieved. The error is given by

$$e(j\omega) = d(j\omega) - y(j\omega) = d(j\omega) - G(j\omega)H(j\omega)e(j\omega) \tag{5.1}$$

which can be rearranged to give the frequency response function of the overall feedback system measured between the disturbance and the error

$$S(j\omega) = \frac{e(j\omega)}{d(j\omega)} = \frac{1}{1 + G(j\omega)H(j\omega)} \tag{5.2}$$

This is called the sensitivity function and is a measure of the overall attenuation of the disturbance in the system. It is desirable to have this value as low as possible which is achieved by making the open loop gain $G(j\omega)H(j\omega)$ as large as possible.

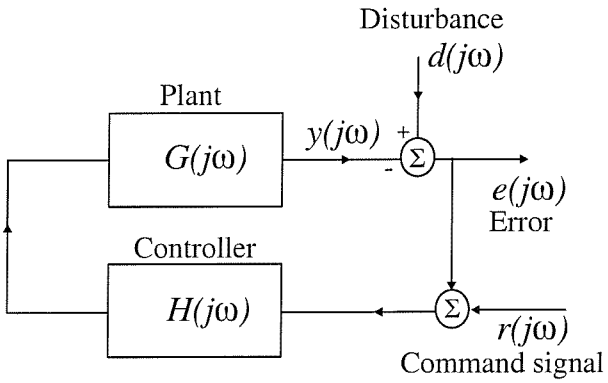

Figure 5.2: Block diagram of a feedback control system including command signal

A command signal $r(j\omega)$ can also be included as an input to the feedback control system as shown in figure 5.2. In this case, the error signal is required to track the command signal. However, for sound and vibration or ASAC problems, it is normally required to eliminate the disturbance as far as possible in which case the command signal is zero. The frequency response function between the commmand signal and the error signal is given by

$$T(j\omega) = \frac{e(j\omega)}{r(j\omega)} = \frac{G(j\omega)H(j\omega)}{1 + G(j\omega)H(j\omega)} \tag{5.3}$$

this is called the complementary sensitivity function and it is related to the sensitivity function equation (5.2), which describes the performance of the system, by

$$S(j\omega) + T(j\omega) = 1 \tag{5.4}$$

It is desirable for this complementary sensitivity function to be as close to unity as possible which again requires making the open loop gain as large as possible. However, the complementary sensitivity function also expresses the effect of measurement noise, also called sensor or

observation noise, on the output which should be as small as possible. From this point of view, the open loop gain should be as small as possible. There is thus a compromise between rejection of disturbances and good command tracking, which require large loop gains, and rejection of sensor noise, which requires low loop gains.

Returning to equation (5.2) it is evident that if, at some frequency, $|G(j\omega)H(j\omega)| = 1$ and the open loop response has exactly 180^0 degrees of phase shift, then the denominator would be zero and the output would become unbounded. This is when instability occurs. To describe this more formally, the closed loop system is stable if none of the poles of $\frac{1}{1+G(s)H(s)}$ (equivalent to the roots of the characteristic equation $1 + G(s)H(s) = 0$) are in the right hand half (within the Nyquist contour) of the s plane as shown in figure 5.3.

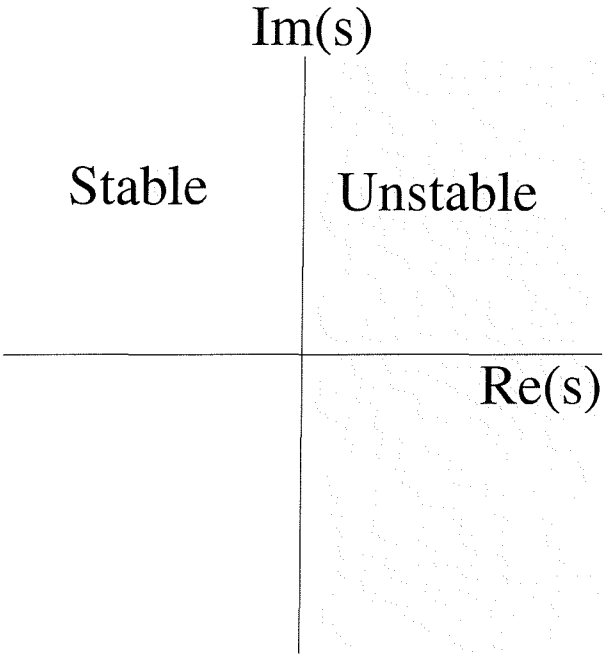

Figure 5.3: Stable and unstable regions of the s plane

This stability criterion can also be represented graphically by using the Nyquist plot of the open loop frequency reponse $G(j\omega)H(j\omega)$. This Nyquist plot must not enclose the point $(-1, 0)$ from $\omega = -\infty$ *to* ∞ if the controller is to be stable, as dealt with in more detail by [30, 76] for example. Figure 5.4 shows the Nyquist plot of a stable and an unstable system when the feedback loop is closed. The gain and phase margins both give an indication of how robust the stability of the controller is to changes. This is important as frequency response functions are normally subject to some uncertainty in the measurement process and can often change with time.

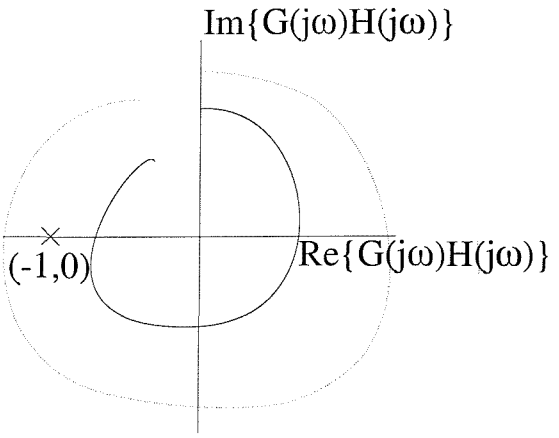

Figure 5.4: Nyquist plot in the $j\omega$ plane showing point of instability. Solid line shows stable FRF, dashed line shows unstable FRF.

The gain margin is defined by

$$Gain\ margin(dB) = -20\log_{10}|GH| \tag{5.5}$$

where $|GH|$ is the open loop response when the phase is 180^0 i.e. when the Nyquist plot crosses the negative x-axis. As an example, when $|GH| = 0.5$, the gain margin is $6dB$ which allows relatively large changes to the open loop response before instability and so could be considered to be a very robust system. A similar definition applies for the phase margin, which is the amount of additional open loop phase lag which would be required to destabilise the system.

As an example of how plant FRF's can change, figure 5.5 shows the FRF of the experimental plant described in section 5.3.1, measured every hour over two days. Figure 5.6 then shows the variation in the second resonant frequency over this period which is seen to vary by approximately 10% over a 5 degree variation in temperature. This variation in natural frequency is greater than one would expect in a free plate and is probably due to the variations in temperature causing a change in the in-plane tension within the plate.

Robust stability is a more formal requirement that the closed loop feedback system must remain stable for a given range of changes in the plant frequency response function. For the case of the plate considered in this thesis for instance, this could be due to temperature changes or other changes in environmental variables. Other sources of differences between the plant model

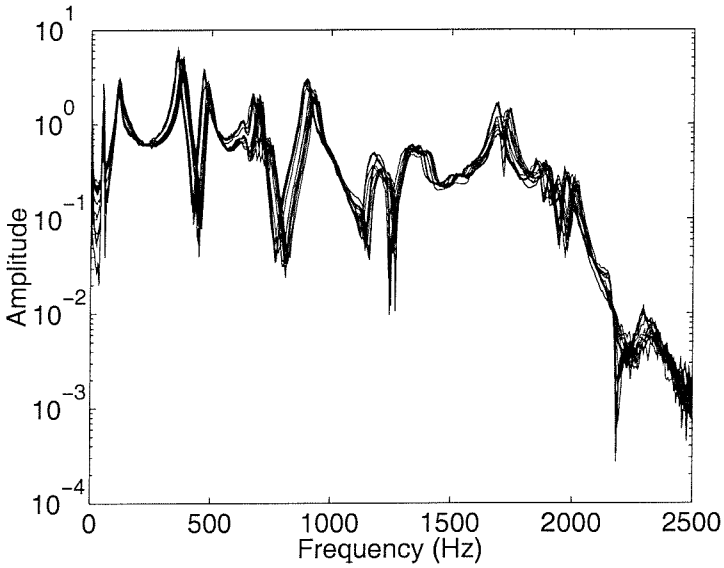

Figure 5.5: Effects of temperature on FRF's

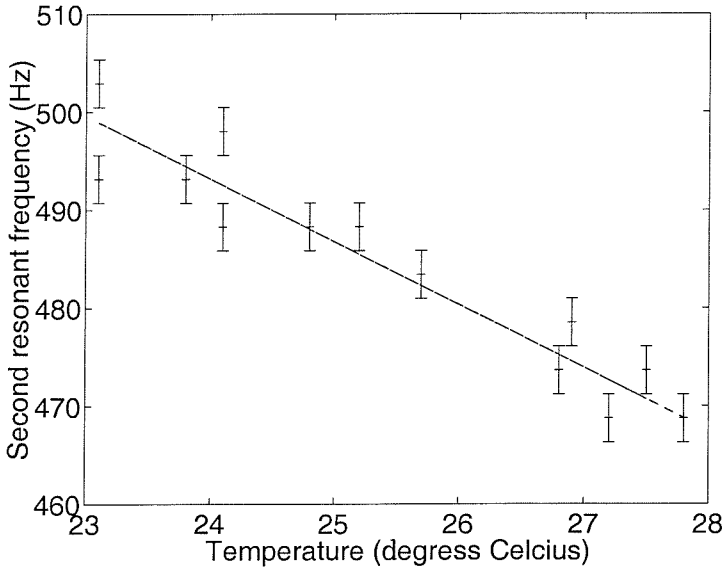

Figure 5.6: Effects of temperature on second resonant frequency. Best fit line shown.

and the true plant could be due to measurement errors or high frequency dynamics which are missed out in low-order models. These plant uncertainties can be modelled in many different ways such as bounds on a parameter of a linear model, bounds on nonlinearities in the models or, bounds in the frequency domain models [77]. These are defined as parametric uncertainties as a given parameter in the plant model can take a given range of values. Another type of uncertainty is unstructured uncertainty, which defines a general set of plants around a nominal value. Again, different types of unstructured uncertainty exist but multiplicative uncertainty will be considered here in which the plant is considered by means of variations from a nominal plant response described by

$$G(j\omega) = G_0(j\omega)[1 + \Delta_G(j\omega)] \tag{5.6}$$

where $G_0(j\omega)$ is the frequency response of the nominal plant and $\Delta_G(j\omega)$ is the fractional uncertainty in the plant response. Multiplicative uncertainty normally increases with frequency and exceeds or becomes equal to unity at high frequencies. This is because $G_0(j\omega)$ tends to become small at high frequencies so any change in absolute value gives rise to large values of $\Delta_G(j\omega)$. A typical variation of multiplicative uncertainty over frequency is shown in figure 5.7 and the block diagram of a feedback controller with multiplicative uncertainty is shown in 5.8.

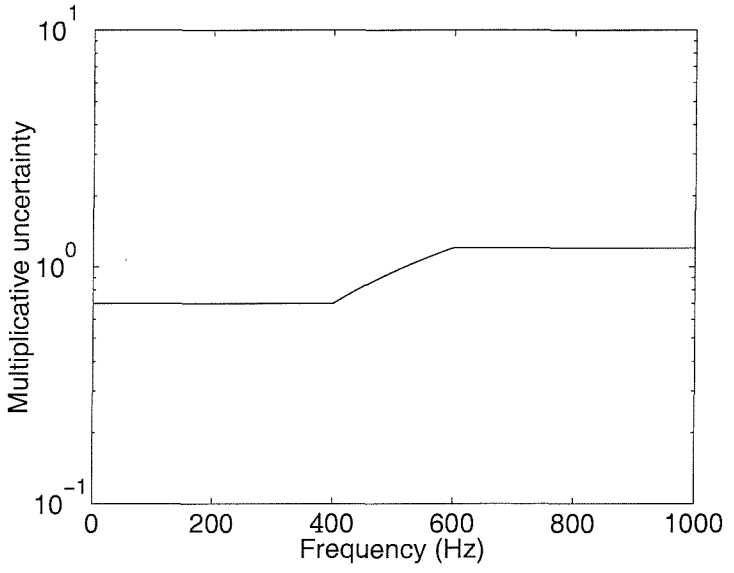

Figure 5.7: Typical form of multiplicative uncertainty bound

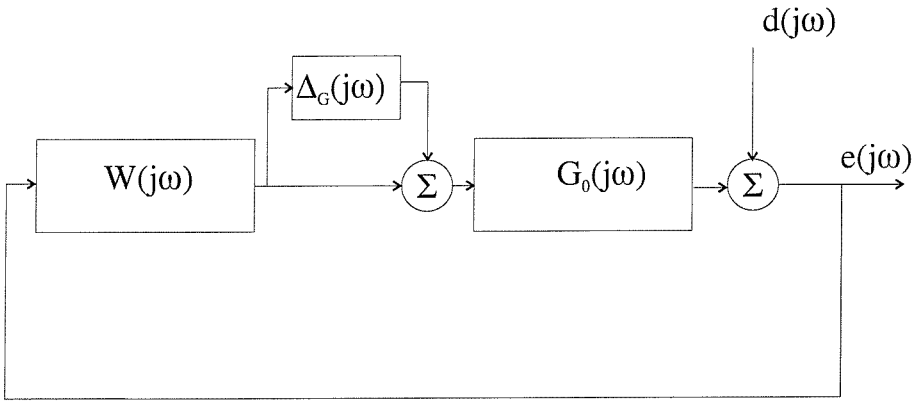

Figure 5.8: Block diagram of multiplicative uncertainty

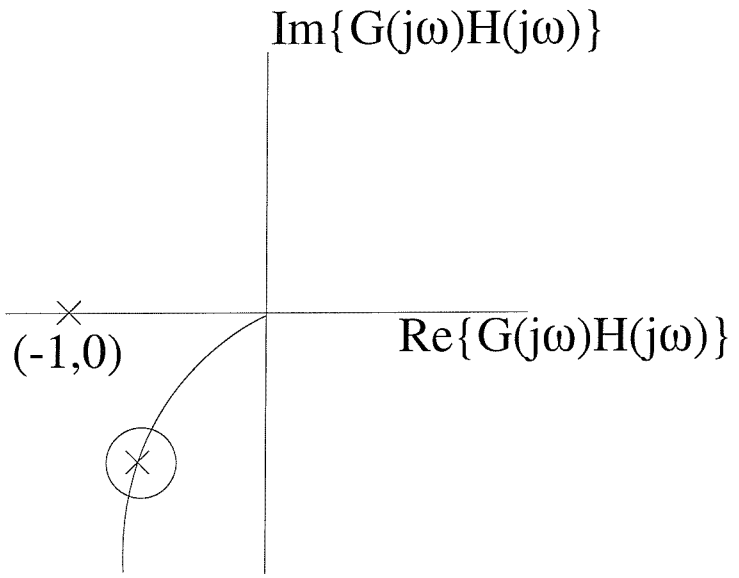

Figure 5.9: Nyquist plot of circle of uncertainty around nominal point

The modulus of $\Delta_G(j\omega)$ is assumed to be less than some upper bound B. This bound is generally frequency dependent so that

$$|\Delta_G(j\omega)| < B(j\omega) \tag{5.7}$$

The Nyquist diagram represents this by a ring of uncertainty around each point of the open loop frequency response. This ring has radius $|G_0(j\omega)H(j\omega)|B(j\omega)$ and is shown in figure 5.9.

It is clear from the figure that the distance from the open loop frequency response to the Nyquist point $(-1, 0)$ is

$$|1 + G_0(j\omega)H(j\omega)| \tag{5.8}$$

For the stability condition to hold at any given frequency, this circle must not enclose the Nyquist point and so,

$$|1 + G_0(j\omega)H(j\omega)| > |G_0(j\omega)H(j\omega)|B(j\omega) \tag{5.9}$$

The condition for robust stability is then

$$\frac{|G_0(j\omega)H(j\omega)|}{|1 + G_0(j\omega)H(j\omega)|} < \frac{1}{B(j\omega)} \tag{5.10}$$

The left hand side of this equation is seen to be equal to the complementary sensitivity function, equation (5.3), and so

$$|T(j\omega)| < \frac{1}{B(j\omega)} \tag{5.11}$$

or

$$|T(j\omega)B(j\omega)| < 1 \qquad \text{for all } \omega \tag{5.12}$$

This means that for robust stability, the complementary sensitivity function weighted by the fractional uncertainty in the plant frequency response should have a magnitude less than unity.

Other types of unstructured uncertainty are described in [77]. The stability of MIMO systems can also be considered using unstructured uncertainty. This is especially straightforward using the generalised feedback control framework introduced in the next section.

The performance of a feedback control system is also dependent on the frequency response of the plate and the autocorrelation, or predictability, of the disturbance signal.

The autocorrelation of the disturbance signal $d(t)$ is given by

$$R_{dd}(\tau) = E[d(t)d(t+\tau)] \tag{5.13}$$

E is the expectation operator, t is time, and τ is the time delay between points. Autocorrelation is discussed in more detail in signal-processing textbooks [78, 79] but provides a measure of how well the signal can be predicted in the future using present and past values of the signal. The two extremes of these are completely periodic or predictable signals or, completely random signals. All real signals fall somewhere in between these two extremes and, the larger the autocorrelation, the more predictable, and hence controllable, the signal.

Another factor which affects the performance of a feedback control system is the phase of the plant frequency response function. In section 4.6 actuator positions were chosen to give a plant FRF as minimum phase as possible. Any delay or phase lag becomes an univertible part of the plant and reduces the performance of feedback control. Additionally, time delay in the plant reduces the bandwidth of control as described by [17, 80] for example.

There is thus an additional trade-off between performance (attenuation), robust stability, and

the delay in the plant FRF which arises as an inherent part of the digital controller and signal conditioning equipment. This specific trade-off is investigated in detail in sections 7.2 and 8.2.2.

Other limitations to performance are discussed in [17] and include the waterbed effect, which means that if good control performance is obtained over a certain frequency range then there will be poor performance over another frequency range and is a consequence of the Bode integral [17, 80].

5.1.2 Generalised feedback control framework

Multi-channel control systems are considered later in this thesis where several actuators, several sensors, or both are present and can be used independently of each other. These are referred to as multi-input multi-output or MIMO control systems as opposed to single-input single-output SISO control systems which have been used up to this point.

A method of describing these MIMO control systems (or SISO control systems) in a convenient way is by using the generalised control framework [80]. The block diagram is shown in 5.10 and shows three blocks, the generalised plant $\boldsymbol{P}$, the generalised controller $\boldsymbol{K}$, and the generalised uncertainty $\boldsymbol{\Delta}$:

P generalized plant matrix, which includes the plant model, the disturbance model, and the interconnection between the plant and controller.

K controller matrix.

w exogenous (external) inputs including disturbances, command signals and noise.

z regulated outputs (error signal).

v sensor outputs (measured values and command signals).

u control signals.

$\boldsymbol{y}_{\Delta}$ input to the uncertainty block

$\boldsymbol{u}_{\Delta}$ output from the uncertainty block

$\boldsymbol{\Delta}$ uncertainty matrix

The control system can then be described using the equations

$$\begin{bmatrix} \boldsymbol{z} \\ \boldsymbol{v} \end{bmatrix} = \boldsymbol{P} \begin{bmatrix} \boldsymbol{w} \\ \boldsymbol{u} \end{bmatrix}, \qquad \boldsymbol{u} = \boldsymbol{K}\boldsymbol{v}, \qquad \boldsymbol{u}_\Delta = \boldsymbol{\Delta}\boldsymbol{y}_\Delta \tag{5.14}$$

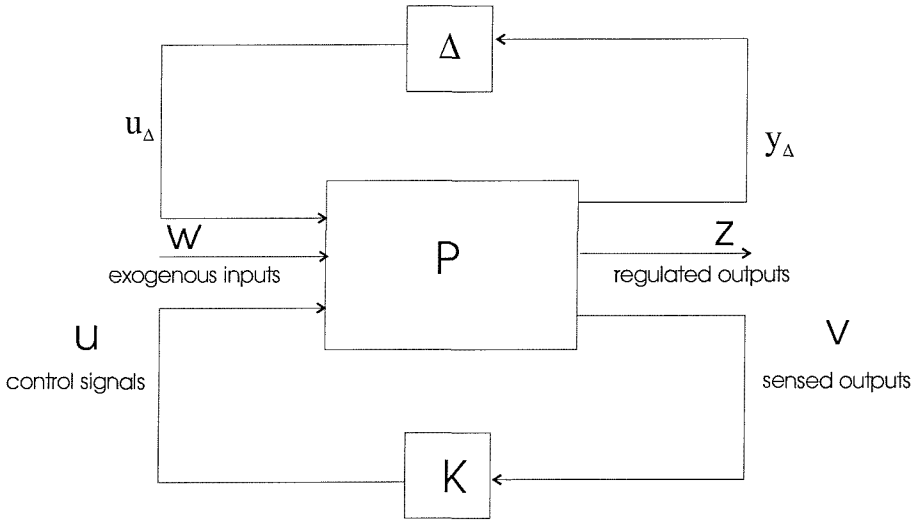

Figure 5.10: General control configuaration with model uncertainty

As an example of the power of this approach, the plant matrix $\boldsymbol{P}$ can be conveniently partitioned as

$$\boldsymbol{P} = \begin{bmatrix} \boldsymbol{P}_{11} & \boldsymbol{P}_{12} \\ \boldsymbol{P}_{21} & \boldsymbol{P}_{22} \end{bmatrix} \tag{5.15}$$

In the experiments described below the primary disturbance is provided by a loudspeaker, whose input signal may be taken to be $\boldsymbol{w}$, and the secondary actuator is a piezoelectric device whose input may be taken to be $\boldsymbol{u}$. The actuator is driven via the feedback loop from accelerometer signals, $\boldsymbol{v}$, and the object is to control or regulate the outputs of a set of far-field microphones, $\boldsymbol{z}$. A simple physical interpretation can thus be given to the different FRF's in equation (5.15) betweeen the different actuators (disturbance loudspeakers and piezoceramic actuators) and sensors (accelerometers and microphones). This is shown in figure 5.11 where

$\boldsymbol{P}_{11}$ represents the transfer functions between the disturbance loudspeakers and microphones

$\boldsymbol{P}_{21}$ represents the transfer functions between the disturbance loudspeakers and accelerometers

$\boldsymbol{P}_{12}$ represents the transfer functions between the piezoceramic actuators and microphones

$\boldsymbol{P}_{22}$ represents the transfer functions between the piezoceramic actuators and accelerometers

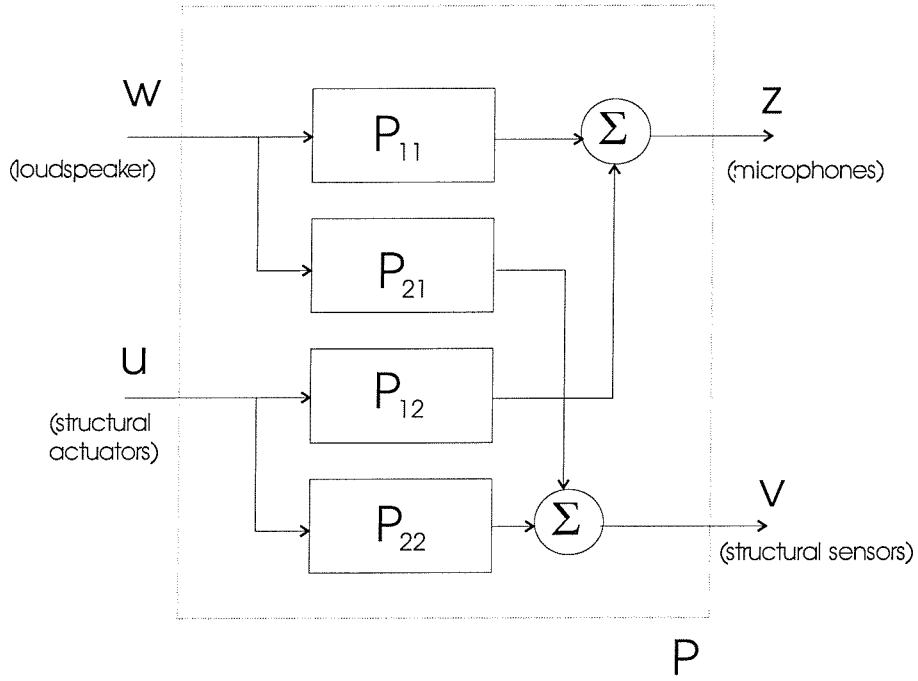

Figure 5.11: Block diagram showing transfer functions between various actuators and sensors used in experiments

This generalised control framework has many uses which simplify the analysis of MIMO control systems. Reduced formats of the block diagram allow analysis of robust performance or robust stability analysis [17, 80]. It is found that almost any linear control problem can be formulated using the generalised control framework block diagram.

5.2 Internal model control

There are many methods of designing the feedback controller H in the feedback control block diagram 5.1. The most common of these, for the purposes of feedback control in acoustics and vibrations problems is called Linear Quadratic Guassian (LQG) control and is usually based on state-space methods [81]. In this approach time domain equations governing the system response are set-up in a standard form in terms of internal state variables of the system. Using

well-established matrix methods, these state variables can be manipulated to derive properties of the system such as controllability, observability, and the effects of various feedback control strategies [81].

A more recent approach has been to use a feedback control method called Internal Model Control (IMC). Reviews of IMC controllers include [17, 77, 82] and this method assumes that a model of the plant frequency response function is available and the feedback controller H is then split up into two parts as shown in figure 5.12. The effect of the parallel path with the plant model within the IMC feedback controller, as shown in the block diagram figure 5.12, is to subtract the effect of the manipulated variables from the process output. If the model is a perfect representation of the plant then the feedback signal is equal to the influence of the disturbance and is not affected by the manipulated variables. In this case, the IMC block diagram can be rearranged into the feedforward diagram shown in 5.13 and the controller and plant model block can then be changed (assuming linear, time-invariant systems) to give the block diagram 5.14. The H_2 control problem can then be solved using conventional Wiener techniques. This block diagram also shows that for perfect control, the controller would be an exact inverse of the plant, as described in section 4.6, $W = G^{-1}$. The IMC method was developed in the 1970's [83–86] and is a particularly convenient form of controller parameterization. This parameterization, also called Q-parameterization or Youla-parameterization, parameterizes all stabilizing controllers for a given plant. The IMC formulation turns out to be identical to Youla parameterization for a stable plant. More recently, IMC has been used in ACS, ACV, and ASAC applications, especially by Elliott [82, 87–89]. Comparisons between IMC and other control techniques are given in [17, 90]. Mørkholt [90] shows that, although the IMC and conventional state-space LQG methods of designing feedback controllers have different approaches to solving the control problem and have varying degrees of computational complexity, the different design methods yield controllers with almost identical performance. These conclusions are expected because all these methods have essentially the same cost function to minimise. These are all known as H_2, or minimum variance, control as they minimise the mean square value of a given error signal. Another recent feedback controller design approach is the H_∞ approach [80]. In SISO systems the H_∞ approach minimises the maximum error at any frequency instead of the mean-square error but for active control it is the mean-square pressure which determines the subjective loudness of a sound and so H_2 control is the most applicable.

Although each feedback controller design method has its own advantages and disadvantages,

IMC is used in this thesis for the following reasons:

1. The plant response at frequencies important for ASAC is high order (theoretically infinite since the plate is actually a distributed parameter system), well damped, and has significant delays due to the reconstruction and anti-aliasing filters essential to stop high frequency noise in digital systems for acoustic applications. Additionally, the plant is uncertain, due to the boundary conditions and in-plane stresses for example. All these factors make state space modelling difficult. Using IMC it is possible to use measured data directly to calculate the controller with an FIR filter to model the plant and so these factors are less important.

2. Due to the plant model within the IMC controller, insight and analytical techniques previously obtained with feedforward techniques can be used, which can then be compared within the same framework.

3. The IMC formulation is relatively easy to reconfigure as an adaptative controller which can be a difficult task for other types of feedback control.

4. Assuming the plant is stable, the overall closed-loop feedback system is stable if and only if the IMC controller filter W is stable as shown below. As the plant is stable for all structures considered in this thesis, only the stability of the control filter then needs to be considered and assuming W to be stable ensures the closed-loop stability of the IMC controller under nominal conditions.

5. Whereas an analysis of robustness can be difficult when using LQG methods, it is relatively straightforward using the IMC formulation.

Two different approaches for calculating the optimum controller are outlined below but the basic steps for the design and implementation of an IMC controller are as follows:

1. Obtain a plant model $\hat{G}$. In this thesis, this is achieved by fitting an FIR filter to measured data.

2. Calculate the feedforward controller W in figure 5.14 by using one of the methods outlined in sections 5.2.1 or 5.2.2. This controller is dependent on the primary disturbance.

3. Calculate the feedback controller H using equation (5.18) and implement as an FIR controller.

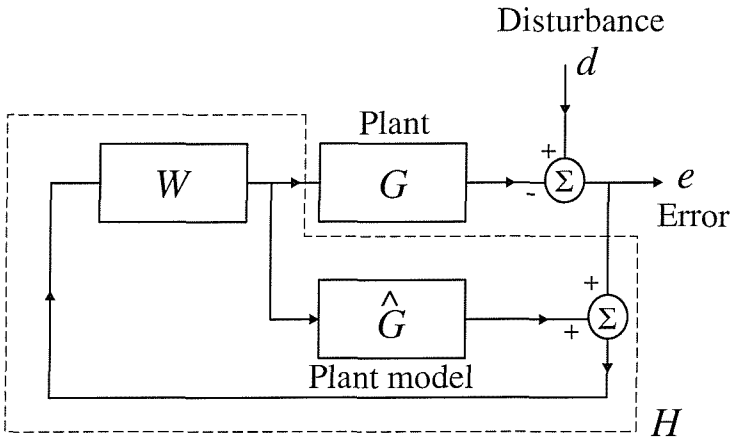

Figure 5.12: Block diagram of an internal model control system

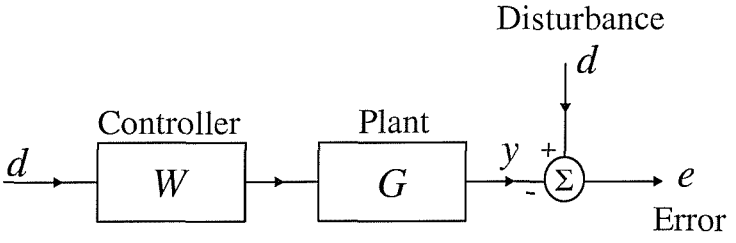

Figure 5.13: Block diagram of IMC reformulated as a feedforward problem

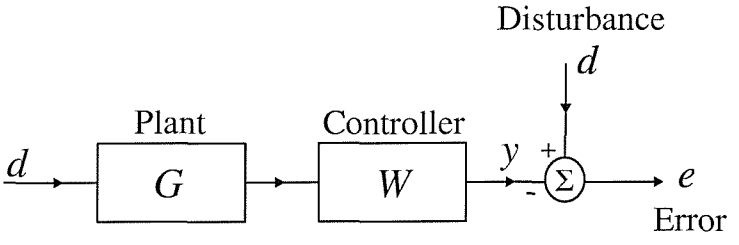

Figure 5.14: Rearranged block diagram of IMC reformulated as a feedforward problem

5.2.1 Optimum least-square controller

To derive the optimum controller after IMC has been reformulated into the feedforward problem shown in figure 5.14, consider the general discrete feedback control equation in the sampled time case

$$e(z) = d(z) - G(z)H(z)e(z) \tag{5.16}$$

where $e(z)$ is the z-transform of the error signal, $d(z)$ is the z-transform of the disturbance signal, $G(z)$ is the transfer function of the plant, and $H(z)$ is the transfer function of the feedback controller. The plant response in the sampled-time case includes ADC and DAC convertors and anti-aliasing and reconstruction filters as well as the actuator and sensor responses and the structural response of the system under control.

This equation can be rearranged to

$$e(z) = \left[\frac{1}{1 + G(z)H(z)}\right] d(z) \tag{5.17}$$

which can be compared to its continuous counterpart, equation (5.2). The internal model controller is formulated such that

$$H(z) = \frac{W(z)}{1 - \hat{G}(z)W(z)} \tag{5.18}$$

and the error can then be written

$$e(z) = \left[\frac{1 - \hat{G}(z)W(z)}{1 + [G(z) - \hat{G}(z)]W(z)}\right] d(z) \tag{5.19}$$

if the plant model is an exact model of the plant so that $\hat{G}(q) = G(q)$ then

$$e(z) = [1 - G(z)W(z)]d(z) \tag{5.20}$$

as shown in figure 5.13.

If $W(z)$ is assumed to be an FIR filter, the mean square error is a quadratic function of the coefficients of $W(z)$ which allows easy calculation of the optimum performance using standard Wiener techniques. An FIR filter is also unconditionally stable, so that the closed loop is also guaranteed to be stable under nominal conditions. There are many different techniques for solving this least-squares problem and two are outlined below and are used in this thesis. These are a fixed solution to the Wiener-Hopf equation in this section, and the filtered-x LMS which is an adaptive method to solve the same quadratic problem, described in the next section. These methods are reviewed in [82].

Considering first the fixed solution, the error can be written from figure 5.14 as

$$e(z) = d(z) - W(z)r(z) \tag{5.21}$$

so that

$$e(n) = d(n) - \sum_{i=0}^{I-1} w_i r(n-i) \tag{5.22}$$

where $r(z) = G(z)d(z)$ is the reference signal given by the disturbance filtered by the plant reponse and w_0 to w_{I-1} are the coefficients of the FIR control filter $W(z)$.

The control coefficients are optimally adjusted to minimise a cost function given by the expected value of the error squared $E[e^2(n)]$ which is equivalent to minimising the total power of the signal. After this optimisation the error signal will be completely uncorrelated with the reference signal for I samples so that

$$E[e(n)r(n-k)] = 0 \qquad \text{for } 0 < k < I-1 \tag{5.23}$$

Substituting equation (5.22) into equation (5.23) gives an expression for the optimal filter coefficients $w_i(opt)$

$$E[d(n)r(n-k)] - \sum_{i=0}^{I-1} w_i(opt)E[r(n-i)r(n-k)] = 0 \qquad for\ 0 < k < I-1 \tag{5.24}$$

The first term of this equation is the expected value of the present disturbance multiplied by the $(n-k)^{th}$ filtered reference signal. To include all values of k this term is represented by an I length vector $\boldsymbol{p}$ which is the cross-correlation function between $d(n)$ and $r(n)$

$$\boldsymbol{p} = [\ E[d(n)r(n)]\ E[d(n)r(n-1)]\ \cdots\ E[d(n)r(n-I+1)]]^T \tag{5.25}$$

Also defining the I by I auto-correlation matrix $\boldsymbol{R}$ as

$$\boldsymbol{R} = \begin{bmatrix} E[r(n)r(n)] & E[r(n)r(n-1)] & \dots & E[r(n)r(n-I+1)] \\ E[r(n-1)r(n)] & E[r(n-1)r(n-1)] & \dots & E[r(n-1)r(n-I+1)] \\ \vdots & \vdots & \ddots & \vdots \\ E[r(n-I+1)r(n)] & E[r(n-I+1)r(n-1)] & \dots & E[r(n-I+1)r(n-I+1)] \end{bmatrix} \tag{5.26}$$

and the vector of control coefficients as

$$\boldsymbol{w} = [w_0\ w_1\ \cdots\ w_{I-1}]^T \tag{5.27}$$

Equation (5.24) can be expressed in matrix form for $k = 0$ to $I-1$

$$\boldsymbol{p} - \boldsymbol{R}\boldsymbol{w}_{opt} = 0 \tag{5.28}$$

The optimal Wiener control filter coefficients are then given by

$$\boldsymbol{w}_{opt} = \boldsymbol{R}^{-1}\boldsymbol{p} \tag{5.29}$$

A direct solution is possible if the matrix $\boldsymbol{R}$ is positive definite which is assumed to be the case if the filtered reference signal persistently excites the control filter [82] and this solution shows that if the plant response and disturbance signals are known, then it is possible to calculate the optimal filter coefficients, and hence the resulting error signal.

For a minimum phase plant, a controller can be designed which perfectly compensates for the plant and drives the error to zero. However, if the plant has K samples delay in it, then $r(n)$ is delayed by K samples with respect to $d(n)$ and so the cross-correlation vector $\boldsymbol{p}$ will not include all the correlated information as $E[d(n)r(n+1)]$ to $E[d(n)r(n+K)]$ will be non-zero. The performance of the control system is thus adversely affected by any delay in the plant. This gives a mathematical interpretation of the need for minimum phase plant FRF's, as introduced in section 4.6.

Returning to the trade-off between robust performance and robust stability, there are various methods of designing controllers which are not necessarily optimal but which provide a good approximation to the optimal solution. A typical cost function in LQG control for example is to minimise

$$J = E[e^2] + \rho E[u^2] \tag{5.30}$$

where $E[u^2]$ is the expectation value of the mean square input signal to the plant and ρ is an effort weighting parameter. The effect of the effort term is to make the feedback control system more robust to plant changes.

A similar technique can be used for IMC by designing the controller to minimise the cost function

$$J = E[e^2(n)] + \beta \sum_{i=1}^{I-1} w_i^2 \tag{5.31}$$

where β is called a regularisation term as it regularises or improves the condition number of the matrix to be inverted. The optimal controller is then given by

$$\boldsymbol{w}_{opt} = E[\boldsymbol{r}^T(n)\boldsymbol{r}(n) + \beta \boldsymbol{I}]^{-1} E[\boldsymbol{r}(n)\boldsymbol{d}(n)] \tag{5.32}$$

which reduces to equation (5.29) if $\beta = 0$. This technique is outlined in more detail in [82].

5.2.2 Adaptive controller

One of the advantages of IMC listed above is that it allows easy adaptive implementations which can be difficult using other feedback control techniques. This is because the feedback control is rearranged as a feedforward problem. One such adaptive technique is the filtered-x LMS algorithm [91]. This method updates the coefficients in the FIR control filter after each measured sample so that they converge to the optimal filter $\boldsymbol{w}_{opt}$. The FIR control filter has a quadratic error surface with a unique minimum and so a gradient descent algorithm is used.

The LMS algorithm estimates the current gradient of the error surface using the most recent error sample multiplied by the previous I reference signals, to update the coefficients of the control filter. The i'th filter coefficient at sample $n+1$ is given by the equation

$$w_i(n+1) = w_i(n) - \alpha e(n) x(n-i) \tag{5.33}$$

α is a convergence coefficient which determines the rate of convergence. The block diagram for this adaptation is shown in figure 5.15

If the output of the filter is filtered by the plant response, as is the case in IMC, then it is also necessary to filter the reference signal by a model of the plant to produce an unbiased estimate of the gradient and this is known as the filtered-x LMS algorithm which is depicted in figure 5.16.

The update equation is then given by

$$w_i(n+1) = w_i(n) + \alpha e(n) r(n-i) \tag{5.34}$$

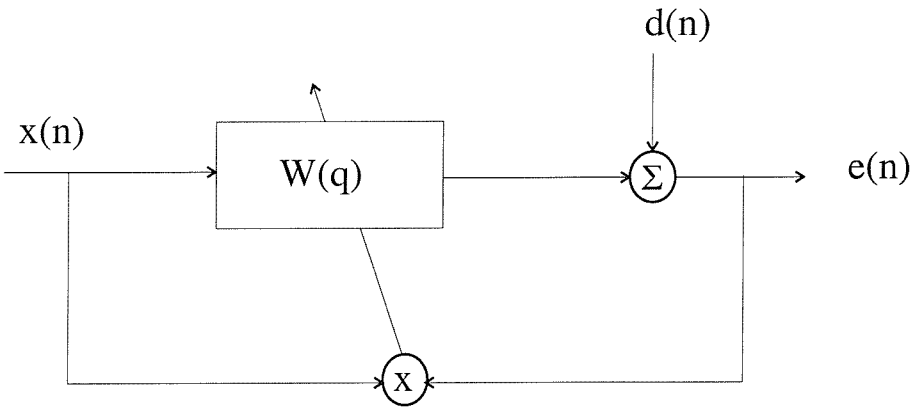

Figure 5.15: Adaptive LMS control system.

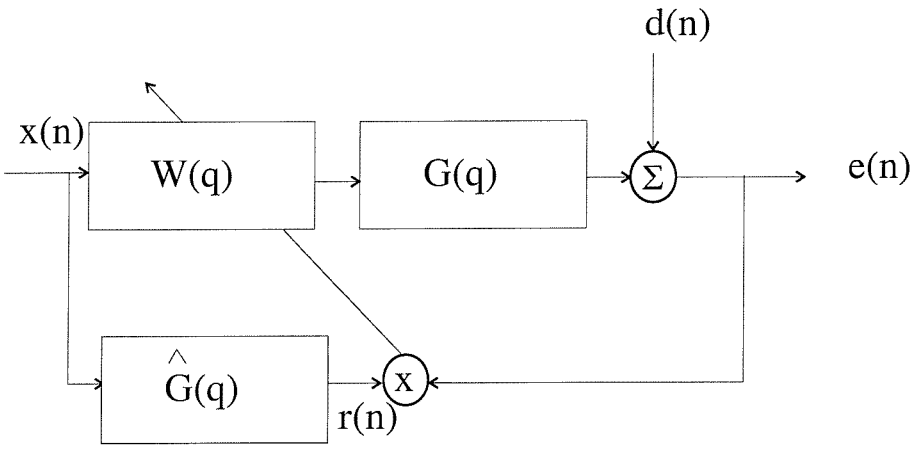

Figure 5.16: Adaptive control system: Filtered-x LMS

$r(n-i)$ is the filtered reference signal given by

$$r(n) = \hat{G}(q)x(n) = \hat{g}_0 x(n) + \hat{g}_1 x(n-1) + \hat{g}_2 x(n-2) + \hat{g}_{J-1} x(n-J+1) \tag{5.35}$$

Once again, the controller can be made more robust to plant changes by using the leaky version of the filtered-x LMS algorithm which includes a term β as above. This is discussed in [92] for example.

5.3 Active structural acoustic control using a distributed volume velocity sensor

An intial set of experiments was carried out using the experimental configuration described in chapter 4 i.e. on a plate with five piezoceramic actuators, a distributed volume velocity sensor, and using an IMC controller. This section describes those experiments and the conclusions which resulted from this set of experiments.

5.3.1 Apparatus

The experimental set-up is shown in figure 5.17. The plate with sensors and actuators is mounted on a heavy, rockwool-filled box with a loudspeaker inside which generates the primary disturbance. The dimensions of the plate are $278mm$ by $247mm$ and $1mm$ thickness and the purpose of the rockwool is to prevent flanking so that the disturbance is only transmitted through the plate. An etched PVDF film is bonded to one side of the plate forming the volume velocity sensor and five piezoceramic patches, arranged as shown in figure 4.10(b), are bonded to the other side of the plate. The signal conditioning components are also shown in figure 5.17. A host PC with a TMS320C30 digital signal processing card was used to measure the necessary FRF's and implement the controller. The two different configurations of actuators are discussed in section 4.6 and shown in figure 4.10. It was expected from the simulations reported in chapter 4 that the five actuator configuration would provide a more minimum phase frequency

response and hence better performance, than the single actuator configuration. Photos of the experimental arrangement are shown in figure 5.18.

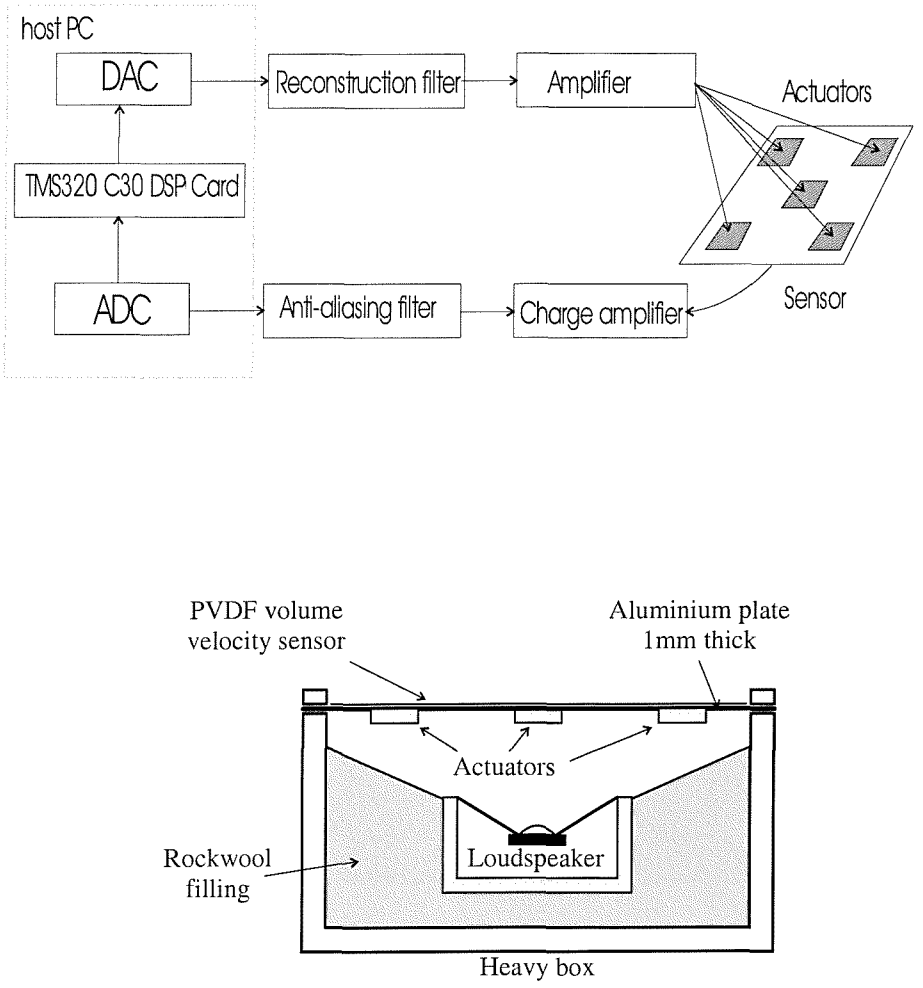

Figure 5.17: Experimental set-up a) Block diagram b)Plate mounting

It should be noted that a major difference between the simulations and the experiments is the different boundary conditions of the plate. In the simulations, simply-supported boundary conditions were assumed, giving rise to purely sinusoidal mode shapes which provide a clear understanding of the plate dynamics. In the experiments, the boundary conditions approximate clamped boundary conditions, simply-supported boundary conditions being very difficult to replicate experimentally. The major difference between the responses of plates with the two types of boundary conditions is that the natural frequencies of the plate were slightly higher when the edges of the plate were clamped as described in appendix A. There was also a slight difference in mode shapes but this is concentrated to the edges of the plate and so these differences were ignored in comparing simulated and experimentally-measured results.

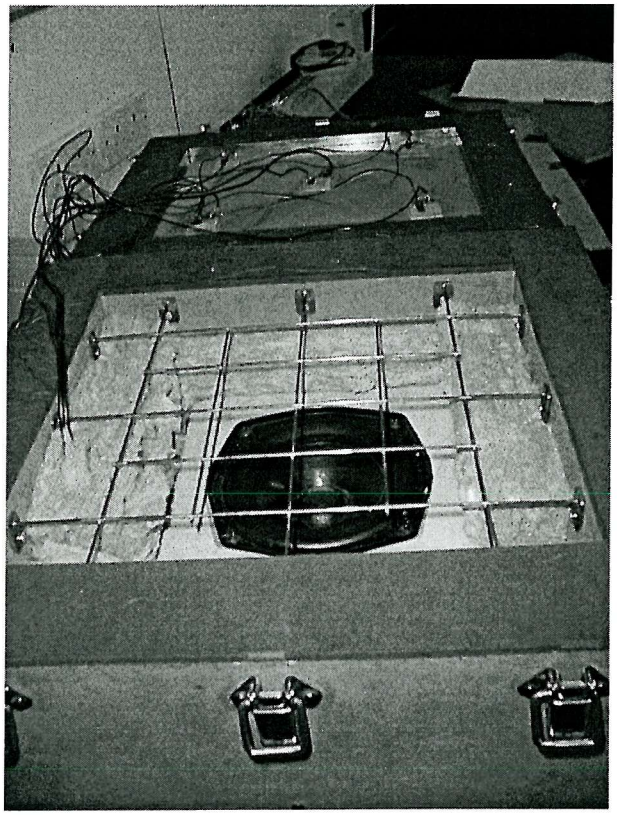

(a)

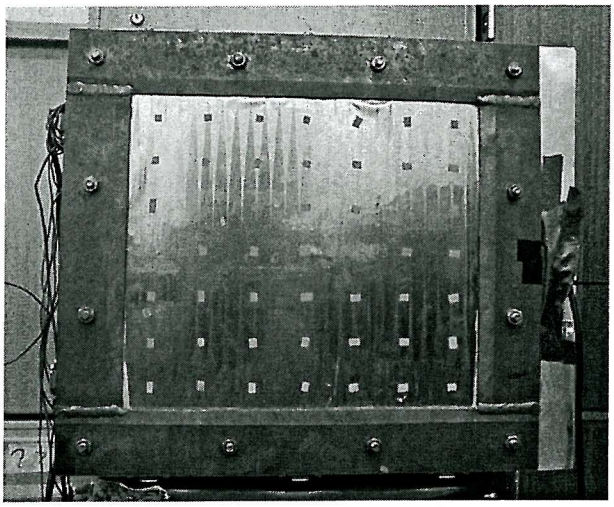

(b)

Figure 5.18: Photographs of the experimental arrangement. a) Loudspeaker generating disturbance and piezoceramic actuators. b) Volume velocity sensor.

The difference in boundary conditions is thus not expected to significantly affect the control strategy used on the plate

5.3.2 Simulations of control using measured frequency response functions

In this section, IMC simulations are used with data measured on an experimental rig to predict the performance of a real control system.

The experimental system is shown in figure 5.17. Where five actuators are used, they are driven in a single channel configuration i.e. they are all driven with the same amplitude and phase. Microphones would also be required to measure the actual attenuation in transmitted sound power after control but below, error measurements are made on the plate itself.

The relevant FRF's which are required for the control predictions are (c.f. figure 5.11)

1. $\boldsymbol{P}_{21}$, the effect of the disturbance on the volume velocity sensor.
2. $\boldsymbol{P}_{22}$, the plant. This is the FRF between a unit input voltage to the five piezoceramic actuators and the output from the distributed volume velocity sensor.

A frequency range $0-1kHz$ is chosen to simulate broadband sound and experimentally measured frequency response functions are used in IMC simulations in this section. These frequency responses were initially measured with an Advantest R9211C FFT Servo Analyzer and the anti-aliasing and reconstruction filters were removed to allow a more direct comparison of the results with simulated transfer functions.

The measured frequency response functions between the PZT sensors and PVDF sensor are shown in figure 5.19 and, apart from a constant factor in the amplitudes due to the callibration of the measurement equipment, are seen to be very similar to the ones obtained in the simulations described in chapter 4 and shown in figure 4.11, especially for the single actuator case. In the five actuator case, there is more phase loss in the experimental system than was predicted from the simulations. One problem seems to be in the way in which the phase is unwrapped. In figure 5.19(b) at around $200Hz$ for example, there is a zero shown in the response of the amplitude but a corresponding loss of 90^0 is shown in the phase response, rather than a corresponding

gain of 90^0 which would be expected. The transfer function of the plant is also very sensitive to the positioning of the secondary actuators. Whereas in the simulations, the position of the actuators is known perfectly, in a practical system, small deviations from these positions will result in the unexpected excitation of modes which could change the results dramatically. This is especially the case when an actuator is placed close to a nodal line for a given node as a small error in the actuator position would then cause it to be on the other side of the nodal line and to excite that particular mode 180 degrees out of phase. Similarly, an imperfect volume velocity sensor will have some response to modes which are not odd-odd, and which do not contribute to the volume velocity. The natural frequencies in the experimental system are also slightly higher than in the simulated system, probably because of the clamped boundary conditions in the experimental system, but otherwise the simulations predict experimental measurements reasonably well.

A further set of plant FRFs as measured by the DSP card is shown in figure 5.20. For calculation of the feedback controller, the complete plant FRF as measured by the DSP card is required, as there are delays inherent to the ADC/DAC processes which need to be included in the plant model. The frequency response functions as measured by the DSP card also include anti-aliasing and reconstruction filters which are required to prevent aliasing.

Approximately one and a half samples delay is inherent to sampling using digital controllers in the ADC/DAC process [93]. This includes a one sample delay for the measured sample to be transmitted between the ADC and the DAC and a one half sample delay corresponding to the phase introduced by the sample and hold operation of the DAC. Other reasons for delay include the anti-aliasing and reconstruction filters. These analogue filters add about 45 degrees of phase lag for each pole. A typical filter will have 8 poles and cause one cycle of delay. The total group delay shown in the PC measurements is approximately 2000 degrees at the Nyquist frequency of $2kHz$, which corresponds to approximately 5.5 samples or $1.4ms$ delay.

A comparison between the plant FRF's as measured by the analyser and by the PC is shown in figure 5.21. These are seen to be similar as expected, except for the extra phase loss in the FRF measured by the PC due to the reasons outlined above.

Using the plant and disturbance frequency response functions, measured by the DSP card in the host PC, MATLAB programs were then used to simulate an off-line IMC controller. The

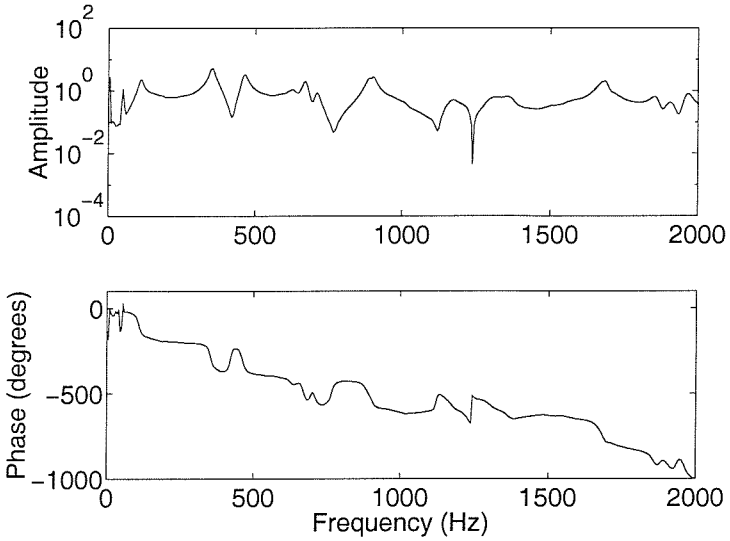

(a)

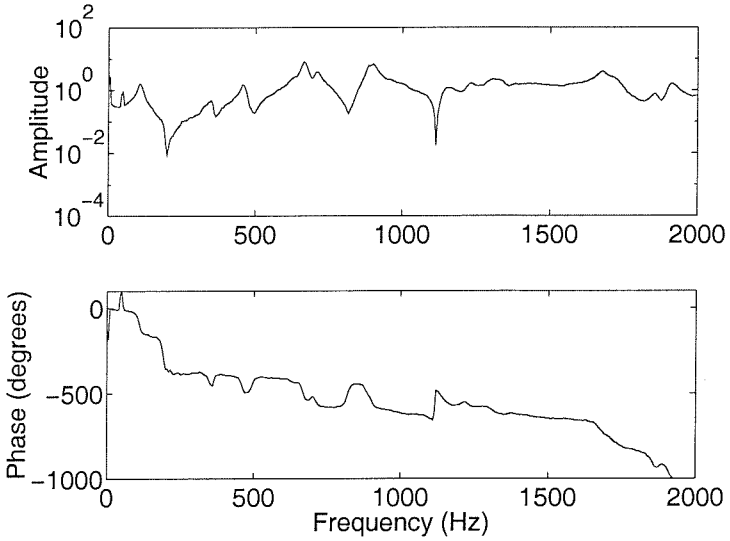

(b)

Figure 5.19: Measured frequency response functions for two actuator configurations (measured using the analyser) a) single central actuator b) 5 actuators driven in phase

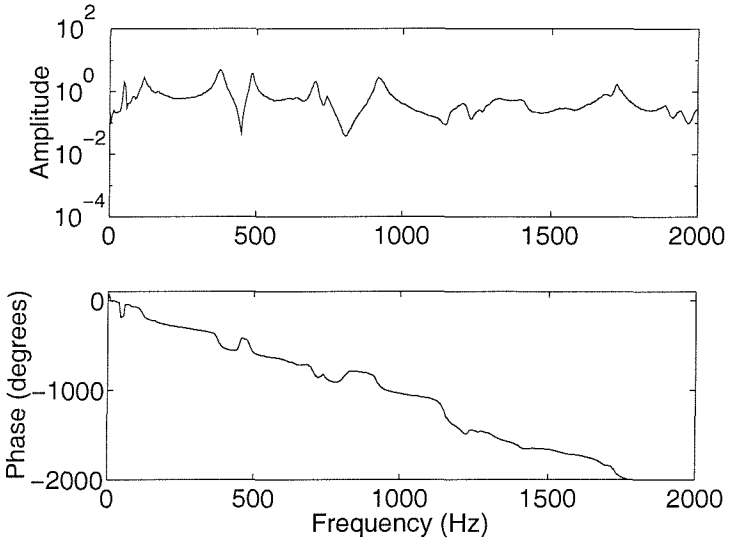

(a)

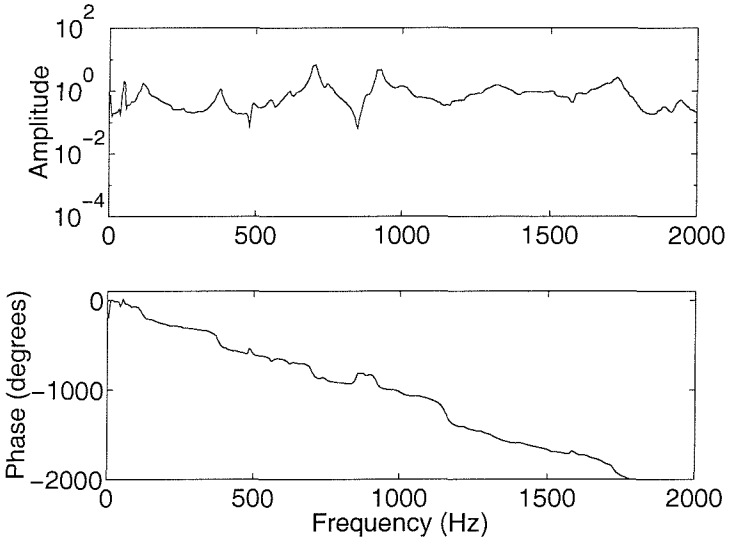

(b)

Figure 5.20: FRF's as measured using PC and TMS20C30 card. a) single centrally-placed actuator b) 5 piezoceramic actuators driven in phase

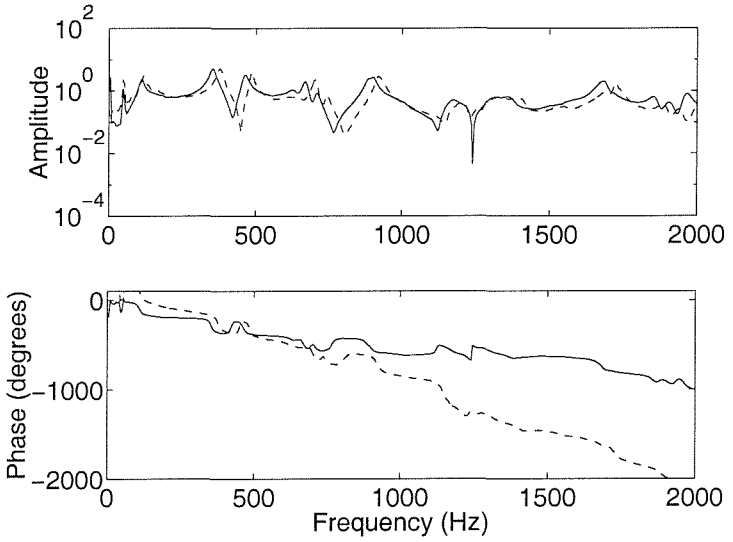

(a)

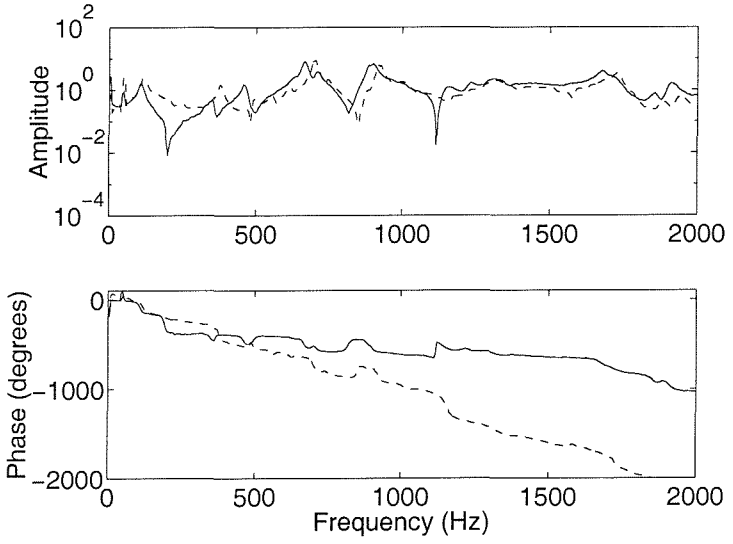

(b)

Figure 5.21: Comparison of FRF's measured by analyser (solid line) and by DSP card (dashed line). a) single centrally-placed actuator b) 5 piezoceramic actuators driven in phase

advantage of the simulations is that there were no restrictions on filter lengths due to lack of processing power and so the effect of large filters with many coefficients could be calculated. The plant and the control filter W were modelled using 512 coefficients. The controller was also designed to be robust to uncertainties in the plant of up to 35 percent by adding regularisation as described in section 5.2.1 and by examining the distance of the Nyquist plot of the open loop frequency response from the point $(-1, 0)$. Figure 5.22(a) shows the results for a single, centrally-placed actuator, where the excitation was band-passed white noise between $200Hz$ and $1kHz$ from the loudspeaker. A total attenuation of $5.8dB$ is obtained and it is clear that the spectrum of the error is whiter after control than before control as would be expected since the predictable parts of the signal have been removed. Some losses in performance are also seen between resonances due to the waterbed effect [94]. Figure 5.22(b) shows the results for the configuration with all five actuators, which gives an overall attenuation of $6.1dB$.

The total attenuation for the five actuator case is greater than for the single actuator case, as expected due to the more minimum phase frequency response, but the difference between the two is not large. It is expected that the performance of the five actuator system would get better relative to the single actuator case, as the sampling rate increases and the delay due to the anti-aliasing filter is reduced.

5.3.3 Real time IMC control

This section outlines some real-time control experiments which were carried out using the experimental rig which has already been presented. The results show that feedback control of both tonal and broadband disturbances can be achieved. However, there are a number of problems which arise in the implementation of the IMC controller which limit the performance.

The disturbance loudspeaker, was driven with band-passed white noise between $200Hz$ and $1kHz$. The sampling rate was $5kHz$ and cut-off frequencies of the anti-aliasing and reconstruction filters were set to $2kHz$.

A real-time adaptive controller was then implemented on the DSP card. Limits on processing power meant that the same number of filter coefficients for the plant model, $\hat{G}$, and the control filter, W, could not be used as in simulations. The best that could be implemented at the

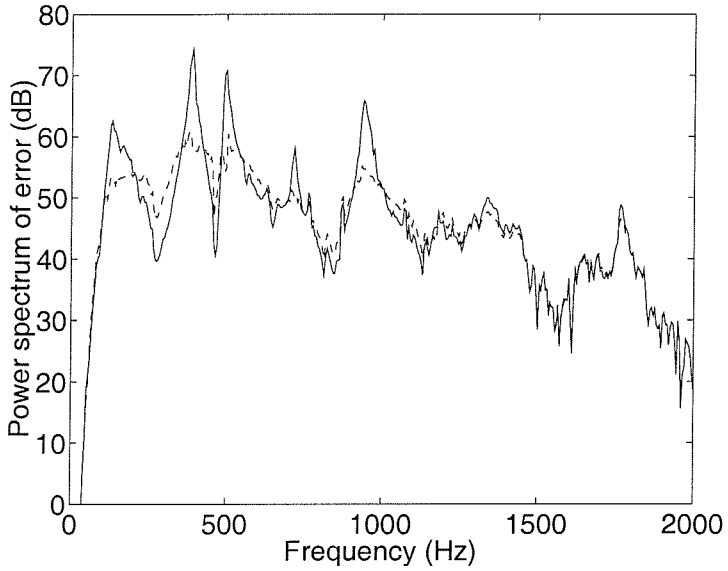

(a)

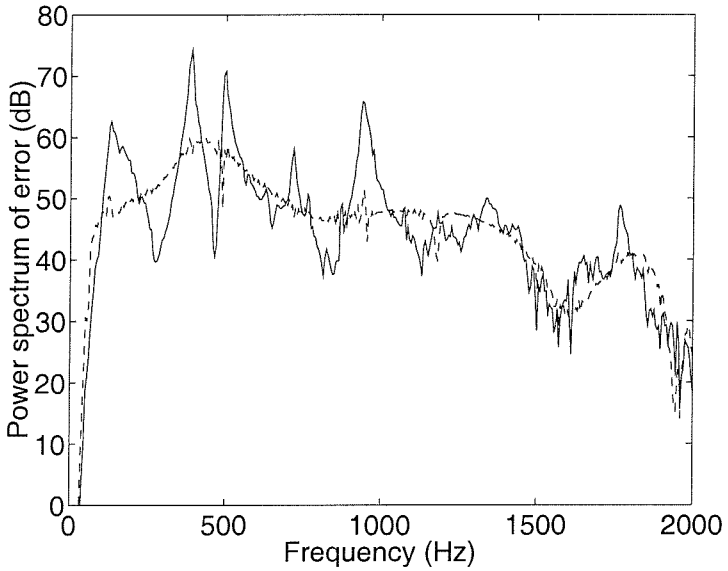

(b)

Figure 5.22: Simulations of IMC feedback control using measured plant and disturbance frequency response functions. Solid line shows error, measured at volume velocity sensor, before control and dashed line shows error after control. a) Single, centrally-placed actuator. $5.8dB$ attenuation. b) Actuators placed as shown in figure 4.10(b). $6.1dB$ attenuation.

chosen sample rate was 195 coefficients for the plant model and 110 coefficients for the control filter, W. Another difference between simulations and real-time control is that in the former, a fixed controller is calculated but in the latter, an adaptive filter was used. This was calculated using the filtered-x LMS algorithm to minimise the volume velocity. A regularisation term was also added to this algorithm to ensure stability of the controller.

It had previously been shown [69] that the volume velocity sensor could be used to control tonal disturbances using feedforward control and figure 5.23 shows the attenuation obtained with feedback control when the disturbance signal was a $380Hz$ sine wave fed into the loudspeaker and a single actuator was used (this disturbance signal was chosen to be close to the $(3,1)$ mode of the plate). A total attenuation of $24dB$ is obtained and the main tone and its second harmonic are well controlled.

Figure 5.24 shows the results of real-time control when the disturbance was band-passed ($200Hz$ to $1kHz$) white noise and a single actuator was used. A $4.2dB$ overall attenuation was obtained, in contrast to the $5.8dB$ expected with long control filters. As with the simulations, control performance at some frequencies is seen to be far better than at others. The $(1,1),(3,1),(1,3)$ modes at $191Hz$, $370Hz$, and $473Hz$ respectively, are controlled especially well, as expected, since these are the dominant volumetric modes.

The performance of the system with five actuators was also tested. It was found that a more accurate plant model was required for stability and hence more coefficients were needed in the FIR plant modelling filter, which it was not possible to implement in real-time due to limitations in computing power. It is expected that if a more powerful computer were available, the five actuator configuration would achieve better results than the single actuator configuration.

5.3.4 Implementation issues

A significant problem encountered with the experimental system described in this chapter is the lack of available computer processing power. This manifests itself in two ways:

1. It limits the number of filter coefficients that can be used in the experimental system. A major difference between simulations and experiments is that, where no time constraints

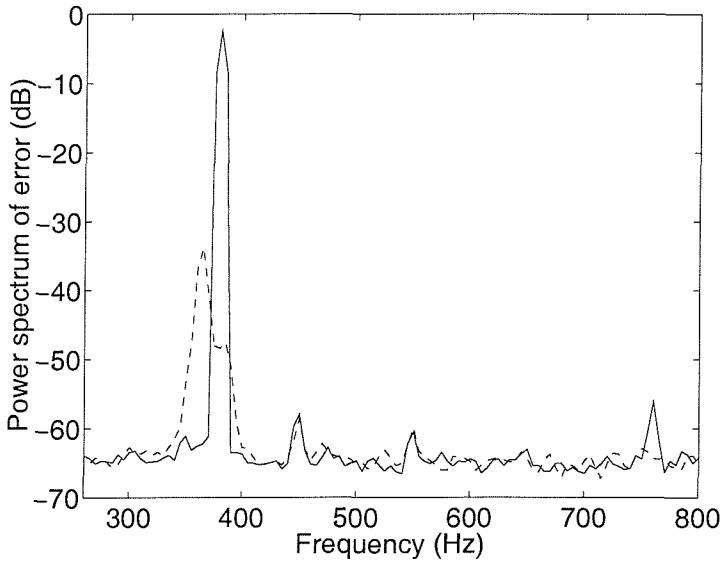

Figure 5.23: Experimental IMC results: Tonal disturbance. Single, centrally-placed actuator. 24dB attenuation. Solid line shows error before control and dashed line shows error after control.

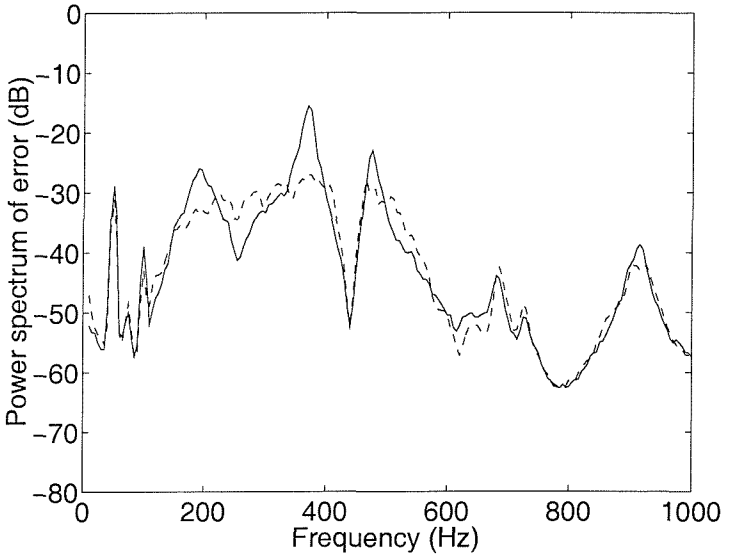

Figure 5.24: Experimental IMC results: Broadband disturbance. Single, centrally-placed actuator. 4.2dB attenuation. Solid line shows error before control and dashed line shows error after control.

were imposed, the plant model and control filter can have large numbers of filter coefficients. This results in accurate plant models and long filters. In practice, once a sampling rate and processor have been chosen, the number of filter coefficients for both plant model and controller is limited.

2. More importantly, section 4.6 describes work which was carried out to obtain minimum phase transfer functions by changing the positions of actuators on the plate. In practice, once anti-aliasing and reconstruction filters are incorporated to the signal conditioning circuitry, the advantages obtained with the five actuator configuration over the single actuator configuration (400^o of phase at the Nyquist frequency) is small compared to the phase loss in the two filters (which accumulate 720^o of phase at the Nyquist frequency).

There are two possible solutions to the latter problem:

1. Depending on the application, it may be possible to reduce the order of, or even to remove, one or both of these analogue filters. For example, where the disturbance is low frequency, it may not be necessary to include a low-pass anti-aliasing filter.

2. Alternatively, if more computing power were available, the sampling frequency could be increased. This would make the effects of the phase loss in the filters smaller relative to the phase advantages gained in changing actuator positions and would eventually result in better performance.

Another option to consider, especially regarding the first problem due to a requirement for large numbers of filter coefficients, would be to use IIR filters instead of FIR filters in the design process.

5.4 Conclusions

Whereas previous chapters have used feedforward simulations to predict the best possible performance which can be achieved using a given experimental set-up, this chapter has considered feedback control which is generally used when the disturbance is broadband.

Using feedback control gives rise to a number of new issues which result in a loss of performance relative to feedforward control. These are considered under the framework of robust stability.

One particular type of feedback control, IMC, has been considered in more detail. This has some advantages over other methods of feedback control including its simple physical interpretation and the fact that it is easy to implement adaptive solutions.

Using IMC and the experimental rig designed in chapter 4, a number of feedback simulations were performed. First, these used modelled FRF's and then measured FRF's were used.

Finally, a real-time adaptive IMC controller to reduce the volume velocity of a plate was implemented. The controller generated for tonal disturbances was found to have good performance. However, the performance was not as good as predicted when using broadband disturbances and this was mainly due to lack of processing power.

Chapter 6

Accelerometer cost functions for active structural acoustic control

6.1 Introduction to accelerometer cost functions

In chapter 4 the coupling of various different transducers into the vibrations of a panel was introduced. The advantages/disadvantages of each type of transducer and their placement was also examined.

Chapters 4 and 5 used a distributed volume velocity sensor for ASAC purposes, following earlier work by Johnson [7]. In this chapter using an array of accelerometers to derive cost functions is discussed. One disadvantage of distributed sensors is that they cannot detect whole-body vibration but accelerometers can.

The basic requirements of the cost functions are

1. The cost function should be measurable on the structure itself
2. The cost function should give a good representation of the total radiated sound power which is the quantity most relevant for subjective performance

In this chapter radiated power itself will initially be considered as the cost function being

minimised. This would, in practice, require far-field microphones which does not meet the first requirement outlined above. However, the control of radiated power will act as a reference case. The aim of using other, structural sensors, will be to get as close to this radiated power curve as possible. Turning to structurally measured cost functions, single localised structural sensors will then be examined i.e. accelerometers. It turns out that the action of these accelerometers can be best understood in terms of vibration control, and may or may not give control of radiated sound. Volume velocity is then used as an error signal. This has been used widely over recent years [1, 3, 69] and relies on a distributed sensor as described in chapter 4. Although these different cost functions have already been introduced in chapter 4, a more in-depth analysis is used in this chapter to investigate the control mechanisms in more detail.

The use of several localised structural sensors will then be investigated and, in particular, the use of a number of accelerometers to approximate volume velocity. The multiple sensors are then used in a number of multi-channel configurations (i.e. independently, where the accelerometer outputs are manipulated in some way other than by a simple summation). A further strategy investigated is the use of a large number of single channel control systems on the plate.

6.2 Radiated power as a cost function

Trying to reduce the radiated sound power is the overall aim of the various control strategies and so the practical aspects of the measurement and control of radiated sound are described in this section.

The calculation of the sound power radiated by a plate has been described in section 3.2.2 and normally uses the Rayleigh integral (equation 3.17). The sound pressure at a point or total radiated sound power can then be calculated analytically for simply-supported plates or using numerical methods if the plate has other types of boundary conditions.

There are many tried and tested techniques for the measurement of sound power and these are outlined in [6, 67, 95] for example. The different techniques available for measuring sound power depend on the measuring environment (anechoic room/reverberation room/free-field etc), the required precision, the mechanical 'mobility' of the noise source, and the presence of other noise sources. Other, more modern sound power measurement techniques, use lasers to measure

surface vibration or intensity meters.

The most accurate standard method of determining the radiated sound power is outlined in ISO 3745 [95] and is realized in an anechoic or semi-anechoic room with a number of microphones surrounding the sound source. The technique thus uses pressure measurements alone and obtains the total radiated power from the mean-squared sound pressure averaged over a hypothetical spherical surface surrounding the sound source, the centre of the sphere corresponding to the geometrical centre of the machine. The sphere should be in the far-field of the source.

Microphone number	$\frac{x}{r}$	$\frac{y}{r}$	$\frac{z}{r}$
1	-0.99	0	0.15
2	0.50	-0.86	0.15
3	0.50	0.86	0.15
4	-0.45	0.77	0.45
5	-0.45	-0.77	0.45
6	0.89	0	0.45
7	0.33	0.57	0.75
8	-0.66	0	0.75
9	0.33	-0.57	0.75
10	0	0	1.0

Table 6.1: Microphone positions from ISO 3745 [95]. In terms of Cartesian coordinates where z-axis is perpendicular (upwards) from horizontal plane and r is radius of measurement hemisphere.

In this thesis the sound power radiated by a small plate needs to be measured. The plate can be considered to be mounted in an infinite reflective half plane. ISO 3745 gives the required positions of the microphones and measurements procedure as shown in table 6.1 and figure 6.1. The surface sound pressure is then given by

$$\overline{L_p} = 10log_{10}\frac{1}{N}\left[\sum_{i=1}^{N} 10^{0.1L_{pi}}\right] \tag{6.1}$$

where $\overline{L_p}$ is the surface sound pressure in decibels ($re\ 20\mu Pa$), L_{pi} is the pressure level from

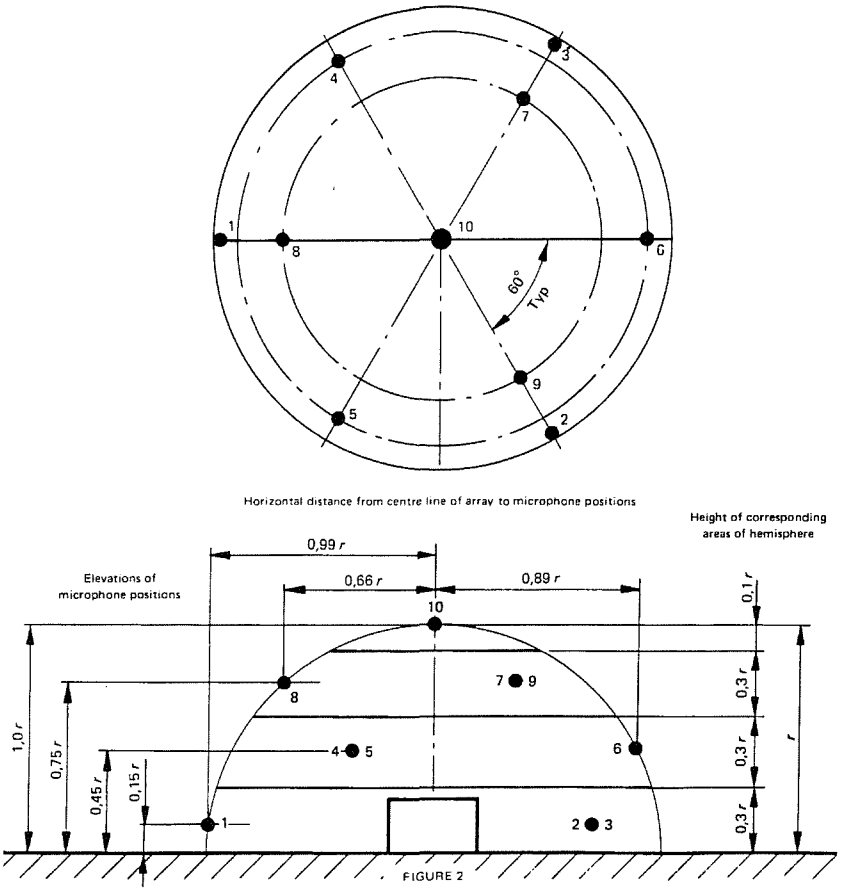

Figure 6.1: Microphone positions for sound power measurement in a free field over a reflecting plane (from [95])

the i^{th} measurement in decibels and N is the number of measurements (10 for measurements made in a half-plane). This can be used to calculate the free-field sound power level L_w using the equation

$$L_w = \overline{L_p} + 10log_{10}(S_1/S_0) + C \tag{6.2}$$

where S_1 is the area of the test hemisphere $2\pi r^2$ and $S_0 = 1m^2$ and, C is a correction term, in decibels, due to the influence of temperature and pressure which is only considered to be necessary if the conditions are very different to standard room temperature and pressure [95].

6.3 Cost functions with a single structural sensor

In chapter 4 the use of different sensors in active control systems has been examined and the performance of these sensors in terms of reductions in radiated sound power were compared. This section takes this analysis further by also considering the control mechanisms which take place for each individual type of sensor. A number of new concepts are introduced including spillover, an effect which causes an unwanted increase in some variable accompanying the control of some other variable (for example increases in kinetic energy due to accompanying decreases in sound power transmission or even increases in some modal amplitudes due to the control of others). Structural and radiation modal amplitudes will also be considered as will the kinetic energy of the plate, which gives a measure of the plate vibration levels before and after control.

The effects of using a single point force actuator to cancel the output of a single accelerometer placed in the centre of the plate were discussed in chapter 4 (figure 4.6). Figure 6.2 shows the vibration distribution of the plate after control of a pure tone disturbance at $72Hz$, the natural frequency of the $(1,1)$ mode of the plate, using a piezoceramic patch actuator with a centrally-placed accelerometer. Before control, the vibration of the plate takes a sinusoidal form. The effect of the actuator cancelling the output of the accelerometer, as described in section 4.5, is to pin that part of the plate. The dynamics of the plate are thus changed and the structure displays a new frequency response function with a new set of resonances as discussed in chapter 4.

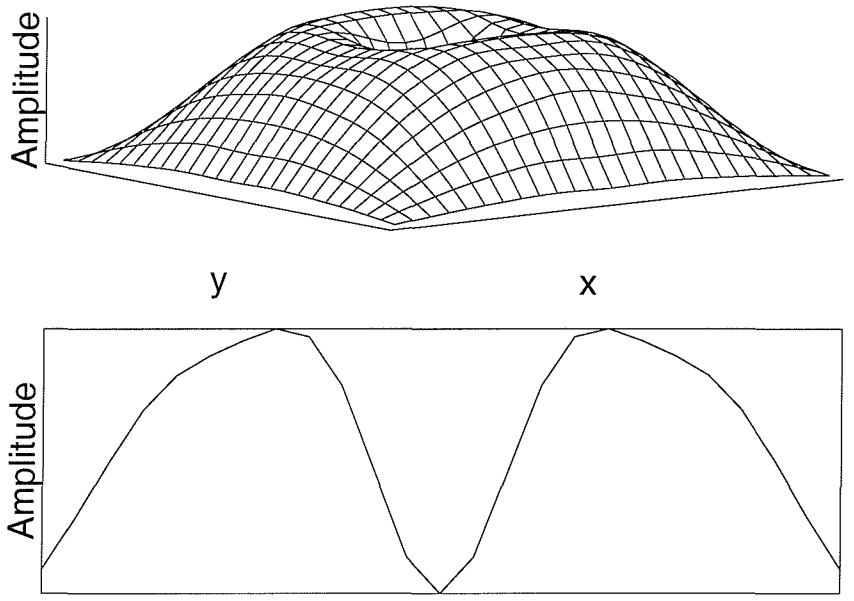

Figure 6.2: First structural mode after control using a single piezoceramic actuator and single accelerometer. a) Whole plate b) Section through mid-plane of plate

Figure 6.3 shows the amplitudes of both structural and radiation modes before and after control of the accelerometer output by the piezoceramic actuator at the natural frequency of the $(3,1)$ mode i.e. $326Hz$, and at a higher frequency of $450Hz$. The figures show the kinetic energy of each structural mode before and after control calculated as $\boldsymbol{v}_i^H \boldsymbol{v}_i$ or the radiation mode sound power outputs relative to the total sound power radiated before control. These graphs demonstrate two different forms of control known as modal suppression and modal restructuring [7, 20, 41]. These two control mechanisms can be used to understand the different methods of control found in this thesis.

At the frequency of the $(3,1)$ mode of the plate, it is clear that the vibrations of the plate before control are dominated by a single mode and this mode of vibration will account for most of the radiated sound power. After control, figure 6.3(a) shows that the amplitude of that mode is reduced and that there is little effect on the other modes. This type of control, where a dominantly radiating mode (or modes) is reduced in amplitude, is called modal suppression.

Modal restructuring is shown in figure 6.3(c). In this case, a number of modes contribute significantly to the sound radiation before control. After control of the accelerometer output by the piezoceramic patch actuator though, not all of the structural mode amplitudes are reduced

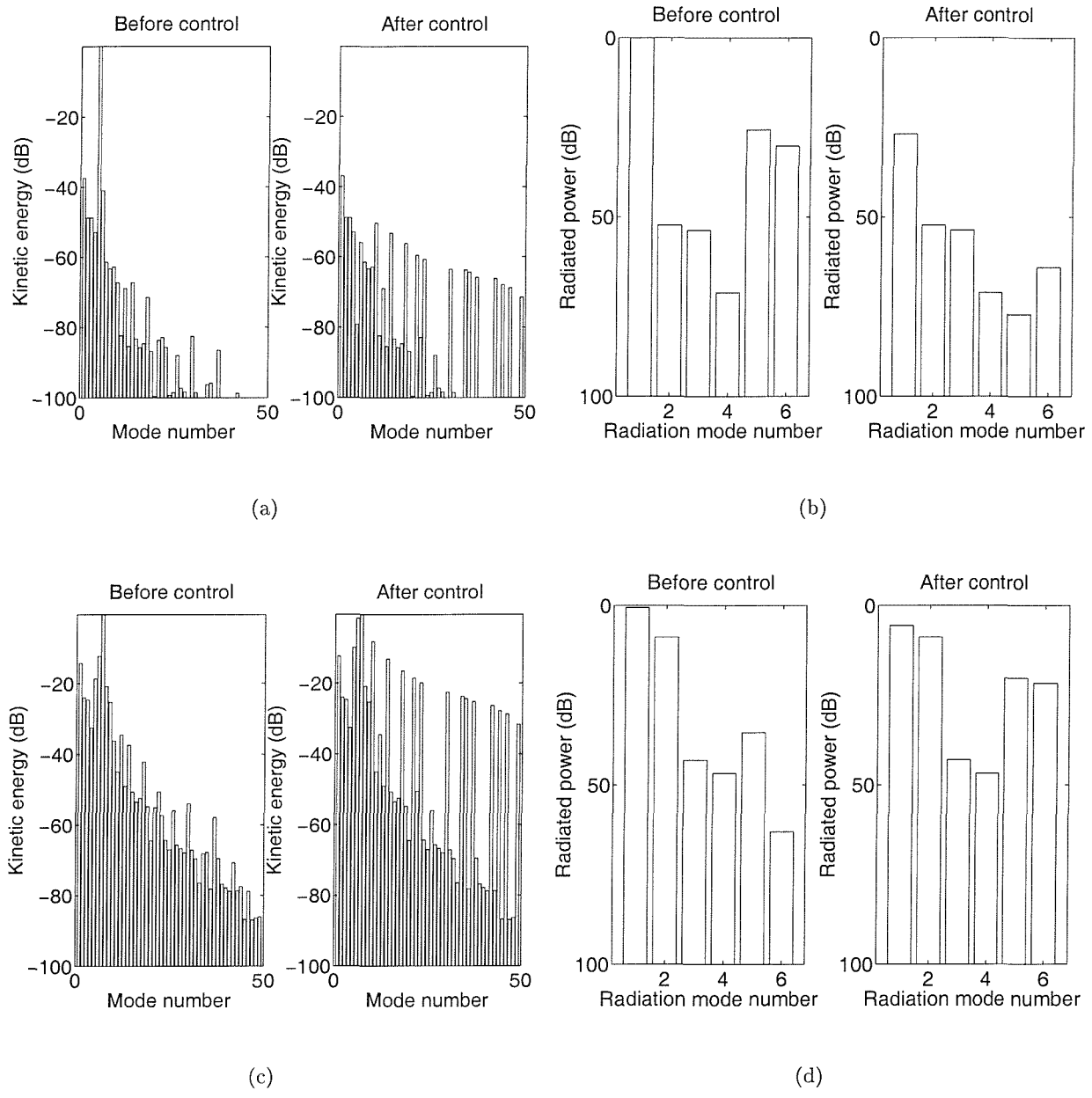

Figure 6.3: Effects of control on structural mode amplitudes, (a) and (c), and radiation mode amplitudes (dB relative to total power radiated before control), (b) and (d), using a single piezoceramic actuator and accelerometer at an excitation frequency of $326Hz$ close to the natural frequency of the $(3,1)$ mode, (a) and (b), where total attenuation is $27.4dB$, and away from any resonances $450Hz$, (c) and (d), where total attenuation is $3.8dB$.

and many are even increased. With modal restructuring, instead of reducing the amplitude of the dominant mode(s), the secondary sources alter the amplitudes and phases of the modes in such a way that their overall radiation efficiency is reduced. The complex interaction of the structural modes, which has been described in chapter 3, results in the modes cancelling each other in the far field such that the overall radiated sound power is reduced.

The figures showing the amplitudes of the radiation modes before and after control give a more intuitive representation of the control process. As these radiation modes radiate sound independently, it has already been shown (section 3.2.3) that by reducing the amplitude of any one radiation mode, the overall sound radiation from the plate is reduced. Thus in figure 6.3(b) the first radiation mode is reduced by approximately $27dB$ after control ensuring that the total radiated sound power is reduced.

A final tool which is used below to analyse the control mechanisms is an estimate of the kinetic energy or vibration levels of the plate. The estimate is given by the sum of the squared velocities of the elemental radiators, and will be discussed later.

$$V = \boldsymbol{v}^H \boldsymbol{v} \tag{6.3}$$

The control of volume velocity can be analysed in the same way as the control of sensor output described above. However, volume velocity control works only by modal restructuring as the volume velocity itself is due to a combination of all odd-odd modes. During control the vibration distribution is changed to less efficiently radiating modes.

6.4 Cost functions with multiple accelerometers

The remainder of the thesis concentrates on arrangements where there are multiple structural sensors, instead of the single distributed volume velocity sensor used in previous chapters. In the first place, a number of accelerometers placed on the plate will be used with their outputs summed to give an approximation to the volume velocity. MIMO control systems are then investigated where the different actuators and sensors can be used as independent input and

output channels respectively. Finally, an arrangement is analysed in section 6.5 which consists of a number of single channel control systems on a plate.

6.4.1 Approximation to volume velocity using multiple accelerometers

In this section, increasing numbers of accelerometers are placed on a plate and their outputs are summed to give a single error signal which is minimised by the feedforward control strategy outlined in section 4.5. This control method has relevance to the elemental approach used to model the plate; in the limit, where the number of accelerometers is equal to the number of elements used in the model, the sum of the accelerometer outputs should be equivalent to the volume velocity and this is found to be the case below. A similar approach, where multiple piezoelectric patch sensors are used instead of accelerometers is described by [96].

The results of cancelling the summed output of different numbers of sensors, as an estimate of the volume velocity are shown in figure 6.4. Each subfigure shows the configuration of piezoceramic actuators and accelerometers, although the x and y dimensions of the plate are not to scale. A single piezoceramic patch actuator is again used for simplicity and is modelled using the forcing coefficient given by equation 4.14. Each figure shows four curves; the power transmission ratio before control (solid), using control of radiated sound power (dotted), using control of true volume velocity (dashed), and using control of the summed accelerometer outputs (dash-dotted). 49 structural modes were used in the model with natural frequencies up to $3527Hz$. The number of elements in the grid was around 20 by 20 but was varied slightly depending on the number of accelerometers such that they were all positioned at centres of elements.

The figures for attenuation, given in table 6.2 are average figures over a $0 - 500Hz$ frequency range which is where the best control performance is achieved. It is evident from examining the figures that large reductions in radiated sound power can be achieved at low frequencies and that at high frequencies, there may even be some increase in the radiated power i.e. spillover, as controlling volume velocity may result in a significant amplification in other radiation modes. This is shown, for example, by an increase in the power transmission ratio at around $950Hz$ for the control of volume velocity. However, the low frequency region is the region of most interest in active control applications and techniques which can be used to reduce the high frequency amplification, which also result in increased robustness, are discussed in [17].

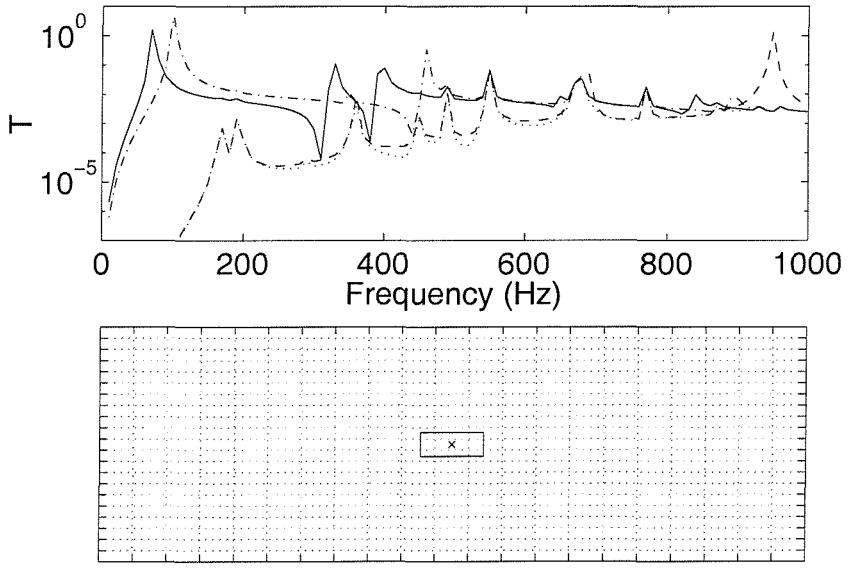

(a)

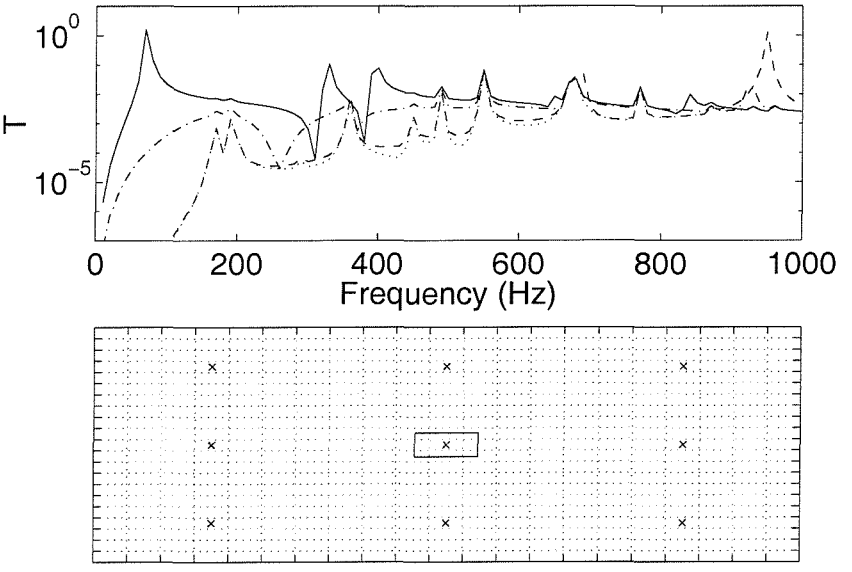

(b)

Figure 6.4: Results of SISO simulations of feedforward active control showing power transmission ratio, T, of radiated sound power to incident sound power for plane wave excitation at $\theta = \phi = 45^0$: A single actuator is used to cancel the summed output from a number of accelerometers or true volume velocity or radiated power. Solid line is power transmission ratio before control, dotted after control of radiated power, dashed after control of volume velocity and dash-dot after control of summed accelerometer output.

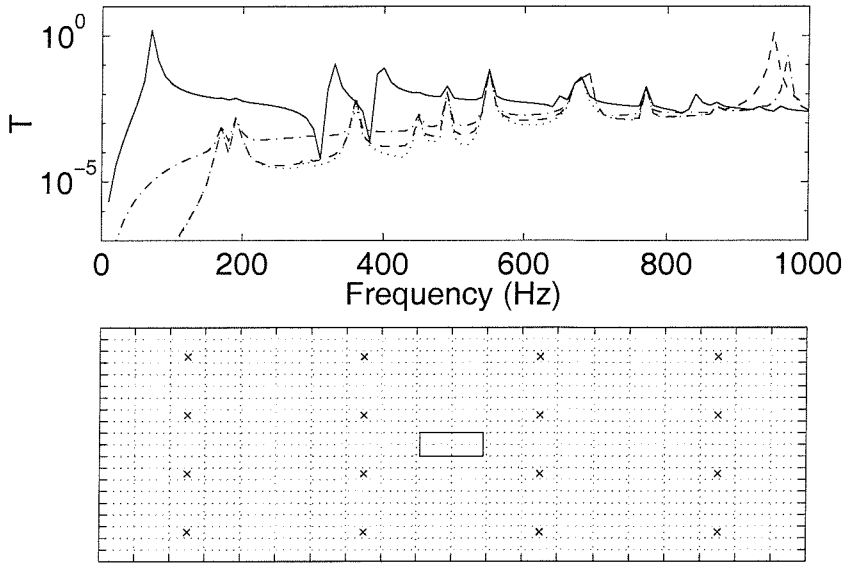

(c)

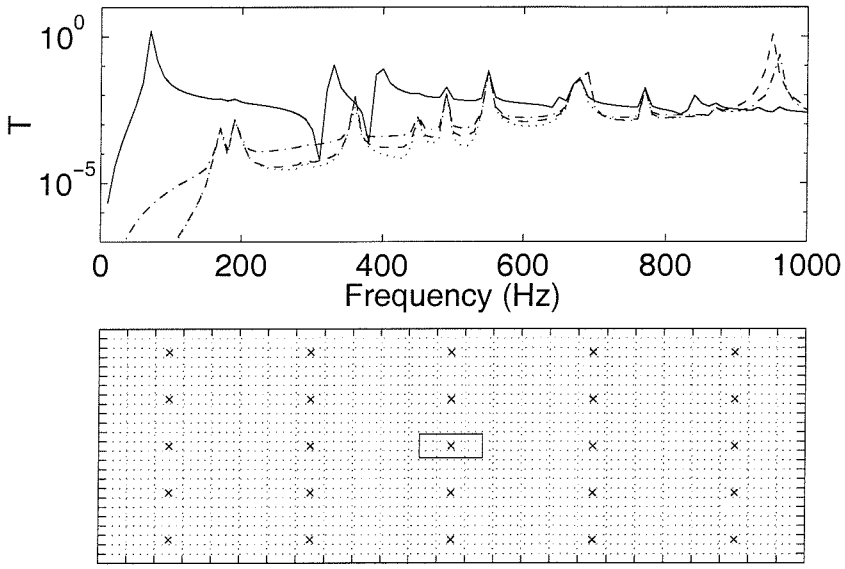

(d)

Figure 6.4: Results of SISO simulations of feedforward active control showing power transmission ratio, T, of radiated sound power to incident sound power for plane wave excitation at $\theta = \phi = 45^0$ (con't): A single actuator is used to cancel the summed output from a number of accelerometers or true volume velocity or radiated power. Solid line is power transmission ratio before control, dotted after control of radiated power, dashed after control of volume velocity and dash-dot after control of summed accelerometer output.

Sensor	Attenuation in transmitted sound power (dB)
Sound power	20.2
True volume velocity	19.1
Volume velocity estimated with:	
1	-3.8
9	14.0
16	18.1
25	18.3
400	19.1

Table 6.2: Table of attenuations in sound power over a $500Hz$ bandwidth for different control strategies and different arrangements of accelerometers used in the estimate of volume velocity.

The results for the control of radiated power and the control of volume velocity with a single piezoceramic actuator remain constant in figures 6.4(a) through to 6.4(d), as these two strategies depend only on the actuator configuration which remains the same. The aim of these figures is to see if, by increasing the number of accelerometers, a good estimate of the volume velocity can be obtained.

The first subfigure 6.4(a) shows the results where only a single accelerometer is used. The curve showing the sound transmission after control using the accelerometer differs greatly from that showing the sound transmission before control but no significant reduction in the power transmission ratio takes place. It has been shown above that the single accelerometer alters the dynamics of the plate. Although this is straightforward to interpret physically with a single accelerometer, when multiple accelerometers are used, the changed dynamic properties are not so easy to predict. The use of 4 equally-spaced accelerometers was also tested in simulations and had a similar effect to the single accelerometer i.e. the dynamics of the plate being completely changed. The sum of the charge outputs of the four accelerometers after control is always zero but the output of any individual sensor is not zero. When the disturbance on the plate is symmetric (for instance an incident wave travelling along the normal to the plate), then the output from each individual sensor is also zero. However, this is not normally the case and so the plate is forced to vibrate in ways which are difficult to predict.

The next subfigure, 6.4(b), shows the use of 9 equally-spaced accelerometers. Figure 6.5 shows the amplitudes of the radiation and structural modes before and after control at two frequencies

($326Hz$ and $820Hz$) with nine accelerometers, and these graphs can be again used to explain the physical mechanisms of control when different cost functions are minimised. Figure 6.5(a) shows the amplitudes of the structural modes of the plate when driven at $326Hz$, the natural frequency of $(3,1)$ mode, before and after control using the various control strategies. It is evident that all three control strategies reduce the amplitude of the $(3,1)$ mode (structural mode number 5). This is modal suppression as described above. Figure 6.5(b) shows the attenuation in the power radiated by each individual radiation mode at the same frequency after the different types of control. Control of volume velocity is again seen to reduce the amplitude of the first radiation mode very efficiently. Controlling the radiated sound power is seen to give very similar reductions in the amplitudes of the radiation modes and results in a slightly increased attenution relative to the control of volume velocity. The other two subfigures show the same graphs for a higher frequency of $820Hz$. It is clear from figure 6.5(c) that at these high frequencies, the different control strategies have little effect on the structural mode amplitudes and there is little attenuation at these frequencies. Figure 6.5(d) shows spillover in the radiation modes after control. For example, in reducing the volume velocity at 820Hz, the power radiated by some higher order radiation modes is increased.

With the use of sixteen or twenty-five accelerometers, figure 6.4(c) or 6.4(d), it becomes clear that a variable similar to the volume velocity is being controlled. The graphs show that at low frequencies, the control of volume velocity is still working better. At high frequencies, there is somewhat less spillover using the accelerometers. Figure 6.6 shows the vibration distributions at $600Hz$ after the control of various cost functions, and the effects of spillover can be seen clearly; in each case, the velocity distribution of the plate after control shows much larger amplitudes than before control. An estimate of the kinetic energy of the plate, equation (6.3), before and after the different types of control is shown in figure 6.7. The figure again shows that after each of the different control strategies, there is a large amount of spillover in the vibration levels of the plate and this indicates the difference between pure vibration control and active structural acoustic control; instead of simply reducing the vibrations, in ASAC, the plate is made to vibrate in a less efficient way. For example, at a frequency of $600Hz$, for the single actuator and 16 accelerometer case described above and shown in figures 6.6 and 6.7, the vibrational energy levels are seen to be increased for all three control strategies. At the same frequency the radiated sound power after each control strategy is reduced and so it is evident that modal restructuring is taking place.

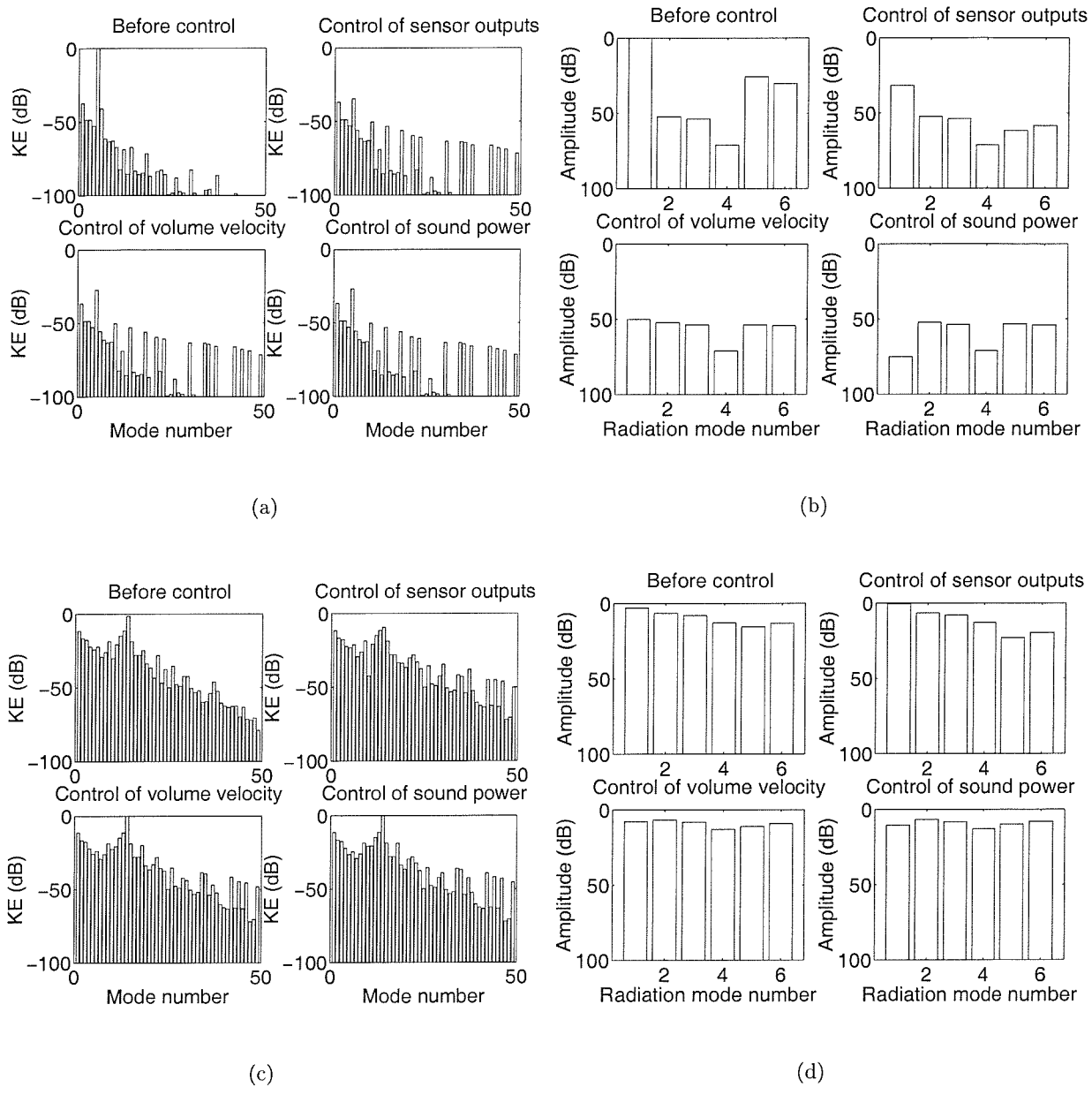

Figure 6.5: Effects of control on structural mode amplitudes and radiation mode amplitudes using a single actuator and nine accelerometers. a) Structural mode amplitudes before and after control at 326Hz (KE is kinetic energy). b) Amplitudes of radiation mode powers before and after control at 326Hz (dB relative to total power radiated before control). c) Structural mode amplitudes before and after control at 820Hz. d) Amplitudes of radiation mode powers before and after control at 820Hz.

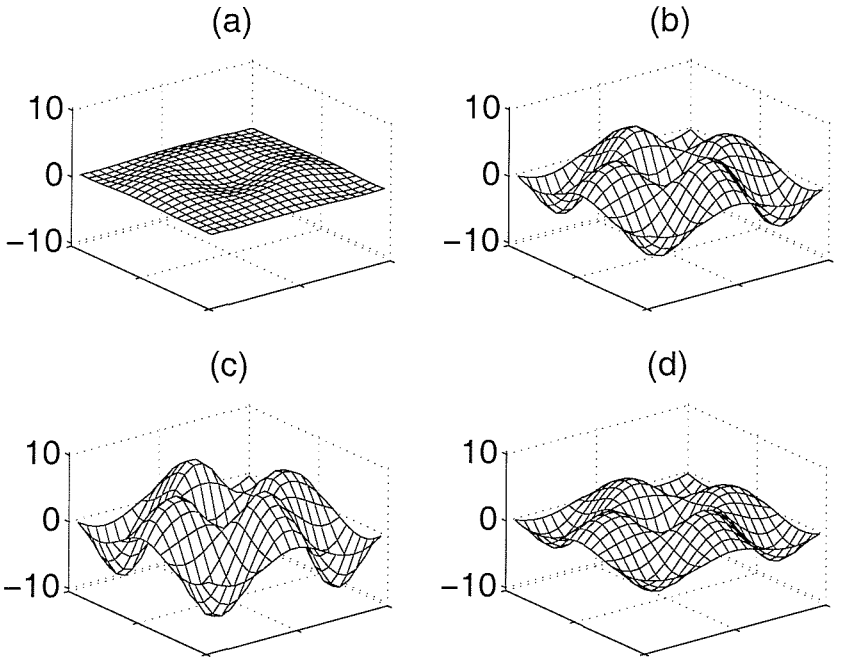

Figure 6.6: Vibration distribution of plate before and after cancellation of various sensor outputs at $600Hz$ with a single actuator. a) before control b) after feedforward control of volume velocity c) after feedforward control of sound power d) after feedforward control of summed outputs of 16 accelerometers

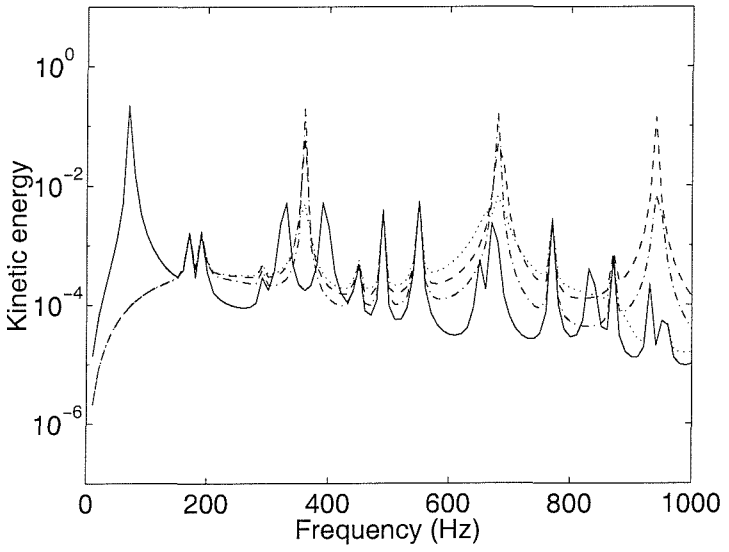

Figure 6.7: Kinetic energy of the plate before and after different types of feedforward control with a single actuator. The solid line shows the kinetic energy before control, the dashed line after control of volume velocity, the dotted line after control of sound power, and the dash-dot line after control of sum of sixteen accelerometer outputs.

Figure 6.8 shows the attenuation in radiated sound power as a function of the number of accelerometers for one particular incident wave and configuration of actuators (a single actuator and a plane wave incident with angles $\theta = \phi = 45^o$ averaged over a $500Hz$ and $1kHz$ frequency range). It is evident that by increasing the number of accelerometers, the attenuation tends to the use of a true volume velocity sensor. In the limit, where the number of accelerometers is equal to the number of elements used in the plate model, the attenuations for the two methods are the same. Although there are differences in the attenuations over these two frequency ranges, the configuration using 16 accelerometers works particularly well. Over a $1kHz$ bandwidth, high frequency enhancements are reduced by having fewer accelerometers and hence there is more overall attenuation than with a larger number of accelerometers as shown in figure 6.8(b) and discussed by Sors and Elliott [2].

An estimate of the number of accelerometers required to give a reasonable practical estimate of volume velocity can be obtained by calculating the number of structural modes with natural frequencies below the frequency for which the radiation efficiency of all the radiation modes becomes similar. Figure 3.6 shows that the radiation efficiencies of the radiation modes become similar at around $kl_x = 10$, which thus sets the upper frequency limit for which volume velocity control alone can be used, and figure 6.9 shows that for the plate considered above, the number of structural modes with a natural frequency below $kl_x = 10$ is in the region of 20 to 25. In order to estimate the volume velocity for the N'th mode, approximately N accelerometers are required, which explains why around 16 to 25 is a good estimate for the number of required accelerometers to estimate volume velocity in this case.

In general, the number of modes with natural frequencies below ω for a flat homogeneous plate of dimensions l_x, l_y, mass per unit area m, and bending stiffness D is approximately [97]

$$N(\omega) = \frac{l_x l_y}{4\pi}\sqrt{\frac{m}{D}}\omega \tag{6.4}$$

If the number of accelerometers is equal to the number of modes when $kl_x = 10$ i.e. $\omega = \frac{10c_0}{l_x}$ where c_0 is the speed of sound, then the required number of accelerometers is

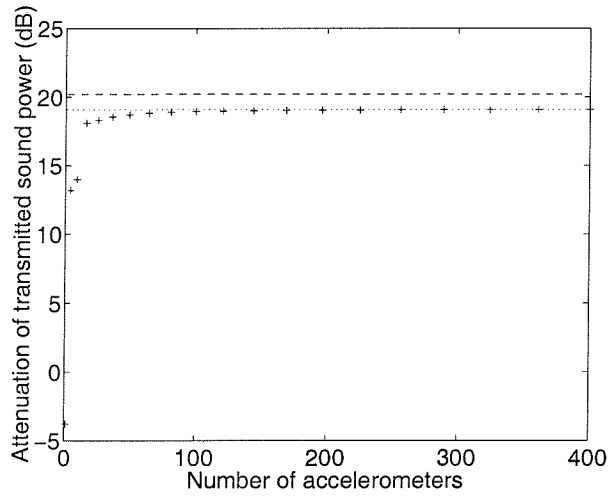

(a)

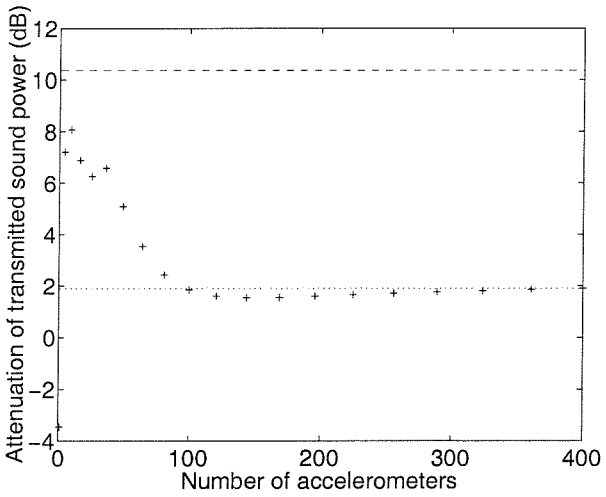

(b)

Figure 6.8: Attenuation in sound power radiated as a function of number of accelerometers for a feedforward active control system using a single central piezoceramic patch actuator to cancel the summed output of increasing numbers of accelerometers. Dashed line represents control of radiated power, dotted line represents control of volume velocity. a) Averaged over $500Hz$ b) Averaged over $1kHz$

$$N = \frac{5}{3\pi} c_0 l_y \sqrt{\frac{m}{D}} \tag{6.5}$$

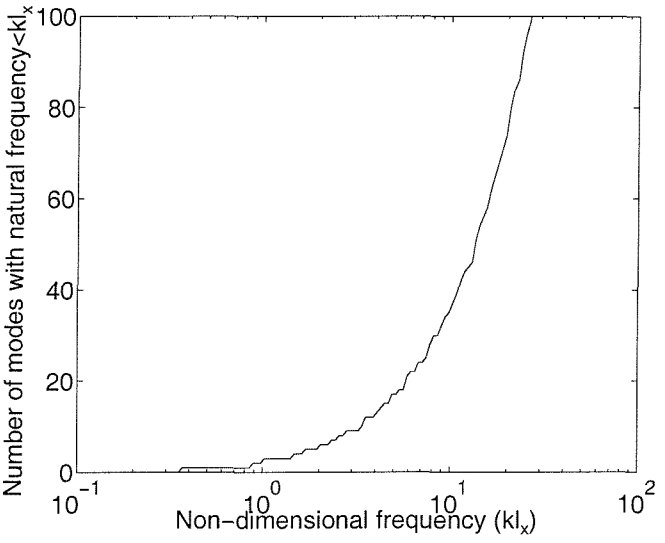

Figure 6.9: Number of structural modes with natural frequency under a given frequency for the simply-supported plate considered above.

6.4.2 Other cost functions with multiple accelerometers

The previous sections have focused on SISO control where all actuators were driven with the same voltage and where the outputs of multiple sensors were summed to give a single error signal. The investigations using a number of accelerometers have also shown their potential as sensors and that they can provide a signal which approximates that of a volume velocity sensor.

With multiple structural sensors, there is the possibility of other multi-channel control strategies where the outputs of the accelerometers are not simply summed but manipulated in some other way to obtain the error or reference signal. Similarly, each of the actuators on the plate can be driven with a separate control signal rather than driving all with the same control voltage. This then leads to MIMO control which has not been considered previously in this thesis. The subject of MIMO control is reviewed in a number of books [11, 80]. Many of the control algorithms are beyond the scope of this thesis and so, only some basic methods are outlined below. The methods described include MIMO feedforward control which can be solved using conventional Wiener techniques. This least squares method of control is found to be better

suited to vibration control than ASAC. Another control method used below is the control of multiple radiation modes, rather than just the volume velocity. As the volume velocity of the plate is so dominant in the frequency ranges used in this thesis, these methods are shown to have little advantage. Considering the changing shape of the first radiation mode results in minor improvements in performance relative to the control of volume velocity. A third MIMO approach is discussed in section 6.5 where a number of local control systems are used on the plate.

Multi-channel feedforward control is described in [11]. The system response can be represented by

$$\boldsymbol{e} = \boldsymbol{d} + \boldsymbol{G}\boldsymbol{u} \tag{6.6}$$

(c.f. equation 4.57), where $\boldsymbol{e}$ is a vector of L error signals where each component relates to a different, independent sensor, $\boldsymbol{d}$ is the vector of sensor outputs due to the primary disturbance only, $\boldsymbol{G}$ is an LxM matrix of transfer responses between the M actuators and the L sensors and $\boldsymbol{u}$ is the vector of input voltages to the actuators. The disturbance is again assumed to be at a single frequency and all acoustic and electroacoustic parts of the control system are assumed to be linear. It is assumed that a reference signal at the excitation frequency, ω, is available.

The complex input voltages to the M actuators are then adjusted to minimise the sum of squared outputs from the L sensors. The cost function in this case is given by

$$J = \sum_{l=1}^{L} |e_l|^2 = \boldsymbol{e}^H \boldsymbol{e} \tag{6.7}$$

which, after substituting equation (6.6) results in the Hermitian quadratic form

$$J = \boldsymbol{d}^H \boldsymbol{d} + \boldsymbol{d}^H \boldsymbol{G}\boldsymbol{u} + \boldsymbol{u}^H \boldsymbol{G}^H \boldsymbol{d} + \boldsymbol{u}^H \boldsymbol{G}^H \boldsymbol{G}\boldsymbol{u} \tag{6.8}$$

(c.f. equation 4.58).

The error surface is a $2M+1$ dimensional surface with a unique minimum which can be found by varying the real and imaginary parts of all the complex control voltages

Three cases of solution exist depending on the number of independent actuators and sensors:

fully determined where $L = M$. The matrix $\boldsymbol{G}$ is assumed to be non-singular and the optimal set of control voltages is given by

$$\boldsymbol{u}_{opt} = -\boldsymbol{G}^{-1}\boldsymbol{d} \tag{6.9}$$

This solution drives each of the individual error signals to zero. In practice however, this may result in large increases in the controlled field away from the control points i.e. spillover.

overdetermined where there are more sensors than actuators i.e. $L > M$. There are more equations to solve than unknowns and, provided that $\boldsymbol{G}^H\boldsymbol{G}$ is positive definite, then the vector of secondary control voltages which minimises the cost function is given by

$$\boldsymbol{u}_{opt} = -\left(\boldsymbol{G}^H\boldsymbol{G}\right)^{-1}\boldsymbol{G}^H\boldsymbol{d} \tag{6.10}$$

This case is the most commonly occuring in practice and results in the maximum amount of minimisation of the error which can be achieved with the system, but not complete cancellation.

underdetermined where the number of error sensors is less than the number of secondary controllers i.e. $L < M$. In this case, there are more unknowns than there are equations to solve and as a result of this, there are an infinite number of solutions. A constraint is normally then included in the cost function and this is often chosen to be the control effort calculated as the sum of the squared input voltages. The problem becomes one of constrained optimisation which can be solved using Lagrange multipliers [11]. A new cost function is formed such that

$$J = \boldsymbol{u}^H\boldsymbol{u} + (\boldsymbol{d}+\boldsymbol{G}\boldsymbol{u})^H\boldsymbol{\lambda} + \boldsymbol{\lambda}^H(\boldsymbol{d}+\boldsymbol{G}\boldsymbol{u}) \tag{6.11}$$

where $\boldsymbol{\lambda}$ is a vector of complex Lagrange multipliers. the solution to this problem is given by

$$\boldsymbol{u}_{opt} = -\boldsymbol{G}^H\left(\boldsymbol{G}\boldsymbol{G}^H\right)^{-1}\boldsymbol{d} \tag{6.12}$$

This type of constrained optimisation problem is rarely encountered in practice but can have advantages if cost, as well as performance, is an important consideration. As an example, the total power required by two loudspeakers to cancel the sound at an equidistant point is half the power required from a single loudspeaker to achieve the same control. If the control effort is expressed in terms of the total power dissipated in the loudspeakers (or equivalently, piezoceramic actuators), the power dissipated in each individual actuator being given by $u_i^2 R$, where R is the impedance and is assumed to be the same for each actuator, the total power dissipated can be expressed as

$$\text{Effort (=power)} = R \sum_{i=1}^{n_{ac}} u_i^2 \tag{6.13}$$

where n_{ac} is the number of actuators. For a large number of symmetric actuators, the individual input forces, f_i, must be the same and their sum must be equal to the total force, so that

$$F_{tot} = n_{ac} f_i \tag{6.14}$$

the control signals are proportional to the input forces and are thus

$$u_i \propto f_i = \frac{F_{tot}}{n_{ac}} \tag{6.15}$$

After substituting equation (6.15) into (6.13), the total effort is seen to reduce with an increasing number of actuators (for example the total effort is halved for two symmetric actuators). This is described further in [11].

Examples of the three different types of feedforward control problem described above (fully-determined, overdetermined, and underdetermined) are shown in figure 6.10. The first subfigure, 6.10(a), shows the results when four actuators are independently controlled to minimise the sum of the mean squared errors from four accelerometers i.e. the fully-determined case. The results resemble those in figure 6.4(a) and it is seen that the dynamics of the plate are again changed and no advantage is to be gained by controlling the actuators independently. Note that minimising the sum of squared outputs of the accelerometers is not equivalent to minimising the sum of

the outputs squared (i.e. the approximation to the volume velocity), as described in appendix B which gives a common formulation for comparing these two methods. In figure 6.10(b) which shows the results for nine independent accelerometers and four independent piezoceramic actuators, the cost function (sum of squared errors) is being minimised but the reduction in radiated sound power is relatively small. The mean square error is not a good representation of the radiated sound power. Finally, figure 6.10(c) shows the underdetermined case where four actuators are used to minimise the mean squared output of one accelerometer with mimimum effort. Figure 6.11 shows an estimate of the kinetic energy of the plate, equation (6.3), before and after feedforward control in the overdetermined case compared to the feedforward control of radiated sound power or volume velocity. Control of volume velocity and of radiated power lead to large amounts of spillover in the vibration levels of the plate indicating the difference between active structural acoustic control and vibration control as shown in figure 6.7. In the overdetermined case however, where four actuators are used to minimise the sum of squared outputs from nine accelerometers, there is hardly any spillover in the vibration levels of the plate which would indicate that the latter technique is in fact, a form of vibration control.

Figure 6.12 shows the attenuations in radiated sound power from an additional feedforward MIMO control strategy. It shows the control of sound power for a MIMO system in which five independently controlled actuators are used to minimise the far-field pressure, where it is assumed that this can be measured perfectly with microphones. The equations used are similar to those in equation (4.57) where, this time, $\boldsymbol{g}$ is an M by (*number of elements in plate model*) matrix (instead of a vector), and $\boldsymbol{u}$ contains the M complex control voltages. This equation can then be solved in the same way equation (4.60) (provided the matrix $\boldsymbol{A} = \boldsymbol{g}^H \boldsymbol{R} \boldsymbol{g}$ is well-conditioned). This graph shows that substantial improvements can be gained in MIMO control if the proper cost function is chosen and if complete knowledge of the radiated pressure field is available.

A modified sensing strategy could involve the control of multiple radiation modes and table 6.3 gives the additional reductions in sound power radiation up to $1kHZ$ obtained when other higher order radiation modes are controlled with a feedforward control system with a single centrally-placed piezoceramic actuator. These can be calculated easily using equation (3.47) in section 3.2.3 where the eigenvalue λ_i can be found from the relevant value of the decomposition of the matrix $\boldsymbol{R}$ (see equation 3.34) and gives the power radiated by the corresponding radiation mode. The small values indicate that, at the frequencies considered, it is far more important

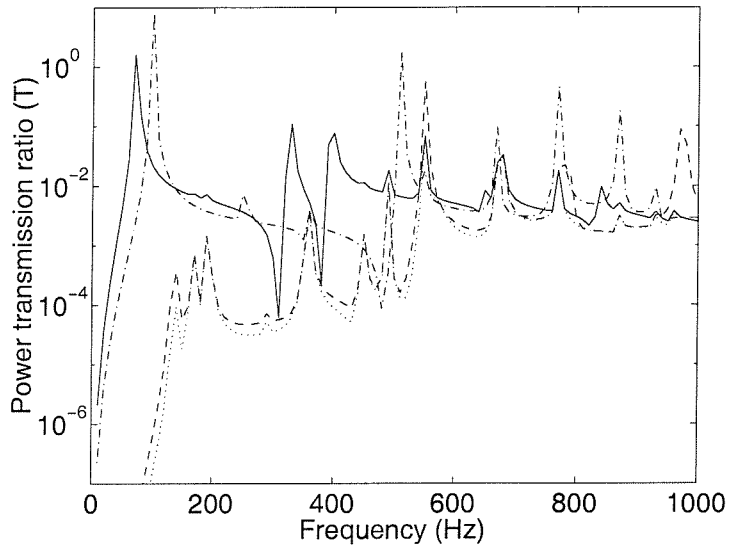

(a)

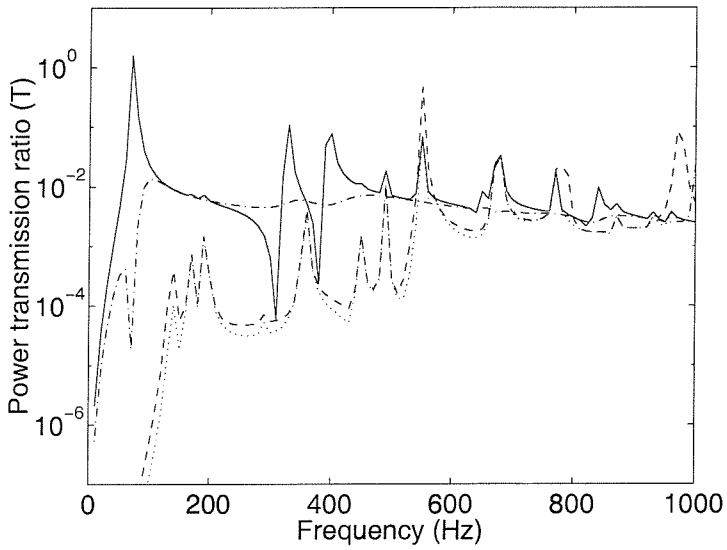

(b)

Figure 6.10: Examples of three different types of feedforward MIMO control problems in which sum of squared outputs of accelerometers are minimised by different numbers of actuators. Solid line shows power transmission ratio (T) before control, dotted line after control of sound power, dashed line shows control of volume velocity and dash-dot line shows control of accelerometer outputs. a) Fully-determined: Four actuators and four sensors. b) Overdetermined: Four actuators and nine sensors.

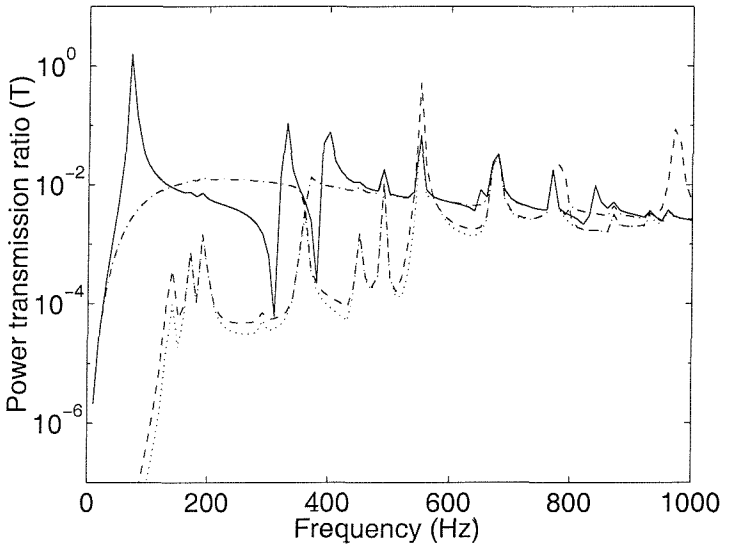

(c)

Figure 6.10: (con't) Examples of three different types of feedforward MIMO control problems in which sum of squared outputs of accelerometers are minimised by different numbers of actuators. Solid line shows power transmission ratio (T) before control, dotted line after control of sound power, dashed line shows control of volume velocity and dash-dot line shows control of accelerometer outputs. c) Underdetermined: Four actuators and one centrally-placed sensor

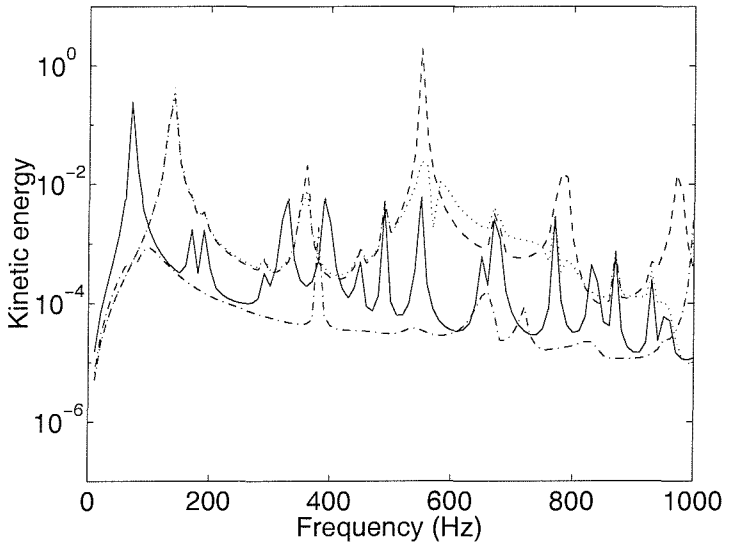

Figure 6.11: Kinetic energy of plate before and after different types of control (four actuators and nine accelerometers). Solid line show kinetic energy before control, dotted line after control of sound power, dashed line after control of volume velocity and dash-dot after control of nine accelerometers.

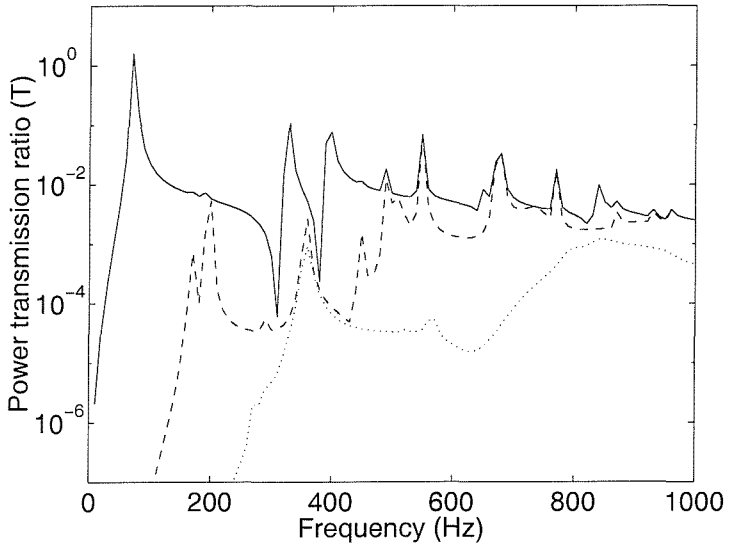

Figure 6.12: Improved MIMO control strategy using a MIMO feedforward system with 5 actuators to reduce radiated power directly (assuming this can be measured). SIMO (dashed line) refers to all actuators driven with same amplitude and phase. MIMO (dotted line) refers to actuators driven independently.

to control the first radiation mode as well as possible than to consider higher order radiation modes.

Radiation mode	Order	Additional reduction in sound power (dB)
1	1	11.3
2	2	0.1
3	2	0.1
4	2	< 0.1
5	3	< 0.1
6	3	< 0.1
7	3	< 0.1

Table 6.3: Reduction in the average power radiated below $1kHz$ when different numbers of radiation modes are controlled.

A final strategy thus examines controlling the frequency-dependent shape of the first radiation mode instead of the volume velocity which is an approximation to the shape of the first radiation mode at low frequencies. The shape was seen to change significantly over a $1kHz$ frequency range in figure 3.8. The following analysis deals with how the multiple accelerometers can best be used to control the first radiation mode in practice and relies on the fact that the radiation mode shapes can be obtained from the eigenvalue/eigenvector decomposition of the matrix $\boldsymbol{R}$. The position of each accelerometer for a given radiation mode at a given frequency can then be calculated and stored in a frequency dependent weighting for the accelerometer instead of using a weighting of unity for each accelerometer, which would be equivalent to minimising the approximation to the volume velocity. As an example, consider an arrangement with four accelerometers used to calculate the ampltiude of the first radiation mode y_1: the weightings for each of the accelerometers at each frequency can be found from the relevant elements of the first eigenfunction of $\boldsymbol{R}$ that

$$y_1(\omega) = \frac{1}{4}\left(Q_1(\omega)v_1 + Q_2(\omega)v_2 + Q_3(\omega)v_3 + Q_4(\omega)v_4\right) \tag{6.16}$$

where $Q_1(\omega)$ refers to the element of the first eigenfunction of $\boldsymbol{R}$ corresponding to the position of the first accelerometer, v_1 corresponds to the velocity at the point of the first acceleromter, etc.

A comparison of the control of volume velocity, an approximation to the volume velocity using sixteen accelerometers, and an approximation to the first radiation mode using sixteen accelerometers, is shown in figure 6.13. Controlling an approximation to the first radiation mode using the sixteen accelerometers rather than an approximation to the volume velocity itself using sixteen accelerometers is seen to give some performance increase in the mid-frequency range, particularly at frequencies away from resonances.

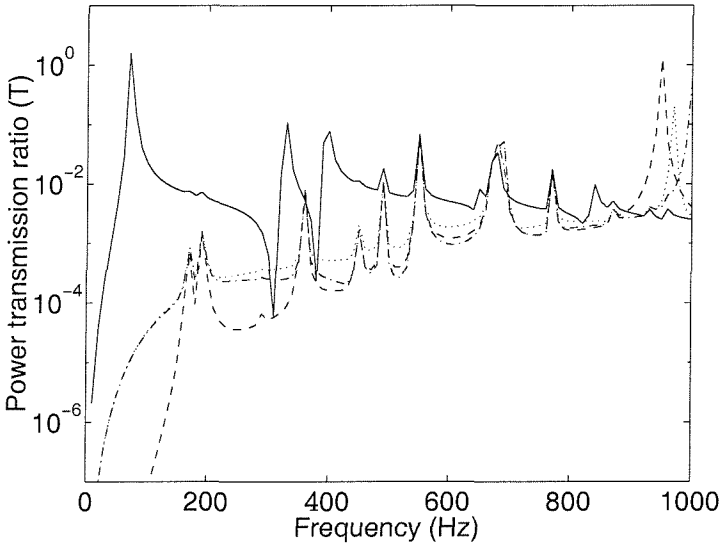

Figure 6.13: Simulations of feedforward control in which a single actuator is used to minimise the output of either a true volume velocity sensor (dashed line), summed output of sixteen accelerometers i.e. approximation to volume velocity (dotted line), or approximation to first radiation mode using sixteen accelerometers (dash-dot line).

6.5 Multiple single channel control systems

This section describes a new configuration for active control with a number of local control systems on a plate. Each control system consists of either a collocated force actuator and velocity sensor, or a piezoceramic patch actuator and a collocated velocity sensor as shown in figure 6.14. In practice a velocity estimate can be obtained by integrating an accelerometer output. A number of these local control systems can be placed on the plate as shown in figure 6.15 and the results can be consistently compared with the control strategy used above by summing the outputs of the sensors and driving the actuators in phase with a SISO controller. This configuration of actuators and sensors could potentially be implemented using microelectromechanical

systems (MEMS) which is currently an area of rapid development [98, 99]. These MEMS could offer a low-cost and practical method of implementing this sort of control arrangement.

Care must first be taken to ensure modal convergence in the plate models as the sensors are very close to the actuators and so subject to their near field effects. Figure 6.16 shows the amplitude of the frequency response measured between a point force or piezoceramic actuator and a collocated velocity sensor at the centre of the plate for a frequency of $300Hz$ as a function of the number of modes used in the model of the plate. With around 300 modes, which could be obtained by setting $M = N = 17$ for example, both sets of frequency responses are seen to be within around 1% of their convergence value.

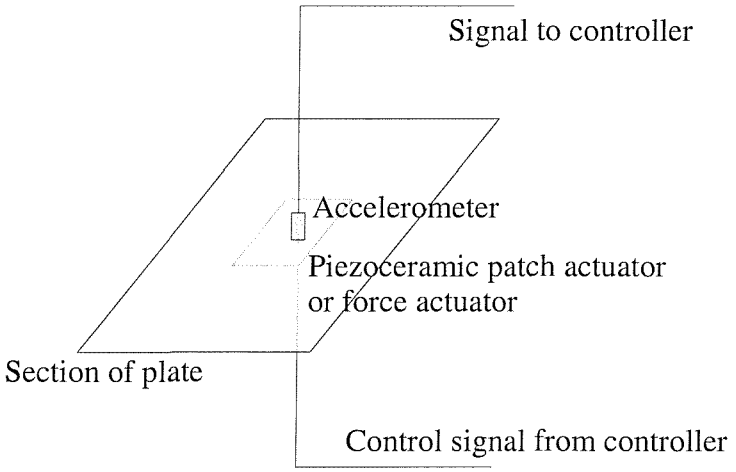

Figure 6.14: A single local control system

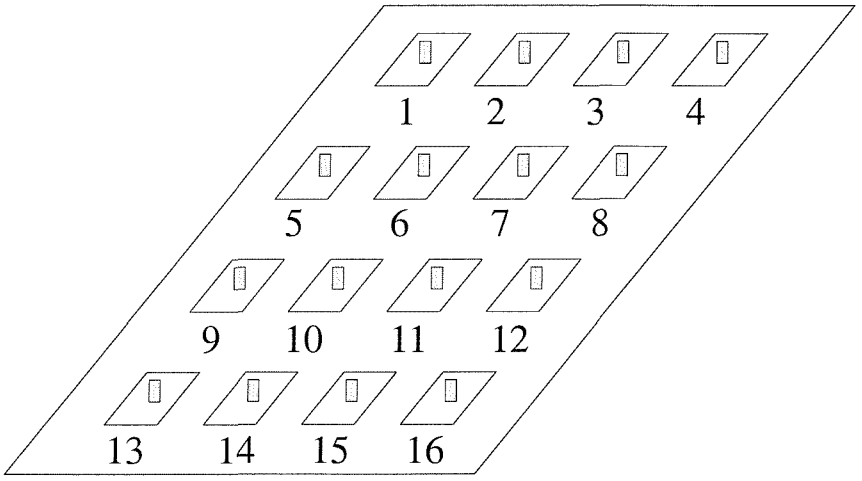

Figure 6.15: Multiple single channel control systems on a plate with numbering system

The plate models described previously (chapter 3) are used to determine the response of the sensors due to excitation by either the primary disturbance or the secondary actuators. The

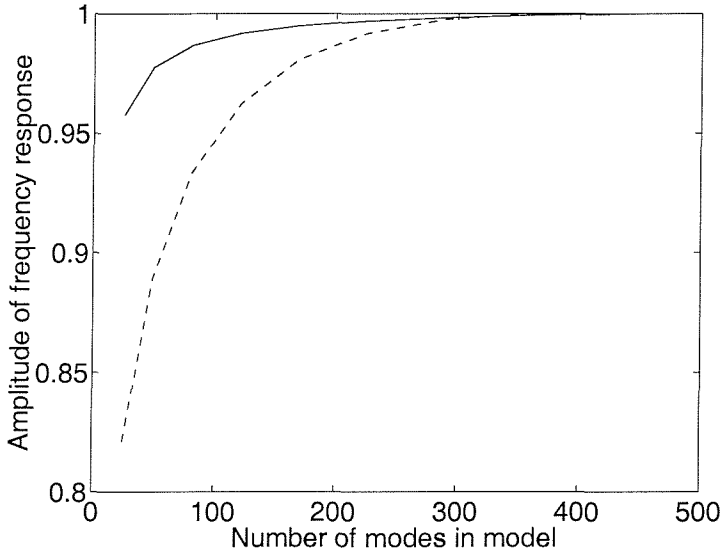

Figure 6.16: Normalised amplitude of frequency response function at $300Hz$ between a central point force (solid line) or piezoceramic actuator (dashed line) and a collocated velocity sensor as a function of number of modes in the simulation. The responses are seen to converge at around 300 modes.

disturbance is again assumed to be a plane wave with angles of incidence $\theta = \phi = \pi/4$. The multiple control systems are designed to minimise the output of the collocated velocity sensors. The frequency response between a single force actuator and a collocated velocity sensor must have an entirely positive real part since the plate itself is a passive system. If a constant gain feedback controller is used then this is unconditionally stable [27], and this property extends to multiple collocated force actuators and velocity sensors [100].

Two sets of figures are shown below, but in each case, the same plate is used and 16 collocated actuator and sensors are positioned on the plate. In the first set of figures, point forces are assumed and in the second set, piezoceramic patch actuators are assumed. The 16 local control systems are then grouped into the following configurations as shown in figure 6.17:

Single channel equivalent to controlling the approximation to the volume velocity with all the actuators driven by the same control system so that $u_1 = u_2 = \ldots = u_N$ are driven to cancel $e_1 + e_2 + \ldots + e_N$.

Four channels Actuators and sensors are grouped together in four groups: group 1 (1,2,5,6), group 2 (3,4,7,8), group 3 (9,10,13,14) and group 4 (11,12,15,16) and each set of actuators

is driven in phase to cancel the sum of the outputs of the corresponding sensors.

Sixteen channels Where all the actuators control their corresponding collocated accelerometer so that actuator 1 controls accelerometer 1, etc.

The power transmission ratio and kinetic energy resulting from these control strategies are shown for the two different sets of actuators i.e. the point force actuators and the piezoceramic patch actuators in figures 6.18 and 6.19.

The case where point force inputs are used is first considered. At low frequencies (up to around $600Hz$), the performance of the system increases with the number of independent channels, both in terms of vibration control, measured by kinetic energy, and in terms of the sound power transmission ratio. Figure 6.18(b) shows that with one or four independent control systems, there is some spillover in the kinetic energy starting with the $(2,1)$ mode at $190Hz$ for the single channel control system or with the $(2,2)$ mode of the plate at $290Hz$ for the four channel system. This is due to a similar effect seen when using a single point force actuator with a single accelerometer; the plate is pinned and exhibits a new set of resonances. This is actually also the case for the sixteen independent channels but this effect occurs at a much higher frequency of around $600Hz$.

Where piezoceramic actuators are used, the effects are changed slightly but using the single channel system, with all the actuators driven together and all velocity outputs summed, works particularly well for controlling the sound power transmission. It is, however, unclear why controlling the sixteen velocities with sixteen piezoelectric actuators should give rise to such large increases in vibration and radiation at about $200Hz$, although the control effort, given by the sum of the squared actuator signals as shown in figure 6.20, is also large at this frequency.

The frequency response functions for the two different sets of actuators and sensors when wired as a single channel system are shown in figure 6.21. Although the FRF between the point force and the velocity sensor is guaranteed to have a positive real part i.e. within $\pm 90^0$, this feature is also found for the piezoceramic patch actuator and the velocity sensor and was found to do so up to a frequency of at least $10kHz$. This is important for feedback control where the plant frequency response function should have as little phase loss as possible as described in chapter 5.

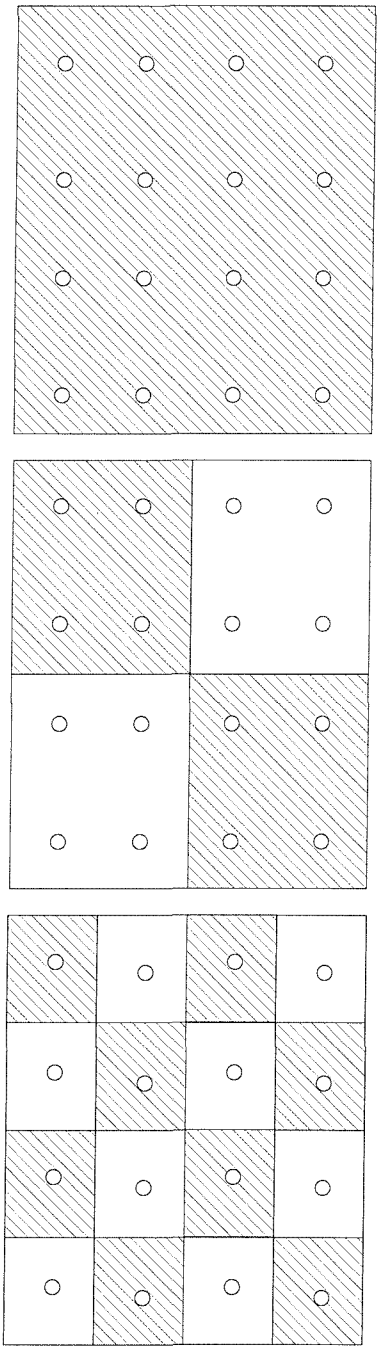

Figure 6.17: Configurations of SISO control systems used on the plate

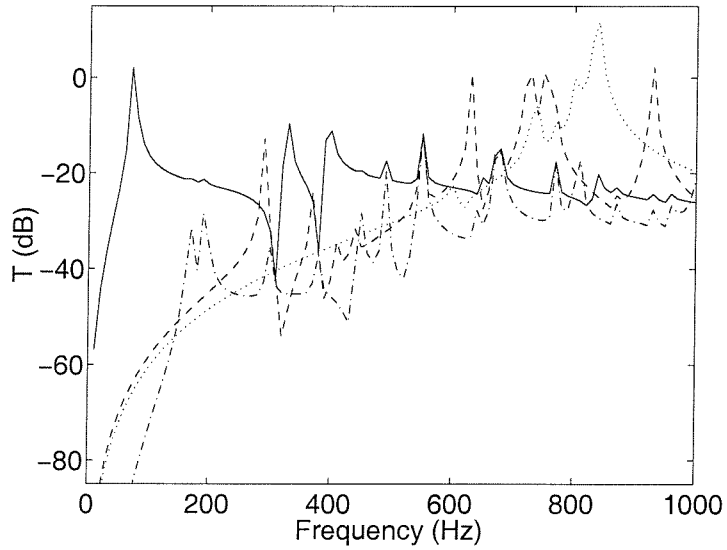

(a)

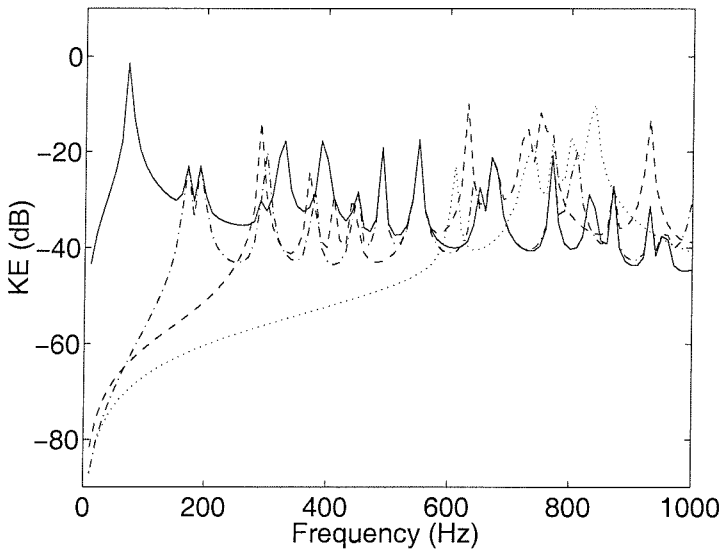

(b)

Figure 6.18: Simulations of controlling the output of 16 velocity sensors with 16 collocated point force inputs. In each case, solid line is before control, dot-dash line is after single channel control case, dashed line is after four channel control case, and dotted line is after sixteen channel control case. a) Transmission ratio. b) Kinetic energy.

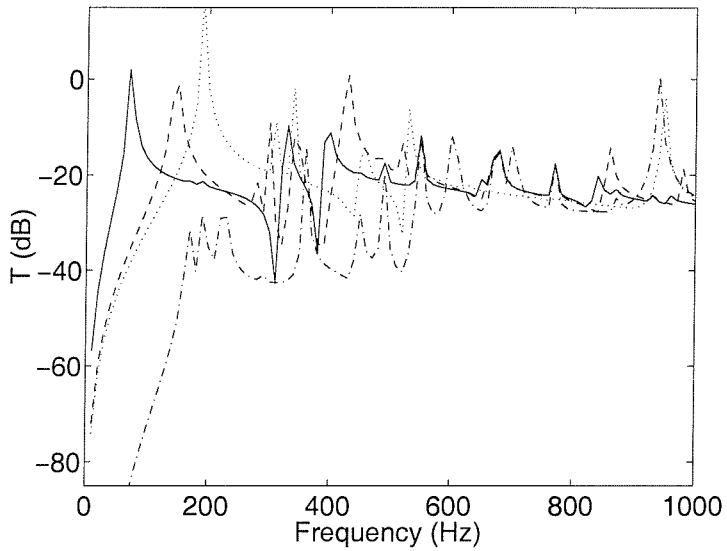

(a)

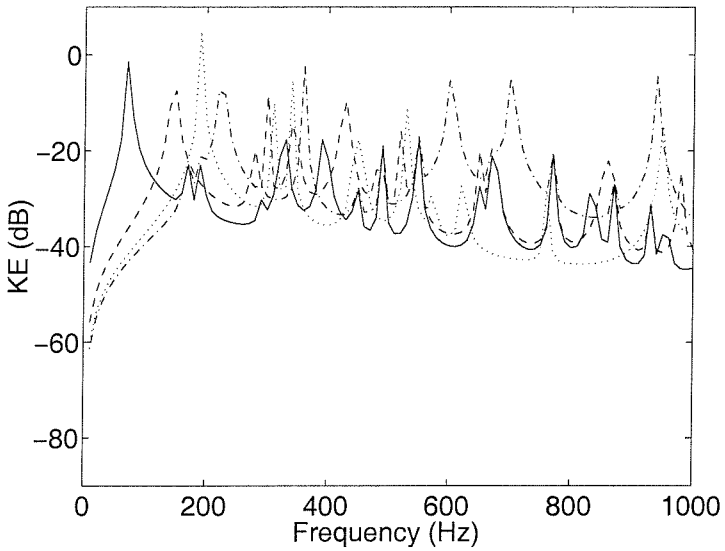

(b)

Figure 6.19: Simulations of controlling the output of 16 velocity sensors with 16 collocated piezoceramic patch actuators. In each case, solid line is before control, dot-dash line is after single channel control case, dashed line is after four channel control case, and dotted line is after sixteen channel control case. a) Transmission ratio. b) Kinetic energy.

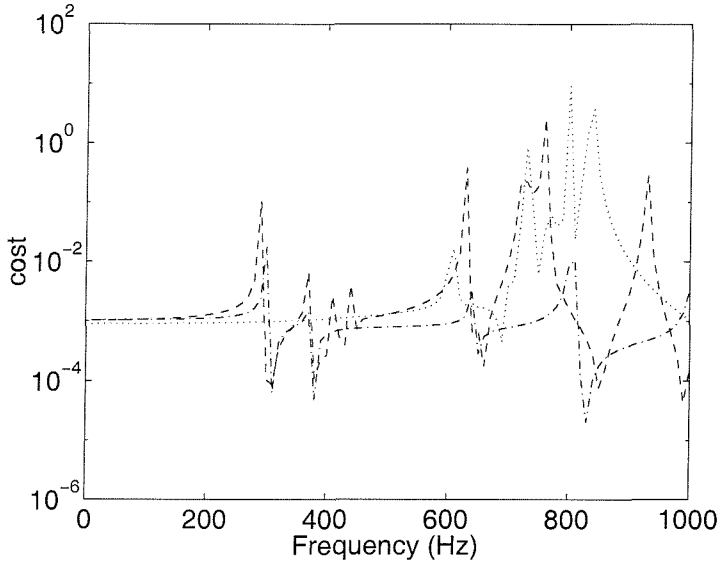

(a)

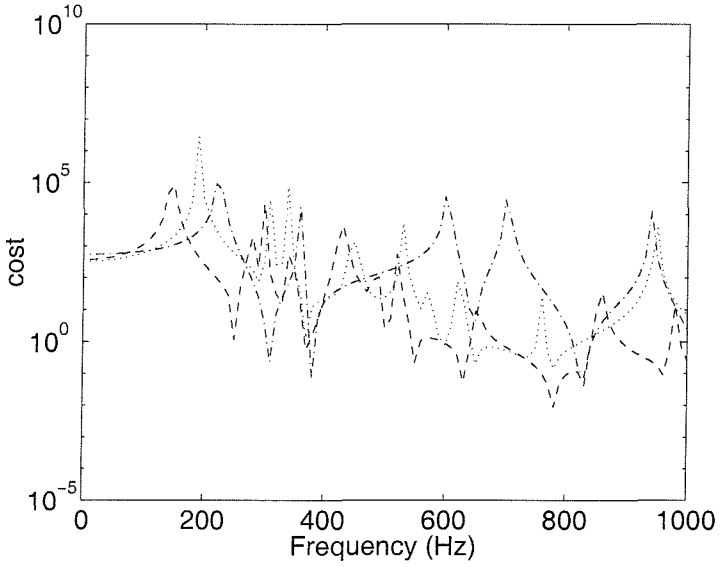

(b)

Figure 6.20: Control effort measured as sum of squared control forces. In each case, solid line is before control, dot-dash line is after single channel control case, dashed line is after four channel control case, and dotted line is after sixteen channel control case. a) 16 point forces. b) 16 piezoceramic patch actuators.

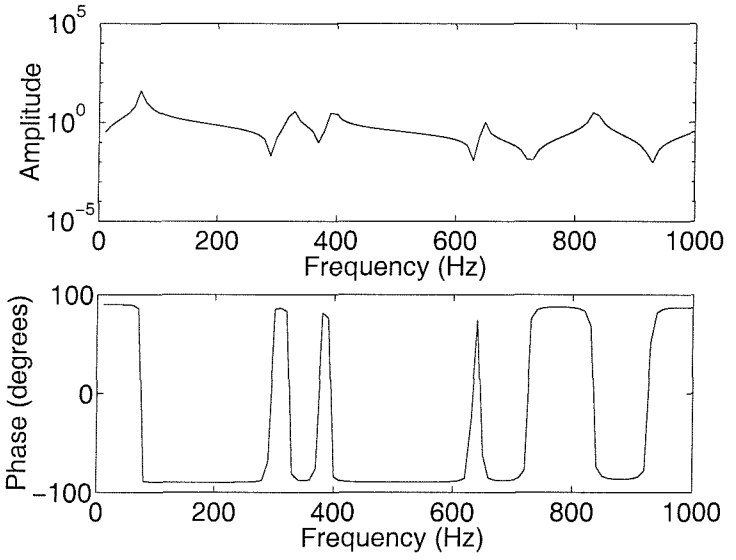

(a)

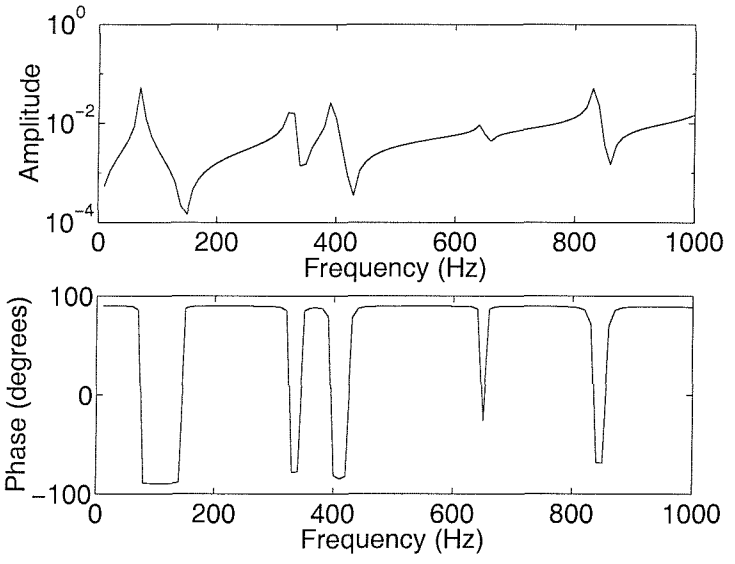

(b)

Figure 6.21: Frequency response function measured by sum of 16 accelerometer outputs. a) With 16 point forces all driven in phase. b) With 16 piezoceramic patch actuators all driven in phase.

The multiple single-channel approach is an idea which holds some potential for the future, especially as microengineered actuators and sensors become more readily available. However, some work is still needed to understand the exact control mechanisms and to work out how best to implement the method [101].

6.6 Conclusions

This chapter has examined a number of possible cost functions which can be used for ASAC purposes. The first of these were simple SISO cost functions which have been examined briefly in previous chapters. These included the control of sound power, volume velocity or an accelerometer output. A more in-depth examination of these control strategies in this chapter showed the actual mechanisms of control and how spillover can effect their performance.

Cost functions with more than one structural sensor were then investigated. In particular, a number of accelerometers were used to give an approximation to the volume velocity. This control strategy was found to result in good performance and also allowed MIMO control strategies to be investigated. A number of MIMO strategies were tested but at the frequencies considered in this thesis, it was found that none of these results in a significant performance increase compared to the approximation to the volume velocity except controlling the frequency dependent first radiation mode rather than true volume velocity. However, some of these strategies did result in good vibration control and one strategy which holds some promise for the future is to use a number of local control systems on a a structure with a simple controller on each one.

Chapter 7

Simulations of feedback control using separate reference and error sensors

This chapter considers a final set of control algorithms which use both structural and far-field sensors. These have been used separately so far, either to control an approximation to the volume velocity (or other related structural variable) or, with the far-field sensors, to control the radiated power directly. This section now considers their combined use and specifically, a feedback control system in which the structural sensors are used to provide reference signals and the microphones are used as error sensors. This approach to ASAC was suggested previously in [89] but a more in-depth analysis is presented here. A related approach is presented by Maillard and Fuller [102–106] in which the outputs of a number of structural point sensors (i.e. accelerometers) are filtered to give an estimate of the radiated sound power in a given direction or a given wave-number component over a broad frequency range. The technique described below however results in a more general control of the radiated sound power.

7.1 Development of control algorithm using separate reference and error sensors

Three main issues can be addressed in choosing suitable sensors for an ASAC system:

1. The choice of reference sensors for feedback control (this has already been considered in some detail)

2. The choice of error sensors for feedback control

3. The combinations of reference and error sensors

This chapter concentrates on the third of these issues and a number of control algorithms which could arise are shown in figure 7.1, which use Internal Model Control (IMC) to explicitly distinguish between reference sensors, which drive the controller, and error sensors, whose output is being controlled.

In each of the block diagrams shown, the purpose is to monitor the change, due to the controller, in the radiated pressure estimated by the n_{mic} microphones

$$\hat{W} = \sum_{l=1}^{n_{mic}} |p_l|^2 \tag{7.1}$$

The different formulations shown are:

1. Microphones used as both the reference and error sensors in a feedback arrangement. (Blocks $\boldsymbol{P}_{11}$ and $\boldsymbol{P}_{12}$ in figure 5.11). The normal IMC arrangement as shown in figure 7.1(a) and explained in chapter 5. It is expected that control using this method will result in poor performance due to large delays in the frequency response functions between the actuators and the microphones (due to the physical time delay for the sound to travel between the two).

2. Accelerometers used as both the reference and error sensors in a feedback arrangement. (Blocks $\boldsymbol{P}_{21}$ and $\boldsymbol{P}_{22}$ in figure 5.11). Same block diagram as above i.e. 7.1(a). Although this configuration is expected to have small amounts of delay, the performance is limited by only measuring a structural variable. This kind of control has been considered in chapter 6.

3. Using the accelerometers as reference sensors and the microphones as error sensors. (All parts of partitioned plant in figure 5.11 are used). The block diagram is shown in figure

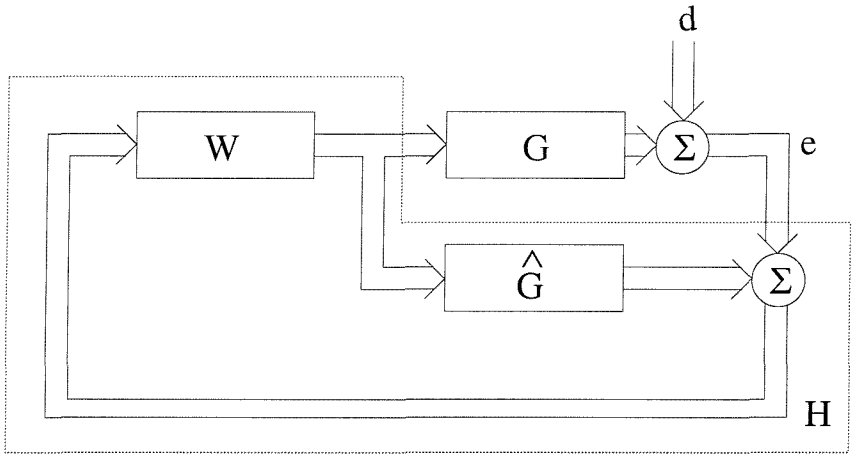

(a)

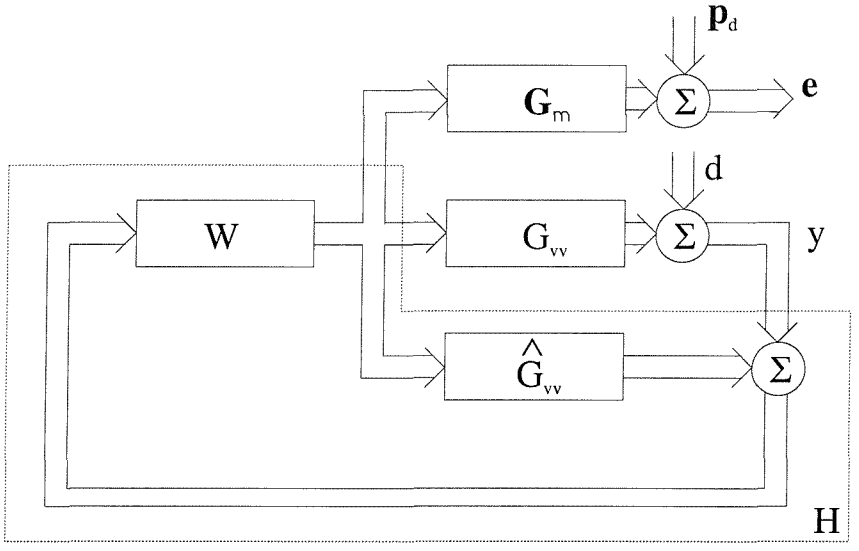

(b)

Figure 7.1: Control block diagrams. a) Normal IMC arrangement. b) Accelerometers used as reference sensors, microphones used as error sensors. G_{vv} represents FRF between actuator and summed accelerometer output and $\boldsymbol{G}_m$ represents FRF between actuator and sum of square microphone outputs.

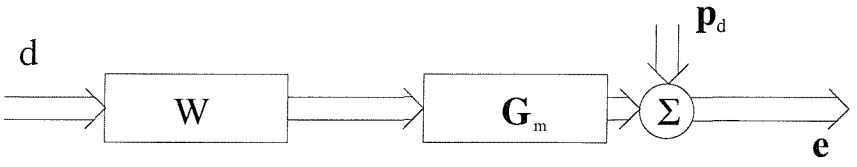

(c)

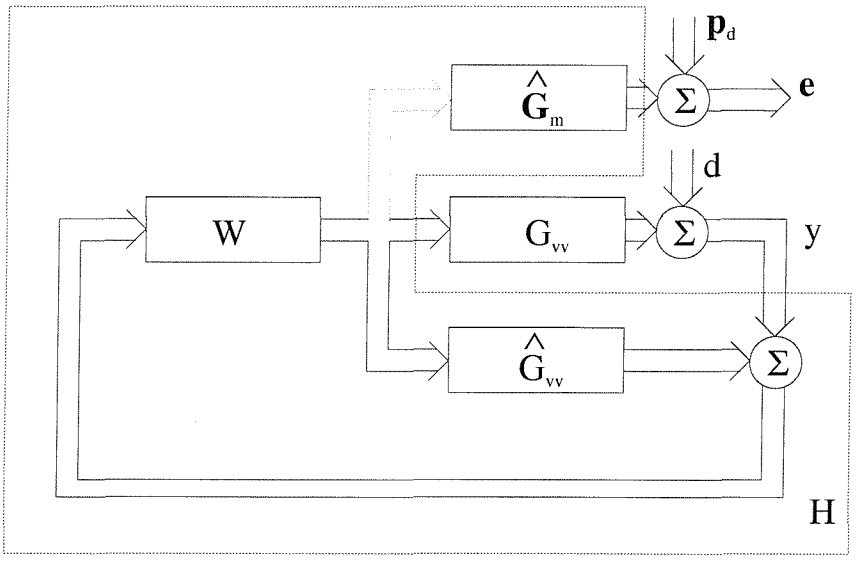

(d)

Figure 7.1: Control block diagrams (con't) c) Figure 7.1(b) rearranged as a feedforward problem. d) Accelerometers used as reference sensors, models of microphone outputs used as error signals.

7.1(b) and uses both frequency response functions between the piezoceramic actuators and the accelerometers and those between the piezoceramic actuators and the microphones. The block diagram can then be rearranged as a feedforward problem shown in figure 7.1(c). It is expected that this combination might result in good reduction of total squared pressure and this will be the technique which is analysed in detail below.

4. This could eventually lead to a final configuration (figure 7.1(d)) which starts to address the problem of practical implementation and instead of using microphones as error sensors, uses models of the frequency response functions between the actuators and microphones. This assumes that these frequency response functions can be measured once before implementation but that afterwards, the microphones are not available. Robust performance would be an important issue in this configuration.

The third technique, where separate reference and error sensors are used, is of particular interest. This technique has a similar block diagram to the conventional IMC but, in the simplified feedforward block diagram, figure 7.1(c) (c.f. figure 5.13), the plant measured between the piezoceramic actuators and the accelerometers is substituted by the plant between the piezoceramic actuators and the microphones and the aim is to design a controller $\boldsymbol{W}$ which manipulates the disturbance measured at the reference sensors $\boldsymbol{d}$ to be equal to the disturbance at the microphones $\boldsymbol{p}_d$. The new control technique is considered using simulated FRFs in this chapter and using measured data in the next chapter. In the first place, the effect of controlling the summed output of the accelerometers, as described in the previous chapter, on the microphone signals is derived. Feedback control of the summed output of accelerometers is then compared with control using separate reference and error sensors.

The experimental arrangement used in chapter 8 and simulated here is shown in figure 7.2 and the physical details are given in table 7.1. The disturbance is generated by a loudspeaker within the enclosure. Sixteen accelerometers are fixed to the plate and nine microphones are arranged in the far-field in the positions given in table 7.2. Although these positions do not correspond to ISO3745, they can still be used to calculate the radiated sound power.

The arrangement can be represented with the generalised control framework shown in figure 7.3 which is a revised version of figure 5.11. In this diagram, the small blocks represent frequency respose functions between different sets of actuators and sensors.

Property	Value
box length	$0.35m$
box width	$0.3m$
box height	$0.4m$
plate length	$0.278m$
plate width	$0.247m$
plate thickness	$1mm$
disturbance	loudspeaker placed one tenth of the way into the corner of the enclosure
secondary actuators	5 piezoceramic patch actuators
structural sensors	16 accelerometers regularly spaced on plate
acoustic sensors	9 microphones placed as shown in table 7.2

Table 7.1: Details of second experimental arrangement which is simulated in this chapter.

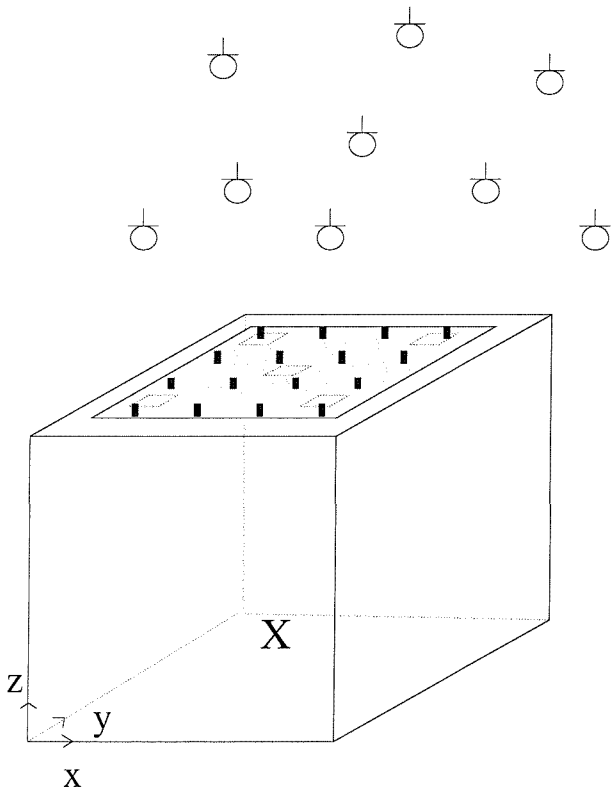

Figure 7.2: Diagram of experimental set-up. The position of the loudspeaker generating the intial disturbance is also shown.

Microphone	r	x	y	z
1	$\sqrt{1.5}$	0.5	0.5	1
2	$\sqrt{1.25}$	0	0.5	0.5
3	$\sqrt{1.25}$	-0.5	0	0.5
4	$\sqrt{1.5}$	-0.5	0.5	1
5	1	0	0	1
6	$\sqrt{1.5}$	0.5	-0.5	1
7	$\sqrt{1.25}$	0.5	0	0.5
8	$\sqrt{1.25}$	0	-0.5	0.5
9	$\sqrt{1.5}$	-0.5	-0.5	1

Table 7.2: Microphone positions for second set of experiments

$\boldsymbol{D}_m$ represents the frequency response function between the disturbance loudspeaker and the error sensors (microphones)

D_{vv} represents the frequency response function between the disturbance loudspeaker and the sum of the accelerometer outputs

$\boldsymbol{G}_m$ represents the frequency response function between the secondary piezoceramic actuator and the error sensors (microphones)

G_{vv} represents the frequency response function between the secondary piezoceramic patch actuator and the sum of the accelerometer outputs

H represents the feedback controller which is implemented by IMC

The effect of feedforward control of the summed accelerometer output on the radiated power is considered first. The total signal at the reference sensor, in this case the sum of the accelerometer signals, is given by a summation of the effects due to the disturbance $D_{vv}x$ and due to the control actuator $G_{vv}u$

$$y = D_{vv}x + G_{vv}u \tag{7.2}$$

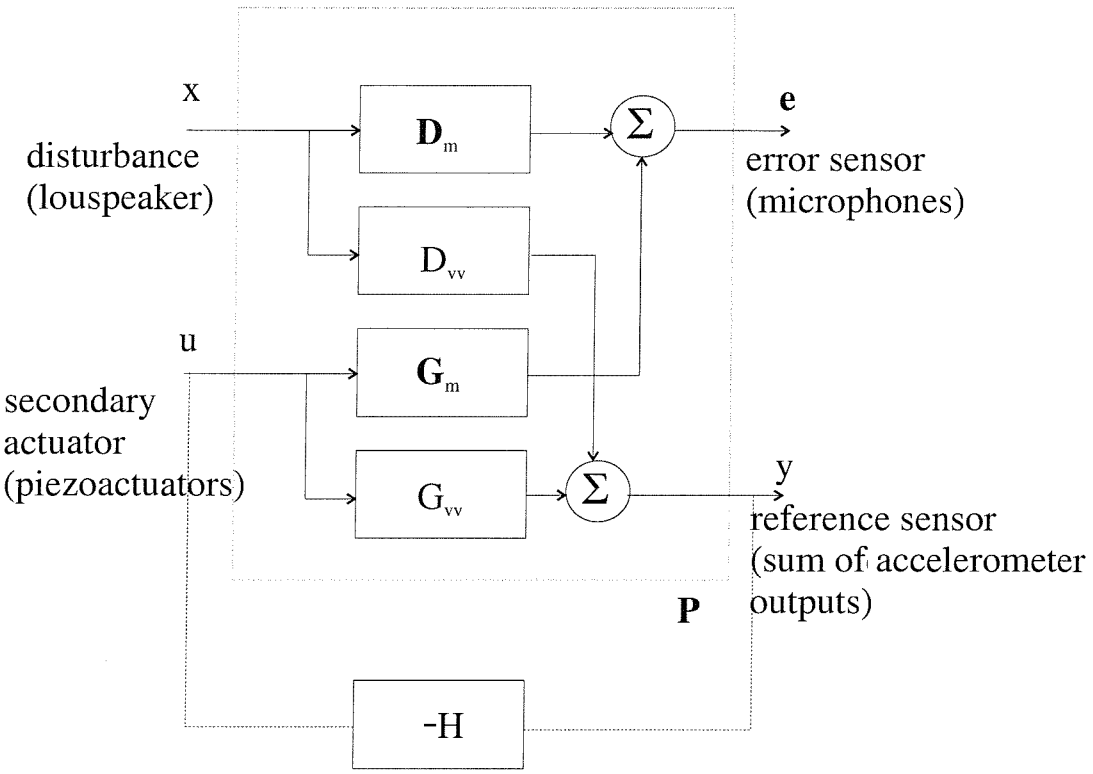

Figure 7.3: Generalised control framework block diagram

and it is evident that to cancel the error signal vv at a given frequency the control input must be set to

$$u = -\frac{D_{vv}x}{G_{vv}} \tag{7.3}$$

The signal at the reference sensors (sum of accelerometer signals) is driven to zero but the effects on radiated power are of more interest. The signal at each of the microphone positions after feedforward control can be calculated by substituting the control voltage, equation (7.3), into the equation

$$e_l = D_{ml}x + G_{ml}u \tag{7.4}$$

where l is the microphone number. This can be represented for all the microphones by the vector equation

$$\boldsymbol{e} = \boldsymbol{D}_m x + \boldsymbol{G}_m u \tag{7.5}$$

which gives the signal at the microphones as a superposition of contributions from the primary and secondary sources.

Then, for a single microphone

$$\begin{aligned} e_l &= D_{ml}x - \frac{G_{ml}D_{vv}x}{G_{vv}} \\ &= \left(D_{ml} - \frac{G_{ml}D_{vv}}{G_{vv}}\right) x \\ &= \left(1 - \frac{G_{ml}}{D_{ml}}\frac{D_{vv}}{G_{vv}}\right) D_{ml}x \end{aligned} \tag{7.6}$$

Good control of the radiated sound power at a given microphone position can thus only take place when

$$\frac{G_{ml}}{G_{vv}}\frac{D_{vv}}{D_{ml}} = 1 \tag{7.7}$$

or when

$$\frac{G_{ml}}{G_{vv}} = \frac{D_{ml}}{D_{vv}} \tag{7.8}$$

This means the ratio of the plant responses measured between the secondary actuator and the error and reference sensors must be equal to the ratio between the disturbance and the error and reference sensors i.e. the secondary actuator must couple into the error and reference sensors in a similar way to the primary source. An example simulation is shown in the next section.

As an example of when good control does not occur consider the situation shown in figure 7.4. A flanking path is shown between the disturbance loudspeaker and the microphones and so the sound at the microphone is not all a result of plate vibrations. In this case, equation (7.7)

will not be satisfied and so the performance of any control sytems on the plate will be low. This problem was experienced in an initial set of experiments in which a $278mm$ by $247mm$ by $1mm$ plate was mounted in the floor of a semi-anechoic room. A loudspeaker beneath the room was used to generate a primary disturbance and piezoceramic actuators, accelerometers, and microphones were placed in the same positions as in the experiments finally carried out and described in this chapter. However, the arrangement by which the plate was mounted into the floor of the semi-anechoic room - by clamping it to a wooden frame which was then fitted into the floor - allowed a large amount of flanking transmission and so simulations of feedforward and feedback control using the measured frequency response functions, could not be conducted successfully.

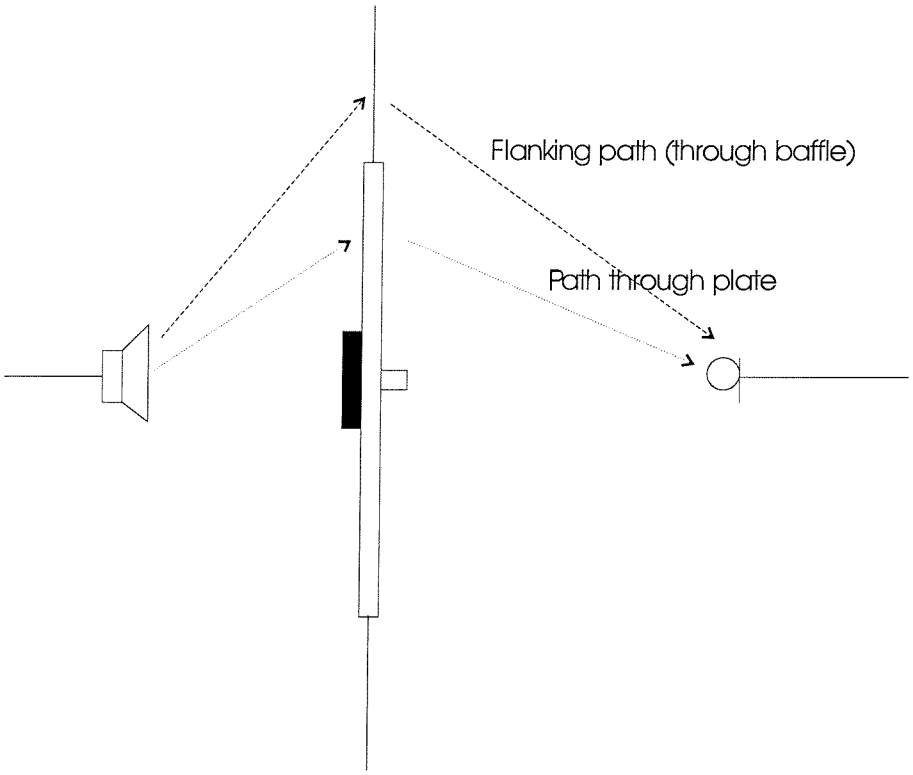

Figure 7.4: Direct and flanking paths between disturbance loudspeaker and error microphones

The reduction at the microphones when an IMC feedback controller is used to minimise the sum of the accelerometer outputs is now derived. The effect for the feedback problem can be calculated from the generalised block diagram, figure 7.3, as

$$y = \frac{D_{vv}x}{1 + G_{vv}H} \tag{7.9}$$

The control signal u output by the control loop is

$$u = -Hy \tag{7.10}$$

which, after using equation (7.9) is

$$u = \frac{-D_{vv}Hx}{1 + G_{vv}H} \tag{7.11}$$

Finally, substituting this value back into the expression for the error signal at a single microphone (equation 7.5) gives

$$e_l = \left(D_{ml} - \frac{D_{vv}HG_{ml}}{1 + G_{vv}H} \right) x \tag{7.12}$$

The cost function which should be minimised before and after control is the power spectrum of the signal at the microphones and for a single microphone is given by

$$\begin{aligned} J_l(no \quad control) &= |D_{ml}|^2 \\ J_l(control) &= \left| D_{ml} - \frac{D_{vv}HG_{ml}}{1 + G_{vv}H} \right|^2 \end{aligned} \tag{7.13}$$

The controller for the case where structural reference sensors and acoustic error sensors are used, as shown in figure 7.1(b), can now be derived in analogy with the discussion of the conventional IMC algorithm given in section 5.2. A comparison of the block diagram for normal IMC (figures 5.12 and 5.13) and for this new algorithm show that the only block which needs changing is the plant, from that measured between the input to the piezoceramic actuators and the output from the sum of accelerometers, to that measured between the input to the piezoceramic actuators and the output from the microphones. The desired signal is also changed from the disturbance measured at the accelerometers to that measured at the microphones. In this case, equation (5.22) becomes

$$e(n) = p_d(n) - \sum_{i=0}^{I-1} w_i r(n-i) \tag{7.14}$$

where this time $r(n)$ is the reference signal given by the disturbance filtered by the plant response measured at the microphones (rather than at the accelerometers). The cost function is again given by the expected value of the error squared $E[e^2(n)]$) and the expression for the optimal filter coefficients $w_i(opt)$, c.f. equation (5.24), becomes

$$E[p_d(n)r(n-k)] - \sum_{i=0}^{I-1} w_i(opt)E[r(n-i)r(n-k)] = 0 \qquad for\ 0 < k < I-1 \tag{7.15}$$

$\boldsymbol{p}$ is then defined as the cross-correlation function between $p_d(n)$ and $r(n)$

$$\boldsymbol{p} = [\ E[p_d(n)r(n)]\ E[p_d(n)r(n-1)]\ \cdots\ E[p_d(n)r(n-I+1)]]^T \tag{7.16}$$

and $\boldsymbol{R}$ given by

$$\boldsymbol{R} = \begin{bmatrix} E[r(n)r(n)] & E[r(n)r(n-1)] & \dots & E[r(n)r(n-I+1)] \\ E[r(n-1)r(n)] & E[r(n-1)r(n-1)] & \dots & E[r(n-1)r(n-I+1)] \\ \vdots & \vdots & \ddots & \vdots \\ E[r(n-I+1)r(n)] & E[r(n-I+1)r(n-1)] & \dots & E[r(n-I+1)r(n-I+1)] \end{bmatrix} \tag{7.17}$$

The optimal Wiener control filter coefficients are again given by

$$\boldsymbol{w}_{opt} = \boldsymbol{R}^{-1}\boldsymbol{p} \tag{7.18}$$

The calculation of the control filter is thus seen to be essentially the same as for the normal IMC case.

7.2 Simulations of the control algorithm using modelled frequency response functions

This section presents control results for the new control algorithm developed above using simulated frequency response functions.

The experimental arrangement is shown in figure 7.2 and all the necessary FRF's are modelled using the techniques described in chapter 3. A disturbance loudspeaker is modelled at position $(L_x/10, l_y/10, l_z/10)$ in an enclosure of dimension $0.4m$ by $0.35m$ by $0.3m$. A $278mm$ by $247mm$ aluminium plate is placed on top of the enclosure and attached to the plate are 5 piezoceramic actuators and 16 accelerometers. Nine microphones are also placed in the far-field in the positions given by table 7.2. Examples of the four different sets of simulated FRFs are shown in figure 7.5. Figure 7.6 shows the effects of feedforward control of the summed accelerometer outputs on the sum of the square microphone outputs, which is seen to give almost as good performance as controlling the sum of the squared pressures directly. Figure 7.6(b) furthermore shows the ratio given by the left hand side of equation (7.7), which should be as close to 1 as possible for good control to occur. The simulations show good control over the whole frequency range as would be expected as feedforward control is being used. The effect of the enclosure is to amplify the first plate structural mode. This makes this structural mode even more important in terms of its sound power radiated, than before. Only the central actuator was used for this simulation.

Figure 7.7 then shows the same results where feedback control of the summed accelerometer output has been used instead of feedforward control and these are compared with the results obtained using the control algorithm with separate reference and error sensors. The figures show the effect at either the sum of the accelerometer outputs (reference signal in figure 7.7(a)) or the sum of the square microphone outputs (error signal figure in 7.7(b)). In each graph, the solid line shows the measured signal before control, the dashed line shows control of accelerometer outputs and the dotted line shows the effects of the control algorithm using separate reference and error signals. No robustness has been included in the feedback control but in practice, this would be required and would result in a loss in performance compared to the case presented here.

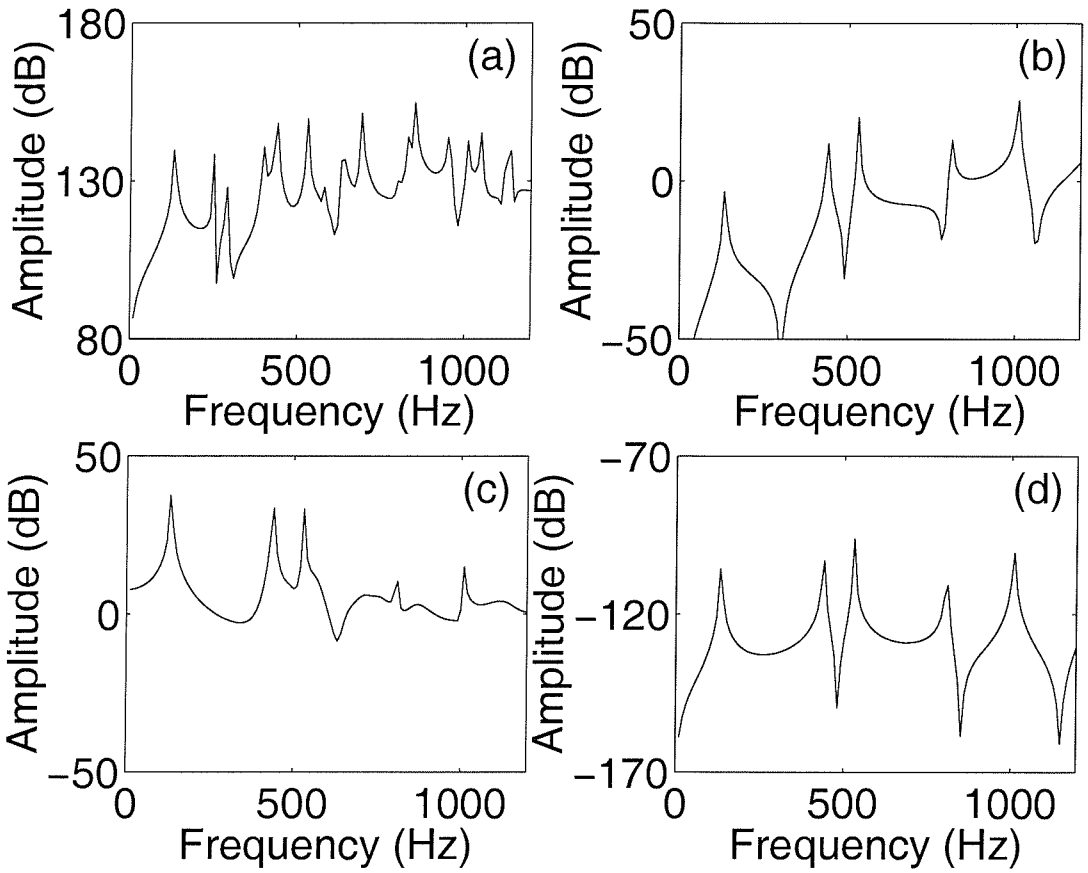

Figure 7.5: Examples of simulated FRFs using a central actuator, almost central accelerometer and central microphone. a) D_{vv}, FRF between disturbance loudspeaker and a reference accelerometer. b) G_{vv}, FRF between piezoceramic actuator and a reference accelerometer. c) D_m, FRF between disturbance loudspeaker and an error microphone. d) G_m, FRF between piezoceramic actuator and an error microphone.

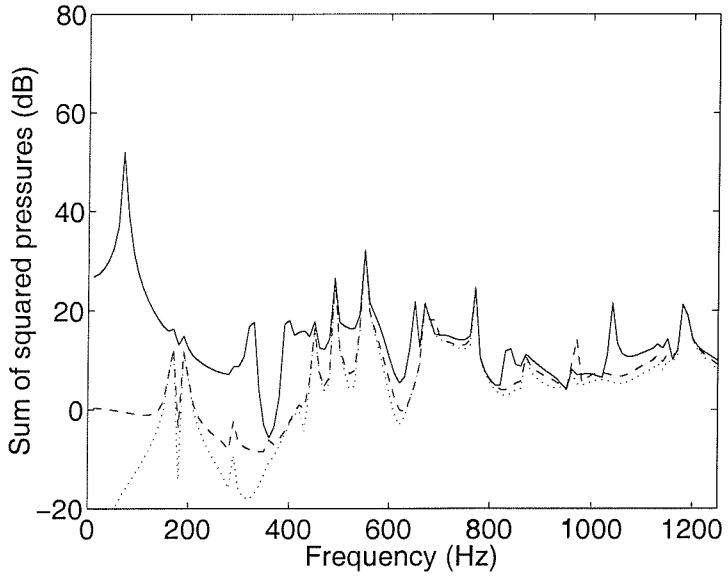

(a)

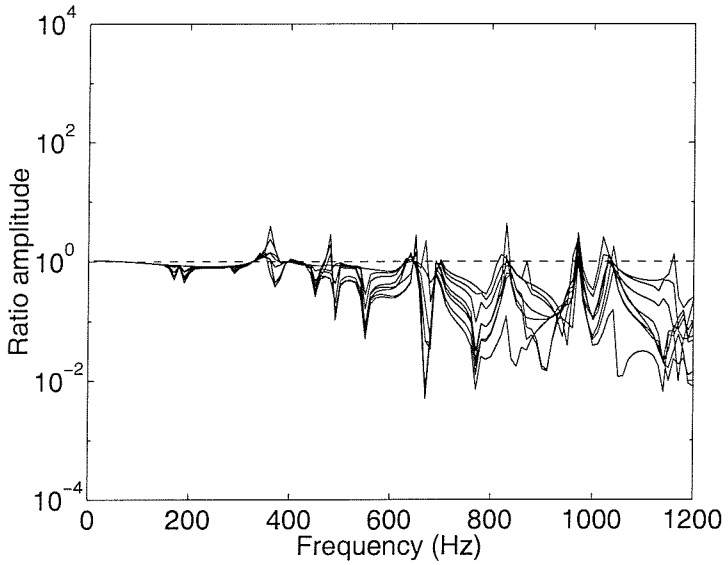

(b)

Figure 7.6: Feedforward control simulations with simulated FRFs. a) The effect of feedforward control on radiated sound. Error signal measured at microphones after feedforward control of summed accelerometer output. Solid line shows signal before control, dashed line shows signal after the control of accelerometer outputs, and dotted line shows signal after controlling sum of squared pressures directly. b) Ratio given by equation (7.7) for each of the 9 microphones. Should be equal to 1 for good control.

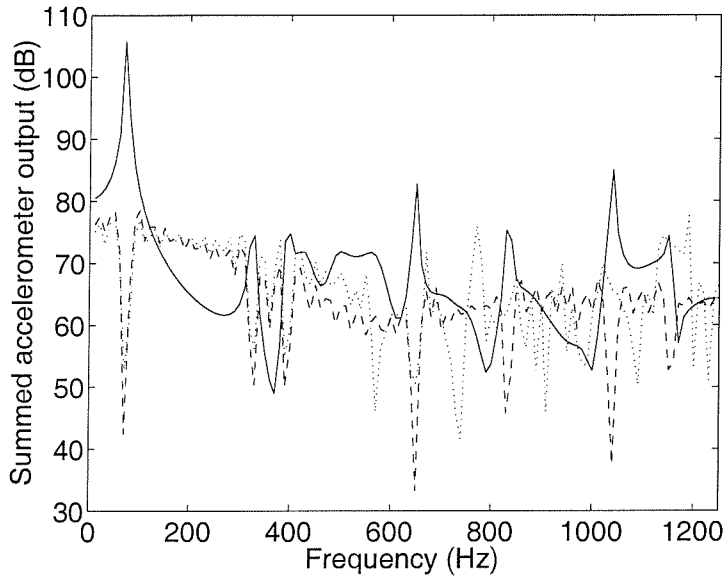

(a)

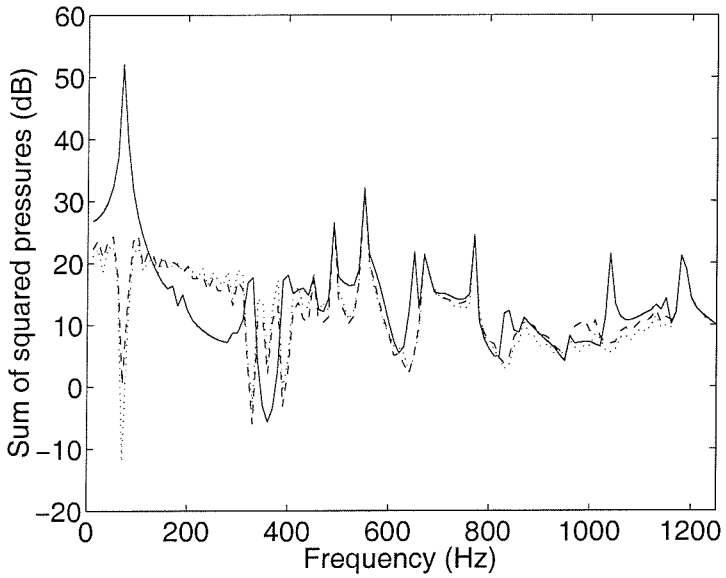

(b)

Figure 7.7: Simulated performance of feedback control, using simulated FRFs. Structural sensors, whose summed output is shown in (a) are used to give a reference signal and microphones whose sum of squared output is shown in (b) are used to give an error signal. The solid line shows the measured signal before control, dashed line shows the result of controlling the summed accelerometer outputs and dotted line shows the effects of the control architecture using separate reference and error signals.

The control architecture using structural reference sensors and acoustic error sensors results in a very slightly improved attenuation at the microphones but slightly decreased performance at the accelerometers, as would be expected. This simulation strongly supports the use of volume velocity as an error signal for the control system.

Using this new feedback approach with remote error sensors, some further simulations were carried out to check the feasibilty of using a reduced number of sensors. Many different variations were tried, initially using the summed output from a reduced number of accelerometers as a reference sensor. An example of this is shown in figure 7.8, when only a single almost centrally-placed accelerometer is used as a reference sensor. The results show that although using a single accelerometer on its own to try and cancel the radiated sound power does not work, when the single accelerometer is used with the microphones as error sensors, good control of the first mode is seen and this could be an important factor during implementation when the number of control channels must be kept to a minimum.

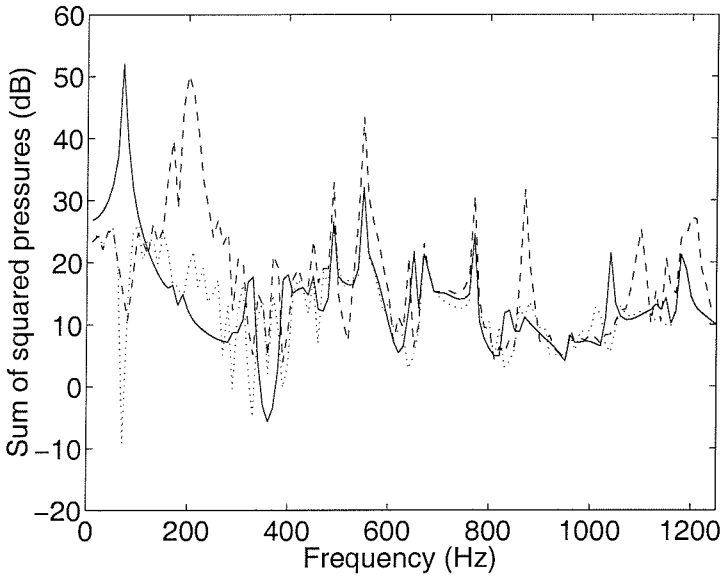

Figure 7.8: Simulated performance of feedback control, using simulated FRFs. A single accelerometer is used to give a reference signal and microphones are used to give an error signal. The solid line shows the measured signal before control, dashed line shows the result of controlling the accelerometer output and dotted line shows the effects of the control architecture using separate reference and error signals.

7.3 Effects of delay and robustness

These simulations have been performed with no robustness/stability included in the plant and assuming no additional delay in the plant response due to controller delay or signal conditioning filters. In practice, a certain amount of stability is required (see section 5.1.1 for example), and a certain fixed amount of delay is inherent to the plant response (section 5.3.2). A further set of simulations was thus carried out to look at the trade-off between these three factors (performance, stability, and delay) and to predict the performance of a real feedback control system.

7.3.1 Effect of delay

Delay can be included by multiplying the plant phase response by $e^{-j\omega\Delta_t}$ where Δ_t is the delay. An example of the effect of delay on the controller performance as measured by the microphones is shown in figure 7.9. After each delay is introduced the optimal control filter is recalculated using equation (7.18).

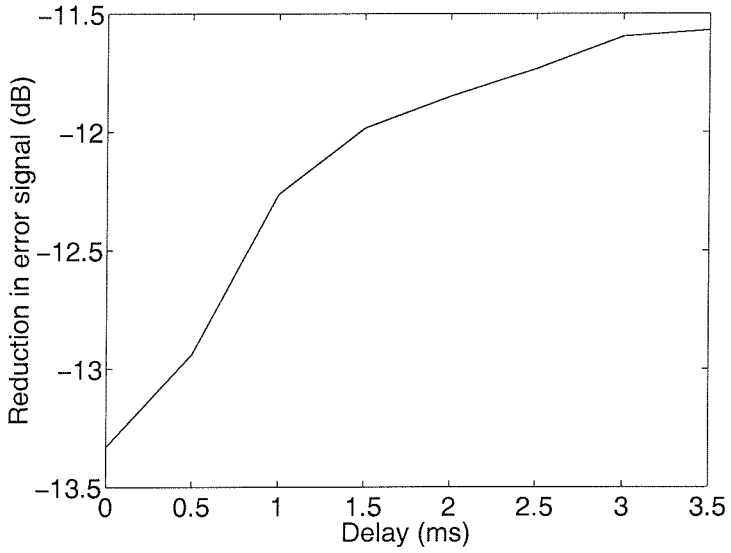

Figure 7.9: Performance of feedback control of summed accelerometer output as a function of delay. No regularisation term is included in the calculation of the feedback controller to ensure robust stability. Performance is measured by sum of square microphone outputs.

7.3.2 Effect of robustness

Robustness is included, as described in section 5.2.1 by using the β term and adding regularisation to the auto-corellation matrix which is required to calculate the controller coefficients. The effect of adding this regularisation term can be measured in two ways (both through the Nyquist plot of the open loop system).

1. The stability measured as Δ_G from equation (5.6) which gives the maximum fractional change in the plant before instability occurs

2. As the loop of the Nyquist plot which comes closest to the point of instability $(-1, 0)$ is in the left-hand plane, it corresponds to an enhancement in the controlled variable (due to the waterbed effect, section 5.1.1) and the point of the Nyquist plot closest to $(-1, 0)$ gives the maximum enhancement.

   An example of the effect of designing a controller with robust stability on performance is shown in figure 7.10.

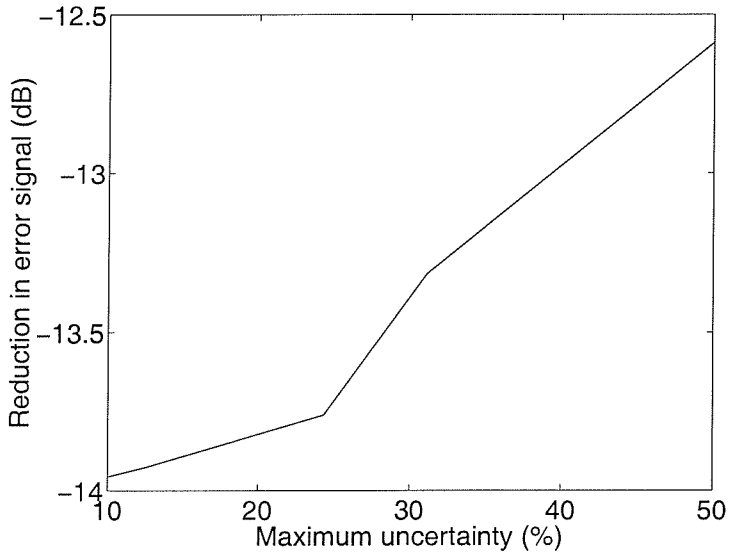

Figure 7.10: Performance of feedback control of summed accelerometer output as a function of maximum uncertainty. No delay is included in the calculation of the feedback controller. Performance is measured by sum of square microphone outputs.

There are then two variables β and Δ_t which have an effect on three measurable quantities; attenuation, stability (or maximum enhancement), and delay. This can be shown as a single

plot as shown in figure 7.11 for example. As an example, stability of 30% is typically sufficient and the typical delay in a control system due to filters and ADC/DAC processes would be about 5 samples as described in section 5.3.2. With these two values, figure 7.11 shows that approximately $12dB$ of reduction at the sum of the squared microphone outputs could be expected from a real system. This is a useful tool which allows the expected performance of a control system to be predicted from only the plant FRF.

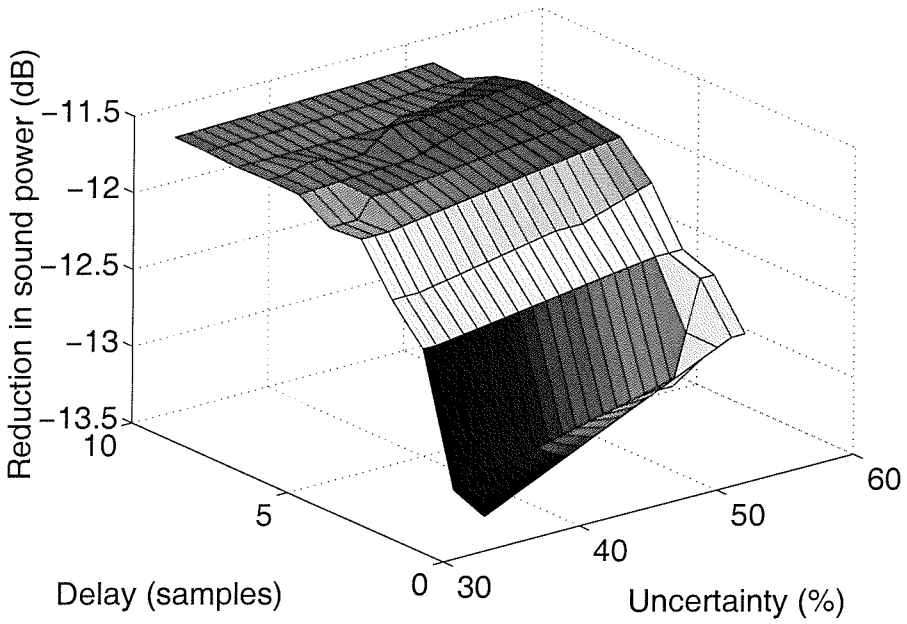

Figure 7.11: Performance of a feedback controller designed to minimise radiated sound power using structural reference sensors and acoustic error sensors as a function of delay in controller and maximum percentage uncertainty. Attenuation is measured by sum of square microphone outputs.

7.4 Conclusions

In this chapter, a control algorithm has been developed in which both structural sensors and far-field sensors were used, the former giving a reference signal and the latter giving the error signal. This was found to have some advantages over the control of the summed accelerometer output, and was tested using simulated FRFs of the plant and disturbance. Predictions of the performance of a real controller were then made by including robust stability and controller delay in the simulations. The final chapter will describe how this new control algorithm is

implemented experimentally.

Chapter 8

Implementation of a real-time active structural acoustic control system

8.1 Introduction to the new experimental system

Chapter 5 described a set of real-time experiments carried out on a plate using a distributed volume velocity sensor and piezoelectric actuators. A number of implementation problems were identified which prevented the control system from achieving the performance that was predicted from simulations. The most significant of these problems was due to delays in the control loop associated with the processor used to implement the digital controller. Chapters 6 and 7 then described a number of different cost functions which could be used for ASAC purposes and focused on those where an array of accelerometers were placed on the plate. Using multiple accelerometers allowed a number of different cost functions to be investigated and, in this chapter, the cost functions developed in chapter 7 are tested experimentally.

The new experimental rig is first described and then, using measured frequency response functions, the expected performance of the control algorithms developed in the previous chapter are presented. Finally, a real time control experiment is described.

8.2 Control using multiple accelerometers

8.2.1 Apparatus (II)

The new experimental apparatus was designed by TNO to overcome some of the problems of the system used in chapter 5. One of the main problems with the previous system was that the controller was implemented on a TMS320C30 card on a host PC, which was unable to implement the necessary high order controllers at the required frequency. There were also large delays due to the chosen reconstruction and anti-aliasing filters which limited the performance. This was overcome in the new arrangement by using a dedicated control unit based on a Pentium PC with real-time Linux and 24 input channels.

A diagram of the experimental apparatus is shown in figure 7.2 and photographs of the completed system are shown in figure 8.1. This is similar to the previous experimental arrangement used in chapter 5 except for the mounting arrangements of the plate and the sensors on the plate. The plate, which has the same dimensions ($278mm$ by $247mm$ with $1mm$ thickness) and is made of aluminium as in the previous experiments, is bolted to a $350mm$ by $400mm$ by $300mm$ perspex box whose walls are $40mm$ thick so as to prevent flanking paths as far as possible. The arrangement of the accelerometers and piezoceramic patches is shown in figure 8.2. The enclosure is placed in an anechoic room and a loudspeaker is placed inside the enclosure to generate the primary disturbance. Instead of the distributed volume velocity sensor, 16 equally-spaced acccelerometers are placed on the plate in the arrangement shown in figure 8.2. B&K type 4375 accelerometers were used which have a weight of $2.4g$ each and a charge sensitivity of $0.316pC/ms^{-2}$. Each accelerometer was connected to a separate charge amplifier and voltage amplifier before input to the control unit. The five piezoceramic patch actuators were driven by a single Quad amplifier. Microphones are placed in the far-field in the positions given by table 7.2. The accelerometers and microphones are all connected to separate channels of the control system.

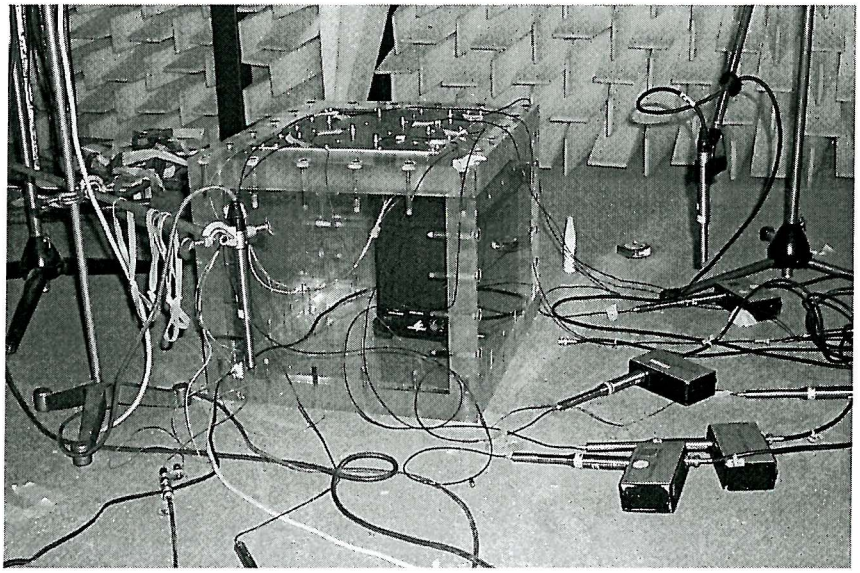

(a)

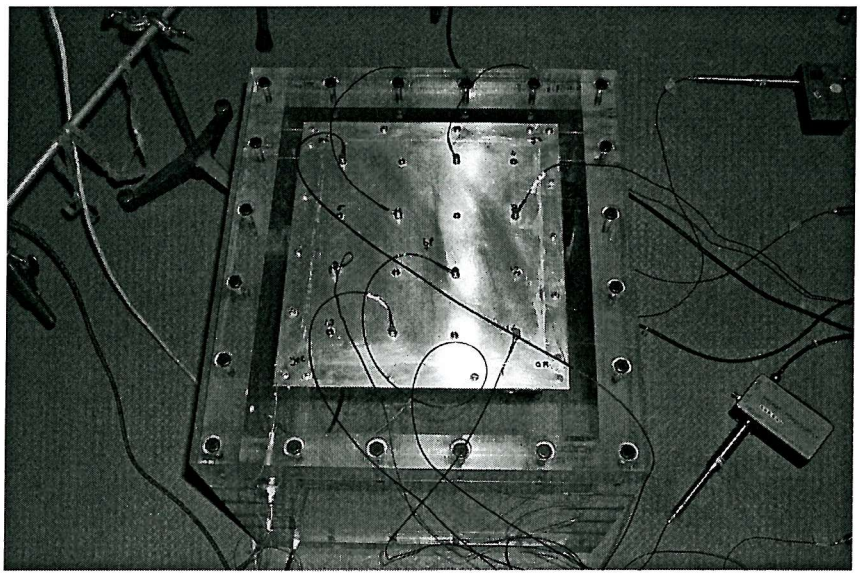

(b)

Figure 8.1: Photographs of the new experimental arrangement. a) Overview of experimental arrangement. b) Close-up of plate.

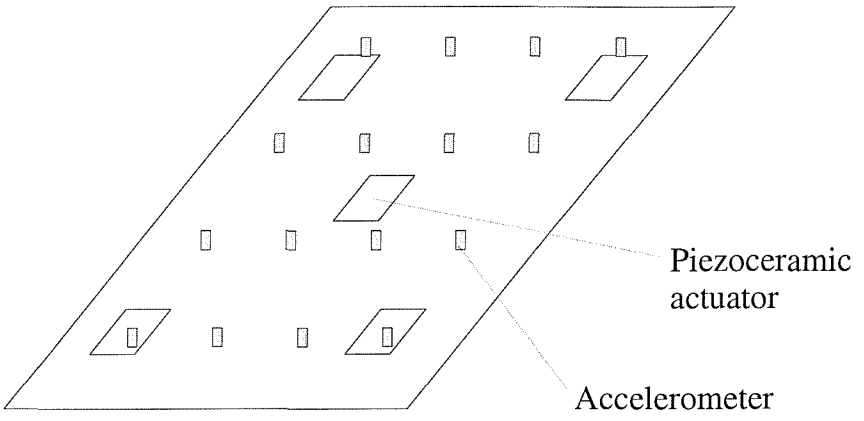

Figure 8.2: Arrangement of transducers on plate for the new experimental apparatus

8.2.2 Simulations of control using measured frequency response functions (II)

In section 7.2 the control performance calculated for simulated data using the summed accelerometer output (as an approximation to the volume velocity) as an error signal was compared with a control strategy using acoustic error sensors and structural reference sensors. Simulated FRFs were used in both feedforward and feedback cases.

FRFs were measured on the experimental rig described above and in this section, these FRFs are presented and compared with the simulated ones. The measured FRFs are then used in feedforward and feedback control simulations to predict the effect of implementing a real controller. The actual implementation is dealt with in the next section.

Comparison between the simulated and measured FRFs are shown in figures 8.3 through to 8.6. Four different sets of FRFs need to be considered; those between the loudspeaker acting as the source of disturbance and the accelerometers, those between the loudspeaker and the microphones, those between the piezoceramic actuators and the accelerometers, and those between the piezoceramic actuators and the microphones. The calibration factors of the actuators and sensors were unknown in the experiment and so an arbitrary factor has been added to the levels of the measured FRFs to allow comparison with the theoretical results. Otherwise, the amplitudes of the simulated and measured results are seen to have similar features, although the natural frequencies for the simulated responses are higher than those for the measured responses. The phase response of the FRFs are less similar and as with the previous sets of

measured FRFs, this seems to be largely due to problems in unwrapping the phase. The frequency response functions measured from the disturbance loudspeaker to the accelerometers or microphones, also include an additional part given by the frequency response of the loudspeaker, which has been modelled as a simple monopole source, and this may account for some extra phase loss. The coherences for the measurements are also shown in figure 8.7 which shows good coherence for the measured results above a frequency of around $50Hz$.

Figure 8.8 shows the effects of feedforward control of the summed accelerometer output on the microphone outputs as given by equation (7.6) using the measured FRFs. The ratio, given by equation (7.7) (c.f. figure 7.6(b)), is also shown. The feedforward control predictions show good levels of attenuation at the microphones, as with the simulated results in figure 7.6(a). A large amount of measurement noise is also present at very low frequencies and so the results are unreliable below about $50Hz$. This is a result of the poor coherence in the measurements at these frequencies. As feedforward control is being used, the summed accelerometer output can be assumed to be driven to zero.

Figure 8.9 then compares the results of feedback control of the summed accelerometer output, and the control architecture which uses separate reference and error sensors. In each feedback simulation, the plants are modelled using 4097 point filters and the control filters have 256 coefficients at an assumed sample rate of $2.5kHz$ where no anti-aliasing and reconstruction filters have been used. The effects of the two control algorithms are shown at the reference sensors (accelerometers, figure 8.9(a)) and at the error sensors (microphones, figure 8.9(b)).

The attenuations seen with both strategies are similar to those predicted from the simulated FRFs (figure 7.7). As was the case with the simulated FRFs, using structural reference sensors and acoustic error sensors results in slight performance improvements at the sum of the square microphones and a slight loss in performance at the summed accelerometer outputs relative to the control of the summed accelerometer output.

The results in figure 8.9 represent the case where no stability or robustness term has been added and this gives rise to the maximum attenuation which could be achieved using feedback control. However, in practice, a degree of stability is required, depending on the application, and there is also additional delay in the plant FRF due to delays inherent to the controller and signal-conditioning equipment. The trade-off between these three factors has already been

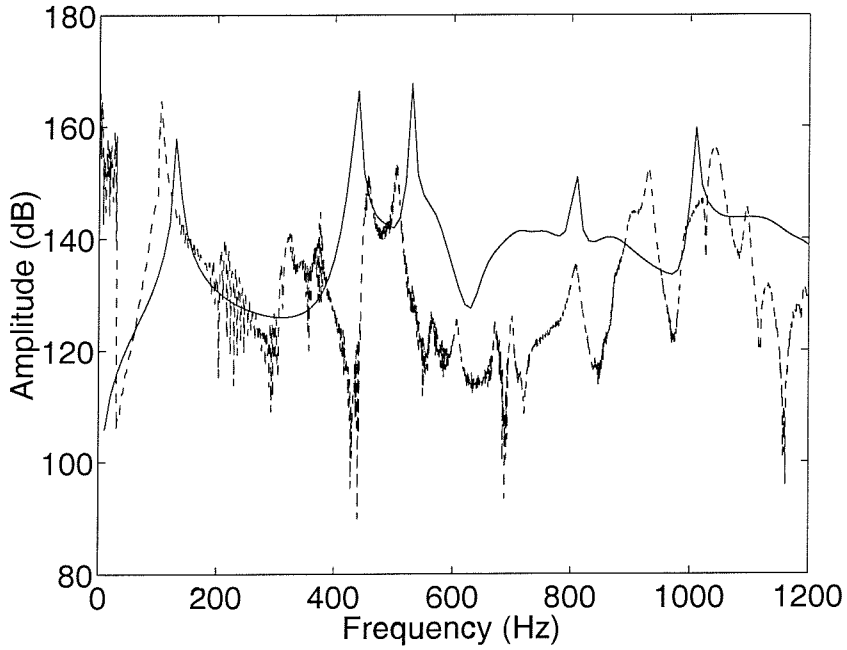

(a)

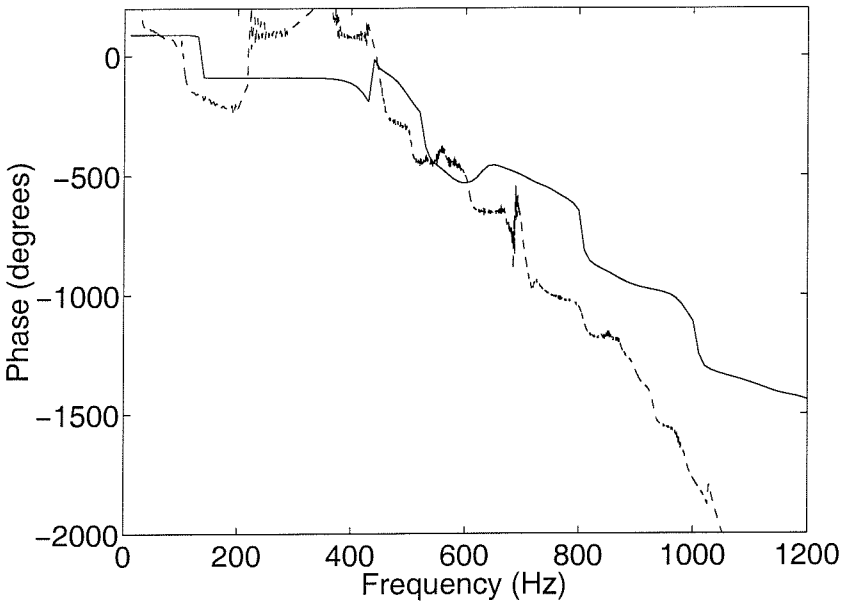

(b)

Figure 8.3: Comparison of simulated (solid) and measured (dashed) FRFs for TNO experimental system: Between disturbance loudspeaker and sum of accelerometer outputs. a) Amplitude. b) Phase.

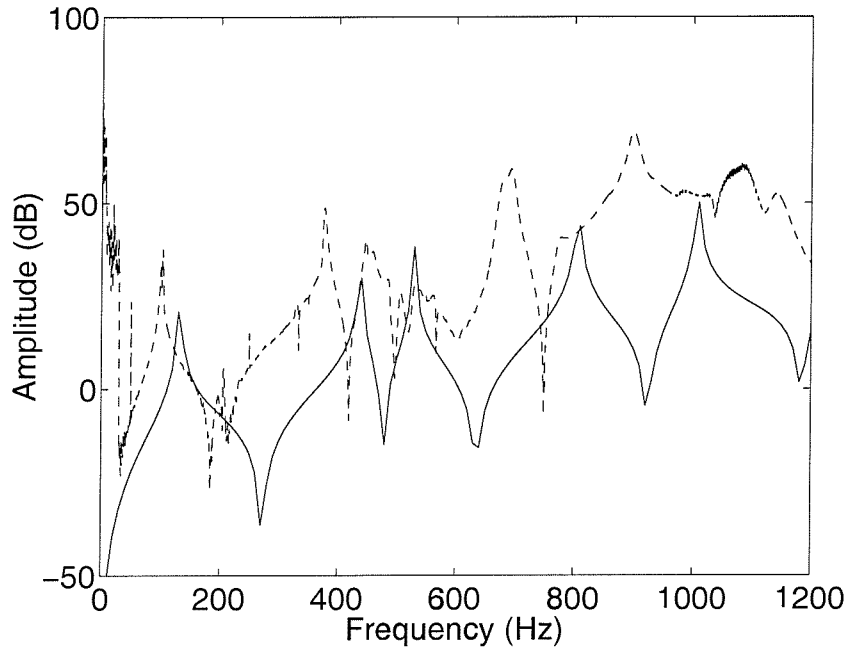

(a)

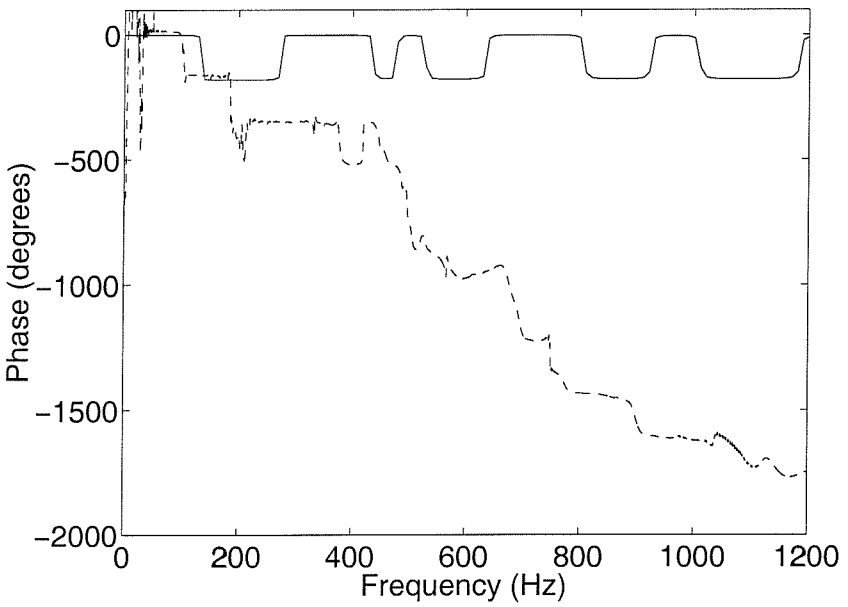

(b)

Figure 8.4: Comparison of simulated (solid) and measured (dashed) FRFs for TNO experimental system: Between the five piezoceramic actuators driven in phase and the sum of the accelerometer outputs. a) Amplitude. b) Phase.

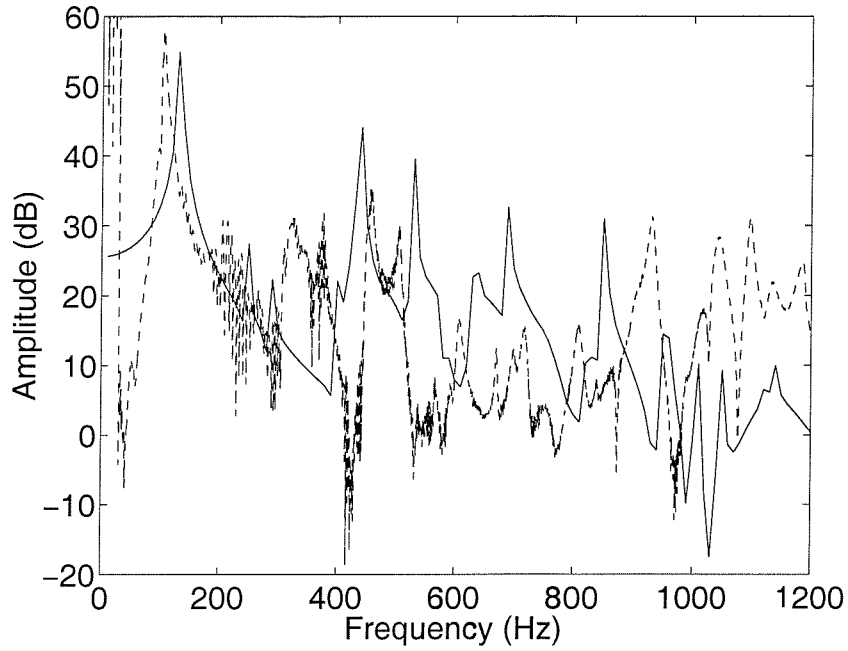

(a)

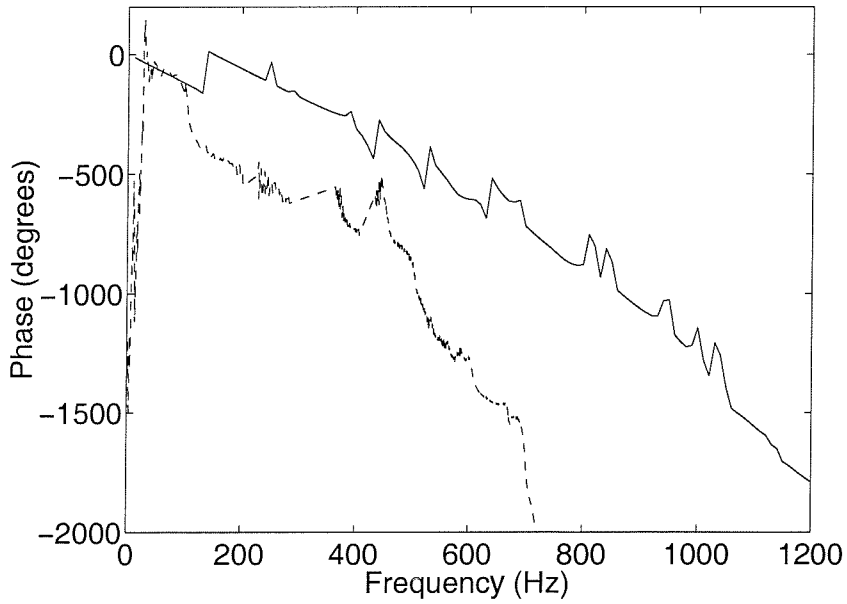

(b)

Figure 8.5: Comparison of simulated (solid) and measured (dashed) FRFs for TNO experimental system: Between disturbance loudspeaker and sum of squared microphone outputs. a) Amplitude. b) Phase.

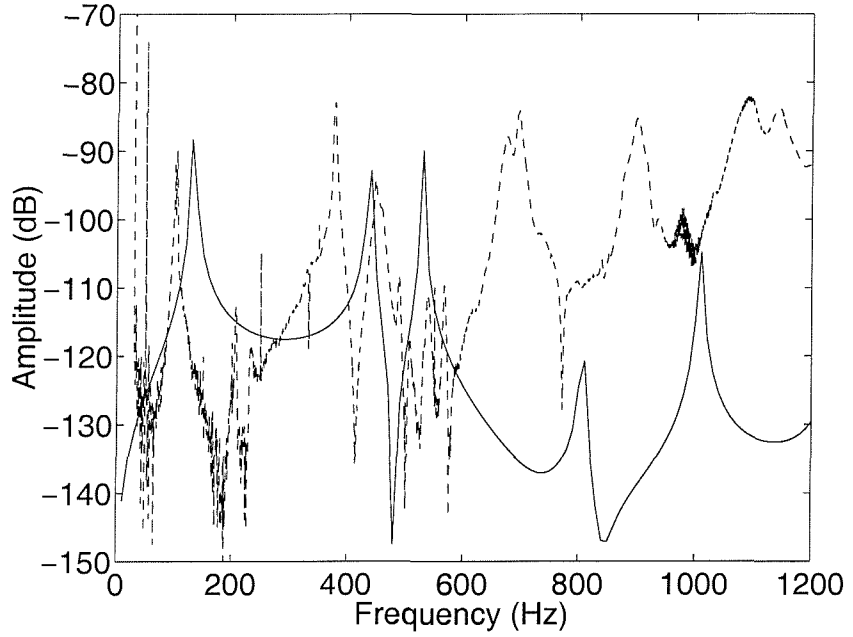

(a)

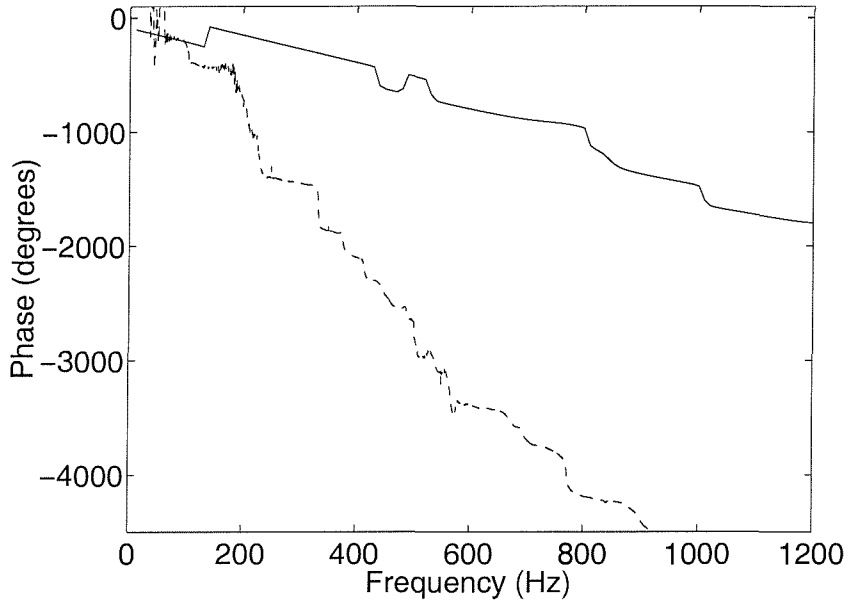

(b)

Figure 8.6: Comparison of simulated (solid) and measured (dashed) FRFs for TNO experimental system: Between the five piezoceramic actuators driven in phase and the sum of the squared microphone outputs. a) Amplitude. b) Phase.

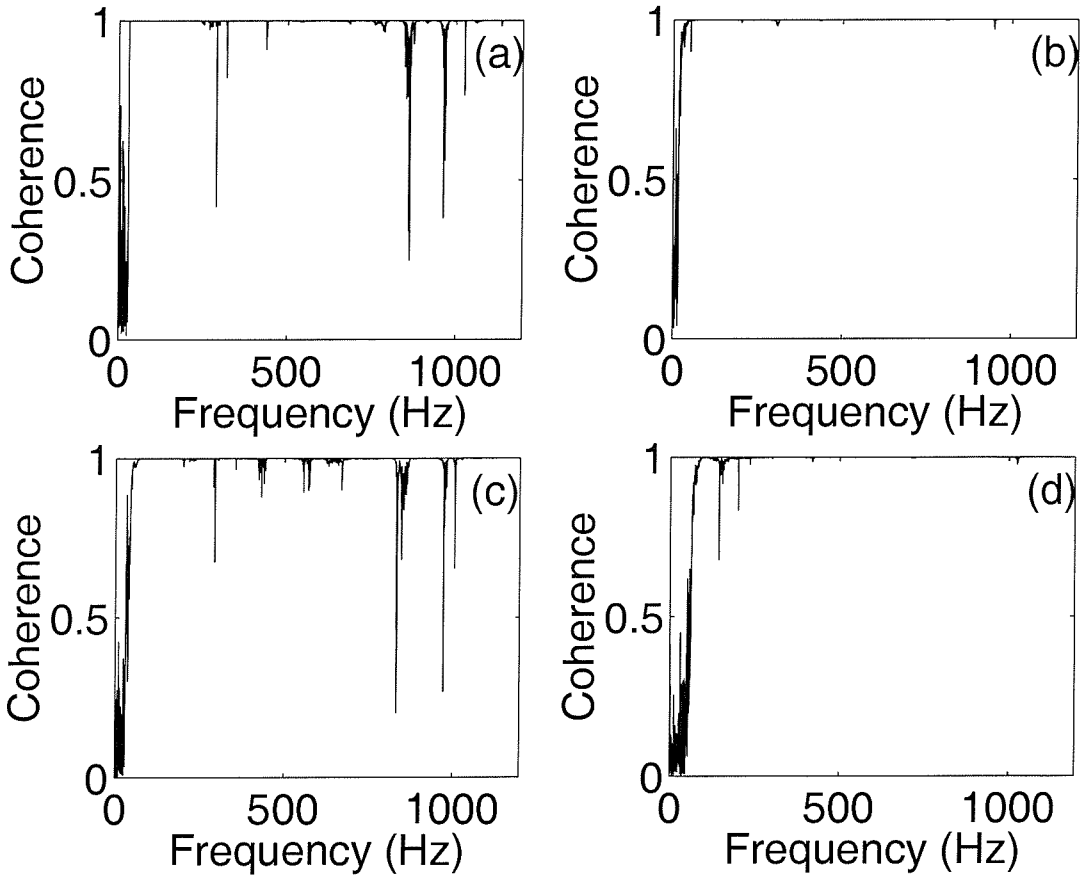

Figure 8.7: Typical coherence for measured results. a) between disturbance loudspeaker and an almost central accelerometer. b) between central actuator and an almost central accelerometer. c) between disturbance loudspeaker and a central microphone. d) between central actuator and a central microphone.

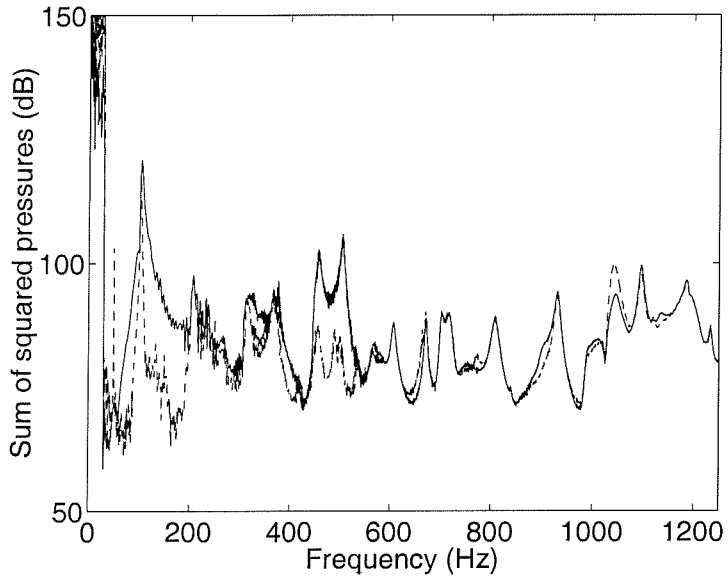

(a)

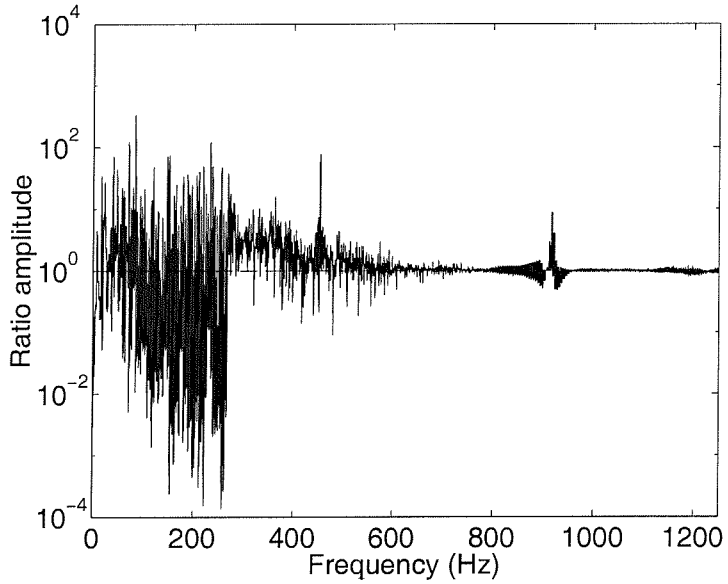

(b)

Figure 8.8: Feedforward control simulations with measured FRFs. a) The effect of feedforward control on radiated sound using measured FRFs. Error signal is measured at microphones after feedforward control of summed accelerometer output. Solid line shows signal before control and dashed line shows signal after control. b) Ratio given by equation (7.7) for each of 9 microphones. Should be equal to 1 for good control.

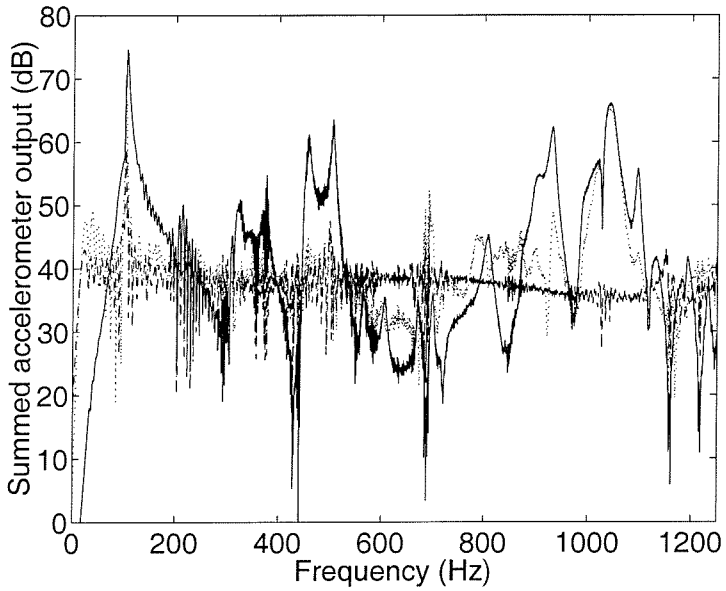

(a)

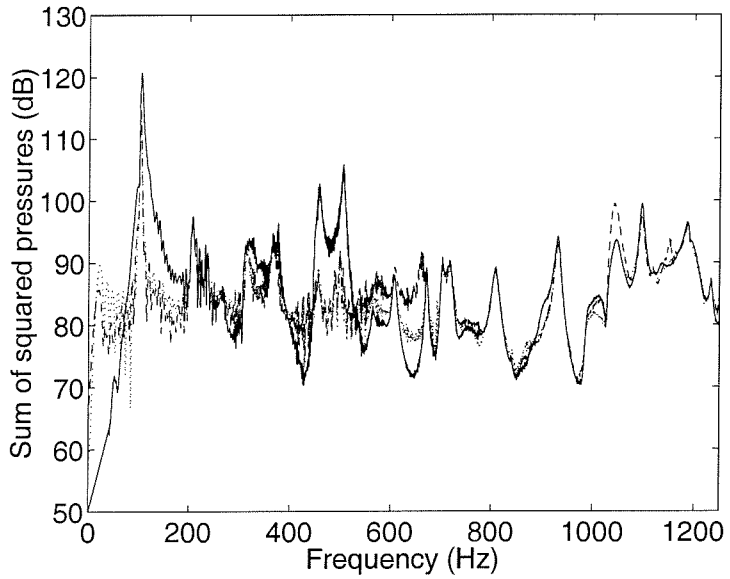

(b)

Figure 8.9: Simulated performance of feedback control, using measured FRFs. Structural sensors, whose summed output is shown in (a) are used to give a reference signal and microphones whose summed output is shown in (b) are used to give an error signal. The solid line shows the measured signal before control, dashed line shows the result of controlling the summed accelerometer outputs and dotted line shows the effects of the control architecture using separate reference and error signals.

discussed for simulated FRFs in section 7.2 and is shown in figure 7.11. The same trade-off is shown for the measured data in figure 8.10. This figure then gives an estimate of the amount of attenuation which could be expected from a control system with a given delay and required stability calculated using only measured FRFs. This is a useful tool and using these figures, it was chosen to implement a feedback controller on the experimental system as described in the next section.

8.2.3 Real time IMC control (II)

A final set of experiments was carried out to verify the results obtained during the simulations using measured FRFs presented in this chapter.

The experimental arrangement was as shown in figure 8.1 and the accelerometers and microphones were all connected to input channels of the control unit. The actuators were driven with a single control voltage. In the final experiments, only 14 accelerometers and 3 microphones were used, due to problems with some of the conditioning amplifiers, which corresponds to a slightly reduced set of sensors compared to simulations.

A 300 coefficient model of the plant, measured between the voltage output from the control unit to the amplifier driving the five piezoceramic and the summed output of the sixteen accelerometers (after charge and voltage amplification), was first identified with the control unit, with a sampling rate of $5kHz$, and this is shown in figure 8.11. The first few samples of the impulse response show only 2 samples delay, or $0.4ms$ at this sampling rate. This is a drastic improvement over the controller used in previous experiments and, comparing this to figure 8.10 shows that an attenuation of around $5.5dB$ with 40% maximum uncertainty could be expected, at the microphones, for control of broadband disturbances using structural reference sensors and acoustic error sensors. The response measured by the controller has similar features to the previous measured FRFs shown in figure 8.9(a) for example but is contaminated by the $50Hz$ line frequency and

Control experiments were then conducted on a tonal disturbance generated by the loudspeaker at a frequency of the first measured plate mode at $110Hz$. A 300 coefficient adaptive IMC controller, with regularisation included to ensure robustness, was used to control the tone,

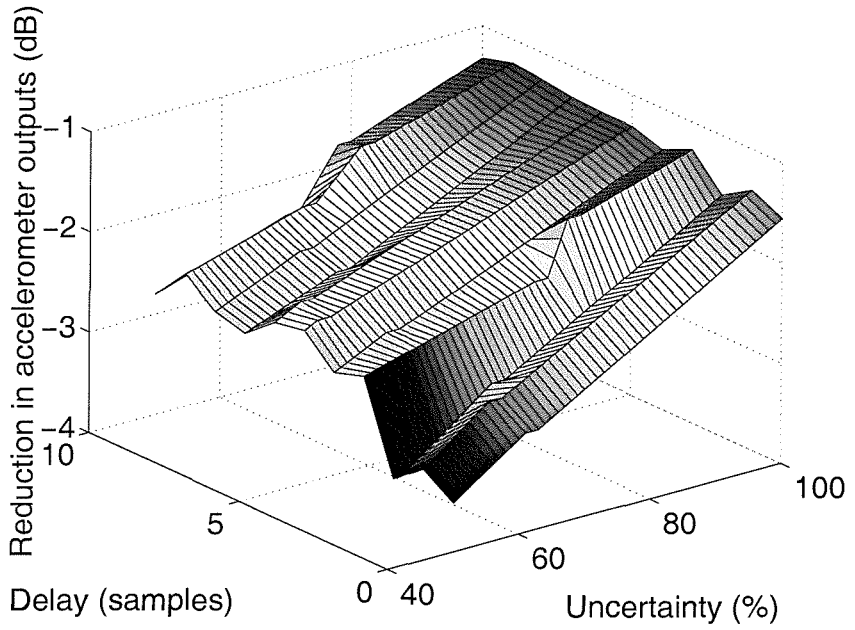

(a)

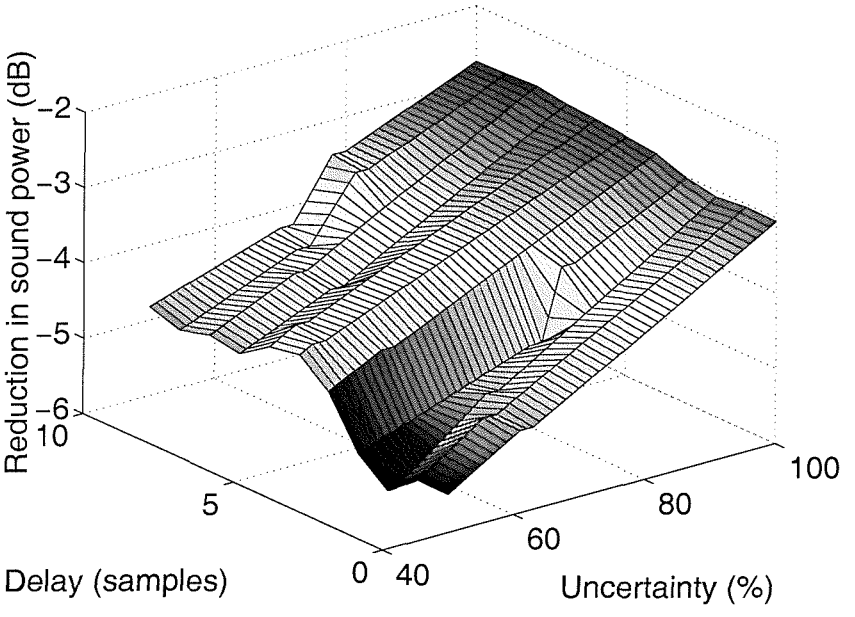

(b)

Figure 8.10: Trade-off between performance, maximum percentage uncertainty, and delay for control using structural reference sensors and acoustic error sensors as calculated from measured data. a) At reference sensor (sum of accelerometer outputs). b) At error sensor (sum of squared microphone outputs).

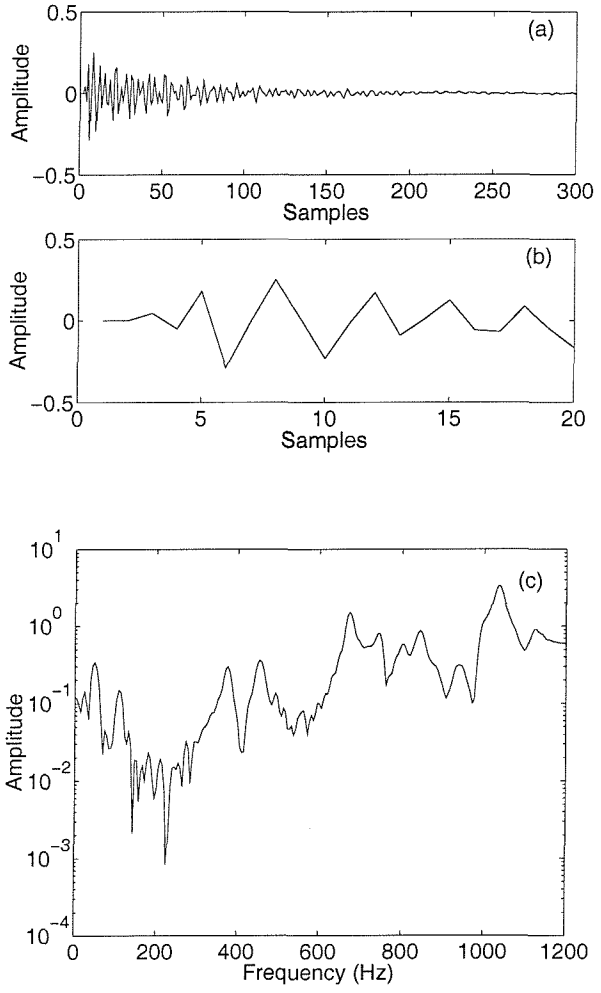

Figure 8.11: Response of plant between 5 piezoceramic actuators driven in phase and sum of accelerometer outputs as measured by control unit. a) Impulse response (sampling rate = $5kHz$). b) First few samples of impulse response showing controller delay. c) Amplitude of frequency response

using the sum of the accelerometer outputs as an error signal. Feedforward simulations, as shown in figure 8.8(a), show that an attenuation of around $40dB$ in the radiated sound power could be expected. Attenuations of up to $17.4dB$ were obtained at the summed accelerometer outputs and $13.7dB$ attenuation was achieved at a single microphone placed directly above the plate. The results are shown in figure 8.12. The main factor which limited the amount of attenuation was that the control actuators could not be driven with enough amplitude to counteract the effect of the disturbance. Unfortunately during the short time available for these control experiments, it was not possible to implement a controller for broadband disturbances.

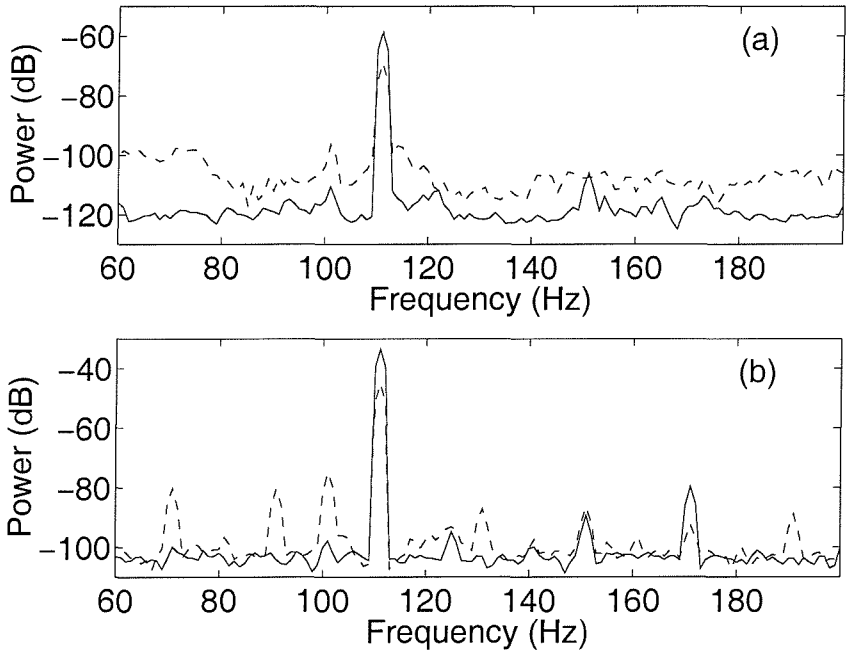

Figure 8.12: Control of a tonal disturbance at $110Hz$ using an adaptive IMC controller to minimise sum of accelerometer outputs. a) At reference sensor, sum of accelerometer outputs, ATT=$17.4dB$. b) At error sensor, microphone placed $1m$ above plate, ATT=$13.7dB$.

Some recommendations for the development of a realisable real-time controller are given in the conclusions, chapter 9.

8.3 Conclusions

This chapter has described the development of a real-time control system using cost functions and control techniques described in the previous chapter.

The experimental rig is similar to the one used in chapter 5 but, instead of using a distributed volume velocity sensor, 16 accelerometers are placed on the plate and their summed output, which gives an approximation to the volume velocity, is used as a reference signal.

The measured frequency responses are seen to be very similar to those predicted from simulations and these are used to give predictions of control performance from a real-time control system including delay in the plant FRF and the requirement for robust stability.

Some experiments were carried out with the experimental rig to control tonal disturbances. The results were similar to those predicted from simulations.

Chapter 9

Conclusions

In this thesis a number of aspects in the development of an ASAC system have been described.

Four main objectives were set out at the beginning of the thesis:

1. To compare the physical limitations of different actuators and sensors and their placement for active structural acoustic control purposes.

2. To investigate the use of Internal Model Control (IMC) and its implementation for active structural acoustic control purposes.

3. To compare the physical limitations of different cost functions for active structural acoustic control.

4. To investigate the interaction between the physical limitations and control limitations of active structural acoustic control.

9.1 Conclusions on actuators, sensors, and their placement

The thesis begins with the development of physical models of the plate vibrations and subsequent sound radiation (chapter 3) which are based largely upon previous work. Radiation modes were discussed, which are a form of decomposing the plate vibration into modes which

radiate sound independently. This is in contrast to the normal method of analysing plate vibrations using structural modes. It turns out that the first radiation mode accounts for most of the sound power radiated at low frequencies and furthermore that at these frequencies, the first radiation mode approximates the volume velocity of a plate. This is the motivation for controlling volume velocity and this thesis starts of as a continuation of previous work in which a distributed volume velocity sensor was developed and used for feedback control experiments.

The next section compared a number of different transducers for the purposes of ASAC. The performance of different combinations of these actuators and sensors was compared and then the placement of these transducers was investigated. Point forces, piezoceramic patch actuators and uniform force actuators were all investigated and their sensor counterparts; accelerometers, piezoelectric patch sensors, and distributed volume velocity sensors. Theoretical models of each actuator and sensor were developed using the elemental model introduced for modelling the plate vibrations and sound radiation.

Point force actuators are largely impractical due to the requirement for reaction mounts. The development of piezoceramic material technology has introduced a number of new actuators which are highly suitable for ASAC since they do not need a reaction mount and because of their low weight, their high control authority, and low cost. The final actuator considered is the uniform force actuator. Although this type of actuator should result in high control performance as it is the reciprocal actuator to the volume velocity sensor, practical problems with control authority and in-plane coupling have been observed by other authors and so it was not used here. Each of these actuators has a spatially-matched sensor. The accelerometers measure structural response at a point. Due to the reciprocal nature of the piezoelectric effect, the same piezoceramic patches which were used as actuators could also be used as sensors. Finally, a distributed volume velocity sensor was considered.

Following the modelling of the various transducers, different combinations of them are tested in feedforward control simulations. Feedforward control assumes that a reference signal is available and gives the best control performance that could be achieved from a given physical system. All the control strategies using structural transducers are compared with the control of radiated power which acts as a reference curve, but would require the use of far-field microphones in practice. The feedforward control simulations show that the cancellation of volume velocity using a uniform force actuator results in almost as good control performance as minimising the

total radiated power. As the uniform force actuator is not currently available, the next best strategy is to use piezoceramic actuators and a volume velocity sensor. Certain combinations of actuators and sensors are also found to be better suited to vibration control than to ASAC.

After choosing suitable actuators and sensors, the next issue is to choose the position of these transducers on the plate. The choice of transducer positions is based upon physical arguments (rather than using exhaustive search methods or genetic algorithms for example). The performance of a feedback control system depends on the frequency response function of the plant and should be made as minimum phase as possible. The actuators can be placed in such a way as to minimise the phase loss in this frequency response function. To do this the spatial forcing functions of the actuators should match the spatial sensitivity of the sensor as much as possible. As an example, when using a volume velocity sensor and piezoceramic actuators, the actuators should be placed as close to the corners of the plate as possible. A trade-off then arises between keeping the phase of the plant frequency response function to a minimum for feedback control performance and control authority as it becomes more difficult for the actuators to drive the plate the closer they are placed to clamped corners. In the thesis a compromise is chosen as one sixth of the way from each of the corners. The concept of matching the spatial forcing function of the actuators and spatial sensitivity of the sensors can be taken a step further by considering collocated transducers in which these two functions are exactly equal. In this case, the frequency response function of the plant is minimum phase which results in good feedback control performance. Care must be taken however that the placement of these transducers does not result in situations where the actuators cannot force an important mode and the sensors cannot measure that mode.

9.2 Conclusions arising from experiments using a distributed volume velocity sensor

Active control systems to control tonal sound and vibration in aircraft are now in mass production. The challenge now is to cancel more broadband disturbances, and this normally requires the use of feedback control as opposed to feedforward control. The use of feedback control introduces a number of further issues which affect the performance relative to their feedforward counterparts. A major issue is the need for robust stability which causes a decrease in the

performance. Phase lag in the plant frequency response also becomes important in contrast to feedforward control where a reference signal can be measured. There is generally a trade-off between these three factors; the performance, required stability, and phase lag in the plant, which can be altered slightly through the use of appropriate signal conditioning equipment.

A number of techniques or algorithms are available for designing feedback controllers ranging from the very simple, such as direct displacement, velocity or acceleration control, through to the more complex, such as the LQG method. In this thesis Internal Model Control (IMC) is used which has some advantages under certain conditions. A generalised control framework is also introduced which provides an analysis tool which can be used on any feedback control method.

An initial experimental apparatus was also designed to test the feedback approach which consisted of a plate with five piezoceramic actuators and a distributed volume velocity sensor mounted on a box. The box contains a loudspeaker which generates the disturbance and the aim is to design and implement a controller that reduces the transmission of sound through the plate.

Frequency response functions of the plant and disturbance were measured and used to give predictions of the control performance using an IMC controller. The measured frequency response functions were found to be very similar to the simulated ones and control simulations showed that an attenuation of around $7dB$ could be expected. One advantage of the simulations though is that controllers with a large number of coefficients can be used. In practice, implementation of these high order controllers is difficult and, with the controller used in these experiments, a TMS20C30, it was not possible to implement these controllers with this number of coefficients.

During the real-time control experiments good control of tonal disturbances was achieved with a total attenuation of $24dB$. For the control of more broadband disturbances, the total attenuation was slightly less than predicted at around $4dB$ although the same control filters were not implemented for the reasons described above.

A number of practical issues were identified after these first set of experiments which were addressed at later stages in the thesis. These mainly arose due to the lack of computing power available during these experiments which manifested itself in two ways; by limiting the number of filter coefficients which could be used as described above, and by introducing a delay due

to the signal-conditioning equipment which is larger than the improvements in delay achieved by using an almost minimum phase plant. Possible solutions to these problems include the removal or lowering the order of the anti-aliasing and reconstruction filters to minimise delay in the plant and increasing the sampling frequency to reduce the relative effects of the filters. This second solution would however require a more powerful controller.

9.3 Conclusions on cost functions using accelerometers

The next chapter of the thesis considered a number of different cost functions for ASAC purposes using accelerometers on the plate. Two mechanisms by which ASAC actually takes place were identified; modal suppression and modal restructuring, which is the dominant mechanism when controlling volume velocity related variables.

The aim of each of the different cost functions is to be as close to the control of radiated sound power as possible. The summed outputs of increasing number of accelerometers placed on the plate was compared with the distributed volume velocity sensor and was found to tend towards the results obtained with a true volume velocity sensor. Some configurations of accelerometers on the plate were found to work particularly well and sixteen accelerometers were chosen to be used in further experiments.

Multi-channel control configurations were investigated next using standard feedforward control techniques. When minimising the sum of the squared accelerometer outputs, these were found to work well as vibration controllers but to have little effect on the radiated sound power. Some further multi-channel control algorithms were tested taking into account the nature of radiation modes. These included looking at higher order radiation modes, which was found to have little effect at the frequencies considered in this thesis, and looking at the frequency dependent shape of the first radiation mode which did provide an improvement to the control of volume velocity.

A final multi-channel technique which was introduced was to use multiple single channel control systems on a plate each with a piezoceramic patch actuator or point force actuator and a collocated accelerometer. This technique holds some promise for the future as MEMS systems become more common and cheaper to manufacture. Some plans for future work on the topic are outlined below.

Finally, a control architecture was outlined which uses both structural reference sensors and acoustic error sensors i.e. accelerometers on the plate and microphones in the far-field. This architecture was compared to control of the approximation to the volume velocity using sixteen accelerometers and found to give a small improvement in performance.

A second experimental arrangement was then designed consisting of a plate mounted on a perspex enclosure housing the disturbance loudspeaker. Five actuators and sixteen accelerometers were mounted on the plate and microphones were placed in the far-field.

Plant and disturbance frequency response functions were measured on this new experimental rig and used to conduct simulations of the new control algorithm using separate reference and error sensors. This control algorithm was only found to perform slightly better than control of the approximation to the volume velocity.

9.4 Conclusions on internal model control and implementation

Although there are several different feedback control techniques of varying complexity, the IMC architecture was used in most cases in this thesis. The IMC algorithm calculates the feedback controller by assuming a model of the plant is available and then the control problem can be reformulated as a feedforward one and standard Wiener techniques can be used to calculate the controller.

Some advantages of the IMC architecture include its ease in physical interpretation, the fact that it guarantees a stable closed loop for a stable controller for the structures considered in this thesis, the fact that it can be reformulated into a feedforward problem, and that it is relatively easy to implement as an adaptive controller. However, for ASAC purposes, the required controllers are high order due to the nature of the plant FRF. These high order controllers can be difficult to implement in practice and require the use of very fast DSP chips which are however becoming more readily available.

Another problem in implementation is the inherent delay in the controller, ADC/DAC convertors, and the filters required to prevent aliasing problems. These additional delays in the plant FRF outweigh the improvements in the phase response of the plant FRF obtained by careful

positioning of the transducers and, along with the requirement for robust stability, limit the overall performance of the control system.

9.5 Recommendations for future work

A major part of this thesis has outlined the theory of plate vibrations, the subsequent sound radiation, feedback control, and various possible cost functions. The experimental part of the thesis was limited to two validation experiments to confirm some of the theories outlined. However, there were some problems with both these sets of experiments, especially in implementing the digital controllers, and in the second set of experiments, due to time constraints. With more time available, experimental and practical issues should be examined in more detail. This could be through the development of the second test-rig which is well built and prevents flanking paths, due to the thickness of the enclosure walls, which have been a problem with previous prototype arrangements. The actuators on the plate seem to be suitable and well-positioned, but care must be taken in the choice of amplifiers used to drive these piezoceramic actuators as control authority was a problem in the second set of experiments. Similarly, the accelerometers seem to be a good choice of sensor but the need for separate charge and voltage amplifiers for each one could cause some practical problems. This could be solved to a degree by using dedicated sensors and a dedicated control system and this should become a more realistic solution with the continued development of transducer technology. The weight of the commercial accelerometers used here was also significant compared with that of the plate, and it could be argued that their cost would also prohibit the practical implementation of such a strategy. The rapid development of vibration sensors using micro electromechanical machine technology (MEMS), however, suggests that both of these problems may be overcome in the not-too-distant future and research into the physical limitations of control systems which use such devices is still worthwhile.

The control architecture with a number of local control systems all working independently is also a concept which is based on the devlopment of MEMS and holds promise for the future. Again, with more time available, it would be of interest to look at implementation issues and also at reducing the number of channels.

A further point concerns the control architecture using structural reference sensors and acoustic

error sensors which is currently implemented using measured microphone signals. It would be advanatageous to remove the microphones in real applications and this would require a model of the FRFs between the actuators and the microphones. The implementation would however still be very similar to the normal IMC algorithm.

ASAC is set to be used in more applications over the next few years, especially with the continued development of actuators, sensors, and faster DSPs.

Appendix A

Boundary conditions for plate vibrations

The equation of motion (3.1) is a general one which does not take into account the boundary effects on a plate. However, it was shown in chapter 3 that, by imposing different boundary conditions, the eigenvalues and eigenvectors, or natural frequencies and mode shapes, can change. Simply-supported boundary conditions were outlined briefly as they give the only analytical solution to the equation of motion. In this appendix, a more in-depth analysis of the effects of different boundary conditions is given. A more complete discussion of different boundary conditions is given by Leissa [35].

There are three types of boundary conditions which can be modelled fairly easily mathematically [19]

Simply supported In this case the beam end is free to rotate but is constrained to have zero displacement and moment.

$$w(x) = 0 \qquad \text{and} \qquad \frac{\partial^2 w(x)}{\partial x^2} = 0 \tag{A.1}$$

Clamped The displacement and rotation are constrained to be zero.

$$w(x) = 0 \qquad \text{and} \qquad \frac{\partial w(x)}{\partial x} = 0 \tag{A.2}$$

Free The shear force and the internal bending moment must dissapear

$$\frac{\partial^2 w(x)}{\partial x^2} = 0 \qquad \text{and} \qquad \frac{\partial^3 w(x)}{\partial x^3} = 0 \tag{A.3}$$

In practice however, any of these idealisations are very hard to achieve perfectly and true boundary conditions lie somewhere in between these.

If the three of these boundary conditions are considered and it is assumed that each of the four edges of the plate can have one of these three boundary conditions then there are 21 combinations of simple boundary conditions for rectangular plates. These are all dealt with separately by Leissa [35] and the plate with all four edges simply-supported or with all four edges clamped are described below. These two particular sets of boundary conditions are covered in more detail because initial simulations in the thesis used simply-supported boundary conditions but later experiments used clamped boundaries. It is also confirmed below that, as far as the radiation properties of the plate are concerned, there is little difference between the two sets of boundary conditions, as shown by a comparison of the radiation efficiencies of the structural modes of simply-supported and clamped plates shown in figures 3.4 and 3.5 respectively.

For each set of boundary conditions, the eigenfunctions are first given for a beam. The plate eigenfunctions are then assumed to be created using the Rayleigh-Ritz method which states that the eigenfunction of a plate is simply the product of eigenfunctions in the x and y directions [35, 37]. The total deflection of the plate at a point (x, y) is then

$$w(x, y) = X(x)Y(y) \tag{A.4}$$

where $X(x)$ and $Y(y)$ are the fundamental mode shapes of beams with the same boundary conditions.

The shapes of the plate eigenfunctions or modes and natural frequencies are then compared, and an analysis of the sound radiation due to these two types of mode shapes is given.

A.1 Simply-supported boundary conditions

Simply-supported boundary conditions have been considered briefly above. They are the only set of boundary conditions which give analytic solutions to the plate equation of motion (3.1) and give rise to pure sinusoidal mode shapes.

The solution to the equation of motion is reviewed below: Consider a simply-supported beam of length L. The beam response is written as the superposition of two travelling waves in the positive and negative directions with unknown coefficients A and B

$$w(x,t) = Ae^{j\omega t - jk_f x} + Be^{j\omega t + jk_f x} \tag{A.5}$$

Now, removing the time dependence and, imposing the simply-supported boundary conditions means that there is zero displacement at the ends and so at $x = 0$

$$w(x)|_{x=0} = 0 \tag{A.6}$$

and so

$$A = -B \tag{A.7}$$

Imposing the same rule at $x = L$

$$w(x)|_{x=L} = 0 \tag{A.8}$$

and so

$$Ae^{j\omega t - jk_f L} + Be^{j\omega t + jk_f L} = 0 \tag{A.9}$$

and, substituting this equation back into equation (A.7) results in the displacement field

$$w(x,t) = -2Aj \sin k_f x e^{j\omega t} \tag{A.10}$$

Again applying the boundary condition of zero displacement at $x = L$ results in the mode shapes

$$\sin k_f L = 0 \tag{A.11}$$

with the eigenvalues

$$k_f = \frac{n\pi}{L} \qquad n = 1, 2, 3, \ldots \tag{A.12}$$

The beam can only resonate at the frequencies given by these wavenumbers. Using these values, the resonance frequencies of the beam can be calculated to be

$$\omega_n = n\pi \left(\frac{c}{L}\right), \qquad n = 1, 2, 3, \ldots \tag{A.13}$$

The first six mode shapes of a beam with both ends simply supported are shown in figure A.1

Once the beam functions have been derived, the total plate vibration pattern can be calculated using Rayleigh's principle. For the simply-supported plate, this is simply the product of sine functions. The shape of a single mode (m, n) is thus given by the equation

$$w_{mn}(x,y) = W_{mn} \sin(k_m x) \sin(k_n y)$$

where W_{mn} is a constant giving the amplitude of the mode.

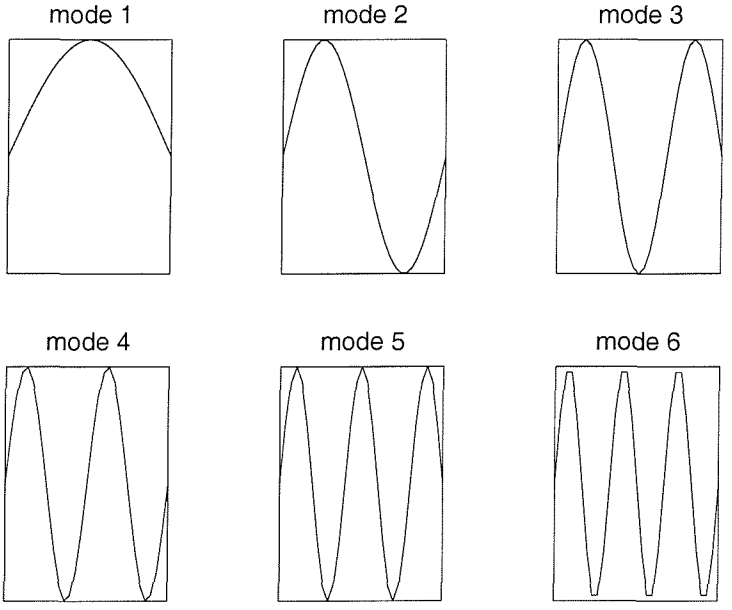

Figure A.1: First six mode shapes for a simply-supported beam

An example of the first six modes of the plate is shown in figure A.2. The equation giving the resonant frequencies of these modes is similar to (A.13)

$$\omega_{mn} = c\sqrt{\left(\frac{n\pi}{l_x}\right)^2 + \left(\frac{m\pi}{l_y}\right)^2} \tag{A.14}$$

Any vibration distribution caused by a disturbance will be a summation of these modes as given by equation (3.13).

As an example to demonstrate the effect of different boundary conditions on the response of a plate, it will be considered to be excited by an acoustic plane wave with angles of incidence $\theta = \phi = 45^0$. Figure A.3 then shows the power transmission ratio of the aluminium plate with simply-supported boundary conditions and excited by an acoustic plane wave.

The natural frequencies of the plate are calculated using equation (A.14) and are tabulated in table A.1

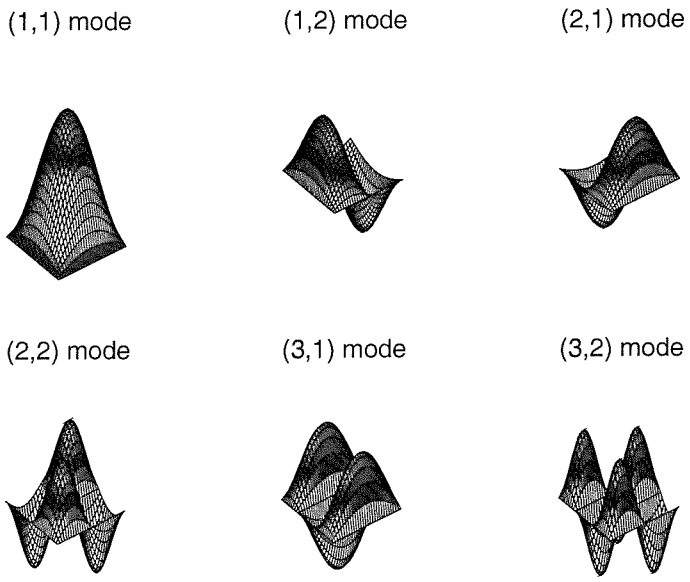

Figure A.2: Six mode shapes for a simply-supported plate

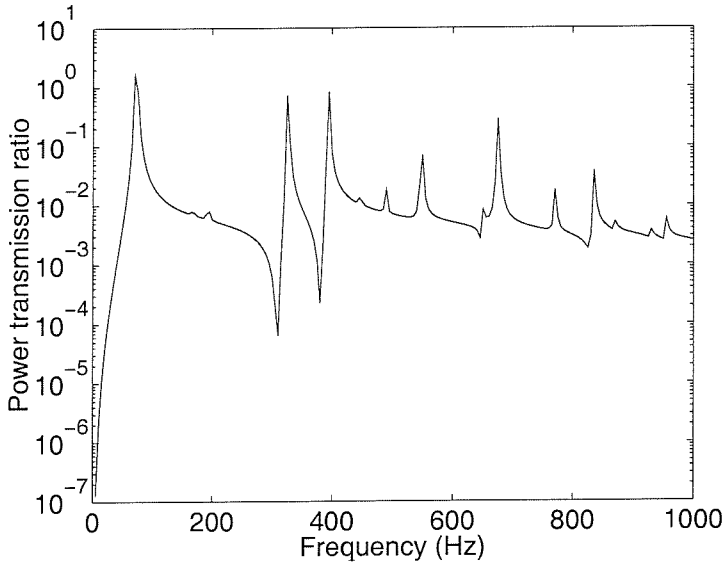

Figure A.3: Power transmission ratio for a simply-supported plate

n/m(Hz)	1	2	3
1	72	193	394
2	167	288	489
3	326	447	648

Table A.1: Natural frequencies of a simply-supported aluminium plate

A.2 Clamped boundary conditions

Unlike with the simply-supported boundary conditions, for beams which are clamped at both ends, the mode shapes and frequencies cannot be calculated analytically

This means that for a simply-supported beam, the eigenvectors can be defined exactly, whereas for a clamped beam, no exact solution can be formulated and hence approximate solutions must be used. There are a number of different approximate solutions and those of Warburton [37] will be used below. Other approximate methods are given in [35, 107–110] for example.

Warburton gives the eigenfunctions for the two sets of boundary conditions as

Simply-supported

$$\Psi(x) = \sin\frac{m\pi x}{l_x} \tag{A.15}$$

Clamped

$$\begin{aligned}
&\Psi(x) = \cos\gamma\left(\frac{x}{l_x} - \frac{1}{2}\right) + k\cosh\gamma\left(\frac{x}{l_x} - \frac{1}{2}\right) \qquad \text{for} \quad m \quad \text{even} \\
&\text{where} \\
&k = \frac{\sin\frac{\gamma}{2}}{\sinh\frac{\gamma}{2}} \qquad \text{and} \qquad \tan\frac{\gamma}{2} + \tanh\frac{\gamma}{2} = 0 \\
&\Psi(x) = \cos\gamma'\left(\frac{x}{l_x} - \frac{1}{2}\right) + k'\cosh\gamma'\left(\frac{x}{l_x} - \frac{1}{2}\right) \qquad \text{for} \quad m \quad \text{odd} \\
&\text{where} \\
&k' = -\frac{\sin\frac{\gamma'}{2}}{\sinh\frac{\gamma'}{2}} \qquad \text{and} \qquad \tan\frac{\gamma'}{2} - \tanh\frac{\gamma'}{2} = 0
\end{aligned} \tag{A.16}$$

(successive roots of equations are taken for increasing modal indices)

The first six modes shapes of a clamped beam are shown in figure A.4. A more direct comparison of the mode shapes for beams with the two different sets of boundary conditions is then shown in figure A.5

The differences between the two sets of mode shapes are seen to be local to the edges of the beam which are slightly flattened in the case of clamped boundary conditions.

The two-dimensional plate eigenfunctions are obtained using the Rayleigh method i.e. by the product of eigenfunctions in the x and y directions. The modal frequencies as well as the eigenfunctions of the clamped plate cannot be calculated analytically and again, approximation methods are used as outlined by Warburton [37] for example. These are quoted by Gardonio and Elliott [111] as

$$\omega_{mn} = \sqrt{\frac{Eh^2}{12\rho(1-\mu^2)}} \left(\frac{\pi}{l_x}\right)^2 q_{ik} \tag{A.17}$$

where $i = m+1, k = n+1$ and

$$q_{ik} = \sqrt{G_x^4(i) + G_y^4(k) \left(\frac{l_x}{l_y}\right)^4 + 2\left(\frac{l_x}{l_y}\right)^2 [\mu H_x(i) H_y(k) + (1-\mu) J_x(i) J_y(k)]} \tag{A.18}$$

The constants $G_x, G_y, H_x, H_y, J_x, J_y$ are given in table A.2.

A comparison of the first mode shape for the simply-supported and clamped plates is shown in figure A.6.

i or k	G_x or G_y	H_x or H_y	J_x or J_y
2	1.506	1.238	1.248
3,4,5,...	$i - \frac{1}{2}$	$\left(i-\frac{1}{2}\right)^2\left(1-\frac{4}{(2i-1)\pi}\right)$	$\left(i-\frac{1}{2}\right)^2\left(1-\frac{4}{(2i-1)\pi}\right)$

Table A.2: Constants to calculate natural frequencies of a clamped plate

A table of natural frequencies for the clamped plate is given in A.3.

Figure A.7 then shows the power transmission ratio for a clamped aluminium plate, again excited by an acoustic plane wave. The two tables of resonant frequencies and the figures of power transmission ratios show the difference between simply-supported and clamped boundary functions. Although the general features of the frequency response functions are similar, resonant frequencies of the clamped plate are around 1.5 times higher than their simply-supported counterparts.

The sound power radiated by plates with simply-supported and clamped boundary conditions has been compared in figures 3.4 and 3.5, which shows that the radiation efficiencies of the struc-

n/m(Hz)	1	2	3
1	132	289	529
2	250	398	634
3	438	578	807

Table A.3: Natural frequencies of a clamped aluminium plate

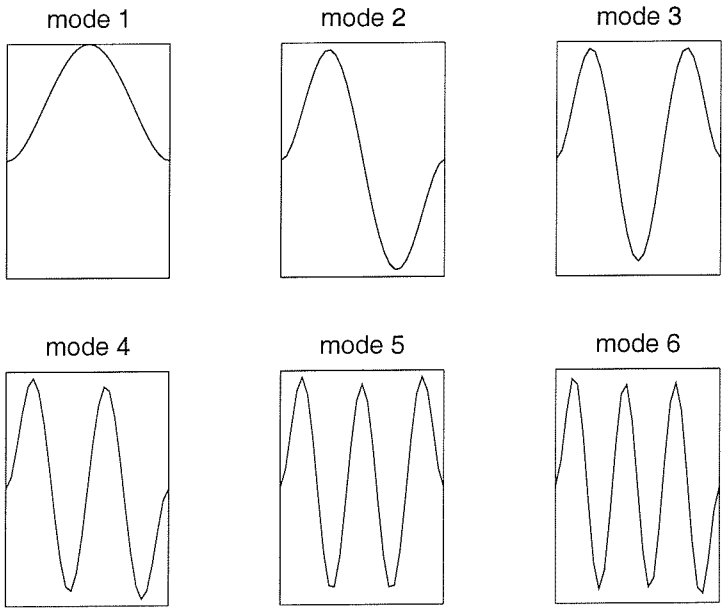

Figure A.4: First six mode shapes for a clamped beam

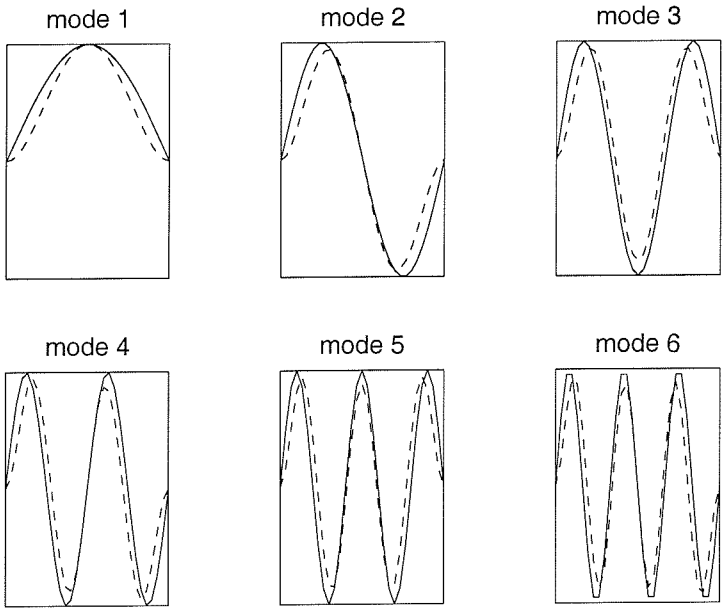

Figure A.5: Comparison of first six mode shapes for simply-supported (solid lines) and clamped (dashed lines) beams

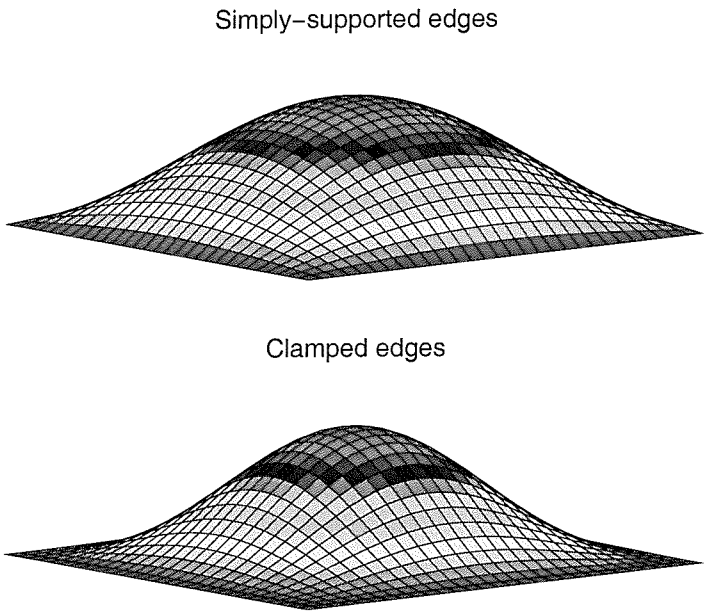

Figure A.6: (1,1) mode of a simply-supported plate and a clamped plate

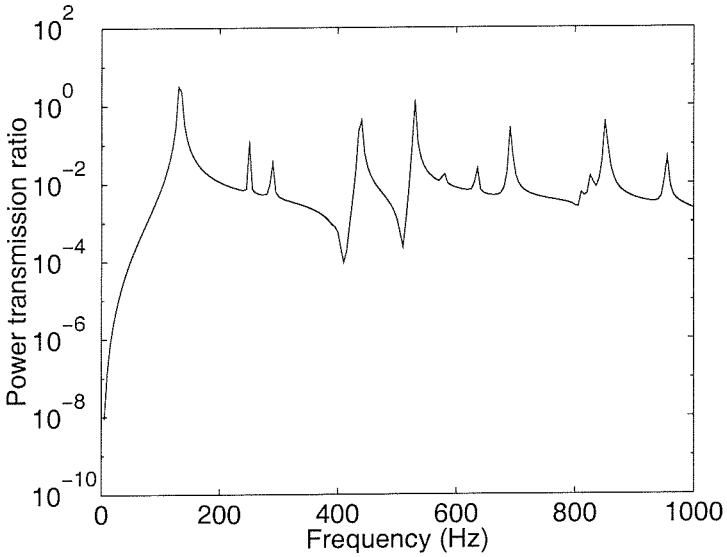

Figure A.7: Power transmission ratio for a clamped plate

tural modes of a clamped plate are similar to those of a simply-supported plate. Several authors [109, 110, 112] also show that, at low frequencies, the sound radiation from plates with the two different types of boundary conditions is very similar. Berry *et al.* [112] in particular compare the radiation efficiencies of individual modes (equation 3.24) for the two sets of boundary conditions and these are seen to differ by no more than $4dB$, the highest differences occuring for high-low modes (e.g. where m is large and n is small). They conclude that an elastic restraint against rotation at the edges does not significantly effect the radiation efficiency. They also note that up to the critical frequency of the plate, only the piston motion, or volume velocity, is required to provide a good estimate of the radiated power. At high frequencies however, a clamped edge can have approximately twice the efficiency per unit length of a simply-supported edge [110].

The radiation modes have also been shown to be dependent on the geometry of the surface but independent of the dynamic properties of the surface so their radiation efficiencies will not be affected by the different boundary conditions.

Appendix B

A common formulation for the control of volume velocity and the control of sum of squared errors

This appendix gives a common formulation for controlling the approximation to the volume velocity using a number of accelerometers, controlling the sum of the squared accelerometer signals, which turns out to be closer to vibration control, and controlling the radiated sound power.

B.1 Weightings on sensors

For a direct comparison between the control of volume velocity and the control of sum of squared errors, the cost equation (6.7), can be expressed as

$$J = \boldsymbol{e}^H \boldsymbol{W}_s \boldsymbol{e} \tag{B.1}$$

where the matrix $\boldsymbol{W}_s$ repreresents the individual weightings for the separate structural sensors.

Three such weighting functions have been examined in the thesis:

1. Vibration control which is equivalent to minimising the sum of the squared errors

$$J = \sum_{i=1}^{n_{se}} |e_i|^2 \tag{B.2}$$

where n_{se} is the number of sensors.

In this case, the weighting matrix $\boldsymbol{W}_s$ is given by the identity matrix. For example, for four sensors, it would be

$$\boldsymbol{W}_s = \begin{pmatrix} 1 & 0 & 0 & 0 \\ 0 & 1 & 0 & 0 \\ 0 & 0 & 1 & 0 \\ 0 & 0 & 0 & 1 \end{pmatrix} \tag{B.3}$$

2. Control of volume velocity as approximated by the accelerometers. This is equivalent to minimising the squared summed error.

$$J = |\sum_{i=1}^{n_{se}} e_i|^2 \tag{B.4}$$

In this case, the weighting matrix for four sensors is given by

$$\boldsymbol{W}_s = \begin{pmatrix} 1 & 1 & 1 & 1 \\ 1 & 1 & 1 & 1 \\ 1 & 1 & 1 & 1 \\ 1 & 1 & 1 & 1 \end{pmatrix} \tag{B.5}$$

With the elemental models used in this thesis, controlling the true volume velocity would require an accelerometer at each element as shown in chapter 6.

3. Control of radiated power. Equation (3.30) shows that the radiated power can also be expressed as

$$power = \boldsymbol{v}^H \boldsymbol{R} \boldsymbol{v} \tag{B.6}$$

with the elemental velocities denoted by $\boldsymbol{v}$ and the radiation resistance matrix $\boldsymbol{R}$ being given by equation (3.34).

$$\boldsymbol{R} = \frac{\omega^2 \rho S^2}{4\pi c} \begin{bmatrix} 1 & \frac{\sin kr_{12}}{kr_{12}} & \dots & \frac{\sin kr_{1I}}{kr_{1I}} \\ \frac{\sin kr_{21}}{kr_{21}} & 1 & \dots & \dots \\ \dots & \dots & \dots & \dots \\ \frac{\sin kr_{I1}}{kr_{I1}} & \dots & \dots & 1 \end{bmatrix}$$

This clearly has a very similar form to equation (B.1) where $\boldsymbol{e}$ represents a reduced version of $\boldsymbol{v}$ where only the relevant values are taken according to the elements in which the accelerometers are placed. In this case, the matrix $\boldsymbol{W}_s$ is given directly by a reduced form of $\boldsymbol{R}$ (again by taking the elements at which sensors are placed).

Note that in the low frequency limit, where $kl \to 0$

$$\lim_{kl \to 0} \boldsymbol{R} = \frac{\omega^2 \rho S^2}{4\pi c} \begin{bmatrix} 1 & 1 & \dots \\ 1 & 1 & \dots \\ & & \dots \\ \dots & \dots & 1 \end{bmatrix} \tag{B.7}$$

which corresponds to the volume velocity weighting matrix given in (B.5).

4. One further weighting which would be of interest would be the matrix $\boldsymbol{W}_s$ which corresponds to the minimisation of the pressure at a number of far-field error sensors. In this case, each element of the matrix would represent the frequency response function between vibration at the positions of the accelerometers and the radiated sound pressure at the microphones.

B.2 Weightings on actuators

In an analogous approach, a variation on the cost function, equation (6.11) is given by,

$$J = \boldsymbol{u}^H \boldsymbol{W} \boldsymbol{u} + (\boldsymbol{d} + \boldsymbol{G}\boldsymbol{u})^H \boldsymbol{\lambda} + \boldsymbol{\lambda}^H (\boldsymbol{d} + \boldsymbol{G}\boldsymbol{u}) \tag{B.8}$$

where $\boldsymbol{W}$ is a weighting matrix for the input voltages. Provided that the matrix $\boldsymbol{W}$ is symmetric, then the vector of control voltages in the underdetermined case described above is

$$\boldsymbol{u}_o = -\boldsymbol{G}^H \left(\boldsymbol{G}\boldsymbol{W}\boldsymbol{G}^H\right)^{-1} \boldsymbol{d} \tag{B.9}$$

(c.f. equation 6.12).

Cancelling the sum of squared errors with minimum effort, outlined above, gives each actuator the same value of unity in the weighting matrix. An example of the weighting matrix for 5 actuators is then given by

$$\boldsymbol{W} = \begin{pmatrix} 1 & 0 & 0 & 0 & 0 \\ 0 & 1 & 0 & 0 & 0 \\ 0 & 0 & 1 & 0 & 0 \\ 0 & 0 & 0 & 1 & 0 \\ 0 & 0 & 0 & 0 & 1 \end{pmatrix} \tag{B.10}$$

The weightings on the different actuators can now be changed and is shown by the corresponding element in the weighting matrix. Further flexibility can be given to this cost function by making the weighting function a function of frequency $\boldsymbol{W}(\omega)$, or by giving separate weighting constants to the parts of the error criterion minimising control effort($\boldsymbol{u}^H\boldsymbol{W}\boldsymbol{u}$) and the sensor outputs ($\boldsymbol{d} + \boldsymbol{G}\boldsymbol{u}$) i.e. by introducing a $\boldsymbol{W}_1$ and $\boldsymbol{W}_2$ say.

$$J = \boldsymbol{u}^H\boldsymbol{W}_1\boldsymbol{u} + (\boldsymbol{d} + \boldsymbol{G}\boldsymbol{W}_2\boldsymbol{u})^H\boldsymbol{\lambda} + \boldsymbol{\lambda}^H(\boldsymbol{d} + \boldsymbol{G}\boldsymbol{W}_2\boldsymbol{u}) \tag{B.11}$$

References

[1] M. E. Johnson, T. Sors, S. J. Elliott, and B. Rafaely. Feedback control of broadband sound radiation using a volume velocity sensor. In *Proc. Active 97*, pages 1007–1020, Budapest, Hungary, August 1997.

[2] T. Sors and S. J. Elliott. Choice of integrated actuators and sensors and their placement for active structural acoustic control of a simply-supported panel. In *Proc. MOVIC 98*, pages 671–676, Zuirch, Switzerland, August 1999.

[3] T. C. Sors and S. J. Elliott. Modelling and feedback control of sound radiation from a vibrating panel. *Journal of Smart Materials and Structures*, 8:301–314, 1999.

[4] J. P. Maillard and C. R. Fuller. Comparison of two structural sensing approaches for active structural acoustic control. *J. Acoust. Soc. Am.*, 103(1):396–400, January 1998.

[5] C. Guigou and C. R. Fuller. Control of aircraft interior broadband noise with foam-PVDF smart skin. *Journal of Sound and Vibration*, 220(3):541–557, 1998.

[6] D. A. Bies and C. H. Hansen. *Engineering noise control.* Unwin Hyman, London, 1988.

[7] M. E. Johnson. *Active control of sound transmission.* PhD thesis, Institute of Sound and Vibration Research, University of Southampton, May 1996.

[8] C. A. Gentry, C. Guigou, and C. R. Fuller. Smart foam for applications in passive-active noise radiation control. *J. Acoust. Soc. Am.*, 101(4):1771–1778, 1997.

[9] P. Lueg. Process of silencing sound oscillations. US Patent No. 2,043,416, 1936.

[10] H. F. Olson and E. G. May. Electronic sound absorber. *J. Acoust. Soc. Am.*, 25(6):1130–1136, 1953.

[11] P. A. Nelson and S. J. Elliott. *Active Control of Sound.* Academic Press, London, 1992.

[12] J. H. B. Poole and H. G. Leventhall. An experimental study of Swinbanks' method of active attenuation of sound in ducts. *Journal of Sound and Vibration*, 49:257–266, 1976.

[13] A. Roure. Self-adaptive broadband active sound control system. *Journal of Sound and Vibration*, 101(3):429–441, 1985.

[14] R. H. G. Thompsett. *Active control of transmitted sound in buidings.* PhD thesis, Institute of Sound and Vibration Research, University of Southampton, July 1998.

[15] A. R. D. Curtis. *The theory and application of quadratic minimisation in the active reduction of sound and vibration.* PhD thesis, Institute of Sound and Vibration Research, University of Southampton, 1998.

[16] C. R. Fuller and A. H. von Flotow. Active control of sound and vibration. IEEE *Control systems magazine*, 15(6):9–19, December 1995.

[17] B. Rafaely. *Feedback control of sound.* PhD thesis, Institute of Sound and Vibration Research, University of Southampton, October 1997.

[18] E. F. Berkman and E. K. Bender. Perspectives on active noise and vibration control. *Sound and Vibration*, pages 80–94, January 1997.

[19] C. A. Fuller, S. J. Elliott, and P. A. Nelson. *Active Control of Vibration.* Academic Press, London, 1996.

[20] C. R. Fuller, C. A. Rogers, and H. H. Robertshaw. Control of sound radiation with active/adaptive structures. *Journal of Sound and Vibration*, 157(1):19–39, 1992.

[21] C. R. Fuller. Experiments on reduction of aircraft interior noise using active control of fuselage vibration. *J. Acoust. Soc. Am.*, 78(S1):S88, 1985.

[22] A. I. Vyalyshev, A. I Dubinin, and B. D. Tartakovskii. Active acoustic reduction of a plate. *Soviet Physics Acoustics*, 32(2):96–98, 1986.

[23] C. R. Fuller, C. H. Hansen, and S. D. Snyder. Active control of sound radiation from a vibrating rectangular panel by sound sources and vibration inputs: An experimental comparison. *Journal of Sound and Vibration*, 145(2):195–215, 1991.

[24] B. Wang, C. R. Fuller, and E. K. Dimitriadis. Active control of noise transmission through rectangular plates using mupltiple piezoelectric or point force actuators. *J. Acoust. Soc. Am.*, 90(5):2820–2830, 1991.

[25] C. K. Lee and F. C. Moon. Modal sensors/actuators. *Journal of Applied Mechanics. Trans. ASME*, 57:434–441, 1990.

[26] P. Gardonio, Y. S. Lee, S. J. Elliott, and S. Debost. Active control of sound transmission through a panel with a matched PVDF sensor and actuator pair. In *Proc. Active 99*, pages 341–354, Florida, USA, December 1999.

[27] A. Preumont. *Vibration control of active structures. An introduction.* Kluwer Academic Publishers, The Netherlands, 1997.

[28] M. W. Hillier, M. D. Bryant, and J. Umegaki. Attenuation and the transformation of vibration through active control of magneto-strictive Terfenol. *Journal of Sound and Vibration*, 134(3):507–579, 1989.

[29] C. Liang, C. A. Rogers, and C. R. Fuller. Acoustic transmission and radiation analysis of adaptive shape-memory alloy reinforced laminated plates. *Journal of Sound and Vibration*, 145(1):23–41, 1991.

[30] G. F. Franklin, J. D. Powelll, and A. Emami-Naeini. *Feedback control of dynamic systems.* Addison-Wesley, USA, 1986.

[31] N. J. Doelman. *Design of systems for active sound control.* PhD thesis, Delft University, The Netherlands, 1993.

[32] W. Tseng, B. Rafaely, and S. J. Elliott. Combined feedback-feedforward active control of sound in a room. *J. Acoust. Soc. Am.*, 104(6):3417–3425, 1998.

[33] L. Cremer, M. Heckl, and E. E. Ungar. *Structure-borne sound.* Springer Verlag, Berlin, second edition, 1988.

[34] F. Fahy. *Sound and Structural Vibration: Radiation, transmission and response.* Academic Press, London, 1985.

[35] A. Leissa. *Vibration of plates.* Acoustical Society of America, USA, reprinted edition, 1993.

[36] L. Meirovitch. *Analytical methods in vibrations.* Macmillan, USA, 1967. Macmillan series in applied mechanics.

[37] G. B. Warburton. The vibration of rectangular plates. *Proceedings of the Institute of Mechanical Engineers*, 168:371–384, 1954.

[38] M. C. Junger and D. Feit. *Sounds, Structures, and their interaction.* The MIT press, USA, second edition, 1986.

[39] C. E. Wallace. Radiation resistance of a rectangular panel. *J. Acoust. Soc. Am.*, 51(3):946–952, 1972.

[40] S. J. Elliott and M. E. Johnson. Radiation modes and the active control of sound power. *J. Acoust. Soc. Am.*, 94:2194–2204, 1993.

[41] M. E. Johnson and S. J. Elliott. Active control of sound radiation using volume velocity cancellation. *J. Acoust. Soc. Am.*, 94:2174–2186, 1995.

[42] P. Vitiello, P. A. Nelson, and M. Petyt. Numerical studies of the active control of sound transmission through double partitions, September 1989. ISVR Technical Report No. 183.

[43] K. A. Cunefare. The minimum multimodal radiation efficiency of baffled finite beams. *J. Acoust. Soc. Am.*, 90(5):2521–2529, 1991.

[44] K. Naghshineh and G. H. Koopmann. Active control of sound power using acoustic basis functions as surface velocity filters. *J. Acoust. Soc. Am.*, 93(5):2740–2752, 1993.

[45] W. T. Baumann, W. R. Saunders, and H. R. Robertshaw. Active suppression of acoustic radiation from impulsively excited structures. *J. Acoust. Soc. Am.*, 90:3202–3208, 1991.

[46] G. V. Borgiotti and K. E. Jones. Frequency dependence property of radiation spatial filters. *J. Acoust. Soc. Am.*, 96(6):3516–3524, 1994.

[47] M. E. Johnson and S. J. Elliott. Active control of sound radiation from vibrating surfaces using arrays of discrete actuators. *Journal of Sound and Vibration*, 207(5):743–759, 1997.

[48] K. Naghshineh and V Bradford Mason. Reduction of sound radiated from vibrating structures via active control of local volume velocity. *Applied Acoustics*, 47:27–46, 1996.

[49] R. L. St. Pierre Jr., G. H. Koopmann, and W. Chen. Volume velocity control of sound transmission through composite panels. *Journal of Sound and Vibration*, 210(4):441–460, 1998.

[50] C. K. Lee. Theory of laminated piezoelectric plates for design of distributed sensors/actuators. Part I:governing equations and reciprocal relationships. *J. Acoust. Soc. Am.*, 87:1144–1158, 1990.

[51] B. Wang, R. A. Burdisso, and C. R. Fuller. Optimal placement of piezoelectric actuators for active control of sound radiation from elastic plates. In *Proc. Noise-con 91*, pages 267–274, New York, USA, July 1991.

[52] K. H. Baek and S. J. Elliott. Natural algorithms for choosing source locations in active control systems. *Journal of Sound and Vibration*, 186(2):245–267, 1995.

[53] L. P Heck, J. A Olkin, and K. Naghshineh. Transducer placement for active vibration control using a novel multidimensional QR factorization. *Journal of Vibration and Acoustics, Trans. ASME*, 120:663–670, 1998.

[54] C. R. Fuller. Active control of sound transmission/radiation from elastic plates by vibration inputs: I. analysis. *Journal of Sound and Vibration*, 136(1):1–15, 1990.

[55] C. R. Fuller. Analysis of active control of sound radiation from elastic plates by force inputs. In *Proc. Inter-Noise 88*, pages 1061–1064, Avignon, France, 1988.

[56] L. Meirovitch and M. A. Norris. Vibration control. In *Proc. Inter-Noise 84*, pages 477–482, Honolulu, USA, 1984.

[57] E. F. Crawley and J. de Luis. Use of piezoelectric actuators as elements of intelligent structures. *AIAA Journal*, 25(10):1373–1385, 1987.

[58] V. R. Sonti, S. J. Kim, and J. D. Jones. Equivalent forces and wavenumber spectra of shaped piezoelectric actuators. *Journal of Sound and Vibration*, 187(1):111–131, 1995.

[59] E. K. Dimitriadis, C. R. Fuller, and C. A. Rogers. Piezoelectric actuators for distributed vibration excitation of thin plates. *Journal of Vibration and Acoustics. Trans. ASME*, 113:100–107, 1991.

[60] L. A. Roussos. Noise transmission loss of a rectangular plate in an infinte baffle. Technical Report NASA-TP-2398, NASA, March 1985.

[61] B. Wang. Active control of noise transmission through rectangular plates using multiple piezoelectric or point force actuators. *J. Acoust. Soc. Am.*, 90(5):2820–2830, 1991.

[62] A. C. Nilsson. Reduction index and boundary conditions for a wall between two rectangular rooms. part I: Theoretical results. *Acustica*, 26:1–18, 1972.

[63] C. H. Jo. *M.Sc. thesis: Active control of low frequency sound transmission.* PhD thesis, Institute of Sound and Vibration Research, University of Southampton, 1990.

[64] S. Kim. *Active control of sound in structural-acoustic coupled systems.* PhD thesis, Institute of Sound and Vibration Research, University of Southampton, April 1998.

[65] R. Josse and C. Lamure. Transmission do son par un paroi simple. *Acustica*, 14:266–280, 1964.

[66] L. L. Beranek. *Noise and Vibration Control.* Institute of Noise Control Engineering, Washington, DC, USA, 1988.

[67] J. T. Broch. *Mechanical Vibration and Shock Measurements.* Bruel and Kjaer, Denmark, 1984.

[68] J. Rex and S. J. Elliott. The QWSIS - a new sensor for structural radiation control. In *Proc. 1st International Conf. on Motion and Vibration Contol*, pages 339–343, Yokohama, Japan, 1992.

[69] M. E. Johnson and S. J. Elliott. Experiments on the active control of sound radiation using a volume velocity sensor. In *Proc. Smart Structures and Integrated Systems Conference, SPIE Vol. 2443*, pages 658–669, San Diego, USA, 1995.

[70] C. Guigou, A. Berry, F. Charette, and J. Nicolas. Active control of finite beam volume velocity using shaped PVDF sensor. *Acustica*, 82:772–783, 1996.

[71] C. Guigou, Z. Li, and C. R. Fuller. The relationship between volume velocity and far field radiated pressure of a planar structure. *Journal of sound and vibration*, 197(2):252–254, 1996.

[72] M. Tohyama and R. H. Lyon. Zeros of a transfer function in a multi-degree-of-freedom vibrating system. *J. Acoust. Soc. Am.*, 86:1854–1862, 1989.

[73] E. H. Anderson and N. W. Hagood. Simultaneous piezoelectric sensing/actuation: Analysis and application to controlled structures. *Journal of Sound and Vibration*, 174(4):617–639, 1994.

[74] S. E. Burke, J. E. Hubbard, and J. E. Meyer. Distributed transducers and collocation. *Mechanical Systems and Signal Processing*, 7(4):349–361, 1993.

[75] G. F. Franklin and J. D. Powelll. *Digital control of dynamic systems.* Addison-Wesley, USA, 1980.

[76] S. J. Elliott. Control theory lecture notes, 1995. ISVR, University of Southampton.

[77] M. Morari and E. Zafiriou. *Robust Process Control.* Prentice-Hall International, Inc., USA, 1989.

[78] D. E. Newland. *An introduction to random vibrations and spectral analysis.* Longman, USA, second edition, 1984.

[79] J. S. Bendat and A. G. Piersol. *Random data. Analysis and measurement procedures.* John Wiley and Sons, USA, second edition, 1986.

[80] S. Skogestad and I. Postlethwaite. *Multivariable feedback control.* Wiley, Great Britain, 1996.

[81] M. J. Grimble and M. A. Johnson. *Optimal control and stochastic estimation. Theory and applications. Volumes 1 and 2.* Wiley, UK, 1988.

[82] S. J. Elliott. Active control using feedback, January 1994. ISVR Technical Memorandum No. 732.

[83] D. C. Youla, J. J. Bongiorno, and H. A. Jabr. Modern Wiener-Hopf design of optimal controllers - part I, the single input-output case. *IEEE Tran. Autom. Control*, AC-21:3–13, 1976.

[84] D. C. Youla, J. J. Bongiorno, and H. A. Jabr. Modern Wiener-Hopf design of optimal controllers - part II, the multivariable case. *IEEE Tran. Autom. Control*, AC-21:319–338, 1976.

[85] G. Zames. Feedback and optimal sensitivity: Model reference transformations, multiplicative seminorms and approximate inverses. *IEEE Tran. Autom. Control*, AC-26:301–320, 1981.

[86] J. C. Doyle. Analysis of control systems with structured uncertainty. *IEE Proc. Part D*, 129:242, 1982.

[87] S. J. Elliott and T. J. Sutton. Feedforward and feedback methods for active control. *Proceedings of the Institute of Acoustics*, 16:255–273, 1994.

[88] S. J. Elliott and T. J. Sutton. Performance of feedforward and feedback systems for active control. IEEE *Transactions on speech and audio processing*, 4:214–223, 1996.

[89] S. J. Elliott, T. J. Sutton, B. Rafaely, and M. Johnson. Design of feedback controllers using a feedforward approach. In *Proc. Active 95*, pages 863–874, Newport Beach, CA, USA, July 1995.

[90] J. Mørkholt, S. J. Elliott, and T. C. Sors. A comparison of state space LQG, Wiener IMC and polynomial LQG discrete time feedback control for active vibration control purposes, December 1997. ISVR Technical Memorandum No. 823.

[91] B. Widrow and S. D. Stearns. *Adaptive signal processing.* Prentice-Hall, USA, 1985.

[92] S. J. Elliott, I. M. Stothers, and P. A. Nelson. A multiple error LMS algorithm and its application to the active control of sound and vibration. *IEEE Transactions on acoustics, speech, and signal processing*, 10:1423–1434, October 1987.

[93] B. C. Kuo. *Digital control systems.* Holt, Rinehart and Winston, New York, 1980.

[94] J. C. Doyle, B. A. Francis, and A. R. Tannenbaum. *Feedback control theory.* Macmillan, New York, USA, 1992.

[95] International organization for standardization. *International Standard ISO 3745, Acoustics - Determination of sound power levels of noise sources - Precision methods for anechoic and semi-anechoic room.*, May 1977.

[96] A. Preumont, A. François, and S. Dubru. Piezoelectric array sensing for real-time, broadband sound radiation measurement. *Journal of Vibration and Acoustics, Trans. ASME*, 21:446–452, 1999.

[97] R. G. White and J. G. Walker (editors). *Noise and Vibration.* Ellis Horwood, Great Britain, 1982.

[98] W. Ko. The future of sensor and actuator systems. *Sensors and actuators*, 56:193–197, 1996.

[99] H. Subramanian, V. K. Varadan, V. V. Varadan, and M. J. Vellekoop. Design and fabrication of wireless remotely readable MEMS based microaccelerometers. *Journal of Smart Materials and Structures*, 6:730–738, 1997.

[100] M. J. Balas. Direct velocity feedback of large space structures. *Journal of Guidance and Control*, 2:252–253, 1979.

[101] S. J. Elliott, T. C. Sors, M. Brennan, and P. Gardonio. Active vibro-acoustic control with multiple local feedback loops. Submitted to Proc. SPIE 8'th Annual International Symposium on Smart Materials and Structures, March 2001.

[102] J. P. Maillard and C. R. Fuller. Active control of sound radiation from cylinders with piezo-electric actuators and structural acoustic sensing. In *Proc. Active 97*, pages 1021–1034, Budapest, Hungary, August 1997.

[103] J. P. Maillard and C. R. Fuller. Advanced time domain wave-number sensing for structural acoustic systems. I. theory and design. *J. Acoust. Soc. Am.*, 95(6):3252–3261, 1994.

[104] J. P. Maillard and C. R. Fuller. Advanced time domain wave-number sensing for structural acoustic systems. II. active radiation control of a simply supported beam. *J. Acoust. Soc. Am.*, 95(6):3262–3272, 1994.

[105] J. P. Maillard and C. R. Fuller. Advanced time domain wave-number sensing for structural acoustic systems. III. experiments on active broadband radiation control of a simply-supported plate. *J. Acoust. Soc. Am.*, 98(5):2613–2621, 1995.

[106] J. Maillard. *Advanced time domain sensing for Active Structural Acoustic Control.* PhD thesis, Virginia Polytechnic Institute and State University, 1997.

[107] R. E. D. Bishop. The analysis of vibrating systems which embody beams in flexure. *Proceedings of the Institute of Mechanical Engineers*, 169:1031–1046, 1955.

[108] Nilsson. Propellor induced hull plate vibrations. *Journal of Sound and Vibration*, 69(4):539–557, 1980.

[109] G. C. Sung and J. T. Jan. The response of and sound power radiated by a clamped rectangular plate. *Journal of Sound and Vibration*, 207(4):301–317, 1997.

[110] N. S. Lomas and S. I. Hayek. Vibration and acoustic radiation of elastically supported rectangular plates. *Journal of Sound and Vibration*, 52(1):1–25, 1977.

[111] P. Gardonio and S. J. Elliott. Driving point and transfer mobility matrices for thin plates excited in flexure, August 1998. ISVR Technical Report No. 277.

[112] A. Berry, J. L. Guyader, and J. Nicolas. A general formulation for the sound radiation from rectangular, baffled plates with arbitrary boundary conditions. *J. Acoust. Soc. Am.*, 88(6):2792–2802, 1990.